The Host Galaxies of Active Galactic Nuclei

Ross James McLure

Presented for the Degree of Doctor of Philosophy
The University of Edinburgh
1999

This thesis is dedicated to my parents.

This thesis is my own composition except where indicated in the text.

January 17, 2000

Acknowledgements

My thanks go primarily to my supervisors, James Dunlop and Marek Kukula, for their invaluable advise throughout the course of my PhD. In addition, I would like to acknowledge the unlimited encouragement and financial support provided by my parents during what must have seemed like my endless student career. I think it is safe to say that this thesis is by far the most expensive coffee-table book they will ever buy. Moreover, I wish to thank Matt Horrobin, Helen Valentine and Thomas Nye for both their friendship, and their consistent willingness to pop out for a quick lager-tops.

Finally, I would like to acknowledge the unique contribution made by a certain Miss Joanne Watkins. From a position of nearly drinking me to death in the summer of 1998, Jo subsequently provided the motivation to complete this thesis before the turn of the century. Thanks Jo.

Contents

1 Introduction 1

1.1 The Discovery of Quasars 1

1.1.1 The Host Galaxies of AGN 3

1.2 An AGN Menagerie 4

1.2.1 Seyfert Galaxies 4

1.2.2 Radio Galaxies 8

1.2.3 Quasars 10

1.2.4 BL Lacs and OVV Quasars 12

1.3 The Standard Model for AGN 14

1.3.1 The Black-hole and Accretion Disc 14

1.4 Unification schemes 17

1.4.1 Radio-Quiet Unification 18

1.4.2 Radio-Loud Unification 20

1.5 Evidence for Supermassive Black-holes 21

1.5.1 HST Imaging and Spectroscopy of M87 21

1.5.2 Water Masers in NGC4258 22

1.5.3 Asymmetric Iron Line Profiles 22

1.5.4 Black-hole Mass Correlations in Inactive Elliptical Galaxies 23

1.6 Host Galaxy Studies Of Powerful AGN 24

1.6.1 Ground-based Imaging Studies 24

1.6.2 HST Imaging Studies 27

1.7 Aims of the Project 29

1.7.1 Thesis Structure 30

2 A Hubble Space Telescope Study of AGN Host Galaxies at z=0.2 **32**

2.1 Introduction 32

2.2 The Sample 33

2.2.1 Sub-sample Matching Criteria 35

2.3 The Wide Field and Planetary Camera 41

2.4 Observing Strategy 43

2.4.1 Filter Choice 43

2.4.2 Detector Choice 45

2.4.3 Exposure Times 48

2.4.4 PSF Observations 48

2.5 Data Reduction 50

2.5.1 Background Determination 51

2.6 Notes about Individual Objects 55

2.6.1 The Radio Galaxies 55

2.6.2 The Radio-Loud Quasars 60

2.6.3 The Radio-Quiet Quasars 63

3 Methods of Host Galaxy Analysis **72**

3.1 Point Spread Function Subtraction 72

3.2 One-Dimensional Profile Fitting 73

3.3 Two-Dimensional Modelling Technique 76

3.3.1 The WFPC2 PSF 78

3.3.2 Error Allocation 80

3.3.3 Minimization 83

3.4 Testing the Modelling Code 85

3.4.1 Synthetic Quasar Construction 86

3.5 Beta Parameter Modelling 91

3.5.1 Testing the Beta Modelling Code 94

3.6 Combined Disk-Bulge Modelling 95

4 Host Galaxy Modelling Results **97**

4.1 Modelling Procedure 97

4.2 Host Galaxy Morphologies 98

4.3 Host Galaxy and AGN Luminosities 105

4.3.1 Host Galaxy Luminosities 106

4.3.2 Nuclear Luminosities 110

4.3.3 Quasar Host-Nuclear luminosity correlation 112

4.4 Scalelengths 114

4.5 Kormendy Relation 117

4.6 Axial Ratios 121

4.7 Tip-Tilt Observations of Quasar Host Galaxies 124

4.7.1 The Sample 125

4.7.2 The Observations 125

4.7.3 Reduction 127

4.7.4 Image Defects 128

4.7.5 The IRCAM3 Point Spread Function 130

4.7.6 Results 131

4.7.7 Host Morphologies 132

4.7.8 Scalelengths 132

4.7.9 Host Luminosities 134

4.7.10 Discussion 135

4.8 Colours 136

4.9 Comparison with Brightest Cluster Galaxies 143

4.10 Interactions 149

4.11 Comparison with results in the Literature 151

4.11.1 Bahcall *et al.* 151

4.11.2 McLeod & Rieke 153

4.11.3 Boyce *et al.* 153

4.11.4 Kotilainen *et al.* 154

4.12 Summary and Conclusions 154

5 AGN Black-Hole Masses **157**

5.1 Introduction 157

5.2 The Host Mass–Black-hole connection 158

5.3 The Radio Power–Black-hole connection 166

5.3.1 Total Radio Power 167

5.3.2 Core Radio Power 173

5.4 Discussion: The Origin of Radio-Loudness 176

6 The Evolution of 3CR Radio Galaxies from z=1 **183**

6.1 Introduction 183

6.2 Data Reduction 188

6.2.1 Empirical PSF Determination 190

6.3 Modelling 191

6.4 Results 192

6.4.1 Scalelengths 193

6.4.2 Absolute Magnitudes 195

6.4.3 The Kormendy Relation 197

6.5 Comparison with low-redshift Radio Galaxies 199

6.5.1 Scalelengths 199

6.5.2 Absolute Luminosity 200

6.5.3 Kormendy Relation 201

6.6 Conclusion 204

7 Conclusions and Further Work **207**

7.1 Conclusions 207

7.1.1 Morphology and Luminosity 207

7.1.2 Characteristic Sizes and The Kormendy Relation 208

7.1.3 Colours 209

7.1.4 Interactions and Morphological Disturbances 210

7.2 Further Conclusions 211

7.2.1 AGN Black-hole Masses 211

7.2.2 The Evolution of 3CR Radio Galaxies 212

7.3 Further Work 213

7.3.1 The Cosmological Evolution of Quasar Host Galaxies 214

7.3.2 The Host Galaxies of the Highest Luminosity Quasars 218

7.3.3 AGN Black-hole Estimators 219

7.4 The Wider Context of Host Galaxy Studies 220

A Surface-Brightness Profiles 221

B HST Images and Models 239

C A Comparative HST Host Galaxy Imaging Study 273

D References 274

List of Figures

1.1 The optical spectrum of the Seyfert 1 galaxy NGC3227. The spectrum is plotted in terms of relative flux (Osterbrock 1989). 5

1.2 The optical spectrum of the Seyfert 2 galaxy Mrk 1157 (Osterbrock 1989). 6

1.3 Greyscale showing the distribution of OIII emission in the Seyfert 2 galaxy NGC 5252. It can be seen that the ionised gas is confined to two cone-like regions, as expected from anisotropic nuclear emission. The overlaid contours map the surface-brightness distribution of the host galaxy (Figure scanned from Peterson (1997), adapted from the original figure of Wilson & Tsvetanov 1994). 7

1.4 Average RQQ and RLQ spectral energy distributions from radio through to X-ray wavelengths (Elvis *et al.* 1984). 11

1.5 The standard model of an Active Galactic Nucleus (see text for description). The right-hand labels illustrate the orientation-based unification schemes, whereby the observational classification of the AGN is dependent on its inclination to the line-of-sight (Adapted from Urry & Padovani 1995). . . . 15

1.6 Radio-loud unification based on orientation of the radio axis and doppler beaming. At viewing angles of $\geq 45°$ from the jet axis a radio galaxy is observed. At angles of $\leq 45°$ a radio-loud quasar is observed. When the AGN is viewed directly along the jet axis then doppler beaming results in a BL Lac or OVV quasar being observed. This figure is adapted from Barthel (1989). 19

2.1 The distribution of the radio galaxy sub-sample (crosses) and the radio-loud quasar sub-sample (open circles) in the $P_{5GHz} - z$ plane. The two P_{5GHz} distributions can be seen to be very similar, an impression which is confirmed by the application of the Kolmogorov-Smirnov test which returns a probability of $p = 0.68$ 37

2.2 The distribution of the radio galaxy sub-sample (crosses) and the radio-loud quasar sub-sample (open circles) in the $\alpha - z$ plane. The two α distributions are distinguishable at the 2σ level, $p = 0.007$. 38

2.3 The distribution of the radio-quiet quasar sub-sample (filled circles) and the radio-loud quasar sub-ample (open circles) in the apparent V magnitude–redshift plane. The two V-magnitude distributions are statistically indistinguishable, the Kolmogorov-Smirnov test returning a probability of $p = 0.25$ 38

2.4 A schematic diagram showing the layout of the PC and WF chips in WFPC2. The direction of read-out for each CCD is shown by the arrows. The various angles shown determine the orientation of WFPC2 on the sky and are included in the image header information. This diagram has been scanned from the WFPC2 Handbook (Biretta *et al.* 1996). 41

2.5 The throughput of the HST+WFPC2 system. The peak throughput of $\simeq 13\%$ occurs at ≈ 6400Å, well matched to the F675W filter used in this study.This diagram has been scanned from the WFPC2 Handbook (Biretta *et al.* 1996) 42

2.6 The profiles for the three filters under consideration for use in the HST host galaxy study; F606W (dot-dash), F675W (solid) and F702W (dot). The filter profiles are shown including the quantum efficiency of the WF2 CCD. Also shown in the figure are the wavelengths covered by the prominent AGN emission lines OIII and Hα over the redshift range of the sample. It can clearly be seen that the F606W and F702W filters are contaminated by OIII and Hα respectively. 44

2.7 An illustration of the inevitable reduction in low surface-brightness sensitivity incurred by using the higher-resolution PC detector instead of the WF chips. Due to the significant read-noise contribution compared to the typical sky background, even binning up PC images to the same resolution of the WF chips is penalised by the introduction of the extra read-noise. 46

2.8 The full WF2 image of 0917+459 showing the obvious cluster environment. The image covers an area of $80'' \times 80''$ 57

2.9 The full WF2 image of 1342-016 covering an area of $80'' \times 80''$. A large number of companion objects can be seen which, if at the redshift of the quasar, would appear consistent with a moderately rich cluster environment. 59

2.10 The full WF2 image of 0052+251 covering an area of $80'' \times 80''$. The grey-scale has been set to highlight the spiral arm features which are not obvious in the detail presented in Appendix B. 64

2.11 The full WF2 image of 0157+001 which covers an area of $80'' \times 80''$. This image clearly shows the Eastern tidal arm terminating on a companion object which lies off the frame shown in Appendix B. The more diffuse Western counter-arm is also apparent in this image, with three companion objects appearing to be embedded within it. 66

3.1 Simulated radial surface-brightness profiles for a typical elliptical (solid line) and disc (dashed line) galaxy from the HST host-galaxy programme. Both galaxies have the same total luminosity ($M_R = -23.6$) and half-light radius ($r_{1/2} = 10$ kpc), and have been simulated as imaged on WF2 at a redshift of $z = 0.2$. Also shown is a typical nuclear component (dotted line) with total luminosity of $M_R = -24.6$, giving a L_{nuc}/L_{host} of 2.4. 74

3.2 Geometry for host galaxy construction. 77

3.3 A comparison of our empirical F675W WF2 PSF (solid line) with the equivalent TINYTIM synthetic PSF (dashed line). Both have been normalized to have the same central surface-brightness. It can clearly be seen that the TINYTIM model is unable to reproduce the halo of scattered light outside a radius of $\simeq 1.5''$. 80

3.4 A typical HST error profile (0923+201). Shown in the figure are the predicted poisson errors (open circles) from the WF noise model, and the actual sampling errors (filled circles), both calculated from azimuthal averaging in circular annuli. It can be seen that outside a radius of $\sim 1''$ the poisson and sampling errors are basically identical. 81

3.5 The reduced χ^2 map for the best-fitting model to the radio-loud quasar 1217+023. The grey-scale is a linear stretch running between $0 \rightarrow 2$. It can be seen that a uniform spread of χ^2 values has been achieved, with no area of the image dominating the fit. The blank areas in the map are due to the masking from the fitting process of two companion objects and the highly variable diffraction spikes. 82

3.6 χ^2 contour maps for the radio galaxy 3C234.0 showing various 2-parameter slices through the 5-parameter hypersurface. Contour levels are spaced at intervals of $\Delta\chi^2 = 100$ from the minimum χ^2 located with the simplex method. 84

3.7 The appearance of a synthetic quasar image with a 10 kpc elliptical host galaxy and $L_{nuc}/L_{host} = 2$ at $z = 0.1$ (top), $z = 0.2$ (middle) and $z = 0.3$ (bottom). Each simulated image is $30'' \times 30''$ in area. 87

3.8 The appearance of a synthetic quasar image with a 10 kpc elliptical host galaxy and $L_{nuc}/L_{host} = 16$ at $z = 0.1$ (top), $z = 0.2$ (middle) and $z = 0.3$ (bottom). Each simulated image is $30'' \times 30''$ in area. 88

3.9 The apparent magnitude versus redshift distribution of the best-fitting host galaxies of the HST sample (see Chapter 4). Shown in the diagram are radio galaxies (crosses), radio-loud quasars (open circles) and radio-quiet quasars (filled circles). Also shown is the apparent magnitude of the synthetic host galaxies used for testing the two-dimensional modelling code (solid line). The dashed line shows the apparent magnitudes of the synthetic hosts dimmed by 0.27 magnitudes (see text). 89

3.10 The distribution of beta values recovered by the β-modelling code from the synthetic quasars with elliptical host galaxies at z=0.2 and z=0.3. 95

4.1 Sub-sample histograms of the best-fit β values from the variable β modelling. The dotted line lies at $\beta = 0.25$, corresponding to a perfect de Vaucouleurs model. 103

4.2 Sub-sample histograms of the host galaxy absolute, integrated R-Cousins magnitudes. 107

4.3 Sub-sample histograms of the nuclear absolute, integrated R-Cousins magnitudes. 108

4.4 The best-fit values for the host and nuclear absolute magnitudes for the RQQ and RLQ sub-samples. The least-squares fit to the RQQs (solid line) and RLQs (dashed line) are shown, with the two lowest luminosity RQQs having been excluded from the fit. 112

4.5 Histograms of the best-fit host galaxy scalelengths for the three AGN sub-samples. 115

4.6 Plot of absolute host magnitude against best-fit host scalelength for the RGs (crosses), RLQs (open circles) and RQQs (filled circles) in the HST sample. The solid line is the least-squares fit to the data, which has the form $L \propto r^{0.75}$. The four RQQ objects for which a combined disc/bulge fit was found have their best-fit bulge parameters plotted. 116

4.7 The Kormendy relation followed by the hosts of all 33-objects in the HST sample. The solid line is the least-squares fit to the data which has a slope of 2.90, in excellent agreement with the slope of 2.95 found by Kormendy (1977) for inactive ellipticals in the B–band. The dotted line is a relation with a slope of 5, which is to be expected if the host galaxy scalelengths are not properly determined (Abraham *et al.* 1992). For the four RQQ objects which have a significant disc component, the best-fitting bulge component has been plotted. 117

4.8 The Kormendy relation followed by the 10 objects in the RLQ sub-sample. The dashed line is the least-squares fit to the three objects which are clearly biasing the relation for this sub-sample (see text) and has a slope of 7.8. The solid line is the best-fit to the remaining seven objects which has a slope of 2.94, in good agreement with the relations followed by the other two sub-samples. 118

4.9 The axial ratio distribution for the three host galaxy sub-samples as determined by the two-dimensional modelling. 123

4.10 A 3-minute integration of 1012+008 showing the bands of spurious electronic noise which affected many of the images from this observing run. . . 128

4.11 The $r_{1/2} - z$ distribution of the best-fitting host models of the RG (crosses), RQQ (filled circles) and RLQ (open circles) sub-samples. 134

4.12 The surface-brightness profiles resulting from the two-dimensional modelling of two radio-loud quasars. Shown in the figure are the data (open circles), the best-fit model (solid line) and the best-fit nuclear component (dashed line). 135

4.13 The surface-brightness profiles resulting from the two-dimensional modelling of two radio-quiet quasars. Shown in the figure are the data (open circles), the best-fit model (solid line) and the best-fit nuclear component (dashed line). 136

4.14 The rest-frame $R - K$ colours for the three host galaxy sub-samples. The three sub-samples can be seen to be consistent with each other, tightly distributed around a value of $R - K \sim 2.5$. 137

4.15 The apparent $R - K$ colours of the hosts (RGs = crosses, RLQs = open circles, RQQs = filled circles) plotted against redshift, compared with the colours predicted from simple k-correction of stellar populations with ages of 7, 10 and 13 Gyr (Guiderdoni & Rocca-Volmerange 1987). It is clear that the hosts of all 3 classes of powerful AGN have colours which are consistent with each other, and with that of mature stellar populations. 140

4.16 Plot of apparent $R - K$ colour versus absolute R-band luminosity of the fitted nuclear components of the objects in the HST sample. Shown in the plot are the RG (crosses), RLQ (open circles) and RQQ (filled circles) sub-samples. Also shown is the least-squares fit to the data which has a slope of 0.68 ± 0.05. 154

5.1 A sequence of histograms illustrating how a small difference in host galaxy luminosity between the RLQs and RQQs can produce a noticeable difference in estimated black-hole mass. Top histogram shows the absolute host galaxy luminosity distributions of the RQQs (black) and RLQs (grey) subsamples. The middle histogram shows the distributions of the resulting galaxy spheroid mass using the mass-to-light ratio given by Magorrian *et al.* (1998). The bottom histogram shows the estimated central black-hole mass distributions as predicted by the Magorrian relation. The two Seyfert-like RQQ objects have been excluded from this figure. 162

5.2 The observed absolute magnitude M_R of the nuclear component in each quasar plotted against the absolute magnitude which is predicted by assuming that each quasar contains a black hole of mass $m_{bh} = 0.006 m_{spheroid}$, and that the black hole is emitting at the Eddington luminosity (RLQs = open circles, RQQs = filled circles). The solid line shows where the quasars should lie if they were all radiating at their respective Eddington luminosities, while the dashed line indicates 10% of predicted Eddington luminosity, and the dotted line indicates 1% of predicted Eddington luminosity. The nuclear components of the radio galaxies are not plotted because all the evidence suggests they are substantially obscured by dust. 165

5.3 Total radio luminosity P_{5GHz}^{total} versus black-hole mass showing the data on low-redshift 'normal' galaxies from Franceschini *et al.* (1998), and the AGN from the HST sample (RGs = crosses, RLQs = open circles, RQQs = filled circles). The solid line is simply the best-fitting relation ($P \propto m_{bh}^{2.7}$) to the nearby galaxy data given by Franceschini *et al.*. The dashed line is a least-squares fit to a combined data-set of the Franceschini *et al.* objects and the radio-loud AGN from the HST sample (see text). For the nearby galaxies m_{bh} has been estimated directly from stellar dynamics, while for the AGN m_{bh} has been estimated from host-galaxy spheroid luminosity using the relations derived by Magorrian *et al.* (1998). 168

5.4 A comparison between of the black-hole masses predicted from host galaxy spheroidal luminosity via the Magorrian relations (m^a_{bh}) and those predicted from the P^{tot}_{5GHz} Franceschini relation (m^b_{bh}). 173

5.5 Core radio luminosity P^{core}_{5GHz} versus black-hole mass showing the data on low-redshift 'normal' galaxies from Franceschini *et al.* (1998), and the AGN from the HST sample (RGs = crosses, RLQs = open circles, RQQs = filled circles) for which a core reliable radio flux was available in the literature. The solid line is the relation $P \propto m^{2.5}_{bh}$ which was calculate from re-fitting the Franceschini *et al.* data while attributing all of the radio emission from M31 (after removal of very extended radio emission linked to star-formation) to the core (see text for discussion). 174

5.6 A comparison between of the black-hole masses predicted from host galaxy spheroidal luminosity via the Magorrian relations (m^a_{bh}) and those predicted from the P^{core}_{5GHz} Franceschini relation (m^c_{bh}). 177

5.7 As Fig 5.2, but this time with Eddington M_R derived for the RQQs using the values of m_{bh} estimated from the P^{core}_{5GHz} relation. The values of m_{bh} for the RLQs has been estimated from the P^{tot}_{5GHz} relation, although for the RLQs the use of any of the three black-hole estimators discussed here leads to very similar results, as is confirmed by an investigation of Table 5.3. . . . 178

6.1 The redshift distribution of the complete 79 object FRII 3CR subsample (Laing *et al.* 1983). The shaded objects are those included in the Best *et al.* sample. Reproduced from Best *et al.* 1997. 184

6.2 Histogram showing the redshift distribution of the virtually complete Best *et al.* sample. Objects shaded grey and black are objects which have been successfully modelled during this re-analysis. Objects shaded in black are members of the 10-object sub-sample. 187

6.3 The F814W filter profile including the system response and quantum efficiency of WFPC2. Also shown is the location of the 4000Å break of an elliptical galaxy spectrum observed at a redshift of $z = 0.9$ 192

6.4 A comparison of the distribution of scalelengths derived from the modelling of the $z \simeq 0.8$ 3CR galaxies with that obtained by Best *et al.* Also shown is the distribution of scalelengths obtained for the 10 radio galaxies and 10 radio-loud quasars in the HST $z \simeq 0.2$ AGN host-galaxy programme. All three histograms assume $H_0 = 50, \Omega_0 = 1$ 194

6.5 Shown in the top-left panel is the Kormendy relation followed by the $z \simeq 0.8$ sub-sample which has a best-fit slope of 3.5. In the top-right panel the $z \simeq 0.2$ radio galaxies (crosses) have been added along with their best-fit relation of slope 2.9 (dashed line). In the bottom-left panel both galaxy subsamples are shown with the best-fit relation forced to have a intermediate slope of 3.20. The bottom right figure shows the best-fit Kormendy relation (slope=3.21) produced by brightening the surface-brightness of the $z \simeq 0.2$ galaxies by 0.6 magnitudes. 202

7.1 The redshift-luminosity distribution of the combined WFPC2/NICMOS sample showing the RQQs (filled circle) and RLQs (open circles) and the appropriate filters. The F814W, F110M and F165M filters approximate the standard I, J and H-bands. The redshift $z \sim 1.5$ redshift sample was eventually dropped due to orbit restrictions. The F675W sample is also shown to illustrate how these objects will provide the low-z baseline against which any cosmological evolution will be measured. Figure courtesy of Marek Kukula. 214

7.2 The apparent I-band Kormendy relation followed by the $z \sim 1$ quasars imaged with NICMOS (triangles), and the $z \sim 0.8$ 3CR radio galaxies imaged with WFPC2 (crosses). The solid line is a least squares fit to the combined sample, and has a slope of 3.23. An elliptical galaxy colour of $I - J = 0.8$ has been assumed. 217

7.3 A plot of the $M_V - z$ plane showing the location of the two $z = 2$ and $z = 4$ samples chosen for imaging with UKIRT (shaded regions). Also shown are the three samples already imaged with a combination of HST WFPC2 and NICMOS. The idealised quasar spectrum shown in the figure is included to emphasis the point that the samples and filters have been specifically chosen to ensure line-free images that always sample the host-galaxy light long-ward of the 4000Å break. Figure courtesy of Marek Kukula. 218

B.1 The radio galaxy 0230−027 240

B.2 The radio galaxy 0307+169 241

B.3 The radio galaxy 0345+337 242

B.4 The radio galaxy 0917+459 243

B.5 The radio galaxy 0958+291 244

B.6 The radio galaxy 1215−033 245

B.7 The radio galaxy 1215+013 246

B.8 The radio galaxy 1330+022 247

B.9 The radio galaxy 1342−016 248

B.10 The radio galaxy 2141+279 249

B.11 The radio-loud quasar 0137+012 250

B.12 The radio-loud quasar 0736+017 251

B.13 The radio-loud quasar 1004+130 252

B.14 The radio-loud quasar 1020−103 253

B.15 The radio-loud quasar 1217+023 254

B.16 The radio-loud quasar 2135−147 255

B.17 The radio-loud quasar 2141+175 256

B.18 The radio-loud quasar 2247+140 257

B.19 The radio-loud quasar 2349−014 258

B.20 The radio-loud quasar 2355−082 259

B.21 The radio-quiet quasar 0052+251 260

B.22 The radio-quiet quasar 0054+144 261

B.23 The radio-quiet quasar 0157+001 262

B.24 The radio-quiet quasar 0204+292 263

B.25 The radio-quiet quasar 0244+194 264

B.26 The radio-quiet quasar 0257+024 265

B.27 The radio-quiet quasar 0923+201 266

B.28 The radio-quiet quasar 0953+415 267

B.29 The radio-quiet quasar 1012+008 268

B.30 The radio-quiet quasar 1549+203 269

B.31 The radio-quiet quasar 1635+119 270

B.32 The radio-quiet quasar 2215−037 271

B.33 The radio-quiet quasar 2344+184 272

List of Tables

2.1 The name, redshifts, apparent V-magnitudes and absolute B-magnitudes of the galaxies in the radio-galaxy sub-sample. 34

2.2 The name, redshifts, apparent V-magnitudes and absolute B-magnitudes of the quasars in the radio-loud quasar sub-sample. 35

2.3 The name, redshifts, apparent V-magnitudes and absolute B-magnitudes of the quasars in the radio-quiet quasar sub-sample. 36

2.4 The radio properties of the radio galaxy sub-sample. The radio structure reference number given for each object refers to the list shown underneath Table 2.6. 39

2.5 The radio properties of the radio-loud quasar sub-sample. The radio structure reference number given for each object refers to the list shown underneath Table 2.6. 39

2.6 The radio properties of the radio-quiet quasar sub-sample. The radio structures reference for each object (where known) refers to the list given below. The radio structures are labelled as in Dunlop *et al.* 1989 :U=Unresolved, P=Partially Resolved, C=Central Component, Do=Double, D2=Flat spectrum core+one-sided extended emission, I/II=FRI/FRII. 40

2.7 The surface-brightness sensitivities of the reduced RG and RLQ data. Column two lists the sky-background brightness (mag.arcsec^{-2}). Column three gives the 3σ pix^{-1} sensitivity limit. Column four gives the the surface-brightness of the host galaxy inside an pixel-wide annulus with a radius of 10″. Column five lists how far above the noise this level of flux has been detected in units of σ. 53

2.8 The surface-brightness sensitivities of the reduced RQQ data. Column two lists the sky-background brightness (mag.arcsec^{-2}). Column three gives the 3σ pix^{-1} sensitivity limit. Column four gives the the surface-brightness of the host galaxy inside an pixel-wide annulus with a radius of 10″. Column five lists how far above the noise this level of flux has been detected in units of σ. 54

3.1 Results of the two-dimensional modelling tests using synthetic quasars with elliptical host galaxies. Column 1 gives the redshift of the quasar. Column 2 gives the actual scalelength of the simulated host in kpc. Columns 3-8 give the mean percentage error in the reclaimed value of the relevant parameter. Each value is the mean for the seven synthetic quasars produced at a particular redshift, with a particular scalelength (for each redshift and scalelength combination there where seven different synthetic quasars produced with L_{nuc}/L_{host}=0, 0.5, 1.0, 2.0, 4.0, 8.0 & 16). 92

3.2 Results of the two-dimensional modelling tests using synthetic quasars with disc host galaxies. Column 1 gives the redshift of the quasar. Column 2 gives the actual scalelength of the simulated host in kpc. Columns 3-8 give the mean percentage error in the reclaimed value of the relevant parameter. Each value is the mean for the seven synthetic quasars produced at a particular redshift, with a particular scalelength (for each redshift and scalelength combination there where seven different synthetic quasars produced with L_{nuc}/L_{host}=0, 0.5, 1.0, 2.0, 4.0, 8.0 & 16). 93

3.3 The range of percentage errors in the reclaimed values of the host-galaxy parameters from the synthetic quasar modelling tests. Columns 1 & 2 detail the actual host-galaxy morphology and redshift of the synthetic quasars. Columns $3 \rightarrow 7$ show the range in percentage error in the reclaimed parameters from the model fits to the 28 synthetic quasars constructed at each redshift, with each of the two host morphologies. 94

4.1 The outcome of attempting to model the AGN host galaxies of the RGs and RLQs as either an exponential disc, a de Vaucouleurs spheroid, or a combination of both. The preferred host-galaxy morphology is given in column 2 (E=Elliptical, D=Disc, B/D=Bulge/Disc), with the $\Delta\chi^2$ between the chosen model and the best alternative model given in column 3. In column 4 $r_{1/2}$ (semi-major axis) is given irrespective of the chosen host morphology ($r_{1/2} = r_e, r_{1/2} = 1.68r_0$). Column 5 lists $\mu_{1/2}$ in units of R mag arcsec^{-2}. Columns 6 and 7 list the integrated apparent magnitudes of the host galaxy and fitted nuclear component converted from F675W to Cousins R-band, while column 8 gives the ratio of integrated galaxy and nuclear luminosities. 99

4.2 The outcome of attempting to model the AGN host galaxies of the RQQs as either an exponential disc, a de Vaucouleurs spheroid, or a combination of both. The preferred host-galaxy morphology is given in column 2 (E=Elliptical, D=Disc, B/D=Bulge/Disc), with the $\Delta\chi^2$ between the chosen model and the best alternative model given in column 3. In column 4 $r_{1/2}$ (semi-major axis) is given irrespective of the chosen host morphology ($r_{1/2} = r_e, r_{1/2} = 1.68r_0$). Column 5 lists $\mu_{1/2}$ in units of R mag arcsec^{-2}. Columns 6 and 7 list the integrated apparent magnitudes of the host galaxy and fitted nuclear component converted from F675W to Cousins R-band, while column 8 gives the ratio of integrated galaxy and nuclear luminosities. 100

4.3 The results of the variable-β modelling of the RGs and RLQs. Column 2 lists the host morphology of the best fitting 'fixed β' model. The best-fitting values for the β profile parameter are given in column 3. The $\Delta\chi^2$ of column 4 quantifies the improvement in fit between this variable-β model and the best-fitting disc or elliptical model. A value of $\Delta\chi^2 \geq 16.3$ is equivalent to an improvement of fit significant at the 3σ level (Press *et al.* 1989). 101

4.4 The results of the variable-β modelling of the RQQs. Column 2 lists the host morphology of the best fitting 'fixed β' model. The best-fitting values for the β profile parameter are given in column 3. The $\Delta\chi^2$ of column 4 quantifies the improvement in fit between this variable-β model and the best-fitting disc or elliptical model. A value of $\Delta\chi^2 \geq 16.3$ is equivalent to an improvement of fit significant at the 3σ level (Press *et al.* 1989). 102

4.5 The sample. The first six objects listed are taken from the original K–band imaging sample (Taylor *et al.* 1996). The final three objects have been taken from the sample imaged by Bahcall *et al.* (1994). Column five lists the on-source integration time for each object. Column six details any problems experienced with the images (see text). Redshifts and V magnitudes have been taken from Taylor *et al.* (1996) and Bahcall *et al.* (1997) respectively. 126

4.6 Results of the two-dimensional modelling of the IRCAM 3 data. Column 3 indicates the morphological type of the best fitting host galaxy. Column 4 gives the difference in χ^2 between the elliptical and disc host galaxy fits. Column 5 details the effective radius of the host galaxy ($r_e = r_{1/2}$ for ellipticals). Columns 6 & 7 list the integrated apparent magnitudes of the host and nuclear component respectively. Column 8 gives the axial ratio (b/a) for the best fit host. Column 9 converts the figures of columns 6 & 7 into a nuclear:host ratio. 131

4.7 Results of the two-dimensional modelling of the HST data. Column 3 indicates the morphological type of the best fitting host galaxy. Column 4 gives the difference in χ^2 between the elliptical and disc host galaxy fits. Column 5 details the effective radius of the host galaxy ($r_e = r_{1/2}$ for ellipticals). Columns 6 & 7 list the integrated apparent magnitudes of the host and nuclear component respectively. Column 8 gives the axial ratio (b/a) for the best fit host. Column 9 converts the figures of columns 6 & 7 into a nuclear:host ratio. 132

4.8 Luminosities for the four best-fitting host galaxies. Column 2 lists the absolute integrated K–band magnitudes. Column 3 restates the absolute magnitudes in term of $L^{\star}$. 134

4.9 Absolute magnitudes (M_R), and optical-infrared ($R - K$) colours of the best-fitting host galaxy and nuclear component for the RGs and RLQs. Columns 2 and 3 give the R-band absolute magnitudes (M_R) derived from the current modelling of the HST data, assuming a spectral index of $\alpha = 1.5$ (where $f_\nu \propto \nu^{-\alpha}$) for the galaxy and $\alpha = 0.2$ for the quasar. Columns 4 and 5 list the apparent and rest-frame $R - K$ colours of the host-galaxies respectively. The colours have been derived by combining 12-arcsec aperture R-band photometry from our HST-based models with the 12-arcsec aperture K-band photometry derived by Taylor *et al.* (1996), to minimize the uncertainty introduced by errors in constraining the galaxy scalelengths at K. 141

4.10 Absolute magnitudes (M_R), and optical-infrared ($R-K$) colours of the best-fitting host galaxy and nuclear component for the RQQs. Columns 2 and 3 give the R-band absolute magnitudes (M_R) derived from the current modelling of the HST data, assuming a spectral index of $\alpha = 1.5$ (where $f_\nu \propto \nu^{-\alpha}$) for the galaxy and $\alpha = 0.2$ for the quasar. Columns 4 and 5 list the apparent and rest-frame $R-K$ colours of the host-galaxies respectively. The colours have been derived by combining 12-arcsec aperture R-band photometry from our HST-based models with the 12-arcsec aperture K-band photometry derived by Taylor *et al.* (1996), to minimize the uncertainty introduced by errors in constraining the galaxy scalelengths at K. 142

4.11 The results of the Schneider, Gunn & Hoessel study of the first-, second- and third-ranked galaxies in a sample of 83 Abell clusters. The results have been converted to the cosmology used throughout this thesis, and an elliptical galaxy colour of $g_r - R_c = 0.22$ assumed to convert from the original Gunn-r filter to the standard Cousins-R filter (Fukugita *et al.* 1995). 147

4.12 The model results for the four brightest galaxies in three of the clusters obtained from the HST archive. The redshifts of the clusters are 0.23, 0.175 & 0.171 respectively. The images of A2390 and A1689 were taken through the F814 (I–band) filter, while the image of A2218 was taken through the F702W (wide R) filter. The conversion between I- and R-magnitudes has been performed assuming $R - I = 0.8$ (Fukugita *et al.*). The final reduced images had signal-to-noise comparable to the HST host galaxy data. 148

4.13 The model results for the four brightest galaxies in the two class 0 Abell clusters obtained from the HST archive. The redshifts of the clusters are 0.11 & 0.19 respectively. The images of both clusters were taken through the F702W (wide R) filter. The conversion between I- and R-magnitudes has been performed assuming $R - I = 0.8$ (Fukugita *et al.*). The final reduced images had signal-to-noise comparable to the HST host galaxy data. 148

4.14 The results of the blind test to determine any difference in the prevalence of features indicative of interaction or disturbance in the AGN sample (active) compared to inactive galaxies, using 20 BCG as a control sample (inactive). See text for description. 150

4.15 The results of the blind test to determine if any differences exist in the occurrence of features indicative of interaction or disturbance between the AGN sub-samples. See text for description. 150

4.16 A comparison of the determined host magnitudes for the quasars from the HST sample which have recently been studied by other authors. All magnitudes have been converted to apparent V-magnitudes. The R–magnitudes from this work have been converted assuming $V - R = 0.8$. The F606W magnitudes of Bahcall *et al.* have been converted using the k-corrections quoted in Bahcall *et al.* (1997). The H– magnitudes of McLeod & Rieke and Kotilainen *et al.* have been converted assuming the $V - H = 2.9$ colour quoted by McLeod & Rieke (1995b) 152

5.1 The results of applying the Magorrian relations to the radio-loud objects. Columns two and three list the predicted galaxy spheroid mass and central black-hole mass respectively. Column 4 lists the predicted absolute R–band Eddington luminosity of the black-hole, assuming a simple accretion-disc model (see text). Column five gives the ratio of the predicted Eddington luminosity to the best-fitting nuclear model component. There are no entries in column 5 for the RGs since their nuclear emission is most likely dust-obscured. 160

5.2 The results of applying the Magorrian relations to the radio-quiet objects. Columns two and three list the predicted galaxy spheroid mass and central black-hole mass respectively. Column 4 lists the predicted absolute R–band Eddington luminosity of the black-hole, assuming a simple accretion-disc model (see text). Column five gives the ratio of the predicted Eddington luminosity to the best-fitting nuclear model component. 161

5.3 Three different estimates of the central black-hole mass of the radio-loud objects. Column 2 gives the black-hole mass estimate from the Magorrian relations. This information is identical to that provided in Table 5.1 and is included here for ease of comparison. Column 3 gives the black-hole mass estimate from the total $P_{5GHz} : m_{bh}$ relation of Franceschini *et al.* (1998). Column 4 gives the corresponding figure estimated from the core $P_{5GHz} : m_{bh}$ relation. The objects for which no core radio power black-hole estimate is given are those for which a reliable measure of the core luminosity could not be readily recovered from the literature. 171

5.4 Three different estimates of the central black-hole mass of the radio-quiet objects. Column 2 gives the black-hole mass estimate from the Magorrian relations. This information is identical to that provided in Table 5.1 and is included here for ease of comparison. Column 3 gives the black-hole mass estimate from the total $P_{5GHz} : m_{bh}$ relation of Franceschini *et al.* (1998). Column 4 gives the corresponding figure estimated from the core $P_{5GHz} : m_{bh}$ relation. 172

6.1 The results of the two-dimensional modelling of the 16-objects from the Best *et al.* $z \simeq 1$ 3CR sample which did not suffer from excessive aligned emission. Listed in column 5 are the fitted scalelengths in kpc, with the surface-brightness at that scalelength in Cousins I-magnitudes arcsec^{-2} given in column 6. Column 7 lists the integrated apparent I–band magnitude of the best-fit host galaxy with column 8 giving the ratio of the integrated luminosity of the best-fit nuclear component and host galaxy. Objects labelled with a * are members of the 10-object sub-sample. 189

6.2 The absolute magnitudes and characteristic surface-brightness of the 10-object sub-sample ($H_0 = 50, \Omega_0 = 1$) 191

6.3 The scalelength results from the two-dimensional modelling of the $z \simeq 0.8$ sub-sample. Columns one and two detail the choice of cosmology. Column three gives the median scalelength values for the 10-objects in the sample. Column four gives the corresponding mean values together with the standard error. 193

6.4 The absolute I-band magnitudes of the two 10-object radio galaxy sub-samples. Column four gives the median figures with column five listing the corresponding mean figures complete with standard error. 196

6.5 The best-fitting Kormendy relations for the 10 $z \simeq 0.8$ 3CR galaxies under four different choices of cosmology. 198

6.6 The scalelength results from the two-dimensional modelling of the $z \simeq 0.2$ sub-sample. Columns one and two detail the choice of cosmology. Column three gives the median scalelength values for the 10-objects in the sample. Column four gives the corresponding mean values together with the standard error. 199

6.7 The results of the tests to determine the influence of different cosmology and formation redshift upon the amount of passive evolution expected between $z = 0.8$ and $z = 0.2$. Columns one and two list the cosmological parameters for each test. Column three lists the amount of evolution required to reconcile the median of the two absolute magnitude distributions. Column four gives the corresponding mean figures complete with standard errors. Columns 5-7 list the amount of passive evolution between $z = 0.2$ and $z = 0.8$ predicted by the spectrophotometric modelling for three galaxy formation redshifts. (The apparently anomalous trend displayed by the $\Omega_0 = 1, H_0 = 70, z_{for} = 3$ model is due to the fact that even at $z = 0.2$ a galaxy is only 6 Gyr old, and remains relatively bright at I.) 201

6.8 The best-fitting Kormendy relations for the 10 $z \simeq 0.2$ radio galaxies under four different choices of cosmology. 203

6.9 The amount of luminosity evolution predicted by forcing both galaxy sub-samples to lie on a Kormendy relation with slope 3.2. Column four lists the implied vertical shift required to over-lay the Kormendy relations of the two samples using the best-fit scalelengths of Table 6.1 converted to the appropriate cosmology. Columns 3 and 5 list the vertical shift implied by shifting the best-fit scalelengths left(-1σ) and right($+1\sigma$) until the scale-length distributions of the two sub-samples differ at the 1σ level. 204

7.1 The results of the modelling of the $z \sim 1$ quasars imaged with NICMOS through the F110M filter. The properties of the F110M filter are sufficiently close to the standard J-band that the apparent magnitudes listed in columns 5 & 6 have simply been listed as J-band magnitudes. The host galaxy of sgp2-47 was not detected at a significantly better χ^2 level than the best-fitting unresolved nuclear component. 216

Abstract

Hubble Space Telescope R-band images of a sample of 10 radio galaxies (RG), 10 radio-loud quasars (RLQ) and 13 radio-quiet quasars (RQQ) at redshift $z \simeq 0.2$ are presented. The sources comprising the radio-loud sub-samples have been selected to be indistinguishable in the $P_{5GHz} - z$ plane. The two quasar sub-samples have been similarly selected to have indistinguishable distributions in the $V - z$ plane. All three sub-samples have been analysed with two-dimensional modelling software, designed to accurately determine the host-galaxy parameters.

The modelling results show all of the RG, and all of the quasars with $M_V < -23$, to have bulge-dominated host galaxies, excluding the hypothesis that host morphology is responsible for the radio-loudness dichotomy. Furthermore, the host galaxies are found to be essentially identical to a de Vaucouleurs ($\beta = 0.25$) law, with 30/33 objects having β parameters in the range $0.2 < \beta < 0.3$. The hosts of all of the objects studied are found to be extremely luminous ($L \geq L_*$), with 25/33 objects having $L \geq 2L_*$. the hosts of the RQQs are found to be typically 0.4 magnitudes fainter than their radio-loud counterparts. The host galaxies of all three sub-samples are found to be larger than average ellipticals ($< r_e >= 10.5$ kpc), with a trend found for the RQQ hosts to be some 20% smaller than those of the RLQs. For the first time it is demonstrated that the hosts of quasars, as well as RG, display a Kormendy relation basically identical to that of inactive ellipticals.

In combination with the previous K-band modelling of this sample (Taylor *et al.* 1996) the first set of reliable optical-infrared colours for a significant sample of AGN host galaxies has been determined. The $R - K$ colours of the hosts in all three

sub-samples are shown to be consistent with each other, with the close agreement of the median colour of $R-K$=2.5 with that expected from a $\sim$ 14 Gyr-old stellar population implying that the host galaxies of both RGs and quasars are consistent with having formed at high redshift ($z \geq 3$).

The nuclear colours of the RGs are shown to be perfectly consistent with those of dust reddened RLQ nuclei. The combined luminosity, scalelength, Kormendy relation and $R-K$ colour results for the RG and RLQ sub-samples clearly demonstrate that they are drawn from the same parent population, in strong support of the orientation-based unification scheme of Barthel (1989). The corresponding results for the full 33 object sample show that, in terms of their global structural parameters, the hosts of powerful AGN are no different to normal massive ellipticals.

The host galaxy–black-hole mass correlations of Magorrian *et al.* (1998) and Franceschini *et al.* (1998) are combined with the AGN modelling results to investigate the quasar radio-loudness dichotomy. All methods of black-hole mass estimation lead to the conclusion that RLQs harbour black-holes of mass $\geq 10^{10}\,M_{\odot}$. The RQQ black-hole masses estimated via the Magorrian relation are typically smaller than those of the RLQs ($\sim 5 \times 10^{9}\,M_{\odot}$), but show sufficient overlap to require the influence of another physical parameter, possibly black-hole spin, to explain the radio-loudness dichotomy. In contrast, the use of the Franceschini black-hole estimator predicts RQQ black-hole masses a factor of two smaller than those of the RLQs, suggesting that black-hole mass alone may be the crucial factor.

The application of the modelling technique to an existing HST survey of 3CR radio galaxies at $z \sim 1$ shows them to have a scalelength distribution and Kormendy relation indistinguishable from their $z \sim 0.2$ counterparts. The implied luminosity evolution between $z \sim 0.2$ and $z \sim 0.8$ is shown to be consistent with that expected from passive evolution alone in a low density Universe, with a high galaxy formation redshift ($z \geq 3$). The lack of evidence for significant merger activity in the redshift range $0.2 < z < 0.8$ leads to the conclusion that the traditional passive evolution interpretation of the radio galaxy $K-z$ relation remains acceptable.

Chapter 1

Introduction

This thesis concerns the study of the host galaxies of a sample of Active Galactic Nuclei (AGN) imaged with the Hubble Space Telescope (HST). This first chapter serves the purpose of placing this work in context by giving an overview of the history of quasar research, and host galaxy work in particular. The properties of the major classes of AGN are described, together with the standard black-hole accretion model and unification schemes which are invoked to explain them. Particular attention is paid to the string of recent research which has placed the existence of supermassive galactic black-holes on a strong footing. The final section of the chapter discusses recent host galaxy studies employing both ground-based and HST imaging. The successes and failures of these projects are examined, and the motivations for the central HST study highlighted.

1.1 The Discovery of Quasars

The initial discovery of quasars can be seen as a direct consequence of the advances in radio technology made during WWII and the immediate post-war period. By the late 1950's and early 1960's the first radio surveys had been being undertaken, including the Third Cambridge Catalog (3C) and the its subsequent revision (3CR), which were sensitive to a limiting flux density of 9 Jy at 158 MHz and 178 MHz respectively.

The vast majority of the new radio sources were found to be associated with resolved elliptical galaxies, the now familiar 3C and 3CR radio galaxies. However, a small number of the detected radio sources could not be connected to obvious galaxies, and when optical counterparts where identified from photographic survey plates, they were found to be apparently stellar in nature (Matthews and Sandage 1963).

Optical spectra of these radio "stars" contained several interesting features. Not only were the spectra very blue in colour, they also showed strong, broad emission lines not seen in stellar spectra. The location of these emission lines also proved problematic since they were not found to match the positions of any known elements. The breakthrough came with the realization by Schmidt (1963) that the broad emission lines present in the spectrum of 3C273, at B=13.1 the brightest quasar in the sky, where in fact the redshifted Balmer series. The implied redshift for 3C273 of $z = 0.158$ was among the largest known at the time, and presented an immediate difficulty in explaining the huge luminosities of these "quasars" (shortened from the original quasi-stellar radio source). If the redshifts calculated from quasar Balmer lines were interpreted as being due to Universal expansion, these redshifts placed the quasars at large, cosmological distances. Consequently, the apparent magnitudes in turn implied intrinsic luminosities between ten and a hundred times that of the brightest known galaxy. This line of reasoning caused major problems when it was combined with one of the first studied properties of quasars; variability. Immediately after their initial discovery, photographic plates which featured quasars, and spanned many years, where examined. The study of the quasar apparent magnitudes over different timescales revealed that many quasars where variable over a timescale of months, with a few varying on timescales as short as a few days. The inescapable conclusion from this short timescale variation was that if quasars were varying in a coherent manner, then they must be confined to an area of less than a light year in diameter, and possibly no larger than the solar system. The seemingly impossible situation of having such a small volume generating a luminosity many times that of an entire galaxy, originally prevented the cosmological interpretation of the quasar redshifts from being universally accepted.

Soon after the discovery of what are now referred to as radio-loud quasars (RLQ), another class of quasar was being identified through optical surveys. In addition to

the broad emission lines and variability, the generally flat nature of quasar spectra ($0 < \alpha < 1$ for $f_\nu \propto \nu^{-\alpha}$) results in much stronger ultra-violet flux than even A0 stars. This so-called "UV excess" means that quasars stand out as clearly separate from normal stars on a $U-B$ v's $B-V$ two-colour diagram. This selection technique led to the discovery of large numbers of quasi-stellar objects (QSO) which shared the same spectral properties as the quasars but lacked the powerful radio emission. These objects, what are now referred to as radio-quiet quasars (RQQ), outnumber their radio-loud counterparts by a factor of between ten and twenty.

As the number of quasars grew it became clear that they were isotropically distributed on the sky, and that none could be identified as having blue-shifted emission lines. These two facts allowed the vast majority of astronomers to except their extra-galactic origin, and meant that the early suggestion that supermassive black-holes could supply the power source (Zel'dovich & Novikov 1964) had to be taken seriously.

1.1.1 The Host Galaxies of AGN

The study of the host galaxies of quasars did not effectively begin until more than a decade after their initial discovery. The first positive identification that quasars had low surface-brightness "fuzz" associated with them was made by Kristian (1973), although the true point-like nature of quasars had been questioned before (Matthews and Sandage 1963).

Although quasars have the distinction of being the most luminous class of AGN, they were not the first to be discovered. Prior to the discovery of quasars the first AGN to be studied were the Seyfert galaxies (Seyfert 1943). Originally these were a set of six nearby spiral galaxies which were studied by Carl Seyfert because of their unusual high central surface-brightness. The spectra of these galaxies revealed strong broad emission lines (compared to galactic absorption lines), with full widths at half maximum (FWHM) of a few hundred, to a few thousand kms^{-1}.

With the benefit of hindsight it seems strange that, given the similarity in the optical spectra of Seyfert galaxies and quasars, it was not quickly realised that quasars

would be found in galactic nuclei also. The reason for this is mainly due to historical accident conspiring to falsely magnify the apparent differences between the two types of object. As with the opening up of any new area of astronomy, the first quasars to be discovered were necessarily amongst the most powerful. The result of this was that the overlap which is now known to exist in the respective Seyfert galaxy and quasar luminosity functions (eg. Koehler *et al.* 1997) was not immediately apparent. Added to this is the fact that the first quasars to be discovered were powerful radio sources while Seyfert galaxies are all radio-quiet (although not radio silent).

It was not until 1982 that examination of the off-nuclear spectrum of the first quasar discovered, 3C48, showed conclusively that it was dominated by starlight (Boroson & Oke 1982). Since then, several studies have shown that the nebulous emission around low-redshift ($z < 0.5$) quasars is dominated by a stellar population.

1.2 An AGN Menagerie

As research into AGN progressed throughout the 1960's and 1970's, many new and subtly different types of object were discovered. Each new type of object to be discovered was classified according to any one of a wide array of observational parameters (eg. optical spectra, radio power, X-ray luminosity and variability). The final result of this botanical exercise is the current bewildering list of different AGN types and classes. The aim of this section is to outline the observational properties of the main types of AGN, before the discussion of the standard model and unification schemes in the next section.

1.2.1 Seyfert Galaxies

Seyfert galaxies were the first class of AGN to be discovered, and because of their relative closeness have been widely studied. There are several characteristics which are common to all members of this class of AGN. Virtually all Seyfert galaxies are apparently normal spiral galaxies distinguished by their unusually bright, point-source

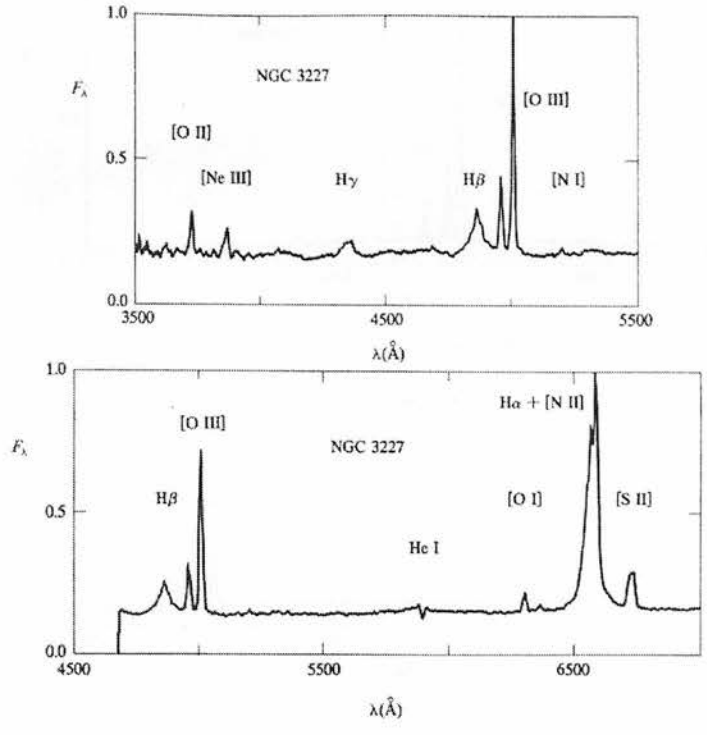

Figure 1.1: The optical spectrum of the Seyfert 1 galaxy NGC3227. The spectrum is plotted in terms of relative flux (Osterbrock 1989).

nucleus. The spectra of Seyfert galaxies reveals the presence of strong, high-ionization emission lines and a featureless (non-thermal) continuum, as well as the expected absorption features due to the stellar population. It is the strength of the featureless continuum and the properties of the emission lines which are used to sub-divide Seyferts galaxies into Type 1 or Type 2 objects.

Type 1 Objects

The spectra of Seyfert 1 galaxies display a strong featureless AGN continuum component, which in many cases can completely swamp the stellar absorption lines due to the host galaxy population. The featureless continuum can not be modelled by a single temperature black-body spectrum, and is therefore sometimes described as the non-thermal continuum. The AGN continuum can vary at the 0.5 magnitude level on a timescale of months, and in some cases can show detectable variations over a period of

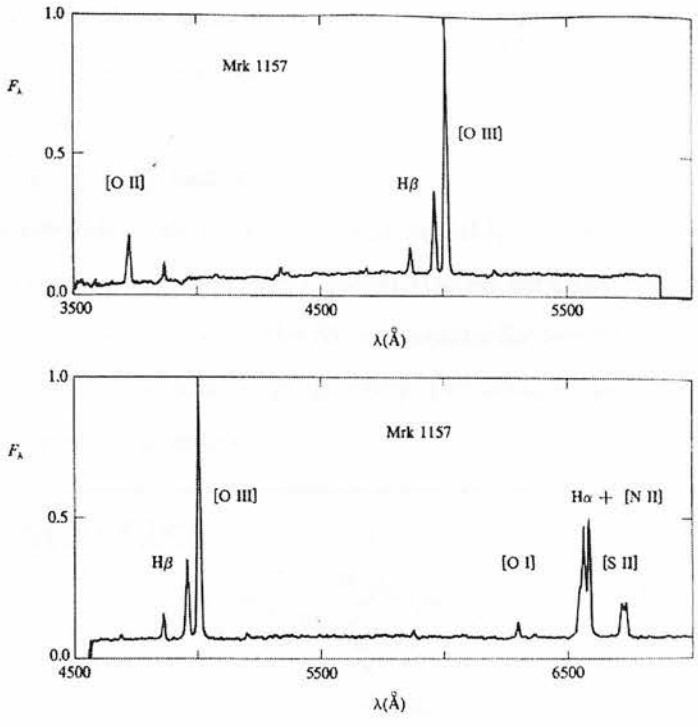

Figure 1.2: The optical spectrum of the Seyfert 2 galaxy Mrk 1157 (Osterbrock 1989).

only a few days. The conclusion from this is that the source of the continuum emission must therefore be confined to a region with a radius of $r \leq 0.1$ pc.

In addition to the featureless continuum the spectra of Seyfert 1 galaxies show two sets of emission lines, described as narrow and broad, superimposed on each other. The broad emission lines typically have FWHM in the range $500 \rightarrow 10000$ kms^{-1} and arise solely from permitted transitions. The lack of forbidden transitions and the huge widths of the emission lines implies that the region responsible for the broad lines, the so-called broad line region (BLR), must be composed of high velocity, high density gas ($n_e = 10^8 \rightarrow 10^{10}$cm^{-3}). The broad emission lines display variability which is well correlated with the variation of the AGN continuum, with a time lag of a few days to a few months. The BLR remains unresolved in even the nearest Seyferts which, combined with the variability data, constrains it to be located within a radius of $r \leq 1$pc from the central ionising source.

The narrow lines present in Seyfert 1 spectra have FWHM in the range $200 \rightarrow 900$

kms^{-1}, and arise from both permitted and forbidden line transitions. The presence of the forbidden line transitions, combined with the smaller line widths, indicate that the narrow line region (NLR) must consist of relatively low velocity, low density gas ($n_e = 10^3 \rightarrow 10^6 \mathrm{cm}^{-3}$). The lack of any clear variability in the narrow lines, in sources showing obvious continuum variation, points to the NLR lying at distances of ≥ 100 pc from the central ionising source. Indeed, recent studies with the HST (eg. Macchetto *et al.* 1994) have successfully resolve the NLR of nearby Seyfert galaxies. These studies have shown the NLR to have a bi-conal structure, providing evidence that the emission from the central source is anisotropic.

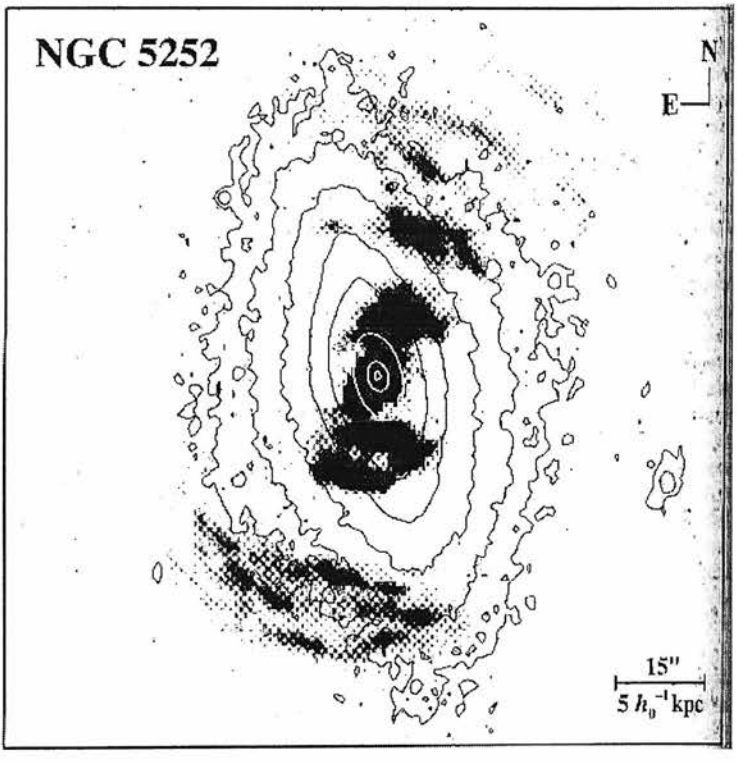

Figure 1.3: Greyscale showing the distribution of OIII emission in the Seyfert 2 galaxy NGC 5252. It can be seen that the ionised gas is confined to two cone-like regions, as expected from anisotropic nuclear emission. The overlaid contours map the surface-brightness distribution of the host galaxy (Figure scanned from Peterson (1997), adapted from the original figure of Wilson & Tsvetanov 1994).

Type 2 Objects

There are two major differences between the optical spectra of Seyfert 2 and Seyfert 1 galaxies. Firstly, the featureless AGN continuum in Type 2 objects is weaker than in Type 1 objects by as much as an order of magnitude. The second difference between the spectra of the two types lies in the properties of the emission lines. Unlike the Type 1 objects, classic Seyfert 2 galaxies do not exhibit any broad line emission, while retaining the narrow line emission. However, further investigation of high-resolution Seyfert 2 spectra led to the discovery that there is no clear separation between the two classes of Seyferts, with many galaxies previously classified as Seyfert 2 being found to have broad components to their emission lines, which are only detectable in very high signal-to-noise spectra. This has led to the adoption of a scheme first proposed by Osterbrock (1981), where Seyferts can be classified as intermediate types 1.5, 1.8 or 1.9 depending on the relative strength of the broad and narrow emission line components.

The presence of an apparent continuum of intermediate objects falling between the classic Seyfert 1 and Seyfert 2 classifications is also suggestive of some sort of obscuration affecting the compact BLR, while leaving the more extended NLR unaffected. As is discussed in Section 1.4, it is the close-by Seyfert galaxies which have provided the most convincing evidence to date for AGN unification.

1.2.2 Radio Galaxies

Most of the powerful radio sources which were detected in the first all-sky radio surveys of the 1950's and 1960's were found to be identified with resolved elliptical galaxy optical counterparts. As the resolution of radio astronomy steadily improved it became clear that these radio galaxies typically displayed two elements to their radio emission, flat- and steep-spectrum, both of which are produced by the synchrotron mechanism.

If the radio emission is modelled as a power-law of the form $f_\nu \propto \nu^{-\alpha}$, then flat-spectrum emission has a spectral index of $0.0 < \alpha < 0.5$, is typically unresolved at the $1''$ level, and usually coincident with the nucleus of the host elliptical galaxy. As the classic

synchrotron spectrum is only flat around the transition between the self-absorbed and optically thin regimes (Rybicki & Lightman 1970), it is thought that the flat-spectrum radio emission from the galaxy core is produced by multiple sources, all with different turnover frequencies, combining to produce a composite flat-spectrum. In some cases this process can be seen in ultra high-resolution VLBI observations (Marscher 1988).

The steep-spectrum radio emission is characteristic of optically thin synchrotron radiation ($0.5 < \alpha < 1.0$) and is produced in the kiloparsec-scale radio jets and lobes displayed by some sources. Depending on the relative contributions of the core and lobe components to the total radio luminosity, radio galaxies are often classified as either core- or lobe-dominated.

The lobe-dominated radio galaxies are usually further classified on the basis of the specific properties of their extended radio emission. Although there are numerous subdivisions used by workers in the field, the basic classification is based on the morphology of the extended emission and is due to Fanaroff & Riley (1974). Fanaroff & Riley Class I (FRI) objects have wide, continuous, twin jets terminating in diffuse lobes situated symmetrically on either side of the nucleus. The FRI sources have their brightest emission near the nucleus, fading away to low surface-brightness at the ends of the lobes (limb-darkening). In contrast, the more powerful FRII sources have highly collimated jets, which are often one-sided, and can be seen to have sub-structure (knots) in high resolution radio maps. In FRII sources with twin jets, one jet is always seen to be significantly fainter than the other, an observation which is attributed to doppler beaming along the line-of-sight (see Section 1.4). The more compact lobes of FRII sources have enhanced surface-brightness where the lobes interacts with the ambient inter-galactic medium, and are described as being edge-brightened. This enhancement is thought to be due to shock heating and suggests that the outflows of FRII sources are super-sonic with respect to the ambient medium, while the outflows of FRI sources are sub-sonic.

Optical imaging studies of the host galaxies of both FRI and FRII radio sources have found both to be consistent with being early-type galaxies. However, there have been differences discovered in the specific properties of the hosts of the two classes. The more powerful FRII sources have been found to reside in apparently normal giant elliptical

galaxies (gE), located in isolated or poor cluster environments (eg. Prestage & Peacock 1988). In contrast, the host galaxies of the FRI sources tend to be larger central cluster galaxies (cD), situated near the centre of relatively rich cluster environments.

The nuclear optical spectra of radio galaxies are also used for classification purposes. The broad-line radio galaxies (BLRG) display similar spectra to Seyfert 1 galaxies, with both broad and narrow emission line components. Analogously, the narrow-line radio galaxies (NLRG) have narrow-line spectra similar to Seyfert 2 galaxies, where the broad lines are absent.

1.2.3 Quasars

Quasars are the most optically luminous of all AGN, with a widely adopted dividing line in luminosity between quasars and Seyferts taken to be $M_B < -23.0$ (Véron-Cetty & Véron 1991). Due to the smooth merging of the Seyfert and quasar luminosity functions this division is inevitably somewhat arbitrary, although, by coincidence, it does seems to mark a distinct change in the properties of the respective host galaxies (see Chapter 4). The optical spectra of both types of quasar are almost identical, and remarkably similar to that seen in Seyfert 1 galaxies, except that the featureless AGN continuum and broad emission lines tend to be stronger. One concrete difference between the optical spectra of RLQs and RQQs was thought to be the presence of broad absorption lines (BAL) in around 10% of RQQ spectra but their total absence from RLQ spectra. These BAL are always found just blueward of strong emission lines, indicating they are produced by some sort of gas outflow close to the central source. Together with the emission line, the BALs form a P-cygni type signature. However, the recent discovery by Wills *et al.* (1999) that the powerful RLQ 1004+130 (featured in the HST sample) may contain BAL features suggests that this phenomenon may also be present in RLQ at a low level. The possible reasons for the apparent lack of quasars with Type 2 spectra are discussed in Section 1.4.

Quasars are generally classified as being either radio-loud (RLQ) or radio-quiet (RQQ) due to the apparently bi-modal quasar radio luminosity distribution (Miller

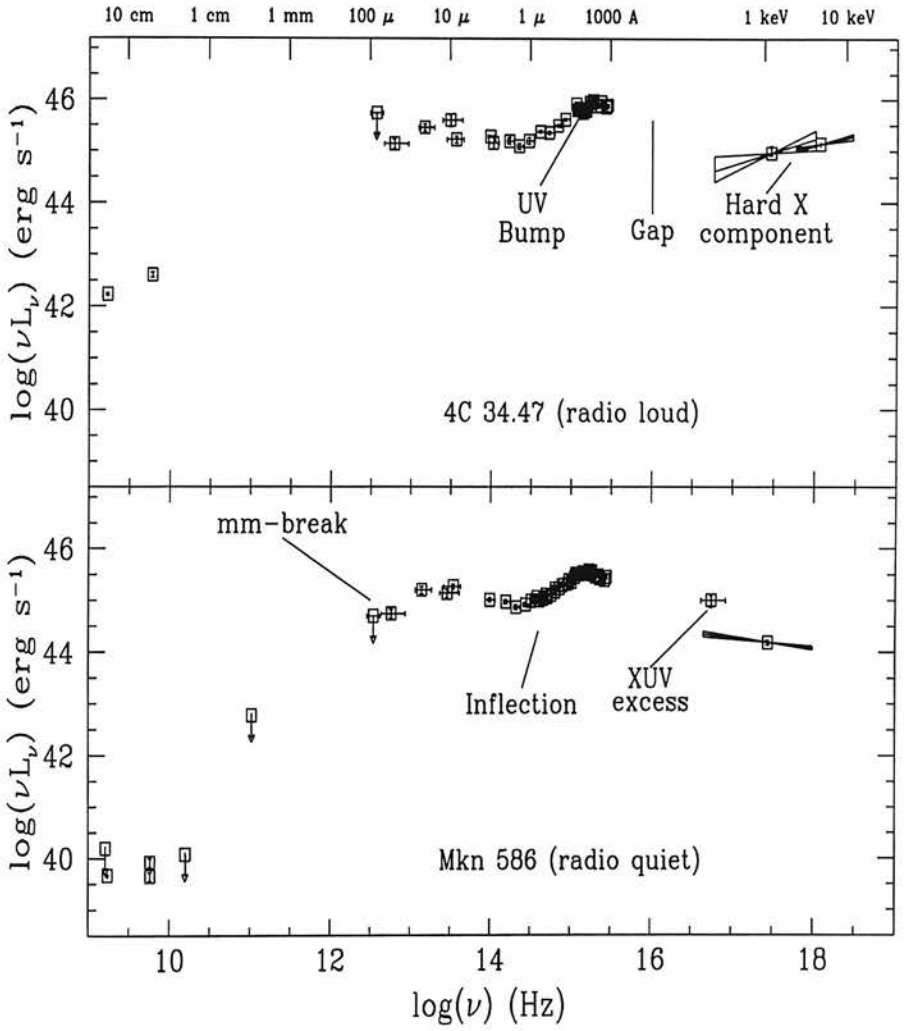

Figure 1.4: Average RQQ and RLQ spectral energy distributions from radio through to X-ray wavelengths (Elvis *et al.* 1984).

et al. 1990). Based on this, the cut-off between RLQs and RQQs used for selecting the quasar samples for the HST study was $L_{5GHz} < 10^{24}\,\mathrm{WHz^{-1}sr^{-1}}$, assuming $\Omega_0 = 1, H_0 = 50, \Lambda = 0$. Radio-loud quasars are considerably rarer than their radio-quiet counterparts, making up only 5-10% of the total quasar population. In the radio the lobe-dominated RLQ are one-sided FRII sources, and constitute some of the highest-luminosity radio sources known.

Until the early 1990's the reason for the so-called radio-loudness dichotomy was thought to be closely connected to the morphology of the respective host galaxies of the RQQ and RLQ. Early imaging studies with the new CCD detectors (see Section 1.6) seemed to show that the RQQs were to be found in spiral galaxies while the RLQs were located in early-type hosts. This seemingly clear morphological preference lent support to the idea that quasars were simply higher luminosity analogs of the Seyfert and radio galaxies found at lower redshifts. However, as will be discussed in detail in Section 1.6, more recent CCD studies in the optical and near-infrared have placed this straightforward picture in doubt, with at least some RQQs now known to have elliptical host galaxies.

1.2.4 BL Lacs and OVV Quasars

The final two categories of AGN to be considered here are the BL Lacs and Optically Violent Variable (OVV) quasars. Both classes of object are radio-loud, with flat spectra, and show large variability at all wavelengths, and on all timescales from years down to hours. Together these two classes of objects are collectively referred to as blazars.

BL Lacs

BL Lac sources are named after the archetypal object BL Lacertae, which was originally misidentified as a variable star in our own galaxy. The continuum emission of BL lacs is featureless, without the absorption or emission features associated with starlight or standard AGN spectra. The continuum can be well modelled by a simple power law, decreasing steadily from the flat-radio component through the optical to the X-ray.

Another unusual property of the continuum emission of BL Lacs is that it is shown to display strong linear polarisation, characteristic of a non-thermal source. The total luminosity of BL Lacs covers a wide range, overlapping the quasar luminosity function at the faint end (Robson 1996), with the variability in luminosity ranging from $0 \rightarrow 4$ magnitudes over timescales of a year, down to 0.1 magnitudes in a matter of hours. Multi-wavelength studies have shown that this variability persists at all wavelengths, with the characteristic timescale for variation showing a strong negative correlation with frequency.

All of these features are consistent with the scenario in which BL Lacs are objects in which relativistic beaming of synchrotron emission from a compact core swamps the normal AGN spectrum, together with the star light from the underlying host galaxy. In combination with the synchrotron spectrum, further support for the relativistic beaming explanation of BL Lacs comes from the numerous examples of apparent superluminal motion, characteristic of relativistic motion close to the line-of-sight (Blandford & Königl 1979). Current thinking favours BL Lacs as the beamed sub-group of a lower luminosity parent population, most likely FRI radio galaxies (see Section 1.4).

OVV Quasars

As a class of object the optically violent variable quasars share many of the properties of BL Lacs, including the power-law continuum, rapid variability and linear polarisation. There are however some important differences between the two classes. Perhaps the most important is that unlike the BL Lacs, OVVs do have the strong broad and narrow emission lines in their optical spectra, typical of other quasars. OVV are also more luminous than BL Lacs, and as a result have been detected over a wider range of redshifts $z = 0.2 \rightarrow 2.0$, although they still remain an extremely rare class of objects, numbering ≤ 100 in total (Robson 1996). Combined with the presence of a normal AGN emission-line optical spectrum and greater overall luminosity, the discovery that OVV have significantly stronger X-ray emission than BL Lac objects suggests that a clearer view of the central emission region is available in OVV quasars. The currently favoured parent population for OVV quasars is the powerful FRII radio galaxy population.

1.3 The Standard Model for AGN

When all of the different classes of AGN are considered together, several common properties start to emerge. The following points highlight the observational properties shared by some, or all, of the major classes:

- High surface-brightness optical nuclei
- UV excess
- emission line optical spectra
- Variability on all timescales
- X-ray emission

More specific evidence that there are strong similarities between the seemingly disparate classes of AGN includes the overlap in the Seyfert and RQQ luminosity functions, and the apparently indistinguishable nature of the extended radio emission of FRII radio galaxies and RLQ. By the end of the 1970's it was clear that there was substantial circumstantial evidence for some sort of orientation-dependent obscuration of the central ionising source, with the apparent array of different morphological and spectral AGN classifications possibly masking a simpler physical picture. The central features of what has become the standard model of AGN are set out below. No attempt has been made to cover the detailed work on the physics of accretion discs and emission line regions, both of which lie outside the scope of this introduction.

1.3.1 The Black-hole and Accretion Disc

For the purpose of this overview it will be taken as granted that the ultimate power source for AGN is accretion onto a supermassive black-hole. A full discussion of why supermassive black-holes are the most likely candidates, and the recent increase in firm observation evidence for their existence, is given in Section 1.5. A schematic of the central kiloparsec of a generic AGN is shown in Fig 1.5. The black-hole is the central

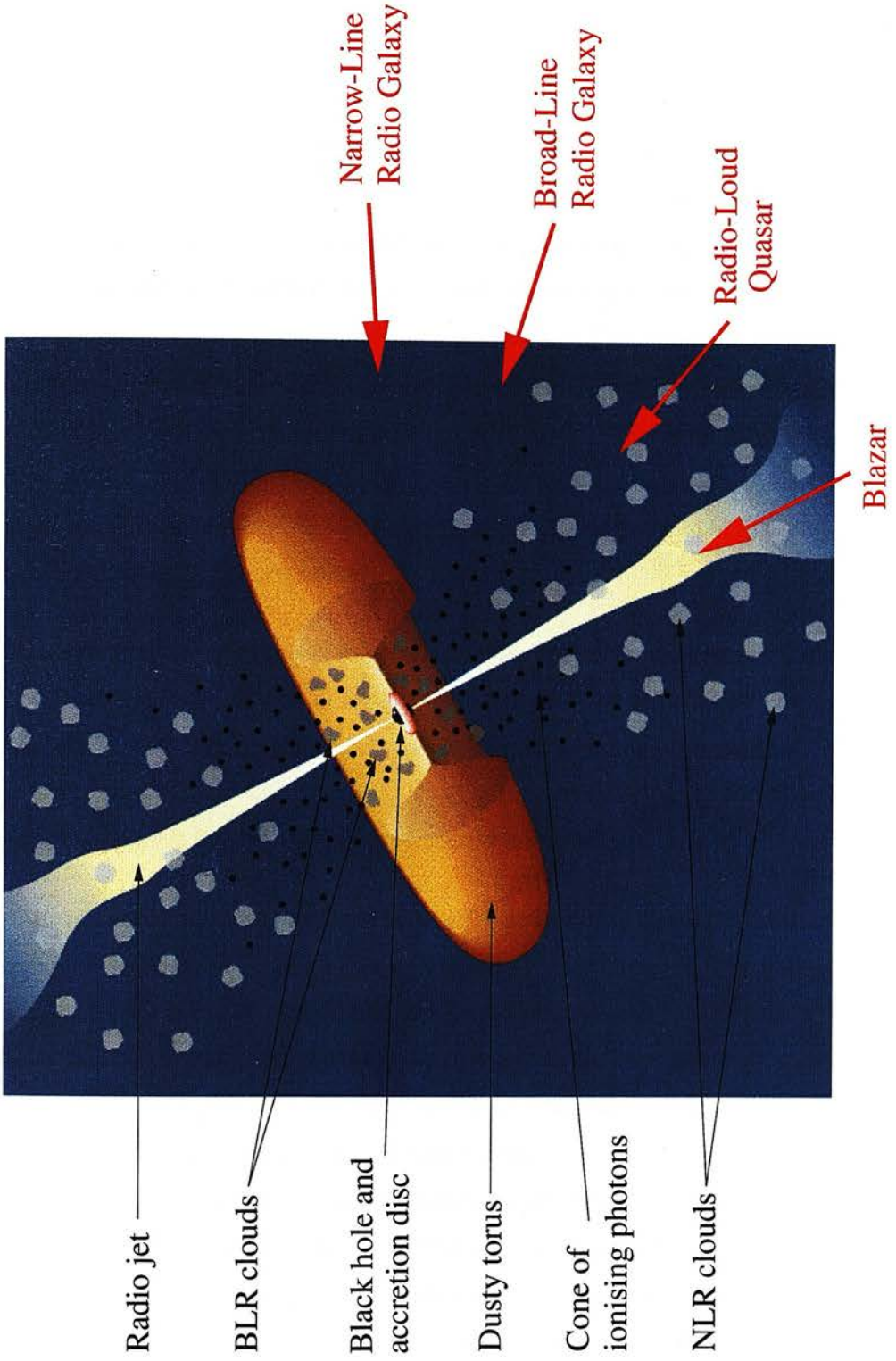

Figure 1.5: The standard model of an Active Galactic Nucleus (see text for description). The right-hand labels illustrate the orientation-based unification schemes, whereby the observational classification of the AGN is dependent on its inclination to the line-of-sight (Adapted from Urry & Padovani 1995).

feature of the model and has a mass of $\sim 10^7\,M_\odot$ for the lowest luminosity Seyfert, to $\sim 10^{10}\,M_\odot$, for the most powerful quasars known. Surrounding the black-hole from a radius of $\sim R_s$ ($10^{-6} \rightarrow 10^{-3}$ pc) out to a radius of a few light-months is the accretion disc. It is due to the conversion of gravitational potential energy to heat through viscous friction that the accretion disc is thought to be responsible for AGN continuum emission from X-rays through to optical wavelengths. The expected spectrum from a thin accretion disc (height<<diameter) can be approximated by considering the superposition of the emission from a series of annuli with different temperatures, which radiate as black-bodies. In this picture the X-ray emission originates from the hottest central regions (as required by the rapid X-ray variability), while the optical emission arises from the cooler outer regions.

Surrounding the accretion disc is the proposed dust torus. Due to its effective blocking of accretion disc emission in the plane of the disc, the torus is the crucial element in the orientation-based unification models described in the next section. The inner wall of the torus should lie at about ~ 1 pc, just outside the typical dust sublimation radius, and extend to a few hundred parsecs in diameter.

Above and below the accretion disc at a distance of ≤ 1 pc lie the BLR gas clouds. It is in these high-velocity, high-density gas clouds that the broad components of the permitted lines typical of Seyfert 1 and quasar spectra are produced. Further out still, at a distance of $\simeq 100$ pc lies the NLR, responsible for narrow permitted and forbidden line emission. The fact that the BLR clouds are located within the coverage of the torus, while the NLR clouds are sufficiently distant to be unaffected by absorption, provides a natural explanation for the differences between Type 1 and Type 2 spectra. If the AGN is viewed in the plane of the torus the isotropic BLR emission is absorbed and a narrow-line Type 2 spectrum is observed. In contrast, if the viewing angle is sufficiently close to normal to the accretion disc, then both the BLR and NLR regions are visible, and a Type 1 spectrum is observed.

Although this provides an explanation of the differences in emission line properties, it fails to explain why Seyfert 2 galaxies display an AGN continuum. In the model as outlined so far the torus is responsible for the near-total absorption of all accretion

emission in the plane of the disc. This then begs the question of why the continuum emission of Seyfert 2 galaxies is only typically one magnitude weaker than that of Seyfert 1 galaxies, and not totally extinguished by the torus. This problem is overcome in the standard model by the introduction of a scattering medium of free electrons between the broad and narrow-line regions. The scattering medium acts as a polarising mirror, reflecting $\sim 10\%$ of the continuum and BLR flux into the line-of-sight.

The introduction of the proposed scattering medium follows the ground-breaking observations of Antonucci & Miller (1985), who detected the broad-line spectrum of the classic Seyfert 2 galaxy NGC 1068 in polarized flux. Indeed, it is probably fair to say that it was this observation, along with numerous further examples in other Seyfert 2 galaxies, which has led to the widespread acceptance of some variant of the standard model. Although the scattering medium could be composed of dust grains, it is currently though to be made up of free electrons due to the detection of polarised X-ray emission.

Depending on whether the AGN is radio-loud or not, powerful radio jets are produced close to the black-hole and projected perpendicular to the accretion axis. The question of why some AGN produce jets, while others remain radio-quiet is not answered by this zeroth order model, although it is widely thought to be related to black-hole spin, black-hole mass, or both (Peterson 1997).

1.4 Unification schemes

The premise of orientation-based unification schemes is that the standard model outlined above can be used to describe the wide range of apparent AGN phenomenon with as few physical parameters as possible. The unification of various AGN classes described below are what are described as "weak", in that they recognised radio-loud and radio-quiet sources as being physically separate objects, with other morphological and spectral classifications explained by a combination of orientation and luminosity differences. The alternative to this are the so-called "Grand" unification schemes, where radio-loud and radio-quiet AGN are considered to be fundamentally the same type of

object, with the total luminosity as the only free physical parameter.

The investigation of the radio-loudness dichotomy is one of the major objectives of the HST imaging study, and is discussed further in Section 1.7. The following discussion of AGN unification schemes is a highly condensed version of that which can be found in the recent review articles by Antonnucci (1993) and Urry & Padovani (1995).

1.4.1 Radio-Quiet Unification

As was highlighted in the overview of the standard model of AGN, the detection of broad emission lines in the polarized flux of Seyfert 2 galaxies (Antonnucci & Miller 1985) is the strongest single piece of evidence that all Seyferts are fundamentally the same object. Although this claim had certainly been made previously (Osterbrock 1978), the Seyfert 2 broad-line detection convinced the astronomy community of the viability of orientation-based unification. At present it is clear that at least some classic Seyfert 2 galaxies are actually obscured Type 1 objects. This belief is reflected in the adoption of the Osterbrock (1981) sub-classification system described in Section 1.2, where Seyferts are grouped by the relative strength of their broad- and narrow-line components, presumed in turn to be dependent on the viewing angle of the active nucleus.

However, the unification of Seyfert galaxies as described above cannot be the full picture, with many Seyfert 2 galaxies not revealing a hidden BLR in polarized flux. Coupled with this, the model prediction that the continuum of Seyfert 2 galaxies should be highly polarized is not frequently observed either. Both of these apparent failures of the standard model point to either the BLR simply being missing in some Seyfert 2's, or the continuum and BLR emission reaching the observer via multiple scattering.

In the current version of radio-quiet unification, Seyferts and RQQ are linked by a simple increase in total luminosity. Solid supporting evidence for this hypothesis is given by the smooth overlap in respective luminosity functions, and the largely identical optical spectra of radio-quiet quasars and Seyfert 1 galaxies. Although the simplicity of this scheme is appealing, there is at least one major difficulty which is as yet not fully

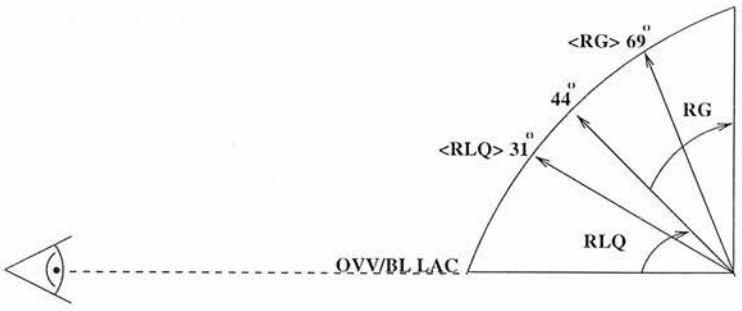

Figure 1.6: Radio-loud unification based on orientation of the radio axis and doppler beaming. At viewing angles of $\geq 45°$ from the jet axis a radio galaxy is observed. At angles of $\leq 45°$ a radio-loud quasar is observed. When the AGN is viewed directly along the jet axis then doppler beaming results in a BL Lac or OVV quasar being observed. This figure is adapted from Barthel (1989).

explained. If radio-quiet quasars and Seyfert galaxies differ only in their luminosity, the question of where the Type 2 radio-quiet quasars are hiding has to be answered. There seem to be two possible solutions to this problem. The first of these proposes that the increased power of quasars may alter the properties of the obscuring torus, either by widening its opening angle or by simply making it thinner. In either case the range of viewing angles from which the BLR region is visible to the observer increases, and correspondingly results in Type 2 quasars becoming very rare objects. The other frequently proposed solution holds that the Type 2 RQQ are in fact masquerading as ultra-luminous infrared galaxies (ULIRGs). These spectacular objects radiate luminosities comparable to quasars in the mid- to far-infrared via re-radiation by cool dust of some unknown nuclear source. ULIRGs are nearly always observed to be in the throws of merger activity, often display narrow-line spectra, and have been observed to display a hidden BLR in polarized flux (eg. Goodrich *et al.* 1996). It is now generally accepted that many of the most luminous ULIRGs harbour a hidden AGN (eg. Sanders *et al.* 1988), although the relative contribution of AGN and merger-induced starbursts have still to be determined.

1.4.2 Radio-Loud Unification

The generally accepted scheme for radio-loud unification was formulated by Barthel (1989), and builds on previous work by Scheuer & Readhead (1979), Orr & Browne (1982) and Peacock (1987). The main premise of this scheme is that radio galaxies, radio-loud quasars and blazars can be united via a combination of orientation and doppler beaming (see Fig 1.6).

By making the assertion that all RLQ are beamed close to the line of sight, this model naturally explains both the apparent superluminal motion, and the ubiquitous high jet:counterjet ratios observed in RLQ. The proposed unbeamed parent population in this model are the normal radio galaxies. By considering a sample of 3C radio galaxies and quasars which had a indistinguishable redshift-luminosity distribution, Barthel (1989) was able to show that the relative numbers of RLQ and radio galaxies are consistent with a jet angle to the line-of-sight of $\sim 45°$ being the transition point between an object being observed as a radio galaxy or a quasar. Any object in this scheme which is viewed directly along the jet axis will be observed to be a BL Lac or OVV quasar, depending on the objects' intrinsic luminosity. The differences in optical spectra between quasars and radio galaxies are again explained by obscuration due to a dusty torus, with RLQ, BLRG and NLRG being viewed at increasing angles to the line-of-sight.

A great deal of work has gone into trying to determine which types of radio galaxy constitute the parent populations of the different radio-loud quasar classes. The favoured picture at present is that the RLQ and OVV quasars are increasingly beamed sub-sets of the powerful FRII radio galaxies, while BL Lacs are beamed analogues of the intrinsically less powerful FRI radio galaxies. Supporting evidence for this picture comes from the good agreement in extended radio luminosity, and the virtually indistinguishable optical and near infrared properties of the respective host galaxies (Taylor *et al.* 1996, Urry *et al.* 1999).

1.5 Evidence for Supermassive Black-holes

The essential feature of the standard model of AGN activity is that the central power source is provided by accretion onto a supermassive black-hole. The hypothesis that black-hole accretion was behind the AGN phenomenon, was originally made because the observed rapid variability required that a vast amount of energy was being created in a volume comparable to the solar system. With a conversion efficiency of gravitational potential energy into radiation of $\epsilon \sim 0.1$, black-holes of the mass of $\sim 10^8\,M_\odot$ are capable of providing this output from a fairly modest accretion rate ($2\,M_\odot yr^{-1}$). The only credible alternative to the black-hole hypothesis is the starburst model (eg. Terlevich *et al.* 1992). In this picture the emission from the AGN is provided by a massive nuclear starburst and the resultant supernovae. Although it is undoubtedly the case that AGN activity and nuclear starbursts are often associated (eg. Davies *et al.* 1998), the starburst model has failed to be widely accepted as the primary power source due to its failure to explain many observational properties of AGN, (eg. X-ray variability) and the recent flood of supporting evidence for the existence of supermassive black-holes in the nuclei of active and inactive galaxies.

As a result of the intrinsically small size of black-holes and their surrounding accretions discs, they are unresolvable with the HST even in the nearest AGN. The evidence for the existence of central black-holes has therefore come from a wide variety of indirect observations, the three most widely celebrated of which are briefly discussed below.

1.5.1 HST Imaging and Spectroscopy of M87

The elliptical galaxy at the centre of the Virgo cluster has been intensely studied over the years due to its relative closeness ($\sim$ 15 Mpc), and its spectacular optical jet. Suspicions that the nucleus of M87 could harbour a supermassive black-hole go back as far as 1978, when detailed surface photometry and spectroscopy had revealed a central cusp in the starlight, and an increasing stellar velocity distribution towards the nucleus (eg. Young *et al.* 1978). Both of these lines of evidence were consistent with a supermassive object on the order of $\sim 10^9\,M_\odot$, but it required the high resolution of

the re-furbished HST to finally provide the evidence that convinced the astronomical community.

Emission-line imaging of the core of M87 (Ford *et al.* 1994) showed a spiral-like disc of gas and dust around the nucleus. Follow up spectroscopy with the Faint Object Spectrograph (FOS) showed that the gas was rotating in Keplerian orbit around a central mass of $2.4 \pm 0.7 \times 10^9 \, M_\odot$, contained within the central twenty parsecs (Harms *et al.* 1994).

1.5.2 Water Masers in NGC4258

Another line of evidence for the reality of supermassive black-holes in AGN comes from the detection of water vapour maser emission from the nuclear regions of the Seyfert 1.9 galaxy NGC4258, with VLBI (Miyoshi *et al.* 1995). The doppler shifts of the maser emission on either side of the nucleus are perfectly consistent with Keplerian orbits around a central mass of $3.6 \times 10^7 \, M_\odot$, contained within a radius of only 0.1 pc. Another interesting aspect of this discovery is that the maser emission is coming from a highly flattened structure, not in particularly good agreement with the inflated torus required by the standard model.

1.5.3 Asymmetric Iron Line Profiles

Perhaps the best evidence for the existence of supermassive black-holes comes from the detection of the Fe Kα emission line in ASCA X-ray observations of the Seyfert 1 galaxy MSG-6-30-15 (Tanaka *et al.* 1995). The emission line is extremely broad ($\sim 1 \times 10^5$ kms^{-1}), and displays a highly asymmetric gravitational redshift. The only viable explain of this phenomenon is that the emission is coming from gas at a distance of only 3-5 R_s from a supermassive black-hole. Interestingly, recent work in this field suggests that Fe Kα line emission may arise from gas within a radius of 3 R_s, indicating that the black-holes in AGN may indeed be rotating (Iwasawa *et al.* 1996).

1.5.4 Black-hole Mass Correlations in Inactive Elliptical Galaxies

Recent studies by Kormendy & Richstone (1995), Magorrian *et al.* (1998) and Franceschini *et al.* (1998), on the presence of black-holes at the centres of inactive ellipticals will turn out to be relevant to the analysis of the HST host galaxy study. By modelling the internal kinematics of a sample of nearby galaxies, Magorrian *et al.* find a linear relation (with a large scatter) between the mass of the galaxy spheroidal component (M_{sph}) and the mass of the central black-hole (M_{bh}) of the form: $M_{sph} = 0.006M_{bh}$. A result which is in good agreement with the relation of $M_{sph} \simeq 0.003M_{bh}$ found for $\geq 20\%$ of nearby galaxy bulges by Kormendy & Richstone (1995). The combination of the Magorrian *et al.* result with the best-fitting mass-to-light ratio, also provided by their modelling, leads to a relation between the galaxy luminosity and the mass of the central black-hole. Given that one of the main aims of the HST study is to determine accurate luminosities for each of the host galaxies, the work of Magorrian *et al.* provides a tool for investigating the distribution of black-hole masses in the three types of powerful AGN.

The study of Franceschini *et al.* is different from that of Magorrian *et al.* in that it features a sample of 13 nearby galaxies for which there is already a good estimate for the central black-hole mass from high spatial-resolution spectroscopy. Comparing the black-hole masses with the emission of the galaxies at various wavelengths, Franceschini *et al.* find strong positive correlations between the black-hole mass and the total and core radio power at 5GHz (6 cm). The form of both of these correlations is $L_{5GHz} \propto M_{bh}^{2.7}$. With 5GHz radio data readily available for the radio-loud objects in the HST study (see Chapter 2), and recently obtained for most of the RQQ (Kukula *et al.* 1998),this provides an opportunity to use the results of the HST study to investigate the quasar radio-loudness dichotomy.

1.6 Host Galaxy Studies Of Powerful AGN

Prior to the advent of CCD technology in the early 1980's the study of the host galaxies of AGN had be restricted to the low luminosity Seyfert and radio galaxies. With the arrival of deep electronic imaging, the detailed study of the host galaxies of powerful quasars became feasible. The obvious difficulty faced by all imaging studies of quasar host galaxies is the decoupling of the low surface-brightness galaxy light from the glare of the dominant unresolved nuclear emission. Host galaxy imaging from the ground is particularly difficult due to the blurring effect of atmospheric seeing causing the nuclear component to dominate the galaxy over angular scales of $1 \rightarrow 2''$. Despite these difficulties, substantial progress was made from ground-based imaging, particularly in the near-infrared, where the form of the nuclear and galaxy spectral energy distributions (SED) causes the contrast between nucleus and host galaxy to be reduced. The next section gives a brief summary of what could be regarded as the most significant host galaxy studies, both ground-based and HST, over the last 10→15 years. This list is in no way exhaustive, and is obviously somewhat subjective.

1.6.1 Ground-based Imaging Studies

Smith *et al.* (1986)

This study consisted of deep V–band CCD images of 31 low-z ($z < 0.3$) quasars. Smith *et al.* concluded from one-dimensional profile modelling (see Section 3.2) of the host galaxies that they were all very luminous, being drawn from the exponential tail of the galaxy luminosity function. They also reported what was to become the two fairly widespread results that the hosts of RLQs were some $0.7 \rightarrow 0.8$ magnitudes brighter than those of RQQs, and that the nuclear and host galaxy luminosities were positively correlated. The morphological discrimination produced by their modelling procedure showed a definite trend for the RQQs to prefer disc-like host galaxies, with the RLQs preferring early-type hosts. This was seen as good supporting evidence that RQQs and RLQs were simply luminosity scaled versions of the low-z Seyfert and radio galaxies.

Smith *et al.* also commented that $\sim 50\%$ of the quasar host galaxies seemed to display low-level morphological peculiarities, suggesting that galaxy interaction may be crucial for triggering AGN activity.

Véron-Cetty & Woltjer (1990)

This was an I-band optical study of 20 ($z \sim 0.3$) quasars, four of which were radio-loud. Like the study of Smith *et al.* before, Véron-Cetty & Woltjer found that the hosts of the RLQs were $0.6 \rightarrow 0.9$ magnitudes brighter than the RQQ hosts. Using R–band images available for a sub-set of the quasars, it was found that both the RQQ and RLQ host galaxies had somewhat bluer colours than normal galaxies. Perhaps the most significant outcome of this study was the suggestion that a substantial fraction of the RQQs were consistent with having early-type hosts, although the data did not allow a definitive morphological discrimination to be made. This can be seen as the first real suggestion that the simple unification of Seyferts and RQQs through an increase in luminosity was not the whole story.

Hutchings & Neff (1992)

Hutchings & Neff imaged 28 low-z ($0.1 < z < 0.5$) quasars in the V- and I–bands. Unlike the two studies above, which were conducted in $\geq 1''$ seeing conditions, this new study was able to achieve $0.5''$ resolution thanks to the adaptive optics of the Canada France Hawaii Telescope (CFHT). High quality luminosity profiles were obtained for the quasars, allowing a reasonable attempt to determine the morphology of the underlying hosts. Fourteen of the quasars were well fitted by $r^{1/4}$ elliptical profiles, four were apparently exponential, with a further ten objects having disturbed luminosity profiles. Like Véron-Cetty & Woltjer before them, Hutchings & Neff concluded that a substantial fraction of the RQQs were lying in early-type hosts. In agreement with Smith *et al.* , morphological disturbance seemed to be a common feature of the host galaxies, again suggesting that galaxy interactions or mergers have a role to play in the quasar phenomenon.

Dunlop *et al.* (1993)

With the arrival of infra-red detectors in the late 1980's the prospect of exploiting the reduced L_{nuc}/L_{host} ratios in the near-infrared became a reality. This programme featured deep K–band ($2.2\mu m$) imaging of a sample of $z \sim 0.2$ quasars, using the IRCAM 1 detector on the 3.9-metre United Kingdom Infrared Telescope (UKIRT), the first instrument of its type on a 4m-class telescope. A unique feature of this study was the selection of the quasars (14 RLQs and 18 RQQs) such that their distribution in the $V - z$ plane was statistically indistinguishable. In contrast to previous host galaxy studies, this allowed the results for the two quasar classes to be directly compared without being subject to possible selection biases. Unlike the existing optical studies there was found to be no significant difference in the luminosity of the host galaxies of RQQs and RLQs in the K–band, with all the hosts being drawn from the high-luminosity tail of the galaxy luminosity function. All of the hosts were found to be good "standard candles", following the established $K - z$ relation for radio galaxies (Lilly & Longair 1984).

McLeod & Rieke (1995)

Like the Dunlop *et al.* programme, McLeod & Rieke used near-infrared imaging (H–band) to minimize the quasar L_{nuc}/L_{host} ratio. The study featured deep images of 26 ($0.1 < z < 0.3$) high luminosity quasars, five of which were radio-loud. The resulting luminosity profiles were fitted with both disc and elliptical models, although the data were of insufficient quality to allow a morphological determination in the majority of cases. Using the best-fit disc models it was found that the hosts were extremely luminous, with the an average luminosity of $2L_\star$, where $L_\star$ is the characteristic luminosity of the Schechter function which best-fits the galaxy luminosity function.

Taylor *et al.* (1996)

This paper was a continuation of the Dunlop *et al.* (1993) study and featured additional K–band imaging of a sample of powerful $z \sim 0.2$ radio galaxies. In keeping with the selection of the two quasar samples, the radio galaxies were selected to have radio luminosities and spectral indexes which were indistinguishable from the RLQ sample. In addition to the extra data, this paper introduced the first use of a fully two-dimensional modelling technique to analyse the host galaxies (see Section 3.3). The results of the two-dimensional modelling of the three AGN sub-samples showed that all of the hosts were large ($r_e \geq 10$ kpc), and luminous ($L \geq 2L_\star$). No difference in host luminosity between the three AGN classes was detected, with the close agreement between the RG and RLQ sub-samples providing good evidence for radio-loud unification. Perhaps the most important result was that $\sim 60\%$ of the RQQs were found to have host galaxies which were significantly better matched by an elliptical model than the traditionally expected disc. Furthermore, The RQQ results also suggested a trend that the probability of finding an early-type host was an increasing function of the quasar luminosity.

1.6.2 HST Imaging Studies

Bahcall *et al.* (1994, 1995a, 1995b, 1995c, 1996, 1997)

This study featured WFPC2 V-band images of 20 ($z \sim 0.2$) luminous quasars, 6 of which were radio-loud. The Bahcall *et al.* programme was the first HST host galaxy study to feature a statistically meaningful number of objects, and received a large amount of publicity due to its initially controversial results. Due to the way in which HST orbits are scheduled, the data for any large observing programme arrives intermittently, which in turn led Bahcall *et al.* to publish results in a somewhat piecemeal fashion. The analysis performed on the first eight objects imaged produced only three positive identifications of underlying host galaxies, in direct contradiction to the findings of the ground-based studies described above. Their inability to detect luminous host galaxies led Bahcall *et al.* to make the controversial proposal that they were seeing "naked quasars", and that the quasar phenomenon may be taking place before

substantial star formation had occurred.

Due to the high dynamic range in quasar imaging the data obtained by Bahcall *et al.* was heavily saturated within a radius of $\leq 0.5''$ from the quasar nucleus. As a result of this, the point spread function (PSF) subtraction analysis which was performed normalized the relative nuclear contribution by matching the PSF to the flux in an annulus between $1 \rightarrow 3''$ radius from the quasar centroid. It is clear from ground-based imaging that, even in the most nuclear dominated objects, the host galaxy will make a considerable contribution to the flux in this region, leading to an inevitable over-subtraction of the nuclear contribution (see Section 3.1). The suspicion that the missing host galaxies may have been lost due to over-subtraction of the nuclear emission was reinforced by the re-analysis of some the data by McLeod & Rieke (1995) which showed that the host galaxies where in fact detectable at low surface-brightness levels.

The final paper in the series Bahcall *et al.* (1997) contained both one- and two-dimensional modelling of the residual flux after PSF-subtraction of the quasar images. Utilising a different empirical PSF than was originally used, the analysis reported in this paper led to the detection of 18 of the 20 host galaxies. The host morphologies were found to be diverse, with elliptical, spiral and irregular types all present. Once again the hosts of RQQs were found to be ~ 1 magnitude fainter that those of RLQs.

Hooper *et al.* (1997)

Hooper *et al.* made use of the HST to image somewhat more distant quasars with redshifts in the range $0.4 < z < 0.5$. A total of 16 objects where imaged through the F702W filter (wide R), 6 of which were radio-loud. Using a two-dimensional modelling technique, Hooper *et al.* successfully detected a host galaxy for each object, finding all of them to be luminous ($L \geq L_{\star}$). The objects in this study were selected to be matched in terms of redshift and apparent luminosity, which may have been instrumental in Hooper *et al.* finding no difference in the luminosity of the RQQ and RLQ host galaxies. Like the findings of Smith *et al.* and McLeod & Rieke earlier, Hooper *et al.* find the luminosity of the nuclear component and the host galaxy to be positively correlated,

albeit with a large scatter.

Boyce *et al.* (1998)

This paper detailed the results from a study of 14 quasars ($0.1 < z < 0.5$) with the F702W (wide R) on HST, the results for four of which had been previously published in Disney *et al.* (1995). Using the same modelling technique as Hooper *et al.* , a morphological discrimination was possible for 11 of the 14 objects. Of these 11 objects, 9 where found to be better described by an early-type host, with all of them having a luminosity of $L \sim L_{*}$. In keeping with previous results, the hosts of the RLQs (6 objects) were found to be ~ 0.7 magnitudes brighter than their RQQ counterparts.

1.7 Aims of the Project

The brief overview of the field of AGN research given in this introductory chapter has attempted to highlight the opportunities presented by the study of AGN host galaxies. It is the prospect of the investigation of the various unification schemes, and the unanswered questions posed by the quasar radio-loudness dichotomy, which provide the fundamental motivation for the HST host galaxy imaging study which comprises the main body of this thesis.

The summary of recent AGN host galaxy studies shows that although a great deal of progress has been made, in spite of the limitations of ground-based seeing, the conclusions of different groups are often contradictory on key issues, including:

- Are luminous RQQs located in disc galaxies?
- Are the hosts of RLQs brighter than the hosts of RQQs?
- Is morphological disturbance of host galaxies universal?
- Are host galaxy and nuclear luminosity correlated?
- Are AGN host galaxies bluer than inactive galaxies?

1.7.1 Thesis Structure

The imaging study reported in this thesis has its foundations in the previous K–band imaging of the same sample of objects by Dunlop *et al.* (1993) and Taylor *et al.* (1996). The two notable features of this existing work are the use of statistically-matched samples and a two-dimensional modelling technique to analyse the host galaxies. The next chapter describes how the knowledge gained from the existing K–band imaging study, combined with lessons learned from the problems experienced by previous HST programmes, was used to construct an observing strategy capable of delivering the specific aims of this study:

- Accurate host-galaxy scalelength and luminosity information.
- Reliable host-galaxy morphology determination.
- Optical-infrared host-galaxy colours.

Chapter three describes the development of the two-dimensional modelling technique adopted to extract the fundamental parameters of the host galaxies. The results from the substantial programme of tests conducted to determine the accuracy of the modelling technique are also reported.

Chapter four details the main results from the two-dimensional modelling of the HST host galaxy images. The relation of the host galaxy morphologies, scalelengths and luminosities to those of normal inactive galaxies are discussed. Both the RQQ and RLQ host galaxies are shown, for the first time, to follow the same Kormendy relation (Kormendy 1977) as that of low-z inactive elliptical galaxies. In the context of the calculation of the host galaxy optical-infrared colours, a short report is given on an exploratory observing run using tip-tilt active optics in the near-infrared. Chapter five explores the possibility of combining the results of Chapter 4 with the host galaxy/black-hole correlations discussed in Section 1.5 to provide insight into the quasar radio-loudness dichotomy.

The contents of Chapter six report on a investigation of the evolution of powerful radio galaxies between $z = 0.2$ and $z = 0.8$. An re-examination of HST imaging of a sample of $z \sim 1$ 3CR radio galaxies (Best, Longair & Röttgering 1997, 1998) allows a comparison with the low-redshift radio galaxy results obtained in Chapter 4. The radio galaxy scalelengths, absolute luminosities and Kormendy relations are examined for the signature of merger activity. In combination with the passive evolution predictions of spectrophotometric models (Jimenez *et al.* 1996), it is shown that the properties of the host galaxies provide no evidence of substantial merger activity in the redshift range $z = 0.2 \rightarrow 0.8$.

The final chapter summarizes the results and consequent conclusions reached in this thesis. A brief discussion of the possible avenues of further research is given.

Chapter 2

A Hubble Space Telescope Study of AGN Host Galaxies at z=0.2

2.1 Introduction

The purpose of this chapter is to discuss the observing strategy that was employed for the HST observations of the host galaxies of the sample of low-z powerful AGN which form the main work of this thesis. The overview of recent host-galaxy imaging studies given in the previous chapter highlighted the improvements that could be obtained by use of either ground-based near-infrared observations, or the high resolution offered by HST. The advantages of ground-based near-infrared observations have already been explored in the existing K-band imaging of the HST sample (Dunlop *et al.* 1993, Taylor *et al.* 1996). Although perhaps the most successful of recent host-galaxy studies, this programme was still limited by the constraints of ground-based seeing which made it impossible to determine host morphology for the brightest quasars. The logical next step in ground-based host imaging is discussed in Chapter 4 with a report on an exploratory observing run combining K–band imaging with recent advances in active-optics technology. This chapter describes what steps were taken to ensure that for the first time, a complete set of reliable host-galaxy parameters and optical-infrared colours could be obtained for a statistically meaningful sample of powerful AGN.

2.2 The Sample

The full sample of objects observed with HST during for this programme consists of 33 powerful AGN spanning the redshift range $0.11 < z < 0.26$. The sample is sub-divided into three statistically matched sub-samples consisting of 10 radio galaxies (RG), 10 radio-loud quasars (RLQ) and 13 radio-quiet quasars (RQQ). This new HST sample is a sub-set of the larger 40-object sample previously studied in the K–band with UKIRT (Dunlop *et al.* 1993, Taylor *et al.* 1996) which covered the redshift range $0.09 < z < 0.35$ and featured 12 RG, 13 RLQ and 15 RQQ. The slight reduction in the number of objects in the sample is as a result of the wish to avoid contamination of the images from strong emission-lines (see Section 2.4.1). The redshifts and optical luminosities of all three sub-samples can be found in Tables 2.1→2.3. The information presented in these tables has been taken from that originally collated by Dunlop *et al.* (1993) and Taylor *et al.* (1996) for the expanded 40-object sample.

For the purposes of this study the dividing line between radio-loud and radio-quiet has been taken as $L_{5GHz} < 10^{24}\,\mathrm{WHz^{-1}sr^{-1}}$, assuming $\Omega_0 = 1, H_0 = 50, \Lambda = 0$. The original reason for the adoption of this cut-off was that it was shown by Miller *et al.* (1990) to provide a good division in the apparently bimodal quasar radio-luminosity distribution. Although recent work in this area by Goldschmidt *et al.* (1999) has shown that the evidence for a bimodal distribution is perhaps weaker than first thought, this cut-off still provides a useful separation between the two traditional quasar classes. Tables 2.4→2.6 detail the radio properties of all three sub-samples. As with the optical data, much of the radio data presented in these tables has been taken from Dunlop *et al.* (1993) and Taylor *et al.* (1996), although Table 2.6 contains new radio detections and upper limits from Kukula *et al.* (1998). It can be seen from Table 2.5 and Table 2.6 that the two quasar sub-samples are well separated in terms of radio power, with the most radio luminous RQQ (1635+119) still more than a factor of twenty less luminous than the weakest RLQ (2355-082).

When observing with a hugely over-subscribed instrument such as HST it is usually unrealistic to expect to be awarded sufficient time to observe a substantial, complete sample of objects. This has caused problems for many previous HST studies which have

Source	Alternative Name	z	V	M_B
0230−027		0.239	19.2	−20.8
0307+169	3C 79	0.256	18.8	−21.5
0345+337	3C 93.1	0.244	19.0	−21.9
0917+459	3C 219.0	0.174	17.2	−22.0
0958+291	3C 234.0	0.185	17.3	−22.1
1215−033		0.184	18.9	−20.5
1215+013		0.118	17.0	−22.3
1330+022	3C 287.1	0.215	18.3	−21.4
1342−016		0.167	17.8	−21.6
2141+279	3C 436	0.215	18.3	−21.4

Table 2.1: The name, redshifts, apparent V-magnitudes and absolute B-magnitudes of the galaxies in the radio-galaxy sub-sample.

been unable to come to robust conclusions due to the restriction of observing small samples, or through poor sample selection. However, the careful sample matching that was performed to construct the original 40-object sample ensures that these drawbacks are not experienced with the imaging of the new HST sample. The three sub-samples are matched in such a way as to allow a meaningful comparison of the host-galaxy characteristics without biasing from possible correlations with radio power or AGN optical luminosity. Therefore, although the new 33-object sample is not complete, the sub-samples are at least statistically indistinguishable, allowing firm conclusions to be drawn about the relative nature of the host galaxies of the three main types of powerful AGN.

Source	Alternative Name	z	V	M_B
0137+012	PHL 1093	0.258	17.07	−23.9
0736+017	OI 061	0.191	16.47	−23.8
1004+130	OL 107.7	0.240	15.15	−25.7
1020−103	OL 133	0.197	16.11	−24.2
1217+023	UM 492	0.240	16.53	−24.3
2135−147	PHL 1657	0.200	15.53	−24.9
2141+175	OX 169	0.213	15.73	−24.8
2247+140	4C 14.82	0.237	15.33	−23.9
2349−014	PB 5564	0.173	15.33	−24.7
2355−082	PHL 6113	0.210	17.50	−23.0

Table 2.2: The name, redshifts, apparent V-magnitudes and absolute B-magnitudes of the quasars in the radio-loud quasar sub-sample.

2.2.1 Sub-sample Matching Criteria

Radio Galaxy - Radio-loud Quasar Matching

As was discussed in the previous chapter, radio-loud unification theory seeks to reconcile the seemingly disparate radio galaxy and radio-loud quasar populations through orientation effects. Therefore, in order to test the resulting prediction from unification theory that the host galaxies of the two AGN populations should be identical, it is necessary to ensure that the RG and RLQ sub-samples contain comparable numbers of objects and are indistinguishable in their radio properties. With this objective in mind the RG and RLQ sub-samples both number ten objects, and have been carefully matched in terms of their radio power (P_{5GHz}), see Fig 2.1. The similarity of the sub-sample P_{5GHz} distributions is confirmed by the application of the Kolmogorov-Smirnov (KS) test, which returns a probability of $p = 0.68$.

Source	Alternative Name	z	V	M_B
0052+251		0.154	15.90	−23.9
0054+144	PHL 909	0.171	15.71	−24.3
0157+001	Mkn 1014	0.164	15.69	−24.2
0204+292	3C 59?	0.109	16.00	−23.0
0244+194		0.176	16.66	−23.4
0257+024	US 3498	0.115	16.10	−23.0
0923+201	Ton 1057	0.190	15.83	−24.4
0953+414	K 438-7	0.239	15.55	−25.3
1012+008		0.185	15.85	−24.3
1549+203	LB 906	0.250	16.50	−24.4
1635+119	MC 2	0.146	16.50	−23.1
2215−037		0.241	17.20	−23.7
2344+184		0.138	15.90	−23.6

Table 2.3: The name, redshifts, apparent V-magnitudes and absolute B-magnitudes of the quasars in the radio-quiet quasar sub-sample.

Radio-quiet Quasar - Radio-loud Quasar Matching

The results of recent quasar host-galaxy studies have undermined the traditional picture that host morphology is solely responsible for the quasar radio-loudness dichotomy (see Chapter 1). However, these results have also suggested that the properties of the host galaxies of these two populations do offer a crucial insight into the mechanism required for producing powerful radio emission. As was discussed in the previous chapter, the discovery that the likelihood of a RQQ having an early-type host is an increasing function of nuclear luminosity (Taylor *et al.* 1996, McLeod & Rieke 1994), combined with the recent work on the masses of black-holes in inactive ellipticals (Magorrian *et al.* 1998) leads to the possibility that it is the size, mass and cluster environments of the host galaxies that hold the key to the radio-loudness dichotomy. Therefore, to facilitate a fair comparison, the RLQ and RQQ sub-samples have been chosen to

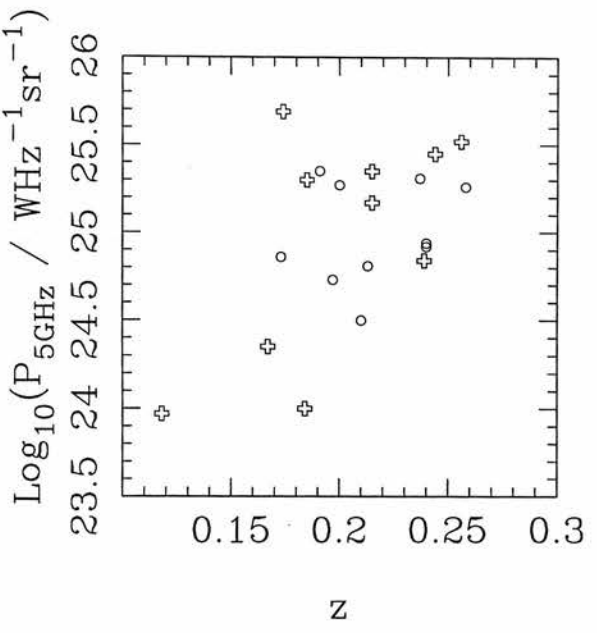

Figure 2.1: The distribution of the radio galaxy sub-sample (crosses) and the radio-loud quasar sub-sample (open circles) in the $P_{5GHz} - z$ plane. The two P_{5GHz} distributions can be seen to be very similar, an impression which is confirmed by the application of the Kolmogorov-Smirnov test which returns a probability of $p = 0.68$

have indistinguishable V-magnitude distributions (see Fig 2.3). The two distributions are not significantly different statistically, with the KS test returning a probability of $p = 0.25$.

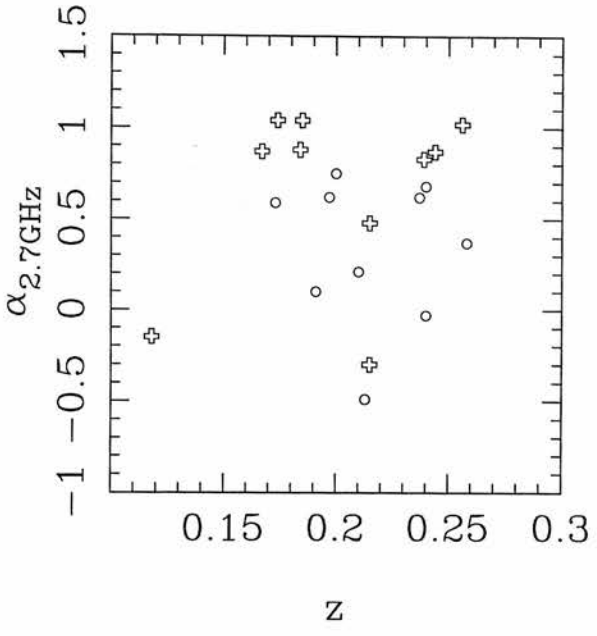

Figure 2.2: The distribution of the radio galaxy sub-sample (crosses) and the radio-loud quasar sub-sample (open circles) in the $\alpha - z$ plane. The two α distributions are distinguishable at the 2σ level, $p = 0.007$.

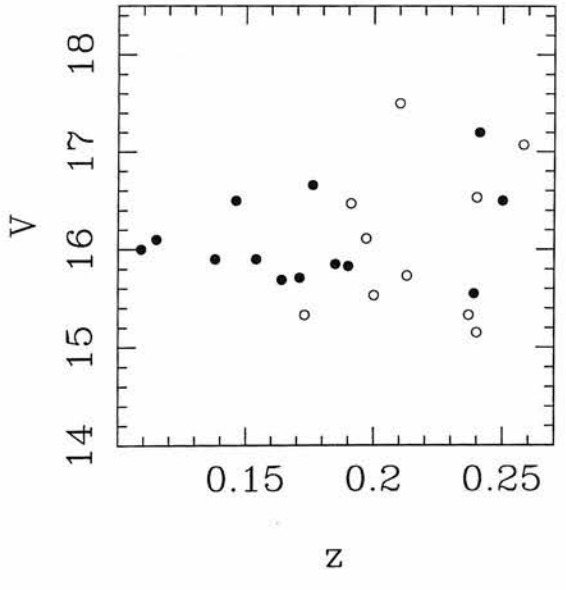

Figure 2.3: The distribution of the radio-quiet quasar sub-sample (filled circles) and the radio-loud quasar sub-ample (open circles) in the apparent V magnitude–redshift plane. The two V-magnitude distributions are statistically indistinguishable, the Kolmogorov-Smirnov test returning a probability of $p = 0.25$

Source	Alternative Name	$\mathrm{Log_{10}}(L_{5GHz})$ ($\mathrm{WHz^{-1}sr^{-1}}$)	S_{5GHz} (Jy)	$\alpha_{2.7GHz}$	Radio Structure	Radio Ref.
0230−027		24.84	0.330	0.83	Do,II	4
0307+169	3C 79	25.52	1.310	1.02	Do,ccII	2
0345+337	3C 93.1	25.45	1.280	0.87	P	1
0917+459	3C 219.0	25.69	4.350	1.04	Do,ccII	3
0958+291	3C 234.0	25.30	1.540	1.04	DoII	10
1215−033		24.00	0.108	0.88	D2	4
1215+013		23.97	0.210	−0.15	U	4
1330+022	3C 287.1	25.35	1.430	0.48	Do,ccII	4
1342−016		24.35	0.224	0.87	Do,II	4
2141+279	3C 436	25.17	1.036	−0.30	Do,II	11

Table 2.4: The radio properties of the radio galaxy sub-sample. The radio structure reference number given for each object refers to the list shown underneath Table 2.6.

Source	Alternative Name	$\mathrm{Log_{10}}(L_{5GHz})$ ($\mathrm{WHz^{-1}sr^{-1}}$)	S_{5GHz} (Jy)	$\alpha_{2.7GHz}$	Radio Structure	Radio Ref.
0137+012	PHL 1093	25.26	0.830	0.37	DoII	6
0736+017	OI 061	25.35	1.920	0.10	U	15
1004+130	OL 107.7	24.94	0.420	0.68	Do,cc II	13
1020−103	OL 133	24.73	0.390	0.62	D2	7
1217+023	UM 492	24.92	0.470	−0.03	D2	4
2135−147	PHL 1657	25.27	1.310	0.75	Do,cc II	7
2141+175	OX 169	24.81	0.500	−0.49	U	5
2247+140	4C 14.82	25.31	1.030	0.62	P	16
2349−014	PB 5564	24.86	0.700	0.59	Do,ccII	2
2355−082	PHL 6113	24.50	0.220	0.21	DoII	7

Table 2.5: The radio properties of the radio-loud quasar sub-sample. The radio structure reference number given for each object refers to the list shown underneath Table 2.6.

Source	Alternative Name	$\mathrm{Log_{10}}(L_{5GHz})$ ($\mathrm{WHz^{-1}sr^{-1}}$)	S_{5GHz} (Jy)	$\alpha_{2.7GHz}$	Radio Structure	Radio Ref.
0052+251		21.55	0.00046			
0054+144	PHL 909	21.87	0.00073			
0157+001	Mkn 1014	22.87	0.008		U	14
0204+292	3C 59?		0.840	0.76	C	12
0244+194		<21.43	<0.025			
0257+024	US 3498	22.19	0.00034			
0923+201	Ton 1057	<21.66	<0.0004			
0953+414	K 438-7	<21.69	<0.0002			
1012+008		22.00	0.0008			
1549+203	LB 906	<21.72	<0.0002			
1635+119	MC 2	23.02	0.0153	0.52		
2215−037		<21.88	<0.0003			
2344+184		<21.18	<0.0002			

Table 2.6: The radio properties of the radio-quiet quasar sub-sample. The radio structures reference for each object (where known) refers to the list given below. The radio structures are labelled as in Dunlop *et al.* 1989 :U=Unresolved, P=Partially Resolved, C=Central Component, Do=Double, D2=Flat spectrum core+one-sided extended emission, I/II=FRI/FRII.

1. Akujor *et al.* (1991)
2. Antonucci (1985)
3. Clarke *et al.* (1992)
4. Dunlop *et al.* (1989)
5. Feigelson, Isobe & Kembhavi (1984)
6. Gower & Hutchings (1984a)
7. Gower & Hutchings (1984b)
8. Kukula *et al.* (1998)
9. Leahy, Pooley & Riley (1986)
10. McCarthy *et al.* (1991)
11. Meurs & Unger (1991)
12. Miley & Hartsuijker (1978)
13. Miller, Rawlings & Saunders (1993)
14. Romney *et al.* (1984)
15. van-Breugel, Miley & Heckman (1984)

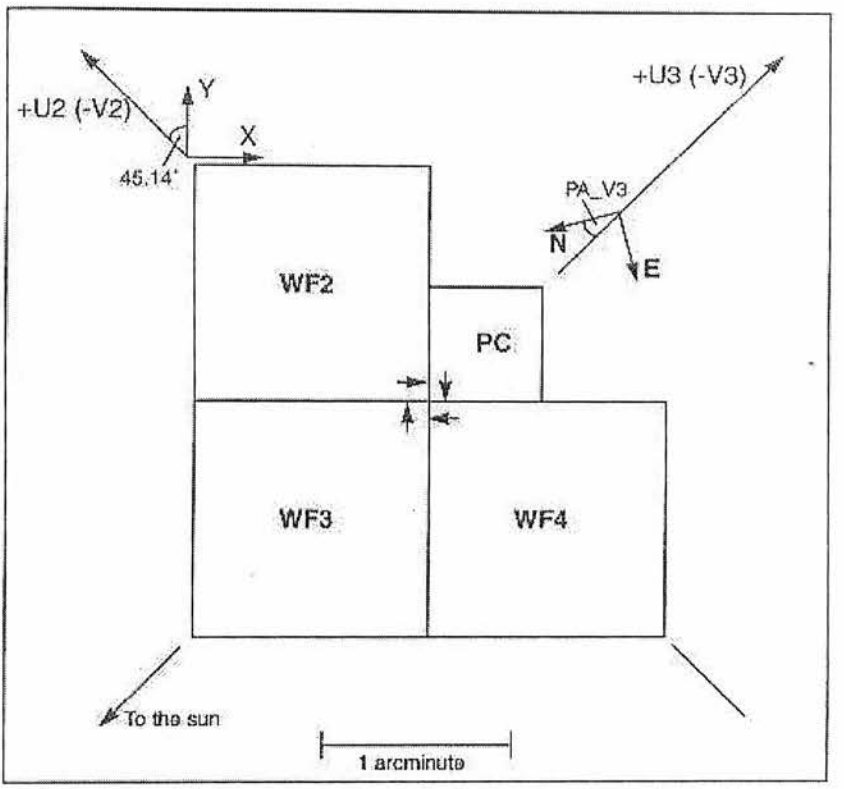

Figure 2.4: A schematic diagram showing the layout of the PC and WF chips in WFPC2. The direction of read-out for each CCD is shown by the arrows. The various angles shown determine the orientation of WFPC2 on the sky and are included in the image header information. This diagram has been scanned from the WFPC2 Handbook (Biretta *et al.* 1996).

2.3 The Wide Field and Planetary Camera

The Wide Field and Planetary Camera 2 (WFPC2) is the main optical camera currently on-board the HST and is sensitive to wavelengths in the range 1150Å→10500Å. WFPC2 features 4 CCD detectors in an L-shaped formation as illustrated in Fig 2.4. All four of the detectors are 800×800 pixels, thick, front illuminated CCD's constructed by Loral. Three of the CCDs (the WF chips) are operated in (F/12.9) mode, giving a plate-scale of $0.1''$ per pixel. The remaining chip, the Planetary Camera (PC), is operated in (F/28.3) mode giving a plate-scale of $0.046''$ per pixel. The resulting field-of-view for WFPC2 is approximately $150'' \rightarrow 150''$ from the L-shaped WF chips, and $34'' \times 34''$ for

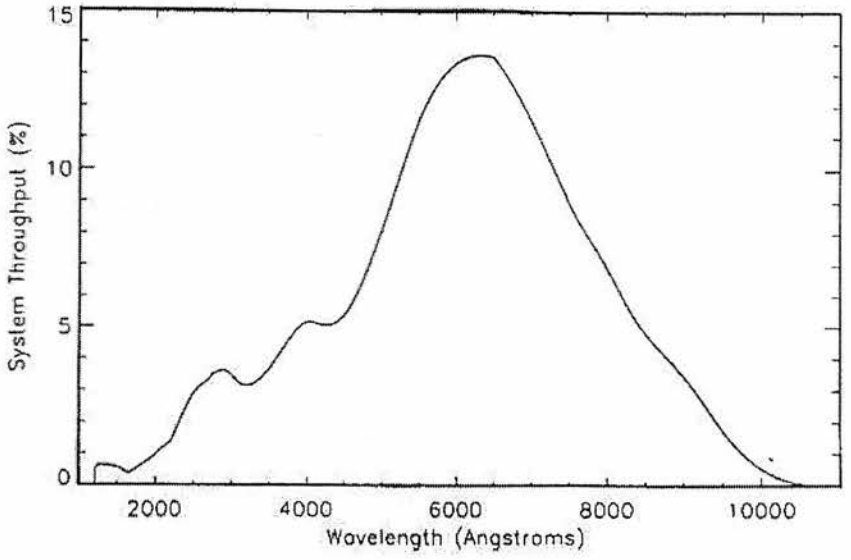

Figure 2.5: The throughput of the HST+WFPC2 system. The peak throughput of $\simeq 13\%$ occurs at ≈ 6400Å, well matched to the F675W filter used in this study.This diagram has been scanned from the WFPC2 Handbook (Biretta *et al.* 1996)

the PC.

The full filter set of WFPC2 numbers 48 and includes broad-band filters which approximate the standard Johnson-Cousin UBVRI set. The F675W filter used in this study (see Section 2.4.1) is the designated R-band WFPC2 filter and closely matches the standard Cousin R–band filter. WFPC2 provides a useful level of quantum efficiency over its full wavelength range and can be seen in Fig 2.5 to peak at an efficiency of 13% at the wavelengths covered by the R-band filter used in this study (see Figure 2.6). WFPC2 was installed on HST during the 1993 refurbishment mission and features internal corrective optics to remove the spherical aberration of the primary mirror. In order to correct for the spherical aberration WFPC2 has aspheric secondary Cassegrain mirrors for each of the four Cassegrain relays that serve the four separate chips individually. These secondary mirrors introduce an inverse aberration which returns a near diffraction-limited PSF close to what was originally designed. The PSF which is recovered by the corrective optics contains $\approx 65\%$ of the flux of a point-source inside a circle of radius $0.1''$. Although the corrective optics incorporated within WFPC2 successfully

remove the spherical aberration of the primary mirror, the final PSF is not as sharp as that delivered by the telescope optics alone, due to the combined effects of the pixel response function and large angle scattering. The pixel response function is a property of the CCDs themselves, and is a wavelength dependent blurring effect (worsening with increasing wavelength) caused by diffusion of photoelectrons across the pixel boundaries. The result of this is that at optical wavelengths only about 70% of the flux of a perfectly centred point-source will actually be detected in the central pixel. Perhaps the more serious concern with reference to host-galaxy studies is the large angle scattering ($\geq 3''$). It is thought that this scattering is due to the front-illumination of the WFPC2 CCDs allowing scattering from the CCD electrode structure. The result is a low-level "halo" of light which can be detected at radii $\geq 20''$ from bright point-sources. A discussions of the problems posed by this defect is given in Section 3.3.1.

2.4 Observing Strategy

2.4.1 Filter Choice

There are two crucial issues which governed the choice of filter for this study. The first of these was that the optical filter needed to sample sufficiently long wavelengths to ensure that even at the high-redshift end of the sample it still sampled light long-wards of the 4000Å break. This requirement is satisfied by three filters from the WFPC2 filter set; F606W, F675W and F702W. The F606W (wide V) filter approximates the standard V–band and was used by Bahcall *et al.* (1994, 1995a, 1995b, 1996, 1997) during their study of the hosts of 20 powerful quasars in a similar redshift range to this sample. The F702W (wide R) filter has also been extensively used for host galaxy work (Hooper *et al.* 1997, Boyce *et al.* 1998), and shares the advantage of the F606W filter in having high throughput. However, both of these filters suffer from the same disadvantage of including major AGN emission lines within their wavelength coverage. The filter profiles of the three filters can be seen in Fig 2.6 complete with the quantum efficiency of the WF2 chip. It can clearly been seen from Fig 2.6 that the F606W and F702W filters are badly affected by the prominent OIII and Hα emission-lines respectively. By

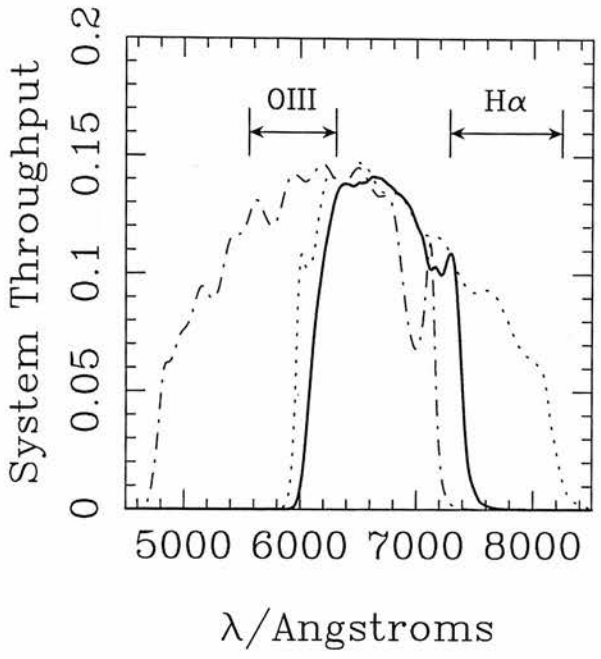

Figure 2.6: The profiles for the three filters under consideration for use in the HST host galaxy study; F606W (dot-dash), F675W (solid) and F702W (dot). The filter profiles are shown including the quantum efficiency of the WF2 CCD. Also shown in the figure are the wavelengths covered by the prominent AGN emission lines OIII and Hα over the redshift range of the sample. It can clearly be seen that the F606W and F702W filters are contaminated by OIII and Hα respectively.

carefully restricting the redshift range of the previous 40-object sample (see Section 2.2) it has been possible to avoid all serious emission-line contamination by adopting the narrower wavelength coverage of the F675W (R–band) filter. As can be seen from an investigation of Fig 2.6, the choice of the F675W filter does incur the penalty of a loss of system throughput. However, with the knowledge gained from the previous off-nuclear spectroscopy programme (Hughes *et al.* 1999) that the hosts generally have a well defined 4000Å break, and the red colours (apparent $B - K \geq 5$) derived from the existing B- and K–band imaging (Taylor 1995), it was felt that the longer mean wavelength of the F675W filter would offer an advantage over the F606W, despite the lower throughput. The following equation describes the signal-noise-ratio of the flux

detected in a single WF pixel:

$$\mathrm{SNR} = \frac{c.t.g}{\sqrt{c.t.g + s.t.g + (t + 46) \times 0.004 + \mathrm{rd}^2}} \tag{2.1}$$

c = source counts ($\mathrm{DNs^{-1}pix^{-1}}$)

s = background counts ($\mathrm{DNs^{-1}pix^{-1}}$)

t = exposure time (sec)

g = analog-to-digital gain ($\mathrm{e^{-}DN^{-1}}$)

rd = readout noise ($\mathrm{e^{-}}$)

Using Equation 2.1 and the appropriate figures for the F606W filter (Biretta *et al.* 1996) the predicted 3σ $\mathrm{pix^{-1}}$ sensitivity limit for the single 1400 second exposures used by Bahcall *et al.* is $\mu_v = 23.8$ mag.arcsec^{-2}. In comparison, the predicted sensitivity limit for the F675W filter, assuming three equal exposures of 600-seconds (see Section 2.4.3) is $\mu_v = 24.0$ mag.arcsec^{-2}, assuming a typical elliptical galaxy colour at $z = 0.2$ of $V - R = 0.8$ (Fukugita *et al.* 1995). Therefore, the predicted performance of the F675W filter should allow deeper surface-brightness limits than the F606W filter, while still avoiding the emission line problems of the F702W filter. One final advantage to be gained from the use of the F675W filter is that it closely mimics the standard Cousins R-band filter, allowing accurate photometric conversion for comparison with results already in the literature.

The surface-brightness predictions performed above can be seen to have been reasonably accurate by an investigation of Tables 2.7 and 2.8 which detail the surface-brightness sensitivities of the reduced data.

2.4.2 Detector Choice

When observing with WFPC2 a choice has to be made as to whether to use one of the three Wide Field chips (WF), or the single Planetary Camera chip (PC). With an approximate factor of two advantage in spatial sampling, the PC would seem to be the obvious choice for quasar host-galaxy work. However, after extensive investigation of archived WFPC2 quasar images and calculations of the expected low surface-brightness

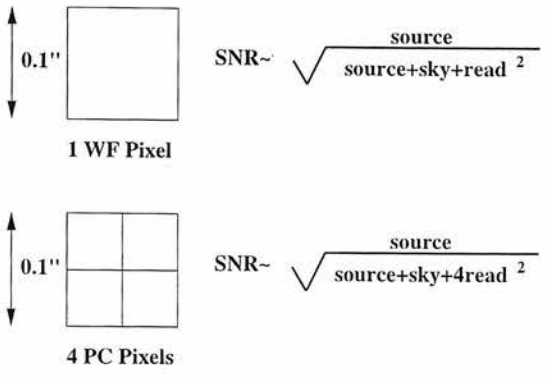

Figure 2.7: An illustration of the inevitable reduction in low surface-brightness sensitivity incurred by using the higher-resolution PC detector instead of the WF chips. Due to the significant read-noise contribution compared to the typical sky background, even binning up PC images to the same resolution of the WF chips is penalised by the introduction of the extra read-noise.

sensitivity of the two detectors under various possible observing strategies, it was actually decided that the WF2 chip was the best detector for this study. The main reasons for this choice are as follows:

- Wide-Field chips offer greater low surface-brightness sensitivity than PC.
- Wide-Field PSF has reduced extended scattered light halo.
- Wide-Field is conducive to accurate sky-background determination.

The first of these points was decisive in the final choice of detector and is illustrated in Fig 2.7. Given that one of the fundamental objectives of this study is to accurately determine the scalelength and morphology of the underlying host galaxies, it is obviously desirable to follow the extended galaxy light out to as great a radius as possible. Although the WF chips clearly provide greater sensitivity on a pixel-by-pixel basis, simply due to their greater area, if the situation were such that the noise contribution from reading-out the CCD was negligible, in comparison to the poisson noise on the detected flux, it would be possible to recover the sensitivity of the larger WF pixels simply by binning up the PC pixels in groups of four. However, since the read-out noise for the WF and PC chips is $\simeq 5.3e^{-1}$ (gain 7) and the typical sky background count

for the F675W filter is $0.056e^{-}s^{-1}$, the contributions from the sky poisson noise and read-out noise to the denominator of equation 2.1 are of comparable magnitude. It can therefore be seen that due to the extra three read-out noise contributions required when binning up the PC pixels to WF resolution, the WF chips offer a significant advantage in term of sensitivity.

The second reason listed above for choosing the WF detectors concerns the extended halo of scattered light which is a characteristic of the PSF of both the WF and PC detectors. Although a low-level feature in comparison to the total flux of a bright point-source (see Fig 3.3) the halo could easily mimic the low surface-brightness of a faint host galaxy underneath the bright nucleus of a quasar. Therefore, the fact that the WF detector PSF has a halo which is approximately a factor of five fainter than that associated with the PC (Krist & Burrows 1994) reinforces the choice of the WF detectors. A more detailed discussion of the WFPC2 PSF and its possible effects on the analysis of the host-galaxy data is given in Chapter 3.

The third reason for the choice of the WF detectors listed above is a practical consideration concerning the likely size of the host galaxies in comparison to the field-of-view of the PC. With its plate-scale of $0.05''\text{pix}^{-1}$ the 800×800 pixels of the PC (only $\approx 750\times750$ are actually exposed) provides a field-of-view of some $35''$ square. Experience gained from the existing K–band images of the sample show that the host galaxies should be detectable over a diameter of $\geq 24''$ (assuming a host colour of $R-K\sim3$), leaving comparatively little "blank" area on the chip from which to determine the true background light level. This problem will only be compounded by the many nearby companion objects that are known to be associated with the sources from the sample. Given that an accurate determination of the background level is crucial if a reliable scalelength, and in extreme cases the host morphology, is to be determined, the greater spatial coverage offered by the WF chips is an obvious advantage. The specific choice of WF2 (see Fig 2.4) instead of the more commonly chosen WF3 was due to its marginally better performance during the period immediately prior to the observations.

2.4.3 Exposure Times

The allocated time for this HST programme was 34 orbits, allowing a single orbit for each target, with a final orbit devoted to observing the empirical PSF. The exposure times chosen for the observations of the AGN host galaxies were carefully tailored such that the final reduced images successfully spanned the huge dynamic range displayed by the quasars. For both the quasars and radio galaxies deep sensitive images are clearly desirable. However, due to inevitable saturation produced by long exposures of the unresolved quasar nuclear components, it was necessary to use slightly different observing strategies for the quasars and radio galaxies respectively.

For the quasar observations, six separate exposures of 5, 26, 40 and 3×600 seconds were taken. The two short exposures at the start were designed to guarantee that even for the brightest quasars one unsaturated image would always be obtained, ensuring that it would always be possible to have a model-independent measure of the nuclear component.

When observing the radio galaxies the risk of saturation was minimal and so no short snapshot exposures were required. Each radio galaxy orbit was therefore broken into three long 700-second exposures. Any time which remained in the orbit was filled with an exposure of flexible length (usually 40→ 100 seconds).

2.4.4 PSF Observations

The form of the WF point spread function (PSF) depends crucially on both the chip position and the spectral energy distribution (SED) of the target. These effects are well-understood and are included in the TINYTIM software package (Krist 1998) which produces synthetic PSFs and has been utilised by several authors (eg. Boyce *et al.* 1998, Hooper *et al.* 1997). However, although providing an excellent fit over the central two arcseconds, the synthetic PSFs produced by TINYTIM deviate strongly from the empirical WF PSF at larger radii as a result of being unable to model the halo of scattered light. As the halo is due to internal scattering within the camera, which

shows complex structure, is not uniform, and which is also wavelength and position dependent, it cannot be readily modelled (A more detailed discussion of the use of TINYTIM, and PSF issues relating to the analysis of the HST data is given in the next chapter). One orbit of the allotted HST time was therefore devoted to constructing a deep, unsaturated stellar PSF using the F675W filter, with the star centred on exactly the same part of the WF2 chip as the target objects (All of the targets were observed in WF-FIX mode which ensured that all of them were imaged at roughly the same chip position).

The star chosen was GRW +70D5824, a white dwarf of spectral type DA3 and apparent magnitude $V = 12.77$. Since this object is also a UV standard star for WFPC2, both its position and spectrum are extremely well determined (Turnshek *et al.* 1990). No stars of a comparable brightness lie within 30 arcsec, ensuring that the stellar PSF is not contaminated by light from nearby sources. GRW +70D5824 has a $B - V$ colour of 0.09, which is close to the neutral colours typical of the quasars in the sample. Therefore, the star's spectrum serves as a reasonable match to a quasar SED over the wavelength range samples by the F675W filter.

The observations of the empirical PSF had to fulfil two separate criterion. In order to be able to represent the full dynamic range of the AGN exposures, the PSF observations had to be simultaneously unsaturated, and have a high signal-to-noise measure of the large radius scattered light. In order to achieve this goal a series of exposures was carried out with durations of 0.23, 2, 26 and 160 seconds. The 0.23 second exposure is the shortest practical exposure available on HST (shorter exposures are comprised by the shutter flight time), after which the stellar image should be between 7.5→10% of the saturation level, depending on sub-pixel centring. The longer exposures were tailored such that, although they became increasing saturated in the core, they never became saturated outside the radius at which the signal-to-noise of the preceeding shorter exposure had become unsatisfactory. During the reduction process this allowed the splicing together of successively deeper annuli to produce a final composite PSF covering an extremely high dynamic range. The PSF star is more than two magnitudes brighter than the most luminous of the quasars ($V = 15.15$), ensuring that the signal-to-noise in the wings is much greater than found in the longest quasar exposures. As

was mentioned in Section 2.3 the WF detectors on HST badly undersample the PSF. Therefore, in an effort to improve the sampling, each of the PSF exposures described above was duplicated in a two-point dither pattern.

All of the measures described here have been designed to produce a final PSF which matches as closely as possible the AGN observations in terms of signal-to-noise, chip position and SED. The one source of PSF variation which it has been impossible to account for is the short-term "breathing" caused by temperature changes in the telescope's environment during the course of an orbit. However, in this case the undersampling of the WF detectors actually improve matters, with the relatively large pixel scale of the WF chips ensuring that the variation in flux detected by the central pixel of a point source is reduced to the level of a few percent only.

2.5 Data Reduction

All of the initial processing of the raw images, flat-fielding, dark frame and bias removal, were preformed prior to the arrival of the data by the standard HST pipeline. This left only two reduction problems that had to be dealt with, namely cosmic-ray contamination and the saturation of the core of the deep quasar exposures.

As mentioned previously, the decision to opt for three equal-length exposures provides the best possible situation for accurate cosmic-ray determination and removal. According to the WFPC2 Handbook (Biretta *et al.* 1996) the cosmic-ray event rate is $\simeq 1.8\,\mathrm{sec}^{-1}$ per CCD. Due to the majority of events affecting more than one pixel this results in the information of approximately 20 pixels sec^{-1} being destroyed by cosmic rays. However, given that the cosmic events are randomly distributed over the area of the CCD, the use of three separate 600- second exposures instead of two longer ones allows this problem to be dealt with much more effectively, justifying the slight drop in sensitivity introduced by the extra read-noise. Assuming a random distribution, a cosmic ray event rate of 20 pixels sec^{-1} results in a total of only 4 pixels which should be affected in all three exposures. In contrast to this, an observing strategy of two 900-second exposures results in over 500 pixels being lost due to being contaminated

in both images.

The cosmic-ray removal was performed by the IRAF task CRREJ which uses an iterative sigma-clipping algorithm to reject high pixels from sets of exposures of the same field with arbitrary exposure time and sky background level. The final images (see Appendix B) illustrate that this routine has been highly successful in removing the vast majority of cosmic-ray events with the only obvious image defects being a small number of hot pixels and a persistent bad column in the WF2 chip.

After the completion of cosmic-ray removal the issue of saturation due to the nuclear component of the quasars had to be dealt with. For all of the quasars, apart from the two lowest luminosity objects (0257+024 and 2344+184), the long 600-second exposures where saturated. The typical extent of the saturated region was a radius of some 0.3″ from the quasar core, which at the WF resolution corresponds to an area of about 30 pixels. It was essential to the modelling procedure (described in the following chapter) that this region, which contains the crucial information concerning the normalization of the nuclear component, was unsaturated. As was discussed in Section 2.4.3 the short snap-shot exposures were included in the observing procedure in order to overcome this problem. The repeatability of the HST pointing between successive exposures is sufficiently accurate ($\simeq 0.003''$) to allow the direct substitution of the core region of the longest unsaturated snap-shot exposure directly into the core of the final 1800-second image. In the majority of cases the 26-second snap-shot exposure remained unsaturated and was used to replace the saturated region of the 1800-second image, with only one object (0953+415) where only the shortest 5-second exposure remained unsaturated.

2.5.1 Background Determination

Before the final images were ready for analysis with the two-dimensional modelling technique described in the next chapter, it was first necessary to determine the "sky" background count. Determining the background level is of vital importance in host galaxy studies where an attempt is being made to discriminate between different host morphologies. Due to the different behaviour of the standard disc and elliptical galaxy

models at large radii (see Fig 3.1), over- (under-) subtraction of the background could bias the modelling procedure into incorrectly determining disc (elliptical) morphology.

The first stage of the background count determination was the calculation of the median background level in a area of the WF2 chip devoid of obvious sources with the IRAF task IMSTAT. This provided a first "guess" which was found to be typically accurate to better than 1% . The second stage involved the combination of the final deep image with itself using the IRAF task IMCOMBINE. An option available with this task is to exclude all pixels which fall outside lower and upper limits, replacing them with a user-defined value. During the combination of the final image with itself, the upper and lower limits were set at the $\pm 1\sigma$ levels calculated from the statistics performed on the blank areas, with the replacement value set at the corresponding first guess at the background level. The effect of this process was to mask all of the pixels on the WF2 chip due to companion objects, and replace them with a reasonable estimate of the background count. The final stage of the process then involved using the IRAF task IMSURFIT to fit a second order polynomial surface (plane) to the masked image, in order to deal with any large-scale flat-field gradients that might have been present. The final value for the background count in each pixel used in all of the proceeding analysis was taken from this best-fit plane.

A list of the sky background levels and resulting surface-brightness sensitivity limits for the fully reduced images is shown Tables 2.7 and 2.8. Two features of these Tables are worthy of comment. Firstly, it can be seen that the 3σ per pixel detection limit can change significantly between objects due to the large variation seen in sky background levels (± 2.3 mag.arcsec^{-2}). Secondly, it is clear that the vast majority of the host galaxies can be comfortably detected at a radius of $10''$, which corresponds to a projected distance of some 50 kpc ($H_0 = 50, \Omega_0 = 1, \Lambda = 0$). It can be concluded from this that the observing strategy described in this chapter has successfully produced extremely sensitive images, which allow the best possible opportunity to reliably determine the host-galaxy parameters.

Source	Sky	3σ pix^{-1}	$10''$	σ
RG				
0230−027	22.0	23.3	26.3	1.6
0307+169	20.7	22.3	26.0	1.3
0345+337	21.5	23.1	26.0	1.8
0917+459	22.2	23.3	24.0	13.8
0958+291	21.3	23.0	26.2	1.4
1215−033	21.7	23.2	26.5	1.2
1215+013	21.6	23.2	25.5	2.9
1330+022	21.9	23.3	25.2	4.3
1342−016	20.6	22.8	23.9	8.9
2141+279	21.9	23.3	24.4	8.8
RLQ				
0137+012	21.3	23.0	25.5	2.4
0736+017	22.1	23.2	25.3	3.7
1004+130	21.6	23.0	25.5	2.6
1020−103	21.2	22.9	25.2	3.1
1217+023	21.3	23.0	26.0	1.5
2135−147	21.7	23.1	26.0	1.7
2141+175	22.3	23.3	25.0	5.1
2247+140	22.1	23.2	24.8	5.9
2349−014	21.7	23.1	23.8	13.2
2355−082	21.9	23.2	25.5	2.9

Table 2.7: The surface-brightness sensitivities of the reduced RG and RLQ data. Column two lists the sky-background brightness (mag.arcsec^{-2}). Column three gives the 3σ pix^{-1} sensitivity limit. Column four gives the the surface-brightness of the host galaxy inside an pixel-wide annulus with a radius of $10''$. Column five lists how far above the noise this level of flux has been detected in units of σ.

Source	Sky	3σ pix^{-1}	$10''$	σ
RQQ				
0052+251	22.1	23.2	25.0	4.8
0054+144	21.4	23.0	24.8	4.7
0157+001	21.3	22.9	24.2	7.9
0204+292	21.5	23.0	23.9	11.3
0244+194	20.5	22.7	26.3	0.9
0257+024	21.1	22.9	24.0	8.9
0923+201	21.9	23.2	26.0	1.8
0953+415	21.7	23.1	26.4	1.2
1012+008	21.7	23.1	24.3	8.4
1549+203	22.2	23.2	28.0	0.3
1635+119	22.0	23.2	25.1	4.3
2215−037	22.0	23.3	27.5	0.5
2344+184	22.0	23.2	25.9	2.0

Table 2.8: The surface-brightness sensitivities of the reduced RQQ data. Column two lists the sky-background brightness (mag.arcsec^{-2}). Column three gives the 3σ pix^{-1} sensitivity limit. Column four gives the the surface-brightness of the host galaxy inside an pixel-wide annulus with a radius of $10''$. Column five lists how far above the noise this level of flux has been detected in units of σ.

2.6 Notes about Individual Objects

In this section a brief discussion of the HST image of each object presented in Appendix B is given, with references to other recent (1994-1999) HST and ground-based data. In several cases an image of the full WF2 chip is presented in order to highlight features not easily visible in the image presented in Appendix B. All projected distances quoted are estimated on the basis of $1'' \sim 5$ kpc at $z = 0.2$ for $H_0 = 50, \Omega_0 = 1$. A full description of the previous K–band images can be found in Dunlop *et al.* (1993) and Taylor *et al.* (1996) together with relevant references dating from before 1994. Sources are listed by IAU name, with alternative names given in parenthesis.

2.6.1 The Radio Galaxies

0230−027 (PKS 0230−027, OD −050)

The new R–band HST image shows this galaxy to be uniform and round with no sign of obvious distortion. The detail of the WF2 image shown in Appendix B shows in the region of 10 apparent companion objects lying in a roughly circular formation around the galaxy, at a radius of $\simeq 30 \rightarrow 60$ kpc. The brightest of these companions lying at a projected distance of $\simeq 60$ kpc to the NW. The full WF2 chip reveals there to be in the region of twenty faint companion objects within a radius of $\simeq 200$ kpc.

0307+169 (3C 079, 4C +16.07)

The R-band image of this source reveals it to be a classic brightest-cluster galaxy (BCG). Two bright companion objects can be seen to the North and South with three or four accompanying tidal arm features emanating from the central galaxy. The suggestion that this source is in the process of undergoing merger activity is strengthened by the overlying contours which show three distinct cores. The image of the full WF2 chip reveals several more bright companions within a radius of ≤ 100 kpc.

This source has recently been imaged by the HST PC during the 3CR snapshot survey (De Koff *et al.* 1996) through the F702W (wide R) filter. The 280-second integration presented by De Koff confirms the complex multiple structure of this object with the authors noting that the optical and radio axes are aligned to within 15°. McCarthy *et al.* (1995) imaged this source both in the R–band and through an Hα emission-line filter, detecting a curving filament of extended Hα emission stretching some 12″ to the NW.

0345+337 (3C 93.1, 4C+16.07)

The new image of this source shows it to be clearly elliptical and possibly extended towards a companion object $\simeq$ 30 kpc to the NNW. A group of five fainter companion objects can be seen $\simeq$ 60 kpc to the SSE. Two bright foreground stars are also present $\simeq$ 13″ to the NW and SEE. The vertical feature seen in the overlying contours for this source are due to a bad column on the WF2 chip.

This source was also imaged during the 3CR snapshot survey (De Koff *et al.* 1996). Their 300 second R–band image revealed an elliptical nucleus with faint emission to the West coincident with the radio emission (Akujor *et al.* 1991). Near-infrared photometry of this source is presented by de Vries *et al.* (1998) at J, H & K.

0917+459 (3C 219, 4C +45.19) This source is clearly large and luminous with the overlying contours showing it to be elliptical and possibly interacting with the bright companion galaxy to the SE. This galaxy would appear to lie at the centre of a cluster (Schmidt 1965) with numerous companion objects detected in the new R-band image. The full WF2 chip image of this radio galaxy is shown in Fig 2.8.

This galaxy was also included in the snapshot survey of 3CR radio galaxies (De Koff *et al.* 1996) . De Koff *et al.* also suggest that there may be an interaction with the large

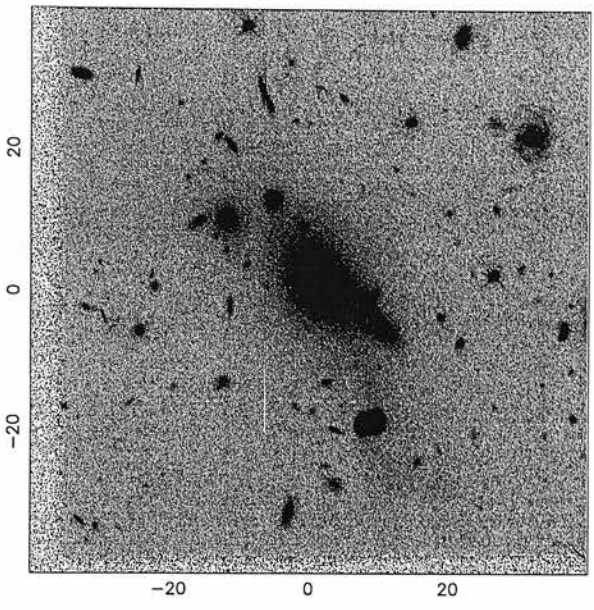

Figure 2.8: The full WF2 image of 0917+459 showing the obvious cluster environment. The image covers an area of $80'' \times 80''$

galaxy to the SE.

0958+291 (3C 234.0, 4C +29.35)

This source would also appear to be located in a cluster with ≥ 10 companion objects lying at a radius of ≤ 60 kpc in the new R–band image. There is evidence that there may be on-going interaction with the overlying contours showing a tidal arm stretching from the galaxy core towards the bright companion object $\simeq 35$ kpc to the West. There is an apparently embedded companion object some 25 kpc to the NE with a further bright galaxy lying just off the image in Appendix B to the South. This source has the largest unresolved nuclear component of all the radio galaxies in this study, all of the 700-second exposures having a saturated central pixel. This is in good agreement with recent work by Young *et al.* (1998) which detected broad Hα emission in both total and polarized flux.

3C234.0 was also a member of the sample imaged for the 3CR snapshot survey (De Koff *et al.* 1996), where features were detected emanating to the east and west of the

galaxy nucleus.

1215−033 (PKS 1215−033)

The R–band image of this source shows it to be a uniform round galaxy with no obvious signs of interaction or disturbance. There are two companion objects lying just on the edge of the detail shown in Appendix B to the SW and ESE at projected distances of $\simeq$ 60 kpc.

1215+013 (PKS 1215+013)

The R–band image of this source reveals numerous faint companion objects around the central galaxy, the brightest lying $\simeq$ 30 kpc to the South. The overlying contours for this source suggest some sort of disturbance immediately to the North of the galaxy core.

1330+022 (3C 287.1, 4C +02.36)

Numerous companion objects are seen in the new R–band image of this source, the brightest of which can be seen some 25 kpc to the NE. There is a linear tidal feature $\simeq$ 35 kpc to the SW. The overlying contours for this source show there to be an apparent second nucleus at less than 1″ separation to the WNW

This object was in the sample imaged in the R–band during the 3CR snapshot survey (De Koff *et al.* 1996). The 280-second image presented by De Koff *et al.* confirms the presence of the second nucleus. 3C 287.1 has been shown to have a power-law X-ray spectrum by Crawford & Fabian (1995).

1342−016 (PKS 1342−016, MRC 1342−016)

The new HST images shows this galaxy to be large, luminous and uniform. A bright

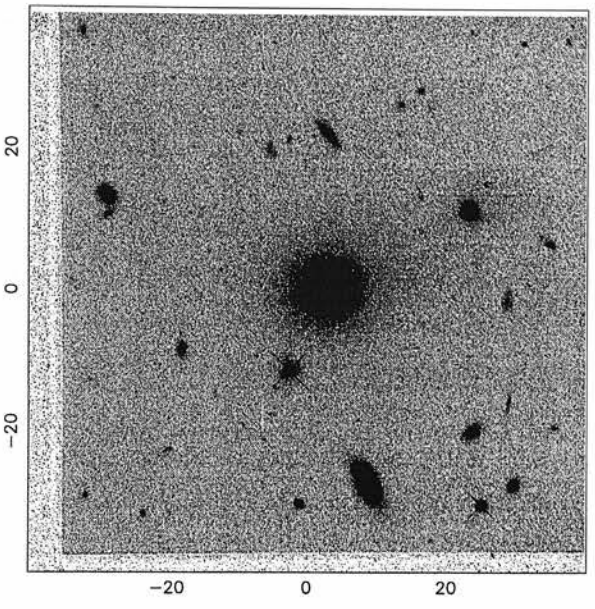

Figure 2.9: The full WF2 image of 1342-016 covering an area of $80'' \times 80''$. A large number of companion objects can be seen which, if at the redshift of the quasar, would appear consistent with a moderately rich cluster environment.

foreground star is present $\simeq 13''$ to the SWW, on the edge of the frame shown in Appendix B. No obvious companion objects are present in the detail shown in Appendix B although the full WF2 chip image shown in Fig 2.9 reveals there to be a large number of companion objects, consistent with a moderately rich cluster.

2141+279 (3C 436, 4C +27.47)

The R–band image of this source shows the galaxy to be large and displaying significant distortion. The galaxy appears to be interacting with the two bright companion objects $\simeq 50$ kpc to the East. A curved tidal arm feature can be seen extending from the North of the galaxy. The overlying contours show the nucleus to have some linear structure associated with it.

This source was imaged as part of the 3CR snapshot survey of De Koff *et al.* (1996). From their 280-second exposure De Koff *et al.* claim the nucleus has "dust features" with filamentary emission.

2.6.2 The Radio-Loud Quasars

0137+012 (PKS 0137+012, PHL 1093)

The image of this source shows the presence of two bright companions at projected distances of $\simeq 40$ kpc to the North and SSW. Also revealed by the contours is a close-in apparent companion only $\simeq$ 5kpc West of the quasar nucleus. The galaxy appears extended along a PA of $\approx 60°$ and there is a suggestion of a tidal feature to the West of the northern companion object.

0137+012 was one of four objects imaged with the PC camera on HST by Disney *et al* (1995), using the F702W filter. Using a two-dimensional cross-correlation modelling technique they found the host to be fitted best by a large early-type galaxy. Disney *et al.* also detected the close-in companion object in their image. This quasar was identified as an X-ray source in the ROSAT All-Sky Survey (Brinkmann *et al.* 1997).

0736+017 (PKS 0736+01, OI 061)

The R–band HST image of this blazar shows it to have a obvious, basically round host galaxy, with a suggestion of an extension towards the SW. There are three bright companion objects, two apparently embedded to the NW and SE, with a third at a distance of some 60 kpc to the NE.

This object has been included in two recent imaging programmes. Wright *et al.* (1998) performed R- and V–band ground-based imaging of 0736+017, confirming the presence of the two close companions in both pass-bands. Using one- and two-dimensional modelling they found the host to be best described by an elliptical galaxy model. This object has also been recently imaged from the ground in the H–band by Kotilainen *et al.* (1998). Using a one-dimensional profile fitting technique Kotilainen *et al.* also find

the host of 0736+017 to be best-fitted by an elliptical galaxy model.

1004+130(PKS 1004+13, PG 1004+130)

As can be seen from the contouring of the image presented in Appendix B this quasar is a highly nuclear-dominated object in the R–band. There is only one companion object visible in the raw R-band image, lying some 30 kpc to the ENE.

1004+130 is one of the quasars which is also included in the sample imaged in the V-band with HST by Bahcall *et al.* (1994, 1995a, 1995b, 1996, 1997), hereafter BKS. The conclusion from their analysis of this object is that the host is an early-type galaxy. BKS suggest that there is some sort of structure close to the quasar nucleus. 1004+130 was imaged in the H–band by McLeod & Rieke (1994) who used PSF-subtraction combined with one-dimensional profile fitting to analyse the host. Due to the high L_{nuc}/L_{host} ratio they were unable to determine the host morphology. In a recent study Wills *et al.* (1999) claim to have detected high-ionization broad absorption lines (BAL) in the ultra-violet spectrum of 1004+130.

1020−103 (PKS 1020−103, UT 1020−103)

The image of this source reveals it to have a comparatively small and faint host, with an obvious PA of $\approx 110°$. There is a triangle of three faint companions directly to the South. This object was identified as an X-ray source in the ROSAT All-Sky Survey (Brinkmann *et al.* 1997).

1217+023 (PKS 1217+02, ON 029)

The R–band image of this relatively nuclear-dominated object clearly shows an elliptical-looking host galaxy with an apparent PA of $\approx 100°$. There is a group of four faint

apparent companion objects running North-South at a projected distance of $\simeq 40$ kpc.

2135−147 (PKS 2135−14, PHL 1657)

The image of this source shows a large companion galaxy at a projected distance of $\simeq 30$ kpc ESE and an apparent close-in companion, or secondary nucleus, at distance of $\simeq 10$ kpc. A recent analysis of the spectrum of the close-in companion by Canalizo & Stockton (1997) has shown that this object is actually a foreground star.

This object is another imaged in the V-band with HST by BKS. Their analysis finds the underlying host to be best matched by an elliptical galaxy model. This quasar was identified as an X-ray source in the ROSAT All-Sky Survey (Brinkmann *et al.* 1997).

2141+175 (OX 169, MC3)

The new R–band image of this complex object clearly shows the linear filaments to the SE and NW which had previously been detected by numerous observers (Smith *et al.* 1986, Heckman *et al.* 1986, Hutchings *et al.* 1994). As reported by Taylor *et al.* (1996), the filaments have been investigated by Stockton & Farnham (1991), who concluded that they were definitely composed of old stars. Hutchings *et al.* (1994) imaged this object using the PC on HST through the F606W (wide V) and F702W (wide R) filters. They detected the two filaments in both filters, again suggesting that they are not composed of line-emission, and using image restoration techniques claim to also detect a "jetlike" feature emerging from the nucleus.

2247+140 (PKS 2247+14, 4C 14.82)

This quasar has a luminous host galaxy which is obvious in the raw R–band image. The host galaxy has a clear PA of $\approx 130°$ and is extended towards a companion object to the SE. Another seven apparent companions are visible in the detail presented in Appendix B. The full WF2 chip image reveals ≥ 10 further faint companions. This object was identified as a X-ray source in the ROSAT All-Sky Survey (Brinkmann *et*

al. 1997).

2349−014 (PG 2349−014, PKS 2349−01)

This object is obviously undergoing an extensive interaction. The new R–band image shows a huge ($\simeq$ 30 kpc) tidal arm to the NNE with large areas of extended nebulosity to the NE and SW. A secondary nucleus or close-in companion object is clearly seen in the overlying contours at a projected distance of some 10 kpc. It would appear that it is this object which is the source of the disturbance, with no obvious evidence for interaction with the bright galaxy to the ESE.

This quasar was imaged in the V-band with HST by BKS. They list the galaxy morphology as interacting although comment that the radial surface-brightness profile is well matched by a de Vaucouleurs $r^{1/4}$ law. This object was identified as an X-ray source in the ROSAT All-Sky Survey (Brinkmann *et al.* 1997).

2355−082 (PKS 2355−082, PHL 6113)

The new R–band HST image of this source reveals the presence of a apparently early-type host with a PA of $\approx 180°$. A group of five small companion objects can be seen to the NE. This object was identified as an X-ray source in the ROSAT All-Sky Survey (Brinkmann *et al.* 1997).

2.6.3 The Radio-Quiet Quasars

0052+251 (PG 0052+251)

The host galaxy of this quasar can be seen to have clear spiral structure in the raw R–band image (Fig 2.10). There are two spiral arms present to the East and West of the nucleus with the Eastern arm being more extended and apparently terminating in a companion object. The overlying contours for this image reveal it to have a highly

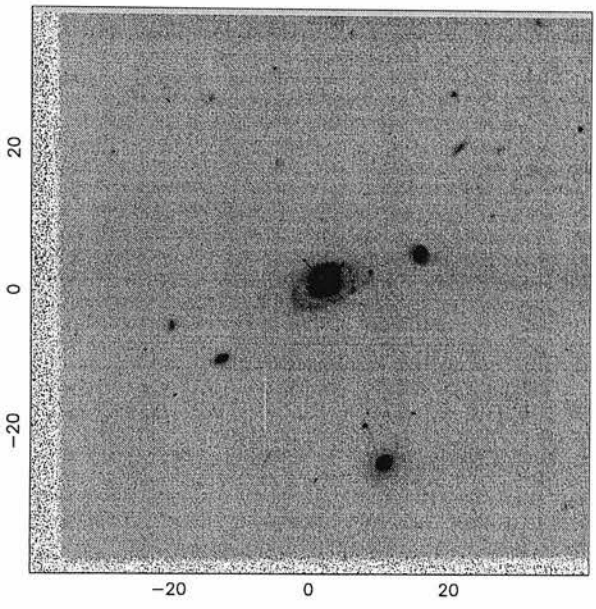

Figure 2.10: The full WF2 image of 0052+251 covering an area of $80'' \times 80''$. The grey-scale has been set to highlight the spiral arm features which are not obvious in the detail presented in Appendix B.

luminous nuclear component.

This image has recently been imaged in the H–band by McLeod & Rieke (1994) and in J, H and K–band by Hutchings & Neff (1997). Hutchings & Neff performed an analysis of the numbers, magnitudes and colours of the companion objects of this source, covering an angular extent comparable to the full WF2 image shown in Fig 2.10. They identify some 22 companion objects brighter than $K = 19.6$, the vast majority of which have colours consistent with mature stellar populations. Comparing their near-infrared images with previous optical studies Hutchings & Neff note that there is no evidence for tidal structure made up of old stars, but conclude that the host is in a phase of secondary star formation possibly induced by interaction with one of the close group of companions. 0052+251 was also included in the V–band HST imaging programme of BKS, who list the host morphology as spiral and identify many of the knots seen in the Eastern arm with HII regions. Interestingly BKS comment that the inner regions of the surface-brightness profile of 0052+251 are well matched by an $r^{1/4}$ law, consistent with the best-fit elliptical host from the K–band imaging of Taylor *et al.* (1996), and suggestive that there may be a strong bulge component to the

host galaxy. This quasar has been identified as an X-ray source in the ROSAT All-Sky Survey (Yuan *et al.* 1998).

0054+144 (PHL 909)

The new R–band image of this source shows a luminous, apparently classic early-type host galaxy. There are two companion objects $\simeq$ 60 kpc to the North and $\simeq$ 40 kpc to the South. There is a further large companion object just of the frame shown in Appendix B to the West. The overlying contours for this object show there to be a luminous nuclear component.

This object also formed part of the quasar sample imaged in the V–band with HST by BKS. Using a combination of one- and two-dimensional modelling they find the host to be best represented by an elliptical galaxy model. This quasar has been identified as an X-ray source in the ROSAT All-Sky Survey (Yuan *et al.* 1998).

0157+001 (PG 0157+001, Mkn 1014)

The host galaxy of this source can clearly be seen to be undergoing a major gravitational interaction in the new R–band HST image. There is a massive tidal arm feature extending to the East of the nucleus before curving South and terminating on a companion object (Fig 2.11). A fainter counter-arm can be seen extending to the West of the nucleus. There are two bright companions present, $\simeq$ 40 kpc to the West and $\simeq$ 70 kpc to the North respectively.

This radio-quiet quasar is also classified as a ULIRG and in this context has been extensively studied in recent years. Clements *et al.* (1996) have imaged this object from the ground in the R–band, confirming the existence of the counter arm to the North and West. Clements *et al.* also suggest that a companion $\simeq 22''$ to the NW shows signs of disturbance. Murphy *et al.* (1996) presented ground-based images of 0157+001 in both the R– and K–band. Their R–band image confirms the structure seen in the image of Clements *et al.* and in our new HST image. Their K–band image

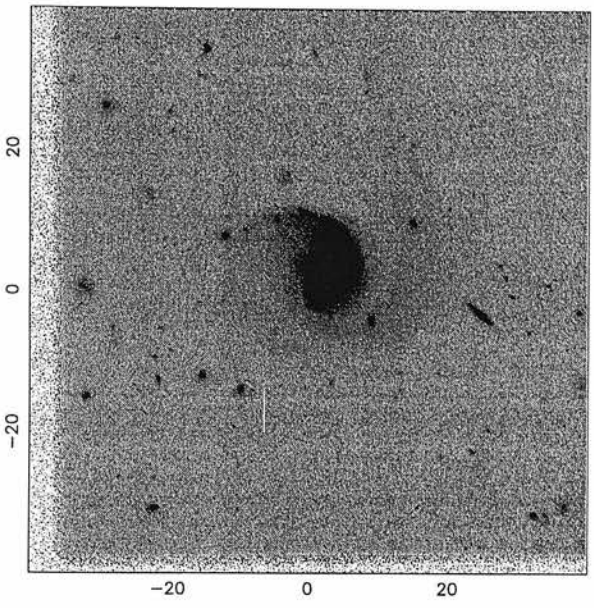

Figure 2.11: The full WF2 image of 0157+001 which covers an area of $80'' \times 80''$. This image clearly shows the Eastern tidal arm terminating on a companion object which lies off the frame shown in Appendix B. The more diffuse Western counter-arm is also apparent in this image, with three companion objects appearing to be embedded within it.

is not sufficiently deep to show the tidal arms, although these features are very strong in the existing K–band image (Dunlop *et al.* 1993). Surace *et al.* (1998) have imaged 0157+001 with the HST PC using B– and I–band filters, allowing them to produce a $B - I$ colour map of the object. Two extremely blue knots are seen within $1''$ of the nucleus in the Surace *et al.* colour maps, along with two further blue knots in the main tidal arm.

Hutchings & Neff (1997) have performed an identical analysis of the host and environment of 0157+001 as was described for 0052+251. They find 20 companion objects brighter than $H = 19.7$, again concluding that the majority are consistent with having mature stellar populations. Hutchings & Neff confirm the finding of Surace *et al.* , concluding that the tidal arm features are significantly bluer than the rest of the host galaxy. Fitting the one-dimensional surface-brightness profile of 0157+001 Hutchings & Neff (1997) find that a standard $r^{1/4}$ law is a good fit in the central $5''$, consistent with the spiral features being tidal distortions of an early-type host, rather than the normal features of a disk galaxy.

Sensitive VLA observations of this object (Miller *et al.* 1993, Kukula *et al.* 1998) have shown this source to have a double radio structure. This quasar was identified as an X-ray source in the ROSAT All-Sky Survey (Yuan *et al.* 1998).

0204+292

In the new R–band image of this quasar the host galaxy appears to be elliptical with a well defined position angle of $\approx 90°$. There are two companion objects on the sub-image shown in Appendix B, $\simeq 70$ kpc to the WSW and $\simeq 45$ to the NW respectively. This quasar was identified as an X-ray source in the ROSAT All-Sky Survey (Yuan *et al.* 1998).

0244+194 (1E 0244+1928)

The host galaxy of this quasar is round and compact. There is a suggestion from the new R–band image that the host may be elongated along the North-South axis. A faint companion object is visible $\simeq 70$ kpc to the SSE. This quasar was identified as an X-ray source in the ROSAT All-Sky Survey (Yuan *et al.* 1998).

0257+024 (US 3498)

This source has an almost perfectly round host, with the overlying contours showing little indication of a substantial unresolved nuclear component. A group of three companion objects can be seen $\simeq 50$ kpc to the SE. This quasar was identified as an X-ray source in the ROSAT All-Sky Survey (Yuan *et al.* 1998).

0923+201 (PG 0923+201, Ton 1057)

This quasar appears to be lying in a group of galaxies. The two large galaxies seen to the SE and SW have been shown to be at the same redshift as the quasar (Heckman *et al.* 1984) and it appears from the image that the quasar host is interacting with the

SE companion. It can be seen from the overlying contours on the new HST image that this is an heavily nuclear-dominated source.

This object has recently been imaged in the H–band from the ground (McLeod & Rieke 1994) and the V–band with HST by BKS. Using a combination of one- and two-dimensional modelling BKS find the host galaxy of this source to be best represented by an early-type galaxy model. This quasar was identified as an X-ray source in the ROSAT All-Sky Survey (Yuan *et al.* 1998).

0953+415 (K438−7, PG 0923+415)

It can immediately be seen from its near-stellar appearance in the new R–band image that this is the most nuclear-dominated object in the whole sample. Three companion objects can be seen, two lying to the North and NW with a third lying to the SSE. The image of the full WF2 chip shows there to be ≥ 10 companions within a radius of 100 kpc from the quasar.

This object caused controversy when the analysis performed by BKS on their V–band HST image suggested that this quasar did not have a detectable host galaxy. This led BKS to initially suggest that this was a so-called "naked" quasar, triggered into activity before substantial star-formation had taken place. This result was in direct contradiction to the findings of near-infrared imaging (Taylor *et al.* 1996, McLeod & Rieke 1994) which showed that although 0953+415 was certainly highly nuclear-dominated, there was no suggestion that there was no host galaxy present. After obtaining further long HST exposures of 0953+415 BKS concluded that there was indeed some "low surface-brightness fuzz" associated with this object, but were unable to determine its morphology. This quasar was identified as an X-ray source in the ROSAT All-Sky Survey (Yuan *et al.* 1998).

1012+008 (PG 1012+00)

This spectacular object can clearly be seen to be experiencing a violent on-going gravi-

tational interaction. Two large companion galaxies are obvious to the North and East, with the quasar host apparently interacting with both. Several other, fainter, companions can be seen within a radius of $\simeq 60$ kpc of the quasar.

This object was a member of the quasar samples imaged from the ground in the H–band by McLeod & Rieke (1994) and with the HST in the V–band by BKS. Both of these images confirm the interacting nature of this system. The analysis of the host galaxy morphology performed by BKS is inconclusive, with the one-dimensional technique preferring an early-type host, while their two-dimensional modelling prefers a disc. This quasar was identified as an X-ray source in the ROSAT All-Sky Survey (Yuan *et al.* 1998).

1549+203 (LB 906, 1E 15498+203)

It is immediately obvious from the new R–band image of this object that the host galaxy is small, and relatively faint compared to the nuclear component. Using a different grey-scale to that used in Appendix B, there is a suggestion of spiral-like features to the NW and SE of the nucleus, with the SE arm terminating at the apparent companion object which can be seen $\simeq 20$ kpc to the E of the nucleus. A large, luminous elliptical galaxy can just be seen on the edge of the frame to the SW, with numerous fainter companions visible inside a radius of $\simeq 60$ kpc. The full WF2 image would appear to show numerous companion objects although, as pointed out by Taylor *et al.* 1996, the density of the environment of this quasar is uncertain due to the presence of a nearby foreground cluster at $z \simeq 0.14$ (Stocke *et al.* 1983).

The first electronic images of this quasar were presented by Hutchings & Neff (1992). They imaged the object in both the V- and I–bands, detecting what looked like a bar structure running North-South through the nucleus, while noting that the surface-brightness profile of 1549+203 was not exponential. This quasar was identified as an

X-ray source in the ROSAT All-Sky Survey (Yuan *et al.* 1998).

1635+119 (MC 2)

The host of this quasar appears to be a classic early-type with a well-defined position angle of $\approx 45°$. Numerous apparent companion objects can be seen, the brightest of which lies at a separation of $\simeq 30$ kpc to the South of the nucleus. There are no obvious signs of any interactions in progress.

This object is the most radio-luminous in the RQQ sub-sample, and is included as being radio-loud in the ROSAT X-ray identifications of Brinkmann *et al.* (1997).

2215−037 (EX 2215−037)

The image of this quasar shows the host to be compact and apparently undisturbed. A small apparently unresolved companion is detected only $\simeq 10$ kpc to the SW of the quasar nucleus. A large elliptical galaxy can be seen some 65 kpc to the North with a second apparently unresolved companion $\simeq 50$ kpc to the East.

This object has been previously imaged on the HST PC using the F702W (wide R) filter by Disney *et al.* (1995). Using a two-dimensional cross-correlation modelling technique Disney *et al.* found the host galaxy to be excellently matched by an elliptical galaxy model. Their wide-R image confirms the existence of the unresolved companion at $\simeq 2''$ separation from the nucleus and suggests that the environment of 2215-037 resembles a poor cluster. This suggestion is supported by the image of the full WF2 chips which shows ≥ 10 companion objects inside a radius of $\simeq 100$ kpc. This quasar was identified as an X-ray source in the ROSAT All-Sky Survey (Yuan *et al.* 1998).

2344+184

The new HST image of this object reveals the host galaxy to be a well defined barred spiral with a significant bulge component. The spiral arms can clearly be seen in

the overlying contours to the NW and SE. Also clear from the contour map is that any unresolved nuclear component which is present appears significantly weaker than average for the quasars imaged in this study. There are no companion objects visible in the frame shown in Appendix B, although the full WF2 chip image reveals numerous apparent companions surrounding the quasar inside a radius of $\leq$ 100 kpc.

The most contemporary image of this object is the ground-based I–band observation presented by Hutchings & Neff (1992). This image also clearly shows the host to be a barred spiral. Interestingly, a recent optical spectrum of this object taken by Goncalves *et al.* (1998) leads the classification of 2344+184 to change from radio-quiet quasar to Seyfert 2 galaxy. This may well explain the spiral host galaxy and relatively weak nuclear emission (see Chapter 4).

Chapter 3

Methods of Host Galaxy Analysis

When analysing sensitive, high-resolution, host-galaxy images, several possible methods of analysis are available. Given below are brief outlines of the two standard techniques which have been traditionally used in the study of AGN host galaxies using lower-resolution ground-based imaging. It was careful consideration of the limitations of these techniques which led to the decision that a fully two-dimensional modelling solution was required to take full advantage of the HST data presented in this thesis.

3.1 Point Spread Function Subtraction

One method which has been extensively used in the study of AGN is the simple removal of the unresolved nuclear component in order to better examine the underlying host galaxy. The simplest way in which this can be attempted is the subtraction of an appropriately-scaled representation of the instrument point spread function (PSF) from the image core. If this can be achieved accurately then the luminosity, and perhaps Hubble type, of the host galaxy can be estimated in a completely model-independent manner. This seemingly straightforward method has been used in several large-scale host-galaxy programmes (Smith *et al.* 1986, Dunlop *et al.* 1993) and was fundamental in originally proving that quasars did have extended low surface-brightness "fuzz" associated with them (see Chapter 1). However, there is one problem inherent to this

technique which severely limits its usefulness.

Even in the situation where it has been possible to obtain an accurate representation of the instrumental PSF (a difficulty with ground-based seeing) the question of how to then appropriately scale this PSF to the actual contribution of the active nucleus must be addressed. The standard technique for this is to assume that the flux in the central pixel of the quasar image is totally dominated by emission from the active nucleus, and to scale the PSF to give zero residual flux in this pixel. However, even when using modern optical CCD's with good sampling, it is inevitable that some galaxy light will contaminate the central pixel, leading to an overestimate of the nuclear contribution. If this effect is compounded by even slight inaccuracies in PSF representation, then it is possible that the host-galaxy luminosity can be seriously underestimated. In the optical, where quasars with $L_{nuc}/L_{host} \simeq 10$ are common, a ten percent overestimate of the unresolved light contribution will result in the host-galaxy flux being completely lost. In this case, even a relatively modest five percent overestimate of the nuclear component will result in the host-galaxy luminosity being under estimated by 0.75 magnitudes. It is still the case however that PSF subtraction can be a useful tool in situations where the quality of the data is poor to moderate. In this situation the method has the advantage of at least providing a solid lower-limit on the host galaxy luminosity.

3.2 One-Dimensional Profile Fitting

If the data to be analysed is of sufficient depth to allow an attempt to extract the host-galaxy parameters, then one-dimensional profile fitting is a standard method which is often adopted. In this method the image of the source is converted into a radial surface-brightness profile by azimuthal averaging along concentric elliptical isophotes. The immediate advantage of this approach is that this "binning-up" of the data produces a $\sqrt{N}$ improvement in signal-to-noise ratio, where N is the number of pixels lying on a particular isophote. A corresponding model surface-brightness profile can then be constructed, compared with the data, and then iterated until the best possible fit is

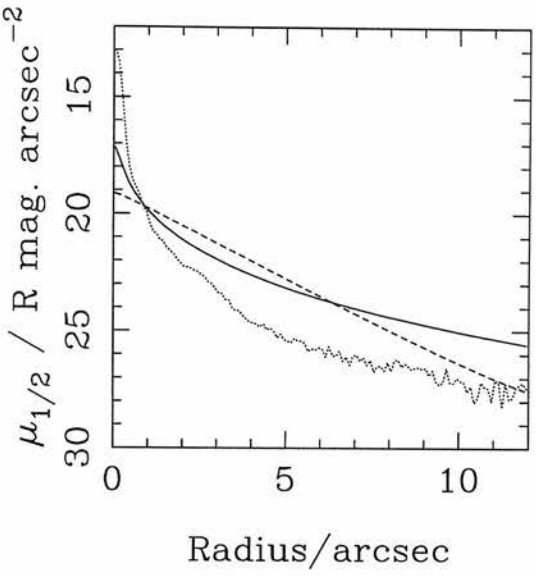

Figure 3.1: Simulated radial surface-brightness profiles for a typical elliptical (solid line) and disc (dashed line) galaxy from the HST host-galaxy programme. Both galaxies have the same total luminosity ($M_R = -23.6$) and half-light radius ($r_{1/2} = 10$ kpc), and have been simulated as imaged on WF2 at a redshift of $z = 0.2$. Also shown is a typical nuclear component (dotted line) with total luminosity of $M_R = -24.6$, giving a L_{nuc}/L_{host} of 2.4.

achieved. In practice this technique usually proceeds in one of two ways. The first of these is in conjunction with PSF-subtraction, where before the surface-brightness profile is produced the image first has the nuclear component removed, with the host galaxy model being fitted to the region of the resulting profile outside of the image core. In combination with the problems of over-subtraction of the nuclear component discussed above, this procedure invariably suffers from being unable to include the central regions of the host galaxy in the fitting process. As illustrated in Fig 3.1 the core of a galaxy surface-brightness profile is a crucial region where galaxies of different morphologies can differ significantly. The result of this drawback is that this form of profile fitting can return very similar quality fits using elliptical or disc host templates, making morphological discrimination impossible.

A more sophisticated variation of the one-dimensional profile fitting technique involves the conversion of the instrumental PSF into a radial surface-brightness profile, dispensing with the need to subtract the nuclear contribution from the image. With the

addition of a central spike to represent the unresolved emission, the host-galaxy profile can be convolved with the PSF in one-dimension to simulate an actual observation. The twin advantages of this approach are that the comparison of the model and data profiles can be extended to include the core of the image, and that the model profile is automatically corrected for seeing effects, which can significantly alter the shape of host-galaxy profiles in ground-based images.

Given that the HST observations presented here are of sufficient depth to allow model fitting to a large radius without the need for binning-up, these one-dimensional techniques suffer from two potentially serious problems which prevent them from being adopted as the correct solution for the data analysis. The first of these concerns the use of a one-dimensional representation of the instrumental PSF. Given that the WFPC2 PSF has proven to be extremely complicated (see Section 3.3.1), containing significant two-dimensional structure within it, it is clear that the destruction of all azimuthal information could cause the modelling process to produce erroneous results. One way of attempting to overcome this problem is to build and convolve the host models in two-dimensions before reverting back to one-dimensional profiles for the fitting process (Wright *et al.* 1998). Although this offers an undoubted improvement, and has the advantage of retaining the signal-to-noise advantage of binning-up the data, it still does not provide an adequate solution to the second problem, which is how the contamination of the modelling by companion objects should be dealt with. The existing K-band observations of this sample (Dunlop *et al.* 1993, Taylor *et al.* 1996) show that many of the sources have several apparent companion objects at a radius of $\leq 15''$. Profile fitting can only deal with such objects in a somewhat unsatisfactory manner by the exclusion of all pixels falling within a particular range of position angle, leading to severe problems if more than one or two companion objects are present. The combination of high resolution HST data, with a fully two-dimensional modelling procedure allows the accurate discrimination, and subsequently masking (c.f. Fig 3.5), of any companion objects from the fitting process, ensuring that the best-fitting host-galaxy parameters are as unbiased as possible.

3.3 Two-Dimensional Modelling Technique

Given the difficulties associated with one-dimensional analysis techniques it was felt that a fully two-dimensional approach was needed to fully exploit the depth and resolution of the HST AGN host-galaxy images. The two-dimensional modelling code used throughout this thesis is a development of that which was originally designed for the analysis of the IRCAM 1 K–band imaging of the expanded sample (Taylor *et al.* 1996). In this section a full description of the central model-building algorithm is given, along with a discussion of several related issues which have a crucial bearing on its successful application.

The model host galaxies are constructed on a two-dimensional array with the surface-brightness of each pixel described by either a de Vaucouleurs $r^{1/4}$ law (de Vaucouleurs & Capaccioli 1979):

$$\mu(r) = \mu_o \exp\left[-7.67\left(\left(\frac{\mathrm{r}}{\mathrm{r_e}}\right)^{1/4} - 1\right)\right] \tag{3.1}$$

or a Freeman disc law (Freeman 1970):

$$\mu(r) = \mu_o \exp\left(-\frac{\mathrm{r}}{\mathrm{r_o}}\right) \tag{3.2}$$

where $\mu(r)$ is the galaxy surface-brightness at a radius r, r_e is the characteristic scalelength, within which half of the total galaxy light falls, and r_o is the exponential scalelength. The radius of a pixel (i, j) which lies on an ellipse with centroid $(0, 0)$, an arbitrary eccentricity and a position angle θ, is allocated as follows:

$$\Delta x = i\cos\theta + \mathrm{j}\sin\theta \tag{3.3}$$

$$\Delta y = -i\sin\theta + \mathrm{j}\cos\theta \tag{3.4}$$

$$r = \sqrt{\frac{a}{b}\Delta x^2 + \frac{b}{a}\Delta y^2} \tag{3.5}$$

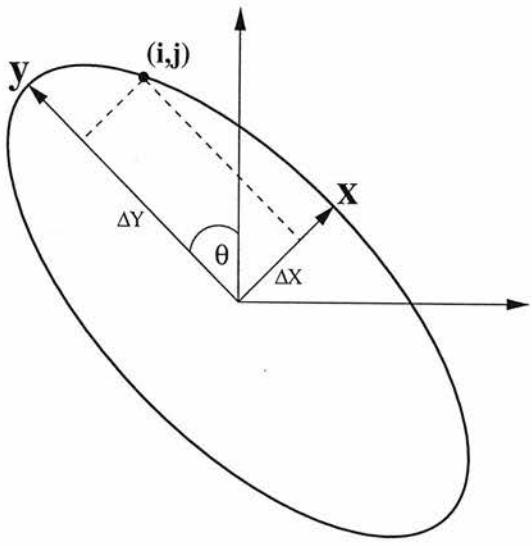

Figure 3.2: Geometry for host galaxy construction.

where a and b are the semi-major and semi-minor axes respectively. The radius of equation 3.5 is a composite, formed by taking a geometric average of the semi-major and semi-minor axes. This differs from the standard definition of radius used in constructing model galaxies, which attributes the length of the semi-major axis to all points lying on that ellipse. This definition is only strictly valid when dealing with an inclined disc system, and does not give a satisfactory measure of the true characteristic "size" of an elliptical galaxy with an axial ratio much bigger than one. However, in order to facilitate a direct comparison between results presented in this thesis and previously published work, it has been necessary to convert scalelengths to their equivalent semi-major axis value in some cases (see Chapter 4).

In order to accurately simulate galaxy light distributions it is insufficient to simply calculate the surface-brightness of each pixel based on the radius of the pixel centre. Therefore, in the central regions of the models ($r \leq 1''$), where the de Vaucouleurs $r^{1/4}$ law in particular is varying rapidly, the galaxies are constructed on a much higher resolution array than the data plate-scale. Inside a radius of $0.5''$ the models are originally built to a resolution of $0.004''$/pix before being re-sampled to the data plate-scale. As the variation of surface-brightness decreases with increasing radius, the resolution of the model building can be gradually tapered-off, reaching a final value of $0.03''$/pix for all pixels outside a radius of $1''$. After the model host galaxy has been constructed,

an arbitrarily large amount of flux is added to the central pixel to represent the unresolved nuclear contribution. At this stage the model is a simulation of a theoretical "zero-seeing" quasar observation. In order to produce a simulated HST observation this zero-seeing model is then convolved, via a FFT (Press *et al.* 1989), with our high signal-to-noise observation of the WF2 PSF (see Chapter 2). The goodness of fit between this convolved model and the actual data can then be tested via the χ^2 statistic, *i.e.*

$$\chi^2 = \sum_{i=1}^{n} \left[\frac{y_i - y(x_i)}{\sigma_i} \right]^2 \tag{3.6}$$

where n is the number of pixels included in the fit, y_i is the value of the ith image pixel, $y(x_i)$ is the value of the corresponding pixel in the convolved model, and σ_i is the error associated with the value of the ith image pixel.

The parameters which determine the form of the convolved model can then be iterated to find the minimum χ^2 solution. The model parameters which are left free during this minimization process are:

1. The luminosity of the nucleus
2. The central brightness of the host galaxy
3. The scalelength of the host galaxy
4. The position angle of the host galaxy
5. The axial ratio of the host galaxy

3.3.1 The WFPC2 PSF

Many authors who have investigated host galaxies using the HST (Hutchings *et al.* 1994, Disney *et al.* 1996, Hooper *et al.* 1997) have made use of the synthetic PSFs produced by the TINYTIM software package (Krist 1998). This software is capable of producing an infinite signal-to-noise representation of the post-refurbishment WFPC2 PSF through any of the on-board HST filters, seemingly removing the need to sacrifice valuable HST

orbits to observe the empirical PSF. Although the advantages to observers of using this software are obvious, TINYTIM has one serious drawback in that it is unable to reproduce the extended halo of scattered light which is associated with the WFPC2 PSF. This shortcoming is acknowledged in the TINYTIM documentation (Krist 1998), where it is recommended that the synthetic PSFs are not used for subtraction in the analysis of data extending to radii $\geq 1.5''$. The unsuitability of these synthetic PSFs for the convolution of model quasars is illustrated in Fig 3.3 which shows a comparison between the high dynamic range empirical PSF used in this project and an equivalent TINYTIM model. It is clear from this that the halo contribution from a highly nuclear-dominated quasar could easily lead to the scalelength of the underlying host galaxy being seriously overestimated, if the extended halo is not also present in the model.

Another issue to be considered with WFPC2 is the inadequate sampling of both the WF and PC cameras. Following the refurbishment mission of 1993, during which WF/PC1 was replaced by WFPC2, the corrective optics included in the design of WFPC2 successfully correct for the spherical aberration of the main mirror, returning a PSF with a FWHM of $0.052''$ (Biretta *et al.* 1996). However, given that the plate-scales of the PC and WF cameras are $0.045''$/pix and $0.099''$/pix respectively, this leaves the PC unable to provide critical sampling and the WF chips severely undersampled. Given that the central $1''$ of the R–band quasar images analysed in Chapter 4 are dominated by the unresolved nuclear component, it was imperative that the undersampling issue was dealt with properly. As was discussed in Chapter 2 the undersampling of the WF chips had been recognised at the planning stage of the HST programme, and a two-stage dither was adopted for the PSF observations in an effort to achieve better sampling. Unfortunately, during the data reduction process it was discovered that one of the two 0.23 second dithered exposures, which gave an unsaturated snapshot of the PSF core, was contaminated by a cosmic-ray event. This meant that there was only one sub-pixel centring for the reduced PSF, making it impossible to match the centroiding of the quasar observations with the required accuracy. In order to deal with this problem a solution was arrived at which makes use of the sub-sampling capabilities of the TINYTIM software. Although inadequate as a substitute for the empirical PSF at large radii, the synthetic models produced by TINYTIM are an excellent match to the empirical PSF in

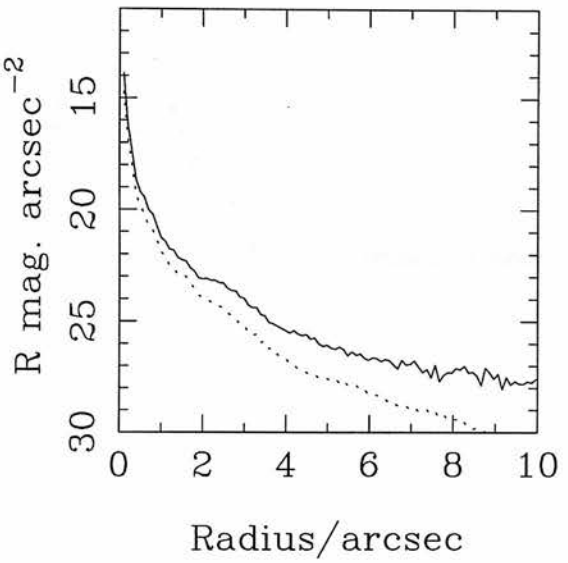

Figure 3.3: A comparison of our empirical F675W WF2 PSF (solid line) with the equivalent TINYTIM synthetic PSF (dashed line). Both have been normalized to have the same central surface-brightness. It can clearly be seen that the TINYTIM model is unable to reproduce the halo of scattered light outside a radius of $\simeq 1.5''$.

the very central regions where the optical effects are well understood. The ability of TINYTIM to produce PSF models at fifty times higher resolution than the WF2 plate-scale is used to predict the appearance of the central nine pixels of the WF2 PSF with any possible sub-pixel centring. These predictions are then χ^2 matched to the core (central nine pixels) of the quasar image to give centroiding with theoretical accuracy of ± 0.02 pixels. Assuming that the TINYTIM model provides an accurate representation of the true PSF in the central $\simeq 0.5''$, it is then possible to correct the sampling of the central regions of the empirical PSF to the same sub-pixel centring as that of the quasar image.

3.3.2 Error Allocation

Regardless of the care with which the model quasars are constructed, in order for this type of two-dimensional modelling to return accurate results it is essential that the error

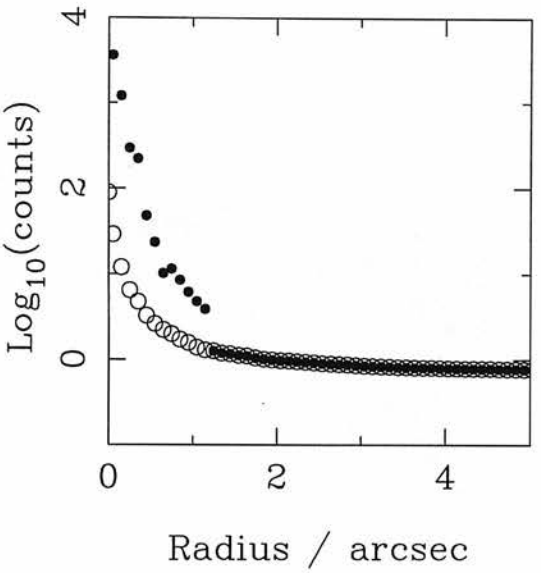

Figure 3.4: A typical HST error profile (0923+201). Shown in the figure are the predicted poisson errors (open circles) from the WF noise model, and the actual sampling errors (filled circles), both calculated from azimuthal averaging in circular annuli. It can be seen that outside a radius of $\sim 1''$ the poisson and sampling errors are basically identical.

weighting used in the χ^2 test between data and model is allocated properly. The use of inappropriate error weighting can cause one area of the image to dominate the fit at the expense of others, leading the modelling process to return biased results. The minimum possible error that can be associated with any pixel is a combination of the poisson error due to photon shot noise, plus the read-noise and dark current contributions. Errors introduced during flat-fielding have proven to be negligible in both the HST data and the IRCAM 3 images considered in Chapter 4. Figure 3.4 shows a comparison between the error weighting calculated using the theoretical noise model for WF2 (Biretta *et al.* 1996) and the actual statistical sampling errors as measured from a typical image.

As can be seen from Fig 3.4 the errors calculated using the noise model are in near-perfect agreement with what is actually seen from the data for all pixels outside a radius of $\simeq 1''$ from the quasar core. As a result, during the model fitting all pixels outside a radius of $1''$ are simply allocated their expected poisson error, based on the noise model. However, Fig 3.4 also demonstrates that this system would grossly underestimate the actual error introduced inside $\simeq 1''$ by the severe undersampling of the WFPC2 PSF.

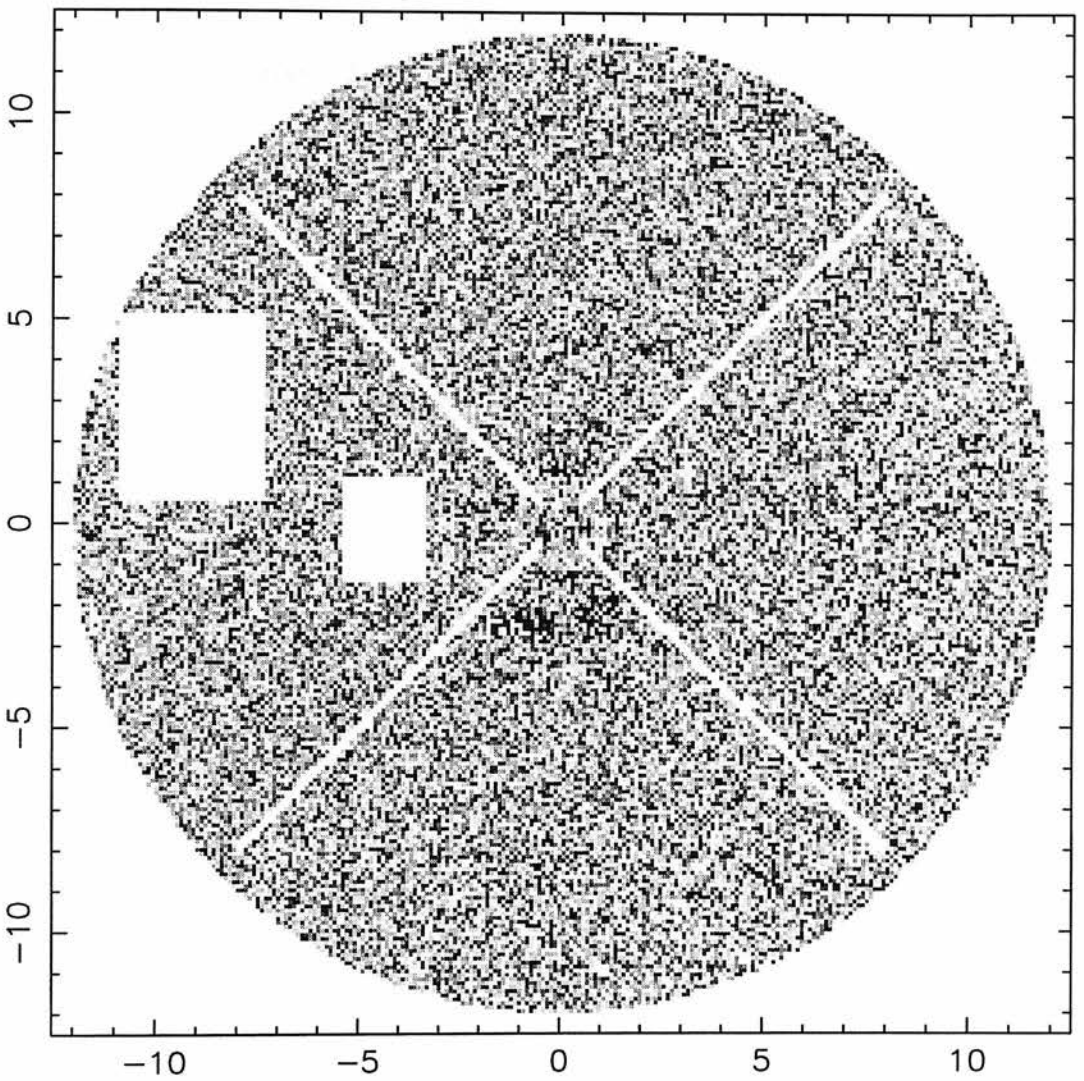

Figure 3.5: The reduced χ^2 map for the best-fitting model to the radio-loud quasar 1217+023. The grey-scale is a linear stretch running between $0 \rightarrow 2$. It can be seen that a uniform spread of χ^2 values has been achieved, with no area of the image dominating the fit. The blank areas in the map are due to the masking from the fitting process of two companion objects and the highly variable diffraction spikes.

Therefore, inside a radius of 1″ a different system is used to allocate the error weighting. A series of ten pixel-wide circular annuli centred on the quasar are constructed, and the variance (σ^2) of the distribution of the pixels falling within each annuli calculated. All of the pixels falling within a particular annulus are then allocated the annulus variance as their error weighting. This procedure is still justified even when the underlying host galaxy has a clear ellipticity since, even at HST resolution, the central 1″ of the quasar images are dominated by the circular symmetry of the PSF. One problem with this method of error weighting is that it obviously fails to provide a prediction for the error on the very central pixel. However, due to the success of the re-sampling technique discussed above, it has been possible to assign the central pixel its poisson error without biasing the fitting procedure. This complicated process has proven to be successful, with the vast majority of the 33 HST objects modelled having minimum χ^2 solutions lying in the $\nu \pm \sqrt{2\nu}$ region expected for correct weighting. Confidence in the weighting system is further strengthened by examination of the pixel maps of reduced χ^2 values produced for the best-fitting models. Show in Fig 3.5 is such a typical χ^2 map from the best-fit to the radio-loud quasar 1217+023. It is clear from this figure that the desired spread of uniform χ^2 values has been achieved, with no one area of the image dominating the fit.

3.3.3 Minimization

The main advantage of the two-dimensional modelling technique being adopted here is that it allows each individual pixel in the image frame to be included in the model fitting as a degree of freedom. However, due to the high angular resolution of the HST, and the depth of the observations for this project, a typical model fit to a radius of 12″ will include some 45000 pixels in each χ^2 evaluation. Given that even in the simplest version of the modelling code the minimum χ^2 value is sitting in a five-dimensional parameter space, a high resolution grid search of all possible parameter combinations is too computationally expensive to use on a sample of 33 objects. The adopted solution was to utilise the Downhill Simplex method (Press *et al.* 1989) to locate the global minimum. Although significantly slower and less elegant than conjugate gradient methods, Downhill Simplex minimization was chosen for its robustness in finding the true

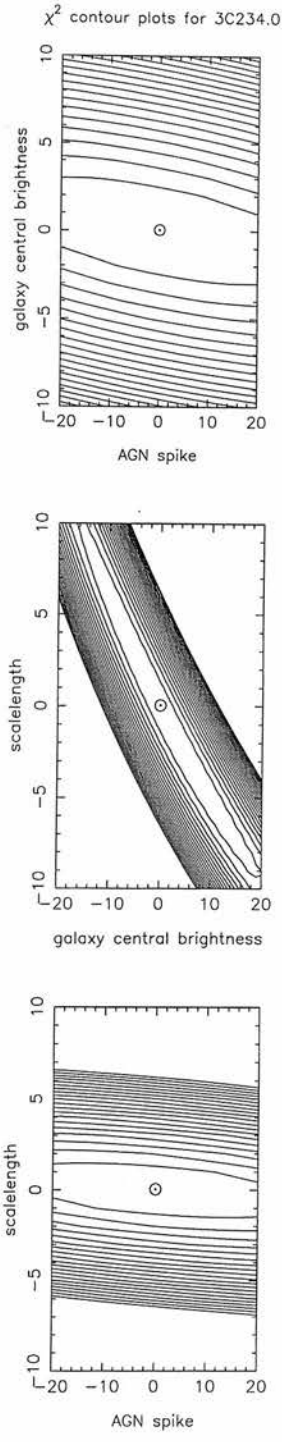

Figure 3.6: χ^2 contour maps for the radio galaxy 3C234.0 showing various 2-parameter slices through the 5-parameter hypersurface. Contour levels are spaced at intervals of $\Delta\chi^2 = 100$ from the minimum χ^2 located with the simplex method.

global minimum, and its insensitivity to the selection of initial conditions. When using any algorithm to reach the minimum χ^2 solution faster than a high resolution grid search, there is always a risk of finding a false minimum, depending on the topology of the hyper-surface. In order to investigate the topology of the hyper-surface, and the prevalence of false minima, it was thought worthwhile to undertake a high-resolution grid search for two objects, with the extent of the search grid being $\pm 20\%$ from the parameter values found by the Downhill Simplex minimization routine.

In both cases the grid search did not find a combination of parameters with a lower χ^2 value than that found by the Downhill Simplex routine. The results of the grid search for the radio galaxy 3C234.0, which contains a 30% nuclear component, are shown in Fig 3.6 with the position of the global minimum marked with $\odot$. Two features of this diagram are worthy of comment. Firstly it can be seen that in all three parameter slices the minimum χ^2 value lies at the bottom of a narrow "valley", suggesting that multiple false minima are not ubiquitous. The section feature is that although the expected correlation between galaxy scalelength and central surface-brightness (Abraham *et al.* 1992) is clearly present, the Downhill Simplex minimization routine has successfully located the global minimum.

3.4 Testing the Modelling Code

Once in possession of the completed two-dimensional modelling code it was considered necessary to obtain a measure of the typical accuracy with which the code could recover the host-galaxy parameters. The ideal situation would be to test the modelling code using a existing data-set for which the relevant parameters had been previously measured to high accuracy. However, due to the very nature of the work carried out in this thesis, such a suitable data-set does not exist, and for this reason it was decided to run an extensive programme of tests using synthetic data.

To allow a realistic representation of the range of redshifts displayed by the WFPC2 data the synthetic AGN were constructed at three redshifts, z=0.1, z=0.2 & z=0.3. At each redshift 28 elliptical and 28 disc host galaxies were simulated. Each group

of 28 host galaxies consisted of a range of four possible half-light radii (5, 10, 15 and 20 kpc for $\Omega_0 = 1.0, H_0 = 50$), all of which had the same integrated luminosity. To each of these four different galaxy scalelengths was added a range of seven different nuclear components, giving L_{nuc}/L_{host} in the range $0 \rightarrow 16$. The synthetic AGN with no nuclear component were included to check that the modelling code did not have a bias towards preferring a nuclear component when none existed. The final ensemble of models totalled 168 and covered the full range of parameters likely to occur in reality.

3.4.1 Synthetic Quasar Construction

When constructing the suite of synthetic quasars several steps were taken to ensure that these simulations reflected the characteristics of actual WFPC2 observations as closely as possible. The first of these being that the final synthetic quasar images were stacked from separate frames in an identical fashion to the real data. As discussed in the previous chapter, the actual quasar observations consisted of three deep 600-second exposures which were complimented by three shorter snap-shot exposures of 5, 26 and 40 seconds, designed to ensure a unsaturated measure of the nuclear component. The final quasar images which have been analysed in Chapter 4 consist of a stack of the three long exposures, with the central regions replaced by a scaled snap-shot exposure to recover the quasar's full dynamic range. The construction of the synthetic quasars proceed in exactly the same fashion, with individual simulations of each of the six separate exposures. The appropriate level of background counts was then added to each of the simulated exposures before they were processed by the IRAF routine MKNOISE which simulated the effects of shot and read-out noise, ensuring that the final stacked quasar simulation accurately reflected the noise characteristics of a typical quasar image.

When producing the simulated quasar images it was obviously necessary to decide upon some fiducial luminosity for the host galaxies. Given the wide range in host luminosities reported in the literature it was necessary to fix this fiducial luminosity from our own HST data. At the time that this model testing programme was undertaken (December 1997) only 12 of the 33 objects from the sample had been observed. It

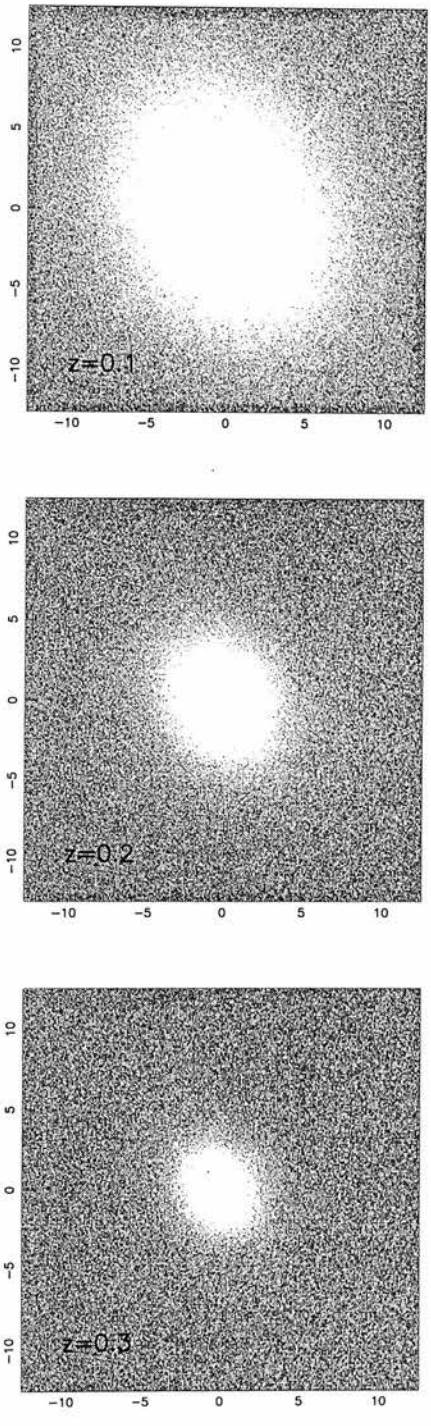

Figure 3.7: The appearance of a synthetic quasar image with a 10 kpc elliptical host galaxy and $L_{nuc}/L_{host} = 2$ at $z = 0.1$ (top), $z = 0.2$ (middle) and $z = 0.3$ (bottom). Each simulated image is $30'' \times 30''$ in area.

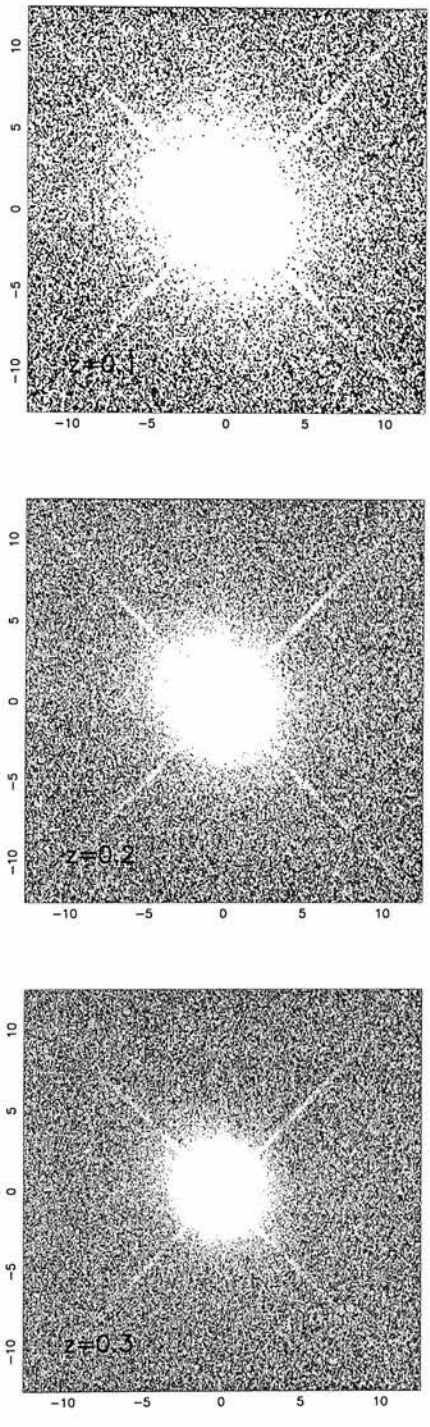

Figure 3.8: The appearance of a synthetic quasar image with a 10 kpc elliptical host galaxy and $L_{nuc}/L_{host} = 16$ at $z = 0.1$ (top), $z = 0.2$ (middle) and $z = 0.3$ (bottom). Each simulated image is $30'' \times 30''$ in area.

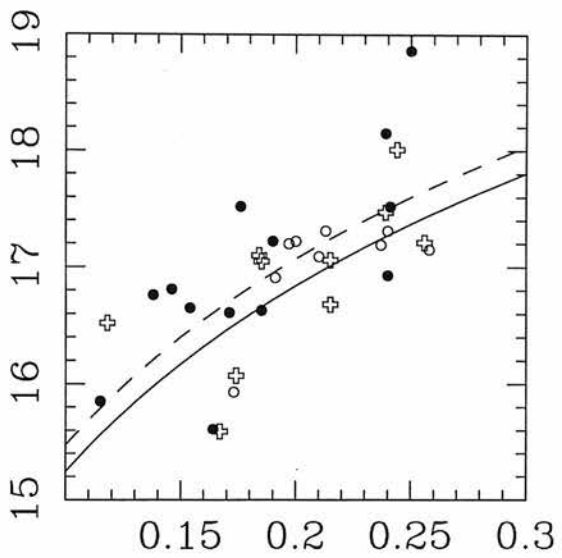

Figure 3.9: The apparent magnitude versus redshift distribution of the best-fitting host galaxies of the HST sample (see Chapter 4). Shown in the diagram are radio galaxies (crosses), radio-loud quasars (open circles) and radio-quiet quasars (filled circles). Also shown is the apparent magnitude of the synthetic host galaxies used for testing the two-dimensional modelling code (solid line). The dashed line shows the apparent magnitudes of the synthetic hosts dimmed by 0.27 magnitudes (see text).

was decided to fix the luminosity of the simulated hosts by forcing them to match the absolute magnitude of the best-fit to PKS 2247+14 ($M_R = -23.8$), typical of the 12 hosts which had been observed at the time. The calculation of the absolute luminosity of the hosts at the three redshifts was determined assuming a typical spectral index of $\alpha = 1.5$ for the F675W filter ($f_\nu \, \alpha \, \nu^{-\alpha}$), and the usual cosmology ($H_0 = 50, \Omega_0 = 1$). The cosmological dimming of the AGN point source assumed a spectral index of $\alpha = 0.2$ (Neugebauer *et al.* 1987). Figure 3.9 shows the apparent magnitudes for all 33 host galaxies from the HST programme (see Chapter 4) plotted against redshift. Also shown are the apparent magnitudes of the synthetic host galaxies. There is a suggestion from Fig 3.9 that the synthetic galaxies are fractionally brighter than average for the data, making it too easy for the code to recover the galaxy parameters. This is confirmed by the results presented in Chapter 4 which show the mean absolute luminosity of the

33 host galaxies to be $M_R = -23.53$, 0.27 magnitudes fainter than the synthetic hosts used in the testing programme. To illustrate this point the dashed line in Fig 3.9 shows the apparent magnitude of the synthetic host galaxies dimmed by a further 0.27 magnitudes, which clearly provides a better match to the data. However, the overestimate of the typical host luminosity should be more that off-set by the much larger range of L_{nuc}/L_{host} tackled by the modelling code during testing. The average L_{nuc}/L_{host} of the quasars from the HST programme is only 2.6 (see Chapter 4), whereas the code was tested with values of L_{nuc}/L_{host} in the range $0 \rightarrow 16$.

One final measure was taken to improve the accuracy of the synthetic quasar images. The empirical PSF which was used during the production of the synthetic data had an artificial centroiding shift of $\simeq 0.01''$ applied to it, significantly greater than the estimated centroiding error. This precaution was taken in light of the fact that using the same PSF to convolve both the synthetic images and the models used in the fitting process is obviously an idealised situation. Two examples of the synthetic quasars used in the testing of the modelling code are shown in Fig 3.7 and Fig 3.8, placed at the three redshifts of $z = 0.1$, $z = 0.2$ and $z = 0.3$.

The results from the modelling of the synthetic quasars are listed in Tables 3.1, 3.2 and 3.3. Two features of these results are worthy of individual comment. Firstly, it can be seen that for both host morphologies the errors associated with the determination of all the parameters steadily increase with redshift. This is of course as is expected due to the constant integration time used for each simulation leading to an inevitable drop in signal-to-noise with increasing redshift. The second feature is that with regards to the host scalelength, it is significantly easier for the modelling code to accurately determine this parameter for the disc hosts than for the ellipticals. This is again as is expected considering the different behaviour of the Freeman and de Vaucouleurs surface-brightness laws in the central $\simeq 1''$. Given the flat behaviour of the Freeman exponential law in this region it is easier for the code to accurately distinguish between the contributions of the host galaxy and unresolved nuclear component. Alternatively, the $r^{1/4}$ law produces a sharp cusp in the surface-brightness of an elliptical host galaxy at small radius (see Fig 3.1) which can lead to difficulty in de-coupling the relative contributions of the host and nuclear components.

The results of the synthetic data testing can be summarized as follows:

- 100% success in host morphology discrimination.
- host flux determination $\geq$ 98% accurate in all cases.
- error in $r_e \leq 10\%$ out to $z = 0.3$ for ellipticals.
- error in $r_0 \leq 3\%$ out to $z = 0.3$ for discs.

where successful morphological determination refers to a $\Delta\chi^2 \geq 25.7$ between the best-fitting model of the correct morphology, and the best-fitting alternative model, a difference equivalent to the 99.99% confidence level for a 5-parameter fit (Press *et al.* 1989).

3.5 Beta Parameter Modelling

Due to the successful performance of the two-dimensional modelling code in the programme of tests outlined above, it was felt that the level of information present in the HST data justified the extension of the modelling code to cover more than just fixed elliptical and disc host galaxies. The modelling code as described so far is able to determine host galaxy morphology only in that it is elliptical-like or disc-like. Given that the results of the synthetic quasar testing show that the code finds it relatively easy to discriminate between idealised elliptical and disc host galaxies, it is interesting to ask whether it is also possible to quantify just how similar the host galaxy surface-brightness distributions are to the classical $r^{1/4}$ or exponential laws. This question has particular relevance because of recent studies of the cores of inactive elliptical galaxies using both HST (Lauer *et al.* 1995) and ground-based imaging (D'Onofrio *et al.* 1994) which suggest that the surface-brightness profiles of these galaxies can deviate significantly from an $r^{1/4}$ law. It is also of some interest to determine whether or not the code can differentiate between the $r^{1/4}$ law and a somewhat flatter relation at large radii ($r \geq r_e$). Substantial evidence exists that brightest cluster galaxies (BCG) display so-called "halos" in their surface-brightness distributions at large radii (Graham

Redshift	$r_{1/2}$ / kpc	Nuclear	$r_{1/2}$	PA	Axrat	Host Flux	Nuc/Host
0.1	5	2.50	2.40	0.04	0.69	0.37	2.62
0.1	10	1.77	2.90	0.13	0.67	0.83	1.15
0.1	15	1.48	3.09	0.13	0.97	1.26	0.35
0.1	20	1.33	3.44	0.30	1.41	1.86	0.82
0.2	5	2.15	5.17	0.71	1.33	0.90	2.67
0.2	10	2.52	6.17	1.02	1.84	1.21	1.47
0.2	15	2.25	6.86	0.59	2.20	2.59	0.80
0.2	20	1.78	7.51	0.46	2.77	3.76	2.03
0.3	5	2.48	8.91	1.51	1.63	1.83	1.73
0.3	10	3.10	9.59	1.63	2.96	1.54	1.43
0.3	15	2.42	10.3	1.13	2.54	3.73	1.48
0.3	20	1.18	9.43	2.31	3.31	4.84	2.29

Table 3.1: Results of the two-dimensional modelling tests using synthetic quasars with elliptical host galaxies. Column 1 gives the redshift of the quasar. Column 2 gives the actual scalelength of the simulated host in kpc. Columns 3-8 give the mean percentage error in the reclaimed value of the relevant parameter. Each value is the mean for the seven synthetic quasars produced at a particular redshift, with a particular scalelength (for each redshift and scalelength combination there where seven different synthetic quasars produced with L_{nuc}/L_{host}=0, 0.5, 1.0, 2.0, 4.0, 8.0 & 16).

et al. 1996, Schombert 1987), and it would be advantageous to discover if the modelling code could detect these features if they proved to be present in the HST host galaxy images.

The Freeman exponential law and the de Vaucouleurs $r^{1/4}$ law can be thought of as special cases of a more general form of surface-brightness distribution:

$$\mu(r) = \mu_o \exp\left(-(\frac{r}{r_o})^{\beta}\right) \tag{3.7}$$

where the form of the radial profile is governed by the extra free parameter β. The

Redshift	$r_{1/2}$ / kpc	Nuclear	$r_{1/2}$	PA	Axrat	Host Flux	Nuc/Host
0.1	5	1.10	0.53	0.11	0.23	0.16	1.30
0.1	10	0.27	0.44	0.30	0.89	0.73	0.48
0.1	15	0.13	0.43	0.34	1.64	1.10	1.22
0.1	20	0.13	0.70	0.66	2.51	1.43	1.40
0.2	5	1.60	1.07	0.43	0.80	0.57	1.83
0.2	10	1.32	1.36	0.69	1.97	1.07	1.13
0.2	15	0.48	1.23	0.67	3.16	2.01	2.12
0.2	20	0.48	1.67	0.65	5.39	2.79	2.60
0.3	5	1.53	1.37	0.67	0.56	0.74	1.73
0.3	10	1.90	1.97	1.47	2.77	1.74	0.75
0.3	15	0.42	1.87	1.20	4.27	2.17	2.10
0.3	20	0.33	1.76	2.11	4.96	2.50	2.67

Table 3.2: Results of the two-dimensional modelling tests using synthetic quasars with disc host galaxies. Column 1 gives the redshift of the quasar. Column 2 gives the actual scalelength of the simulated host in kpc. Columns 3-8 give the mean percentage error in the reclaimed value of the relevant parameter. Each value is the mean for the seven synthetic quasars produced at a particular redshift, with a particular scalelength (for each redshift and scalelength combination there where seven different synthetic quasars produced with L_{nuc}/L_{host}=0, 0.5, 1.0, 2.0, 4.0, 8.0 & 16).

prospect that the radial profiles of galaxies may be better fitted by a more general form of surface-brightness law such as Equation 3.7 was first proposed by Sersic (1968). Extending the model-building algorithm to include β as an extra free parameter was a reasonably trivial task. However, it was felt that another batch of testing was required in order to determine whether the new version of the code could recover the value of the β parameter with useful accuracy.

Host Type	z	$r_{1/2}$	PA	Axrat	Host Flux (12″)	L_{nuc}/L_{host}
disc	0.1	0.2→1.3	0.0→2.3	0.8→5.4	0.1→5.0	0.0→4.5
elliptical	0.1	1.6→4.8	0.0→0.6	0.0→2.3	0.1→2.3	0.0→4.0
disc	0.2	0.8→1.9	0.0→2.3	0.8→5.4	0.1→2.5	0.0→4.5
elliptical	0.2	2.4→11.5	0.0→1.7	0.8→3.1	0.2→4.3	0.0→4.5
disc	0.3	0.0→2.6	0.0→3.7	0.0→5.4	0.1→3.0	0.0→4.0
elliptical	0.3	6.0→13.7	0.0→6.3	0.8→4.6	0.2→5.0	0.0→6.8

Table 3.3: The range of percentage errors in the reclaimed values of the host-galaxy parameters from the synthetic quasar modelling tests. Columns 1 & 2 detail the actual host-galaxy morphology and redshift of the synthetic quasars. Columns 3 → 7 show the range in percentage error in the reclaimed parameters from the model fits to the 28 synthetic quasars constructed at each redshift, with each of the two host morphologies.

3.5.1 Testing the Beta Modelling Code

The question which was asked of the β-modelling code during the testing programme was whether, given a sample of synthetic quasars with idealised de Vaucouleurs host galaxies, could it return a range of β values narrow enough to provide useful extra information. If alternatively, an acceptable fit could be achieved with a wide range of β values, then the inclusion of β as an extra free parameter could not be justified on the grounds that it was providing extra morphological information about the nature of the host galaxies. The accuracy of the β-modelling code was tested using the 56 synthetic quasars with elliptical hosts and redshifts of $z = 0.2 \,\&\, z = 0.3$ from Section 3.4, the results of which are presented in the form of a histogram in Fig 3.10. It was not considered necessary to test the β-modelling code using idealised Freeman disc hosts since the test results presented in Section 3.4 had confirmed that it is substantially more difficult to recover the parameters of elliptical hosts in all cases. The success of the β-modelling code can be immediately seen from Fig 3.10. Out of the 56 synthetic quasars tested, the β value recovered by the modelling code lies in the range $0.225 < \beta < 0.275$ in 53 cases.

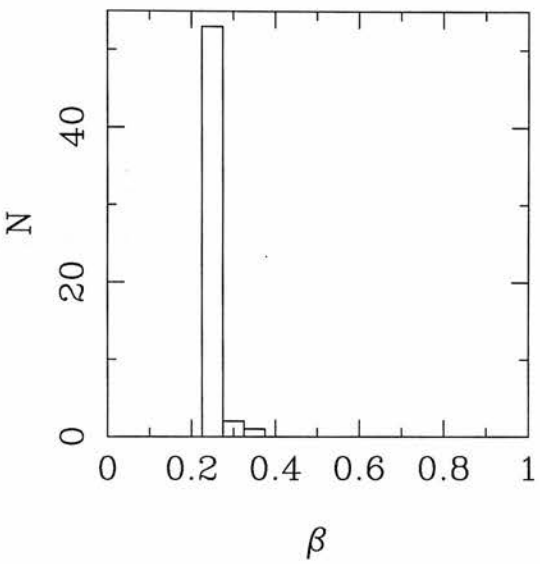

Figure 3.10: The distribution of beta values recovered by the β-modelling code from the synthetic quasars with elliptical host galaxies at z=0.2 and z=0.3.

3.6 Combined Disk-Bulge Modelling

During the latter stages of the analysis of the HST host galaxies presented in Chapter 4, it became necessary to extended the modelling code further than has been described above. The β-modelling of four of the radio-quiet quasars from the the HST sample showed that the underlying host galaxy was a hybrid of both disk and bulge (elliptical) forms. To investigate whether an improved fit could be achieved with a two-component model the central model-building algorithm was extended to produce combined disk and bulge models. During the fitting of these combined models the eight parameters controlling the form of the galaxy surface-brightness distributions were left free. In combination with the normalization of the nuclear component this required the fitting of a total of nine free parameters. This hybrid version of the modelling code was not subjected to the same rigorous testing as described in Sections 3.4 and 3.5.1. The reason for this is that it was a relatively late development in terms of the timescale of the thesis (April 1999), and that the use of its results for only four objects from the 33-object sample does not have a significant impact on the conclusions of Chapter 4.

With regards to host-galaxy morphology, the clear conclusion from both sets of

modelling tests presented in this Chapter is that if the host galaxies of the AGN in the HST imaging study are consistent with standard de Vaucouleurs or Freeman models, then the two-dimensional modelling code will successfully discriminate between the two. In addition to this, if the distribution of β values returned from the modelling of the host galaxies does not show a strong peak around either $\beta = 0.25$ or $\beta = 1.0$, then this can be taken as strong evidence that due to either possible gravitational interaction, or the presence of the active nucleus, the host galaxies deviate significantly from the standard elliptical and disc forms.

Chapter 4

Host Galaxy Modelling Results

4.1 Modelling Procedure

The modelling of the HST sample was carried out in three separate stages. The first stage utilised the standard version of the two-dimensional modelling code (Section 3.3) to determine whether the underlying host galaxies were better matched by either a standard exponential disc or $r^{1/4}$ de Vaucouleurs law. Each host was modelled with each host galaxy type, with the initial values of the galaxy parameters chosen to fully span the five-dimensional parameter space. As with all the modelling performed on the HST sample, once the minimum χ^2 solution had been found the modelling code was repeatedly re-started from close to the minimum χ^2 solution, in order to ensure that the solution was stable. The results of the first stage of the modelling programme are listed in Table 4.1 & Table 4.2.

The second stage of the modelling procedure removed the restriction of assuming the form of the underlying galaxy surface-brightness distribution *a priori*. To achieve this, all of the objects were analysed with the second version of the modelling code which incorporates a sixth free parameter β, where $I(r) \propto exp(-r^{\beta})$ describes the galaxy luminosity profile (Section 3.5). The results of this stage of the modelling process, including the best-fit values of β and the significance of the improvement in fit over the

standard disc and elliptical galaxy models, can be found in Table 4.3 & Table 4.4.

An examination of Table 4.4 reveals that, in contrast to the RGs and RLQs, several of the RQQs have best-fit β values which are intermediate between the values of 0.25 or 1.0 expected for pure elliptical or disc hosts. For this reason it was decided that the RQQs should also be modelled with a 9 free-parameter fit, which allowed for the combination of both disc and bulge contributions to the host's surface-brightness distribution (Section 3.6). For four of the thirteen RQQs this procedure produced a significantly improved model fit, and it is the L_{host} and L_{nuc} values from these combined fits which are used in all the of the subsequent analyses. In the results presented in Table 4.2 it is the scalelength, axial ratio and position angle of the dominant scalelength component which is listed for these combined-fit objects.

Luminosity profiles which have been extracted from the two-dimensional model fits are presented in Appendix A. The profiles are followed out to a radius of $10''$, which is representative of the typical outer radii used in the modelling ($< r >= 11''$). The HST images of each object are presented in Appendix B, along with the best-fitting models and model-subtracted images.

4.2 Host Galaxy Morphologies

An investigation of the results presented in Table 4.1 and Table 4.2 confirms that the complicated observing strategy outlined in Chapter 2 has successfully allowed the determination of the host-galaxy morphology for all 33 objects in the sample. Also immediately apparent from Tables 4.1 & 4.2 is that the huge amount of information available to the modelling code as a result of the high resolution of HST, and the decision to opt for a fully two-dimensional modelling approach, has not only allowed a morphological preference to be made, but can formally exclude the alternative host in all cases ($\Delta\chi^2 = 25.7$ corresponds to 99.99% confidence level for a 5 parameter fit (Press *et al.* 1989)).

The results from the modelling of the RG and RLQ sub-samples are in good agree-

Source	Host	$\Delta\chi^2$	$r_{1/2}$/kpc	$\mu_{1/2}$	R_{host}	R_{nuc}	L_{nuc}/L_{host}	b/a	PA/°
RG									
0230−027	E	5920	7.7	21.8	17.5	-	-	0.95	113
0307+169	E	3535	9.4	21.4	17.2	20.9	0.03	1.00	13
0345+337	E	2349	13.1	23.3	18.0	21.1	0.06	0.70	99
0917+459	E	33245	21.9	23.0	16.1	19.4	0.05	0.76	36
0958+291	E	7793	8.5	22.0	17.1	18.5	0.27	0.95	45
1215−033	E	9305	8.5	22.0	17.1	22.3	0.008	0.87	60
1215+013	E	13987	4.7	21.0	16.5	19.9	0.05	0.94	142
1330+022	E	7354	15.7	22.9	17.1	19.5	0.11	0.79	79
1342−016	E	28748	23.3	22.9	15.6	21.8	0.003	0.93	96
2141+279	E	8530	24.8	23.5	16.7	25.6	0.0003	0.74	148
RLQ									
0137+012	E	5093	14.2	22.6	17.2	17.3	0.8	0.85	35
0736+017	E	8909	13.3	22.9	16.9	16.2	1.9	0.97	13
1004+130	E	501	8.2	21.5	16.9	15.0	5.8	0.94	29
1020−103	E	4209	7.1	20.8	17.2	16.8	1.4	0.73	46
1217+023	E	2359	11.1	21.7	17.3	16.3	2.5	0.8	16
2135−147	E	2670	11.6	22.7	17.2	16.2	2.5	0.95	72
2141+175	E	565	8.2	21.2	17.3	15.9	3.7	0.47	118
2247+140	E	8092	13.5	22.4	17.2	16.9	1.3	0.63	118
2349−014	E	13463	19.2	22.7	15.9	16.0	0.9	0.89	45
2355−082	E	2998	10.4	22.0	17.1	17.4	0.77	0.73	177

Table 4.1: The outcome of attempting to model the AGN host galaxies of the RGs and RLQs as either an exponential disc, a de Vaucouleurs spheroid, or a combination of both. The preferred host-galaxy morphology is given in column 2 (E=Elliptical, D=Disc, B/D=Bulge/Disc), with the $\Delta\chi^2$ between the chosen model and the best alternative model given in column 3. In column 4 $r_{1/2}$ (semi-major axis) is given irrespective of the chosen host morphology ($r_{1/2} = r_e, r_{1/2} = 1.68r_0$). Column 5 lists $\mu_{1/2}$ in units of R mag arcsec^{-2}. Columns 6 and 7 list the integrated apparent magnitudes of the host galaxy and fitted nuclear component converted from F675W to Cousins R-band, while column 8 gives the ratio of integrated galaxy and nuclear luminosities.

Source	Host	$\Delta\chi^2$	$r_{1/2}$/kpc	$\mu_{1/2}$	R_{host}	R_{nuc}	L_{nuc}/L_{host}	b/a	PA/°
RQQ									
0052+251	D/B	2467	11.8	21.8	16.7	15.4	3.2	0.61	117
0054+144	E	6050	10.4	21.7	16.6	15.5	2.7	0.61	108
0157+001	B/D	3860	15.5	22.0	15.6	16.2	0.57	0.88	116
0204+292	E	32954	8.8	20.9	15.9	16.0	0.89	0.73	71
0244+194	E	2744	9.3	22.7	17.5	16.8	1.9	0.92	77
0257+024	D/B	10025	11.7	21.7	15.9	21.0	0.009	0.88	134
0923+201	E	1733	8.2	22.1	17.2	15.7	4.2	0.98	141
0953+415	E	91	7.6	22.4	18.2	15.2	15.4	0.86	115
1012+008	E	1056	28.7	23.8	16.6	16.2	1.5	0.64	109
1549+203	E	511	5.0	22.2	18.9	16.8	6.5	0.88	34
1635+119	E	34765	7.6	21.6	16.8	18.1	0.3	0.69	179
2215−037	E	1506	6.7	21.4	17.5	18.2	0.56	0.84	88
2344+184	D/B	8868	17.5	23.8	16.8	20.3	0.04	0.67	103

Table 4.2: The outcome of attempting to model the AGN host galaxies of the RQQs as either an exponential disc, a de Vaucouleurs spheroid, or a combination of both. The preferred host-galaxy morphology is given in column 2 (E=Elliptical, D=Disc, B/D=Bulge/Disc), with the $\Delta\chi^2$ between the chosen model and the best alternative model given in column 3. In column 4 $r_{1/2}$ (semi-major axis) is given irrespective of the chosen host morphology ($r_{1/2} = r_e, r_{1/2} = 1.68r_0$). Column 5 lists $\mu_{1/2}$ in units of R mag arcsec^{-2}. Columns 6 and 7 list the integrated apparent magnitudes of the host galaxy and fitted nuclear component converted from F675W to Cousins R-band, while column 8 gives the ratio of integrated galaxy and nuclear luminosities.

Source	Host	β	$\Delta\chi^2$
RG			
0230−027	Elliptical	0.252	0
0307+169	Elliptical	0.208	52
0345+337	Elliptical	0.249	2
0917+459	Elliptical	0.229	264
0958+291	Elliptical	0.253	16
1215−033	Elliptical	0.241	0
1215+013	Elliptical	0.254	3
1330+022	Elliptical	0.237	16
1342−016	Elliptical	0.229	90
2141+279	Elliptical	0.246	2.2
RLQ			
0137+012	Elliptical	0.185	126
0736+017	Elliptical	0.193	239
1004+130	Elliptical	0.253	5
1020−103	Elliptical	0.191	132
1217+023	Elliptical	0.255	2
2135−147	Elliptical	0.250	0
2141+175	Elliptical	0.280	23
2247+140	Elliptical	0.249	17
2349−014	Elliptical	0.258	10
2355−082	Elliptical	0.262	383

Table 4.3: The results of the variable-β modelling of the RGs and RLQs. Column 2 lists the host morphology of the best fitting 'fixed β' model. The best-fitting values for the β profile parameter are given in column 3. The $\Delta\chi^2$ of column 4 quantifies the improvement in fit between this variable-β model and the best-fitting disc or elliptical model. A value of $\Delta\chi^2 \geq 16.3$ is equivalent to an improvement of fit significant at the 3σ level (Press *et al.* 1989).

Source	Host	β	$\Delta\chi^2$
RQQ			
0052+251	Disc/Bulge	1.091	267
0054+144	Elliptical	0.251	3
0157+001	Bulge/Disc	0.238	133
0204+292	Elliptical	0.236	216
0244+194	Elliptical	0.220	47
0257+024	Disc/Bulge	0.754	2792
0923+201	Elliptical	0.299	44
0953+415	Elliptical	0.266	9
1012+008	Elliptical	0.377	102
1549+203	Elliptical	0.251	0
1635+119	Elliptical	0.183	550
2215−037	Elliptical	0.250	0
2344+184	Disc/Bulge	0.428	1044

Table 4.4: The results of the variable-β modelling of the RQQs. Column 2 lists the host morphology of the best fitting 'fixed β' model. The best-fitting values for the β profile parameter are given in column 3. The $\Delta\chi^2$ of column 4 quantifies the improvement in fit between this variable-β model and the best-fitting disc or elliptical model. A value of $\Delta\chi^2 \geq 16.3$ is equivalent to an improvement of fit significant at the 3σ level (Press *et al.* 1989).

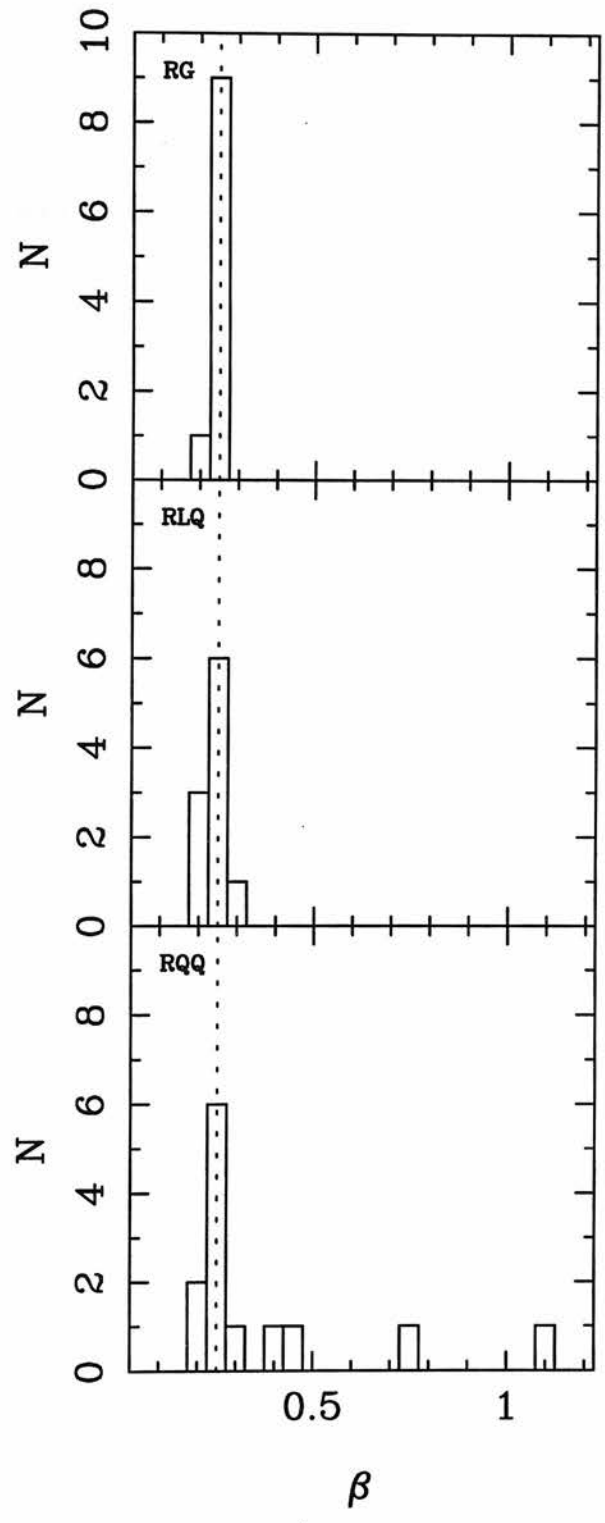

Figure 4.1: Sub-sample histograms of the best-fit β values from the variable β modelling. The dotted line lies at $\beta = 0.25$, corresponding to a perfect de Vaucouleurs model.

ment with orientation-based unification, with all 20-objects found to have elliptical host galaxies. A perhaps more striking feature of these results is the extent to which the classic $r^{1/4}$ de Vaucouleurs law provides a near-perfect description of the host galaxies of the radio-loud objects (see Fig 4.1). As can be seen from Table 4.3 the best-fitting β values for the combined RG and RLQ sub-samples all lie between $0.19 < \beta < 0.26$, with the RGs alone lying in an even tighter range, $0.21 < \beta < 0.25$. This result is even more remarkable considering the deviations from the $r^{1/4}$ law for the central regions of low-z inactive ellipticals commonly reported in the literature (see Section 3.5). The radial profiles extracted from the HST images of the RGs (Appendix A) show no evidence for any large-scale deviation from a de Vaucouleurs profile in the central arcsecond ($\sim$ 5 kpc). This conclusion is further strengthened by a comparison of the beta histogram for the three sub-samples with that from the β-modelling tests performed in Chapter 3. The application of the Kolmogorov-Smirnov test to the β distribution of the 29 objects which were found to have single-component elliptical host galaxies, and those resulting from the β-model testing, returns a probability of p=0.23. This confirms that, as far as the modelling code is concerned, any differences between these hosts and pure elliptical galaxies are not statistically significant. The best match between the test results and the actual data is for the RG sub-sample (p=0.39), perhaps as would be expected considering the lack of a dominant point-source contribution.

Considering the still prevalent belief that RQQs are often located in disc galaxies, the results from modelling of the RQQ sub-sample are perhaps surprising, with 9 of the 13 host galaxies showing no evidence for any disc component. Of the four objects which are best matched by a combined disc/bulge model, the luminosities of 0157+001 and 0052+251 are dominated by their bulge components, which respectively account for 83% and 71% of the total host luminosity. This means that the number of bulge-dominated RQQ hosts is 11 out of the 13 objects.

It is interesting to note that the two remaining objects, 0257+024 and 2344+184, are by far the lowest luminosity objects in the entire 33-object sample. In fact, converting their total luminosity (host+nucleus) from the model fits for these two objects (Table 4.10) to the equivalent absolute V-magnitudes gives $M_V = -22.6$ and $M_V = -21.9$ respectively (assuming $V - R = 0.8$ at $z = 0$, Fukugita *et al.* 1995). Given that for

this study the adopted quasar/Seyfert borderline is $M_v = -23.0$, it is clear that these two objects, plus 1635+119, are not actually *bona fide* RQQs. The clear implication from this result is that all *true* quasars, with $M_V < -23.0$, reside in luminous bulge-dominated hosts, irrespective of their radio power.

The morphological determinations for the RQQ host galaxies have placed on a firm footing the suggestion made previously by Taylor *et al.* (1996) and McLeod & Rieke (1995a) that the probability of a RQQ having an early-type host was an increasing function of the quasar luminosity. Unlike the previous ground-based studies, the high resolution and temporally stable PSF offered by HST has permitted the confirmation of what where necessarily tentative conclusions, due to the uncertainties introduced by ground-based seeing conditions. Therefore, a strong conclusion from the morphological results from the new HST images is that, unlike in low-z radio galaxies and radio-quiet Seyfert galaxies, the radio luminosity of a quasar is not apparently related to host galaxy morphology.

4.3 Host Galaxy and AGN Luminosities

In this section the luminosities of the best-fitting model galaxy and nuclear components are presented, and the question of whether the two quantities are correlated is investigated. The host and nuclear luminosities are presented in the form of integrated absolute Cousins R–band magnitudes. The apparent magnitudes have been calculated by integrating the best-fit model components to infinite radius, and use the F675W flight-system zero-point given by Holtzman *et al.* (1995). The similarity between the F675W filter and the standard Cousins R–band is such that, with the use of this zero-point, the difference is of the order ± 0.05 magnitudes. The conversion from apparent to absolute magnitudes has been performed using $H_0 = 50, \Omega_0 = 1$ and k-corrections assuming spectral indices of $\alpha = 1.5$ & $\alpha = 0.2$ for the host and nucleus respectively ($f_\nu \propto \nu^{-\alpha}$). The value of $\alpha = 1.5$ was determined from inspection of a 13 Gyr-old single-burst elliptical galaxy model (Guiderdoni & Rocca-Volmerange 1987). This value of spectral index produces k-corrections in good agreement ($\Delta m \leq 0.1$) with

those calculated from linear interpolation of the values tabulated for the same model by Rocca-Volmerange & Guiderdoni (1988). The value of $\alpha = 0.2$ adopted for the nuclear k-corrections was the mean quasar spectral index, in the wavelength range covered by the F675W filter, found from the study of a complete sample of Palomar Green quasars (Neugebauer *et al.* 1987).

4.3.1 Host Galaxy Luminosities

The integrated (to $r = \infty$) absolute luminosities for the best-fitting hosts and nuclear components for the full sample can be found in Tables 4.9 and 4.10. These results are displayed in the form of histograms for the separate sub-samples in Fig 4.2 & Fig 4.3. The mean and median integrated luminosities of the best-fit host galaxies in each sub-sample are:

$$< M_R >= -23.53 \pm 0.09 \quad \text{median=-23.52} \quad \text{(ALL)}$$
$$< M_R >= -23.66 \pm 0.16 \quad \text{median=-23.63} \quad \text{(RG)}$$
$$< M_R >= -23.73 \pm 0.10 \quad \text{median=-23.67} \quad \text{(RLQ)}$$
$$< M_R >= -23.28 \pm 0.15 \quad \text{median=-23.30} \quad \text{(RQQ)}$$

Two features of these results are worthy of individual comment. Firstly, the agreement between the absolute magnitudes of the host galaxies of the RG and RLQ sub-samples can be seen to be extremely good, with the median figures differing by only 0.04 magnitudes. This can be interpreted as strong evidence in favour of orientation-based radio-loud unification. The second obvious feature of the host luminosity results is that these new HST images appear to confirm the traditional finding that the hosts of RQQs are less luminous than those of RLQs, although the median difference of 0.37 magnitudes is a factor of two smaller than the difference typically claimed (see Section 1.6). This does not seem to be an artifact of the inclusion of RQQ hosts with a substantial disc component. The absolute luminosity figures for the 9 RQQs with solid elliptical model fits are :

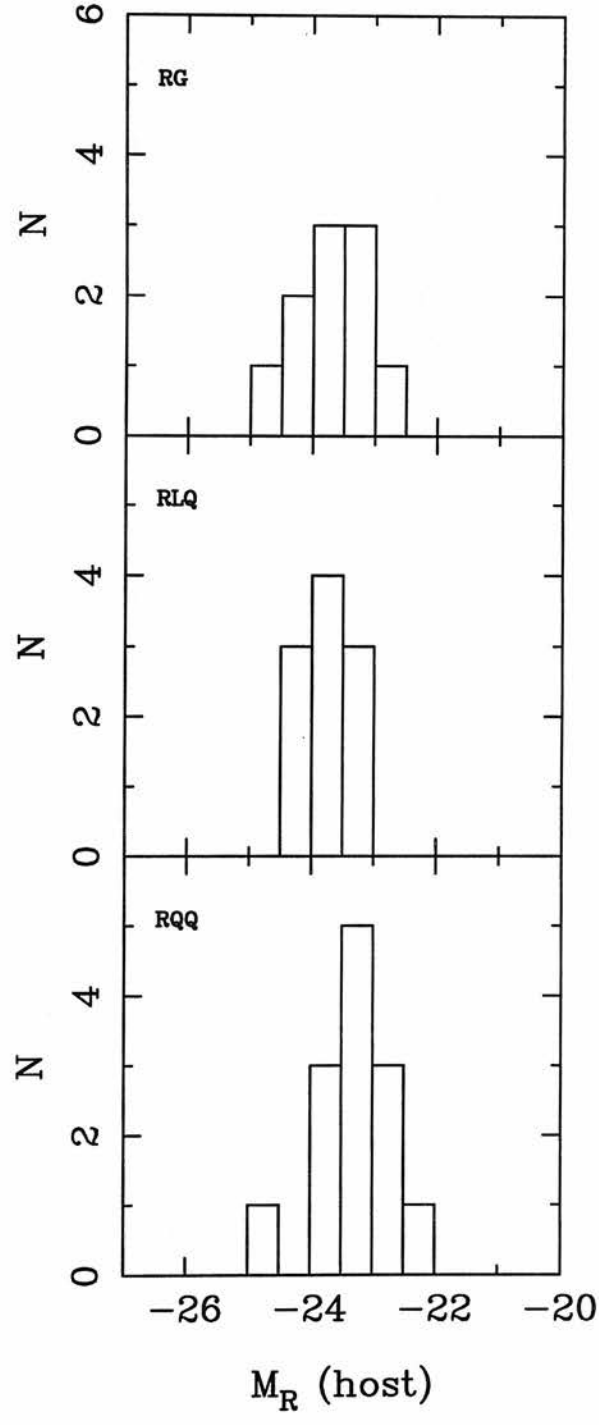

Figure 4.2: Sub-sample histograms of the host galaxy absolute, integrated R-Cousins magnitudes.

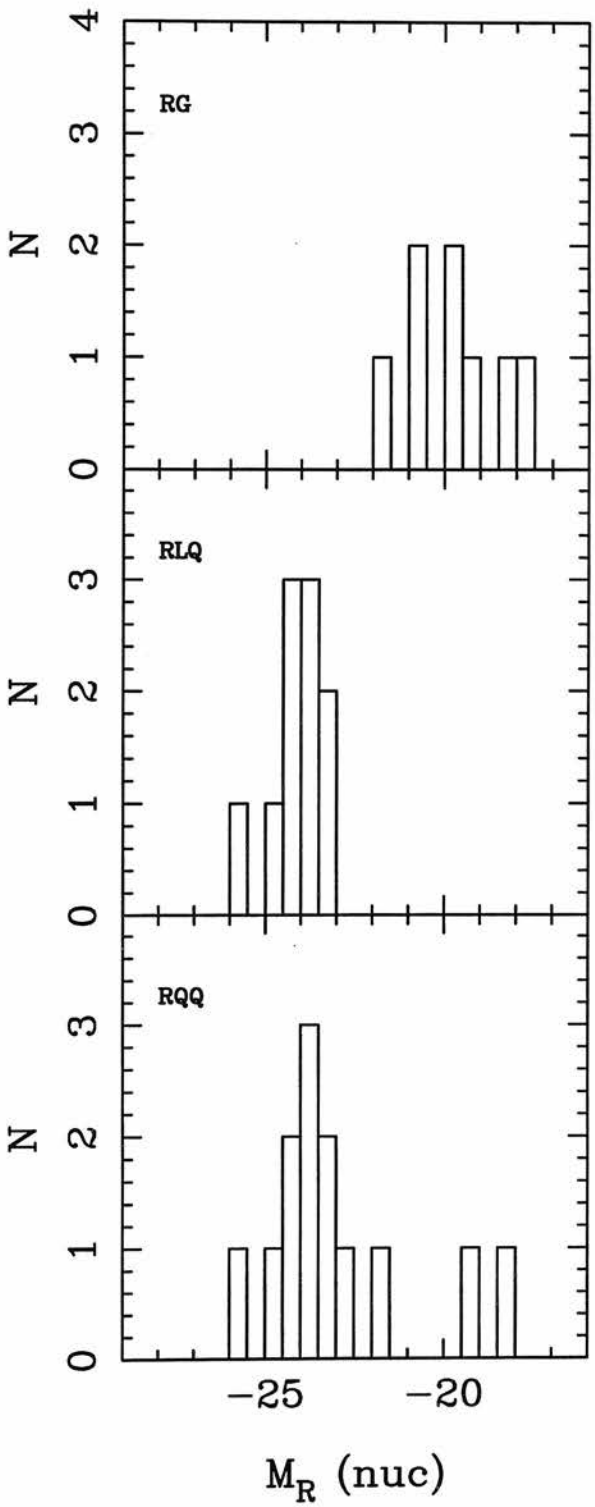

Figure 4.3: Sub-sample histograms of the nuclear absolute, integrated R-Cousins magnitudes.

$< M_R >= 23.30 \pm 0.17$ median=23.30 (RQQ, bulge-dominated)

As was highlighted in Chapter 1, there has been a large variation in the luminosity difference between RQQ and RLQ host galaxies reported in the literature. These differences have ranged from RQQ hosts being fainter than their RLQ counterparts by $0.7 \rightarrow 1.0$ magnitudes in optical studies (eg. Smith *et al.* (1986), Véron-Cetty & Woltjer (1990), Bahcall *et al.* (1997)), to no formal luminosity difference being detected in the near-infrared images of this HST sample (Taylor *et al.* 1996). It is therefore interesting to compare the difference in luminosity detected here with the results of the other two recent HST R–band imaging studies of Hooper *et al.* (1997) and Boyce *et al.* (1998), both of which also used two-dimensional modelling to analyse the host galaxies. The following table lists the mean differences detected in the three studies ($< M_{RQQ} > - < M_{RLQ} >$) with the associated standard error. In calculating the figures for the Hooper *et al.* programme, where no attempt was made to distinguish the host-galaxy morphologies, the luminosities of the best-fit $r^{1/4}$ model have been used.

Δ M$= 0.43 \pm 0.20$	This Work
Δ M$= 0.53 \pm 0.23$	Hooper *et al.*
Δ M$= 0.67 \pm 0.29$	Boyce *et al.*

The clear implication from these results is that the host galaxies of RQQs are consistently fainter than those of RLQs by ~ 0.5 magnitudes in the R–band. Unlike in earlier studies, this difference can no longer be attributed to the model fitting of RQQs producing disc fits, since only 2 of the 26 RQQs host magnitudes included in the above figures are derived from an exponential host model. The common bias of the RLQ redshifts being consistently higher than those of the RQQs can also be firmly rejected as a possible cause of the difference, with the two quasar types having well matched redshift distributions in all three studies. At least for the results presented here, and

those of Hooper *et al.* , the selection of the RLQ and RQQ samples to have matched optical magnitudes, also excludes the possibility that the host magnitude difference is as a result of the RLQs being intrinsically more luminous. However, it is possible that the host galaxy results of Boyce *et al.* may have been influenced by this affect, considering that the RLQs in that study are intrinsically 0.6 ± 0.8 magnitudes brighter than the RQQs, although, as can be seen from the large error associated with this difference, the overlap of the total quasar luminosities is significantly larger than that of the hosts. It is worth noting at this point that, although the results of Taylor *et al.* certainly do not formally support a difference in host magnitudes, Δ M$= 0.4 \pm 0.3$, they are in fact perfectly consistent with the three sets of R–band HST results. The question of whether there is any detectable correlation between the host galaxy and nuclear luminosities is explored in Section 4.3.3.

A general result that can be taken from the luminosities of the best-fitting host galaxies is that, with the exception of the two Seyfert objects, all of them lie at the extreme end of the elliptical galaxy luminosity function. Taking the latest determination of the R–band luminosity function as having $\mathrm{M}_R^\star = -22.2$ (Lin *et al.* 1996), after having converted the published value of $\mathrm{M}_R^\star = -21.8$ to an integrated magnitude, it can be seen that *all* of the hosts have luminosities of $L \geq L^\star$, with 25 of the 33 having luminosities $L \geq 2L^\star$. These results are in good agreement with those of the previous K–band imaging study which also found all the hosts to be brighter than $L_K^\star$. Independent support for this result comes from the findings of Hooper *et al.* (1997) and Boyce *et al.* (1998), both using the F702W (wide R) filter on WFPC2. Using the Lin *et al.* value for $M_R^\star$, Hooper *et al.* found 15 of their 16 ($z \simeq 0.4$) quasars to have $L \geq L_\star$, while Boyce *et al.* found all 11 of their 14 objects, for which a host model was fitted, to have $L \geq L_\star$ (both sets of results have been converted to the cosmology adopted for this thesis).

4.3.2 Nuclear Luminosities

The integrated luminosity of the best-fit nuclear components from the two-dimensional modelling of the HST images are given in the table below. The radio galaxy 0230-

027 has been excluded from these figures as the modelling code found no unresolved component for this object.

$$< M_R >= -22.27 \pm 0.45 \quad \text{median=-23.36} \quad \text{(ALL)}$$
$$< M_R >= -19.27 \pm 0.64 \quad \text{median=-19.64} \quad \text{(RG)}$$
$$< M_R >= -24.07 \pm 0.22 \quad \text{median=-24.01} \quad \text{(RLQ)}$$
$$< M_R >= -22.95 \pm 0.57 \quad \text{median=-23.70} \quad \text{(RQQ)}$$

As expected, the unresolved nuclear components displayed by the RGs are nearly two orders of magnitude less than those of the RLQs, in good agreement with the orientation-based radio-loud unification scheme described in Chapter 1. It would appear from the mean figures above that there is a substantial difference in the nuclear components of the RQQ and RLQ samples. However, the noticeable offset in the difference between the mean and median figures (combined with the histogram of Fig 4.3) suggests that the RQQ result is being biased by the three objects identified in Section 4.2 as having total luminosities fainter than $M_V = -23.0$. If these three objects are excluded from the RQQ sample, the nuclear luminosity mean/medians become:

$$< M_R >= -23.95 \pm 0.26 \quad \text{median=-23.97} \quad \text{(RQQ, } M_V < -23.0\text{)}$$

which are very consistent with the equivalent RLQ figures. The similarity between the nuclear components of the RQQ and RLQ sub-samples is reassuring considering that the sample selection process described in Chapter 2 was designed to produce two quasar samples well-matched in luminosity. This result also implies that the measured difference in the respective host magnitudes of the RQQs and RLQs cannot be due to bias from higher luminosity RLQ.

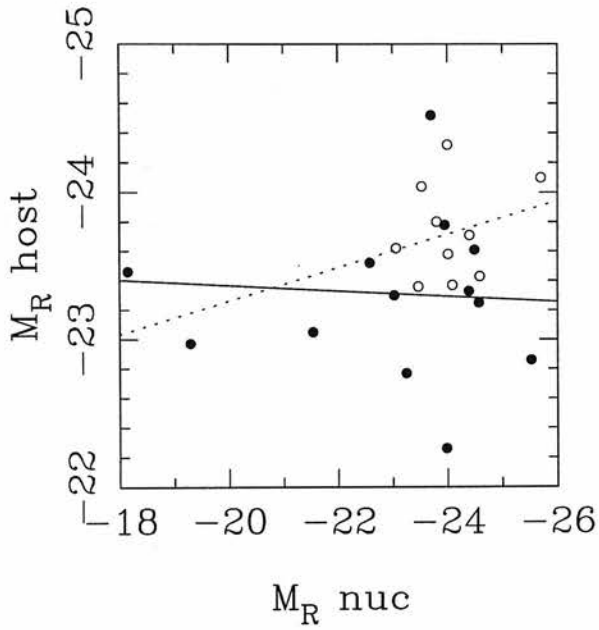

Figure 4.4: The best-fit values for the host and nuclear absolute magnitudes for the RQQ and RLQ sub-samples. The least-squares fit to the RQQs (solid line) and RLQs (dashed line) are shown, with the two lowest luminosity RQQs having been excluded from the fit.

4.3.3 Quasar Host-Nuclear luminosity correlation

Considering the measured difference in the RQQ and RLQ host-galaxy magnitudes is substantially greater than the difference in their respective nuclear components (excluding the three sub-luminous objects) it is not expected that there should be a strong host-nuclear luminosity correlation. This is indeed the case, as can be seen from the plot of host and nuclear luminosities shown in Fig 4.4. The least-squares fit to the two sub-samples are :

$$M_{host} = -23.73(\pm 4.29) - 0.018(\pm 0.18) M_{nuc} \quad \text{RQQ}$$
$$M_{host} = -20.98(\pm 3.72) + 0.114(\pm 0.15) M_{nuc} \quad \text{RLQ}$$

where the two lowest luminosity "Seyfert" RQQs have been excluded from the fit. The application of the Spearmann Rank correlation test confirms that there is no evidence for any correlation, returning a probability of p=0.95 that the null hypothesis of no

correlation is acceptable. It is clear that both sub-sample fits are perfectly consistent with there being no correlation between host and nuclear luminosity, just as was found from the previous modelling results at K (Taylor *et al.* 1996).

The null result found here is in contrast to the positive correlations found previously by many authors (eg. Smith *et al.* (1986), Bahcall *et al.* (1997), Hooper *et al.* (1997)). The suspicion often cast upon the detection of a positive host galaxy-nuclear correlation is that there are two obvious selection effects at work. The first of these is that it is obviously much more difficult to detect faint galaxies which are the hosts to bright quasars. It seems clear that given the difficulties associated with ground-based seeing, and the perils of PSF-subtraction on HST data (eg. Bahcall *et al.* 1997), that this could well be a contributing factor. An examination of Fig 4.4 shows that there is a group of several RQQs in this study with bright nuclear components, and relatively faint host galaxies (eg. 0953+415), providing confidence that the techniques employed here have been succesful in overcoming this possible source of a false correlation. The other selection effect which could contribute to a false positive correlation is that weak AGN in bright host galaxies will not be classified as quasars.

Although the results presented here for powerful low-z quasars show no evidence for a correlation, it does appear to exist for lower luminosity Seyfert galaxies. This trend may actually be seen in the HST sample, with the probabilty of there being no correlation between host galaxy and nuclear luminosity dropping from 0.95 to 0.51 if the three lowest luminosity RQQs are included in the Spearmann rank test.

In the case of Seyferts, the reduction in both redshift and contrast between the host and nuclear components means that it can be confidently assumed that all of the host galaxies are being detected, removing one of the sources of bias mentioned above. Indeed, the work of McLeod & Rieke (1994, 1995) on two samples of low- and high-power AGN at low-z has led them to suggest that the relation between host and nuclear luminosity is of the form that there is a minimum host luminosity required to produce a particular quasar luminosity. This would be consistent with both the positive correlation found at lower AGN power, and the flat relation found here for higher powered quasars. The host galaxies for the quasars studied here have already

been shown to be among the brightest known, and therefore demand that the galaxy-quasar relation tails-off at high quasar luminosity. The question of how the nuclear and host galaxy luminosities relate to central black-hole mass and quasar fuelling rate is pursued in Chapter 5.

4.4 Scalelengths

The best-fitting values of the host-galaxy scalelengths shown in Tables 4.1 and 4.2 are displayed as histograms for the separate sub-samples in Fig 4.5. The average figures for the three sub-samples are :

$$< r_{1/2} >= 12.23 \pm 1.00 \quad \text{median}=10.45 \quad \text{(ALL)}$$
$$< r_{1/2} >= 13.76 \pm 2.18 \quad \text{median}=11.27 \quad \text{(RG)}$$
$$< r_{1/2} >= 11.73 \pm 1.07 \quad \text{median}=11.28 \quad \text{(RLQ)}$$
$$< r_{1/2} >= 11.45 \pm 1.66 \quad \text{median}= 9.30 \quad \text{(RQQ)}$$

Given the low numbers of objects in each sub-sample, the median figures will be the more robust measure of the typical scalelength. Taking the median figures, the RG and RLQ sub-samples can again be seen to be in remarkable agreement, with the RQQ hosts being $\sim 20\%$ smaller.

Galaxy half-light radii of $\simeq 10$ kpc mark out these radio galaxies and quasar hosts as being substantially larger than normal inactive ellipticals. In a study of the galaxies of the Virgo cluster, Capaccioli *et al.* (1992) found that beyond a scalelength of ~ 3 kpc the only galaxies to be found were extremely luminous ellipticals, or cD type brightest cluster galaxies (BCG). The question of how the properties of the host galaxies studied here related to those of BCG is explored in Section 4.9. In further support of the radio-loud unification scheme, the scalelength figures obtained here for the RG and RLQ sub-samples can be compared with the B- and V–band study of Smith & Heckman (1989), who determined the scalelengths of 41 powerful radio galaxies in the redshift

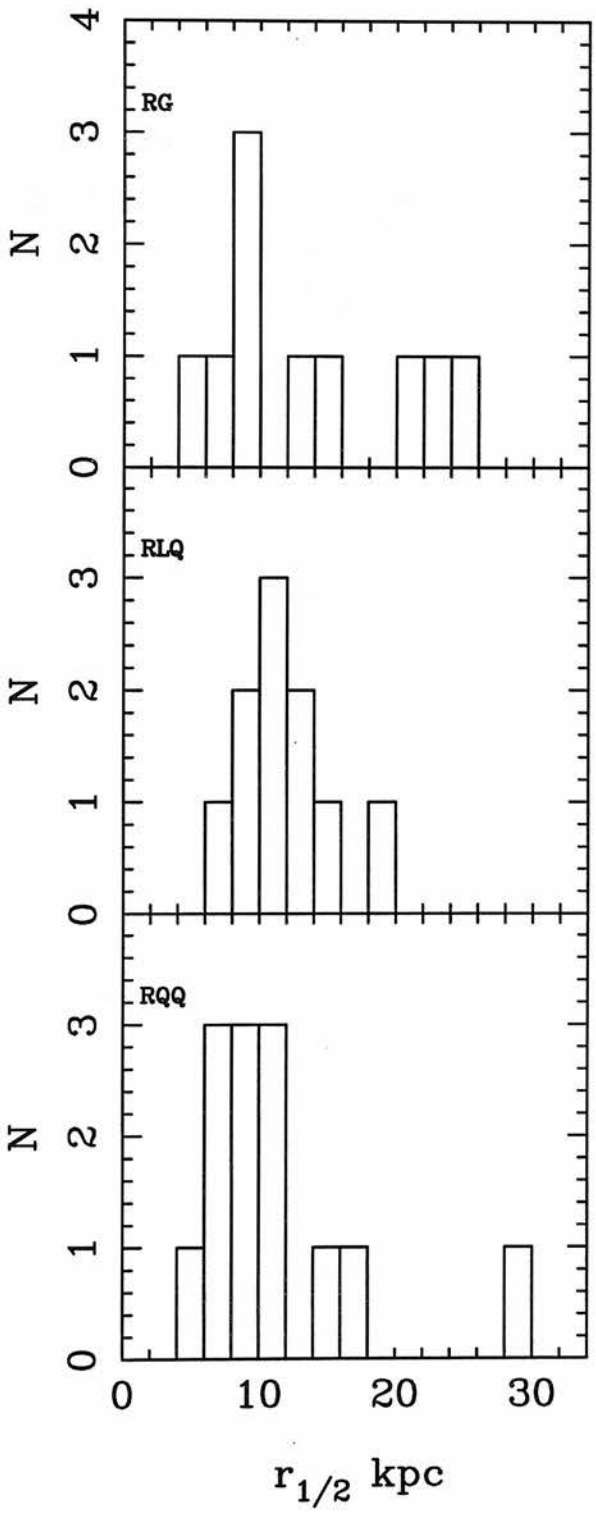

Figure 4.5: Histograms of the best-fit host galaxy scalelengths for the three AGN subsamples.

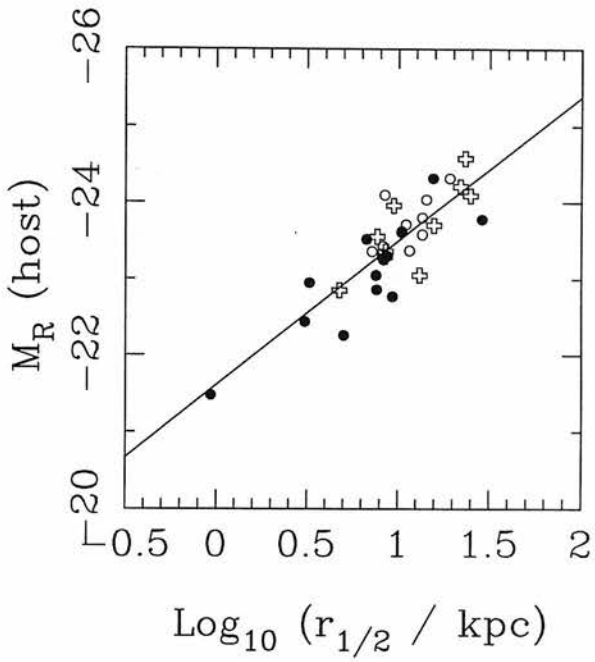

Figure 4.6: Plot of absolute host magnitude against best-fit host scalelength for the RGs (crosses), RLQs (open circles) and RQQs (filled circles) in the HST sample. The solid line is the least-squares fit to the data, which has the form $L \propto r^{0.75}$. The four RQQ objects for which a combined disc/bulge fit was found have their best-fit bulge parameters plotted.

range $0 < z < 0.26$. The median scalelength figure determined is equivalent to ~ 17 kpc in the cosmology adopted here, somewhat larger than the results presented above. However, if the comparison is restricted to the 22 objects which were identified as having strong optical emission lines, more likely to have the same FR II morphology as the radio-loud objects studied here, then the median scalelength falls to 13 kpc, in excellent agreement with the figures presented above.

If the host scalelengths are plotted against the integrated model luminosities, as in Fig 4.6, a tight correlation is seen to be present. The least-squares fit to these data produces a relation of the form $L \propto r^{0.75}$. This is in impressively close agreement with the corresponding result of $L \propto r^{0.70}$ found for low-z inactive ellipticals by Kormendy (1977). In possession of this result it is interesting to ask whether the best-fit model parameters for $\mu_{1/2}$ and r_e presented in Tables 4.1 and 4.2 lie along a Kormendy relation of slope ~ 3.

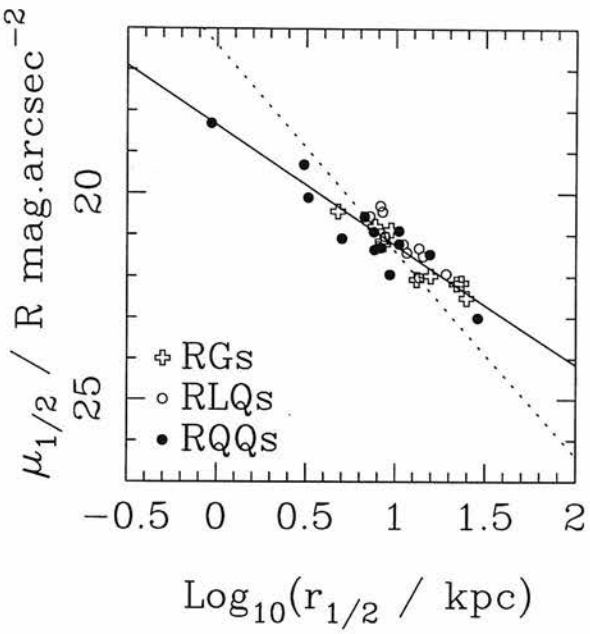

Figure 4.7: The Kormendy relation followed by the hosts of all 33-objects in the HST sample. The solid line is the least-squares fit to the data which has a slope of 2.90, in excellent agreement with the slope of 2.95 found by Kormendy (1977) for inactive ellipticals in the B–band. The dotted line is a relation with a slope of 5, which is to be expected if the host galaxy scalelengths are not properly determined (Abraham *et al.* 1992). For the four RQQ objects which have a significant disc component, the best-fitting bulge component has been plotted.

4.5 Kormendy Relation

The $\mu_{1/2} - r_e$ relation for the host galaxies of all 33 objects is shown in Fig 4.7. For the four RQQ sources which have combined disc/bulge fits it is the parameters for the bulge component that have been plotted. The least-squares fit to the data (solid line) has the form: $\mu_{1/2} = 2.90_{\pm 0.22} \log_{10} r_{1/2} + 18.35_{\pm 0.22}$, (errors are $\pm 1\sigma$) showing for the first time from optical imaging, that the host galaxies of powerful AGN lie on this projection of the fundamental plane. The individual fits to the $\mu_{1/2} - r_e$ relations for the individual sub-samples are:

It is readily apparent from the individual Kormendy relations that the RG and RQQ sub-samples follow very similar relations, consistent with each other in terms of

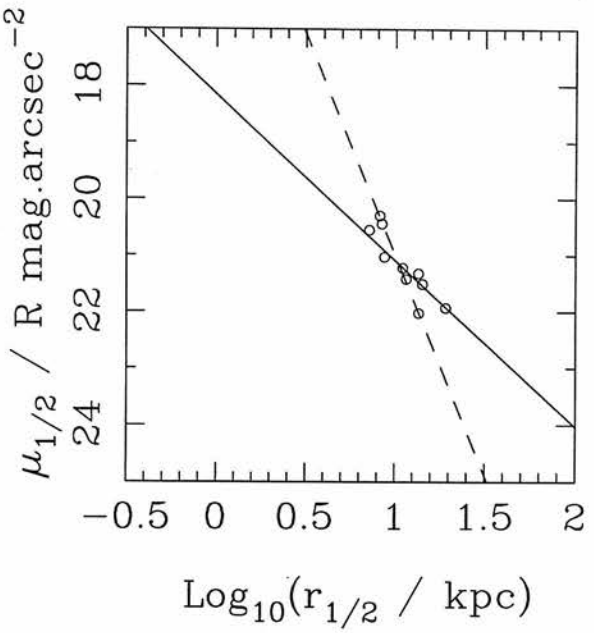

Figure 4.8: The Kormendy relation followed by the 10 objects in the RLQ sub-sample. The dashed line is the least-squares fit to the three objects which are clearly biasing the relation for this sub-sample (see text) and has a slope of 7.8. The solid line is the best-fit to the remaining seven objects which has a slope of 2.94, in good agreement with the relations followed by the other two sub-samples.

$$\mu_{1/2} = 2.86_{\pm 0.34} \log r_{1/2} + 18.44_{\pm 0.36} \quad \text{(RG)}$$
$$\mu_{1/2} = 3.98_{\pm 0.71} \log r_{1/2} + 17.02_{\pm 0.75} \quad \text{(RLQ)}$$
$$\mu_{1/2} = 2.99_{\pm 0.34} \log r_{1/2} + 18.39_{\pm 0.30} \quad \text{(RQQ)}$$

slope and normalization. Perhaps the most encouraging aspect of this is that the best-fitting bulge components for the RQQ objects which have combined disc/bulge model fits lie naturally on the Kormendy relation defined by the other nine, single component, RQQ objects. With no restrictions placed on the range of parameter values available to the modelling code, the fact that the fitted bulge components have physically sensible values gives further confidence that the introduction of the combined disc/bulge fits was justified, and does not involve over-fitting of the data. However, it would appear from the individual fits given above that the RLQ sub-sample follows a steeper slope, compared with the best-fit relation to the other two sub-samples. It is also noticeable that the 1σ error returned by the least-squares fitting procedure is more than twice that

returned from the fitting to the RG sub-sample, also containing 10-objects, suggesting that there may well be outlying objects in the RLQ sub-sample which bias the fit.

This suspicion is confirmed by Fig 4.8 which shows the $\mu_{1/2} - r_{1/2}$ plot for the RLQ sub-sample alone. It is clear that the best-fitting slope of the RLQ Kormendy relation is being seriously biased by three outlying objects (1004+130, 2141+175 and 0736+017). The least-squares fit to these three objects alone (dashed line) produces a relation with a slope of 7.80($\pm$0.24), symptomatic of the scalelengths having not been properly constrained. If these objects are excluded from the least-squares fit (solid line) the relation becomes:

$$\mu_{1/2} = 2.94_{\pm 0.35} \log_{10} r_{1/2} + 18.15_{\pm 0.38} \tag{4.1}$$

in much better agreement with the RG and RQQ relations. It is also noteworthy that the errors associated with this new 7-object fit are now comparable with those returned from the 10- and 13-object fits to the RG and RQQ sub-samples.

Although it is always the case that when dealing with small samples the slope of the Kormendy relation is going to be vulnerable to a few outlying objects, it is interesting to investigate if there are any obvious reasons why the model fits to the three objects mentioned above should be less reliable than average. For two of the three objects the reasons for the difficulty in constraining the host scalelength are readily apparent. 1004+130 is the most nuclear dominated RLQ in the sample, which alone means it will be one of the most difficult objects to model. Coupled with the difficulties presented by the nuclear dominance is the underlying structure revealed in the central $\sim 1''$ by the model-subtracted image presented in Appendix B. This structure, which was also noted by Bahcall *et al.* (1997), appears to be spiral arm-like in form, and caused concern during the modelling process that it may have been biasing the play-off between unresolved nuclear component and the central surface-brightness of the host galaxy. The RLQ Kormendy relation shown in Fig 4.8 would suggest that this was indeed the case, with the central surface-brightness of the model host biased to higher levels in an attempt to match the central structure, with the inevitable shrinking of the best-fitting scalelength.

The second of the three outlying RLQs, 2141+175, is a case where the reasons for

possible inaccuracies in the best-fitting model are obvious from the raw R–band image alone. Investigation of the image presented in Appendix B shows that this object is involved in an extensive interaction, with two filamentary structures emanating from the host to the SE and NW (see descriptions of each image given in Chapter 2). It is not immediately obvious from this image which areas should be masked from the modelling process in order to obtain the most unbiased representation of the underlying host galaxy. As a result of the sensitivity of the model parameters to the exact form of the image masking used for this object, it appears from Fig 4.8 that once again, the scalelength has probably been underestimated in order to better match high surface-brightness structure in the central regions of the image.

The third of the three outlying RLQ objects presents more of a mystery. As can be seen from the R-band image of 0736+017 shown in Appendix B, this object is neither heavily nuclear dominated, nor involved in any significant interactions. There therefore appears to be no obvious reason why the scalelength and surface-brightness parameters for this host should be in error. In light of this it is reassuring that, of the three outliers, 0736+017 is the object which appears to be least in error. If the three outlying objects are re-instated in the least-squares fit individually, then the resulting 8-object fits including 1004+130 and 2141+175 result in best-fit slopes of 3.45 and 3.32 respectively. In contrast, when 0736+017 is re-instated the resulting best-fit becomes :

$$\mu_{1/2} = 3.19_{\pm 0.67} \log_{10} r_{1/2} + 17.95_{\pm 0.72} \tag{4.2}$$

which is perfectly consistent with the expected slope of ~ 3, and the RG and RQQ sub-samples.

With the exclusion of the two outlying RLQ objects the three Kormendy relations obeyed by the sub-samples are internally consistent with each other, and perhaps more importantly, formally inconsistent with a slope of 5. As pointed out by Abraham *et al.* (1992), a clear indication that the modelling procedure employed to analyse host galaxies is unable to break the $\mu_{1/2} - r_{1/2}$ degeneracy is that the objects are seen to lie on a best-fit slope of 5 in the $\mu_{1/2} - r_{1/2}$ diagram. The simple reason for this is that the integrated luminosity of an $r^{1/4}$ galaxy model follows the relation:

$$L_{int} \propto I_{1/2} r_{1/2}^2 \tag{4.3}$$

where $I_{1/2}$ is the surface-brightness at $r_{1/2}$. Given that $\mu_{1/2} \propto -2.5 \log I_{1/2}$, it follows that if the modelling procedure can successfully constrain the host luminosity, but not the scalelength, then the best-fit $\mu_{1/2} - r_{1/2}$ parameters will be randomly distributed along a relation obeying:

$$\mu_{1/2} \propto 5 \log r_{1/2} \tag{4.4}$$

with appropriate normalization to fit the integrated luminosity. Due to the fact that the host galaxies (including the four RQQ bulge components) are found to have a relatively small spread of luminosity (mean = -23.44, σ = 0.64) it might be expected that, if the modelling procedure was unable to accurately determine the individual host scalelengths, the resulting $\mu_{1/2} - r_{1/2}$ relation would be well fitted with a slope of 5 and a normalization to match $M_R = -23.44$. Such a relation has the form:

$$\mu_{1/2} = 5.0 \log_{10} r_{1/2} + 16.40 \tag{4.5}$$

and is plotted as the dashed line in Fig 4.7. It is obvious from Fig 4.7 that this relation is not consistent with the data, giving confidence that the methods of analysis employed here have allowed the accurate determination of the host-galaxy scalelengths.

4.6 Axial Ratios

If the AGN host galaxies are indeed indistinguishable from massive inactive ellipticals then they should display an axial ratio distribution which is also identical. The axial ratio distribution of normal ellipticals is well studied and known to peak at values of $b/a \geq 0.8$ (Sandage, Freeman & Stokes 1970; Ryden 1992). The best-fitting axial ratios from the two-dimensional modelling are listed in Tables 4.1 and 4.2 and displayed in the form of separate sub-sample histograms in Fig 4.9. The corresponding mean and median values are as follows:

$< b/a >= 0.81 \pm 0.02$ median=0.85 (ALL)

$< b/a >= 0.86 \pm 0.03$ median=0.90 (RG)

$< b/a >= 0.80 \pm 0.05$ median=0.82 (RLQ)

$< b/a >= 0.78 \pm 0.03$ median=0.84 (RQQ)

It can be seen from these figures that the axial ratio distributions of all three sub-samples are perfectly consistent with that expected from a sample of elliptical galaxies. There is a slight suggestion that the RG sub-sample objects tend to have higher axial ratios than average, but considering the small number of objects this is certainly not significant.

The axial ratio results from the two-dimensional modelling agree well with the recently published findings of Boyce *et al.* (1998) ,who found that all 11 of the quasars from their 14 object ($z \sim 0.3$) sample for which a model fit was possible, displayed axial ratios with b/a> 0.65. In contrast, Hooper *et al.* (1997) found only 2 of their 16 ($z \sim 0.45$) quasars to have axial ratios with b/a> 0.6. The reasons for this apparently contradictory result probably lie in a combination of the higher redshifts of the Hooper *et al.* objects, and their use of the PC instead of the WF detectors. As has been explained, these two factors will undoubtedly result in a reduced sensitivity to low surface-brightness features, given that the exposure times used were the same as adopted in this study. In fact, Hooper *et al.* noted themselves that they had some concern that their modelling technique, two-dimensional cross-correlation, could have been fooled by high surface-brightness features such as bars or tidal tails. Given the clear result presented here, and the support of the Boyce *et al.* results at similar redshifts, it seems likely that this is indeed what has taken place.

The results presented in the last two sections strongly suggest that in terms of morphology, luminosity, scalelength and Kormendy relation, the hosts of powerful AGN are identical to the normal, massive, inactive ellipticals studied at low redshift. The one final parameter which can be readily recovered from the modelling is host galaxy colour. The desire to obtain reliable optical-infrared colours for the host galaxies was one of the original motivations for this HST imaging study. Given that the results presented thus far suggest the host galaxies are otherwise normal massive ellipticals, it is now even more

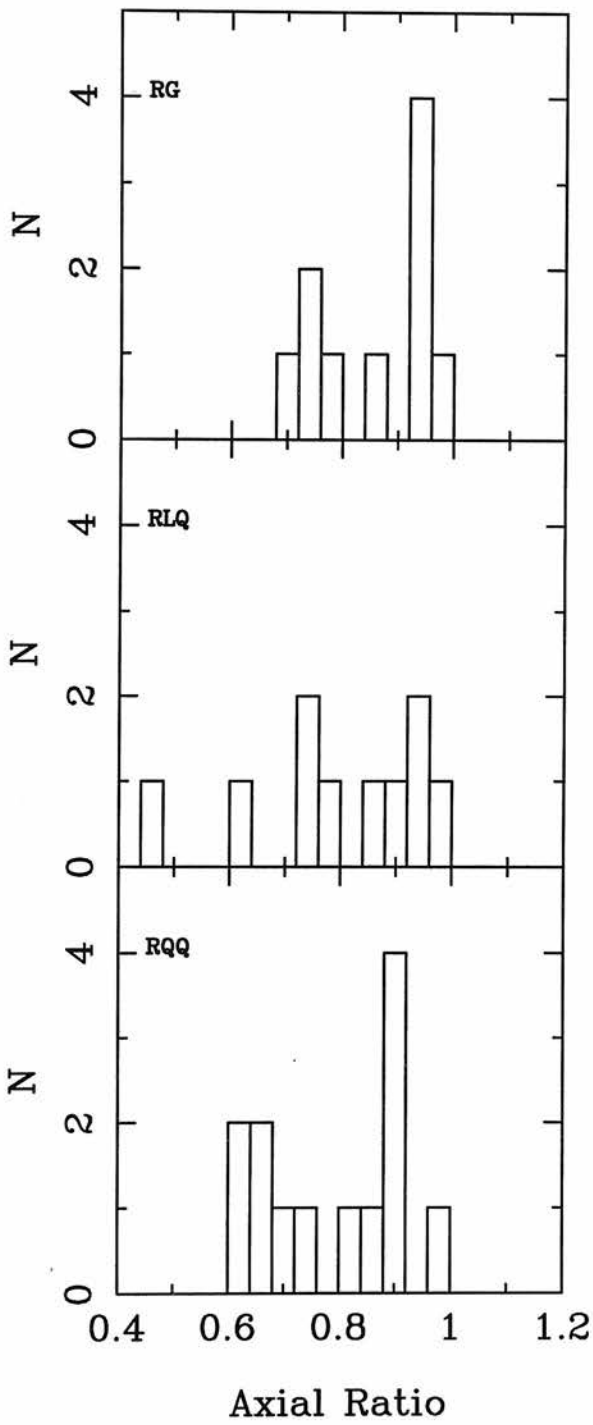

Figure 4.9: The axial ratio distribution for the three host galaxy sub-samples as determined by the two-dimensional modelling.

interesting to investigate whether the hosts also display the red colours associated with old stellar populations, or whether they have significantly bluer colours, indicative of either a generally young stellar population, or of substantial secondary star formation induced by interactions, the central AGN, or both. Armed with the model results presented so far, and those previously obtained from the existing K–band imaging of this sample (Taylor *et al.* 1996), there is now an opportunity to answer these questions. Before the $R-K$ colours of the host galaxies are presented however, the next section reports on a short exploratory observing run which investigated the benefits to host galaxy imaging of tip-tilt active optics in the near-infrared. As a result of comparing the results of this observing run with those obtained from the existing IRCAM 1 K–band imaging, a possible bias was discovered in the previous modelling results. Obviously, as a result of this discovery, the procedure for calculating the host galaxy $R-K$ colours had to be adapted, and it is for this reason that the observing report is included at this juncture.

4.7 Tip-Tilt Observations of Quasar Host Galaxies

While the undoubted resolution benefits available from HST observations have provided the main motivation behind the work of this thesis, in recent years there has been an substantial increase in the amount of effective host galaxy work which is possible from the ground. With the arrival of active and adaptive optics systems on the world's largest telescopes, the prospect of near diffraction-limited ground-based imaging has become a reality. Within the context of the study of quasar host galaxies this development perhaps has most relevance in the near-infrared. The inherent advantages of observing host galaxies in the near-infrared were briefly discussed in Chapter 2, and formed the motivation for the original IRCAM 1 K–band imaging of the HST sample (Dunlop *et al.* 1993, Taylor *et al.* 1996). As has been previously discussed, the main limitation of the existing K–band imaging is the inability to reliably distinguish the host galaxy morphology in quasars where the $L_{nuc}/L_{host} \geq 5$ due to the ground-based seeing of the order $1''$. In this section the results are presented from a short observing run which investigated the possibilities of sub-arcsec imaging of host galaxies in the K–band using

active optics.

4.7.1 The Sample

The relatively small amount of observing time available for this project (3 dark nights) meant that it was not practical to undertake observations of a large sample of objects. Consequently, it was decided to restrict the observations to obtaining deep images of a sample of only 9 objects which would fully quantify the improvements that could be gained over the previous K–band imaging study. The redshift, magnitudes and observational parameters of the sample are listed in Table 4.5. Six of the quasars were taken from the original 40-object sample described in Chapter 2, with five of these also featuring in the new HST sample. The remaining three objects were taken from the sample of Bahcall *et al.* 1994, and were chosen because of their original failure to detect a host galaxy from their V–band HST imaging (Bahcall *et al.* 1994, 1995a). Four of the six objects taken from the original 40-object sample (marked with a $\star$ in Table 4.5) were specifically chosen for this project because the modelling of the original IRCAM 1 observations was unable to determine the host morphology due to their high L_{nuc}/L_{host}. It was considered that these objects presented an ideal opportunity to investigate the advantages to be gained by confining the nuclear flux to within the central $0.5 \rightarrow 1''$ with active optics. The remaining two objects, on the contrary, were specifically chosen because the model fits from the previous analysis were regarded as secure, with a strong preference being shown for one particular host morphology. It was hoped that a comparison with the new higher resolution observations would either confirm the existing modelling results, or highlight any possible problems or biases which were present in the previous analysis.

4.7.2 The Observations

The new K-band observations were made on 5-7th April 1997 using the IRCAM 3 infrared camera on the 3.9m United Kingdom Infrared Telescope (UKIRT) on Mauna Kea, Hawaii. IRCAM 3 is a 256×256 InSb array which was operated in 0.281 arcsec

Source	Type	z	V	Time (mins)	Comment
0923+201⋆	RQQ	0.190	15.8	72	Good
0953+415⋆	RQQ	0.239	15.6	72	Good
1004+130⋆	RLQ	0.240	15.2	72	Good
1217+023	RLQ	0.240	16.5	72	Good
1012+008	RQQ	0.185	15.9	72	Electronic Noise
1048−090⋆	RLQ	0.345	17.0	72	Pointing Drift
1202+281	RQQ	0.165	15.6	36	Low signal-to-noise
1302−102	RLQ	0.286	15.2	72	Pointing Drift
1307+085	RQQ	0.155	15.1	72	Cloud

Table 4.5: The sample. The first six objects listed are taken from the original K–band imaging sample (Taylor *et al.* 1996). The final three objects have been taken from the sample imaged by Bahcall *et al.* (1994). Column five lists the on-source integration time for each object. Column six details any problems experienced with the images (see text). Redshifts and V magnitudes have been taken from Taylor *et al.* (1996) and Bahcall *et al.* (1997) respectively.

pixel^{-1} mode, providing a field-of-view of approximately 70″. The observing run for this project was among the first ever to make full use of the tip-tilt active optics system, which was installed on UKIRT in October 1996. The following observational procedure was used.

Each object was observed using a 4-point jitter pattern with each point consisting of 3 minutes of integration broken into 18 co-adds of 10-seconds duration. This combination was chosen specifically in order to provide unsaturated but background-limited images. It was originally envisaged that this 12-minute jitter pattern would be repeated six times for each object, providing a total of 72 mins of on-source integration. Despite problems focusing the telescope on the first night (see Section 4.7.4), coupled with the loss of 3 hours due to partial cloud-cover on the third night, this objective was realised for eight of the nine objects (Table 4.5). When using the tip-tilt system on UKIRT it

is necessary to observe a bright enough guide-star such that the wavefront sensors can detect sufficient photons quickly enough, to correct for the short-timescale variations of the atmospheric distortions. The other criterion that must be met is that the guide-star and target must be close enough on the sky to lie within the system's isoplanic angle in order to achieve the best possible correction for the target object. Considering the desirability in host galaxy observations of confining the quasar nuclear flux to as small an angular extent as possible, it was decided that the quasar nucleus itself would be used as the guide-star in an attempt to obtain the best possible resolution from the tip-tilt correction. In order to provide high signal-to-noise measurements of the IRCAM 3 PSF, and to calibrate our photometry, observations of standard stars were taken before and after the completion of each jitter pattern.

4.7.3 Reduction

The first step in the reduction process was the dark-frame subtraction of the individual 3-minute integrations for each object. Two separate dark-frames were taken for each object observed, before commencing the first integration, and then again after 36 minutes of the total 72-minutes of integration. The use of two dark-frames allowed each of the twenty four object frames to be dark-frame subtracted using the most contemporary measure of the instrument dark current. Concurrent sky flat-fields were produced for each object by a process of median filtering the individual 3-minute integrations. The reason for the adoption of this technique was to overcome the rapid variability of the IRCAM 3 flat-field, and, considering the tight observing schedule, to save the large amount of time required to frequently observe the flat-field alone. As a result of the considerable angular extent of the host galaxies ($\simeq 15''$) compared with the IRCAM 3 field-of-view, this had to be performed on a quadrant-by-quadrant basis. As a result of the jitter pattern, each quadrant of the array looked at blank sky for 3/4 of the total integration time for each object. These frames could be median filtered without fear of contamination from host galaxy light. The four flat-field quadrants produced in this fashion were then added together and normalized to unit median to produce the final flat-field.

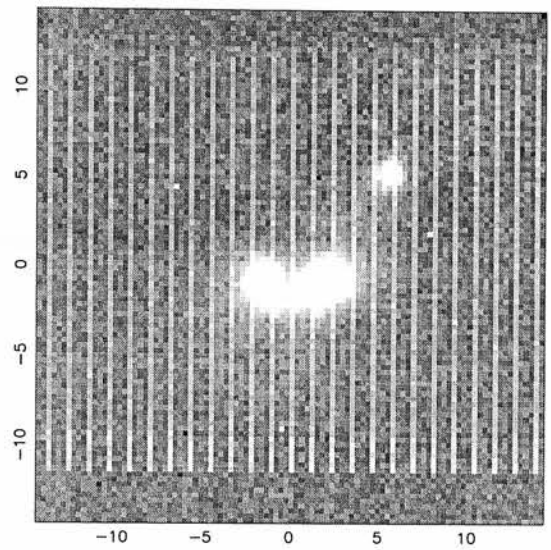

Figure 4.10: A 3-minute integration of 1012+008 showing the bands of spurious electronic noise which affected many of the images from this observing run.

After flat-fielding the individual 3-minute frames were corrected for the known non-linearity of the IRCAM 3 detector above 8000 counts, using the prescribed formula:

$$T = M\left[1 + 3.3 \times 10^{-0.6} M\right] \tag{4.6}$$

where T & M are the true and measured counts respectively. It was not necessary to make this correction prior to the construction of the flat-fields, since only the quasar nuclei produced ≥ 8000 counts, and were excluded from the median filtering procedure. After the flat-fielding and linearity corrections the individual object frames were re-registered and stacked to produce the final deep images for analysis.

4.7.4 Image Defects

During the reduction process it became apparent that there were various problems with the final mosaiced images of the majority of the quasars observed. Throughout the observing run there had been great difficulty with a constant drift in the telescope focus, which required to be manually re-set at thirty minute intervals. The result of this was that the FWHM of the individual 3-minute integrations was reduced to $\simeq 0.7''$. With the inevitable errors introduced by the re-registering and stacking of the individual

frames to produce the final deep images, it was expected that the final FWHM would be further degraded to $\simeq 0.8''$. However, upon investigation of the completed mosaics it became clear that for 2 of the 9 quasars studied (1048-09 & 1302-102), the final FWHM was much larger than was anticipated, lying in the region of $1 \rightarrow 1.2''$. The reason for this blurring of the final images was revealed by further investigation of the individual 3-minute integrations for these objects. As was mentioned in Section 4.7.2, the pointing for these observations made use of the quasar nucleus itself as the guide-star. Although the quasar nuclei were theoretically bright enough for this to be possible, in practice this turned out not to be the case. During the 3-minute integrations the pointing had wandered around sufficiently to produce the described image degradation. Given the need to accurately de-couple the relative nuclear and host galaxy light contributions, the images of these two source where therefore unsuitable for analysis with the two-dimensional modelling code.

In combination with the problems experienced with telescope focusing and guidance, all of the images were affected to some extent by bands of spurious electronic noise. The source worst effected by this problem was 1012+008, an example 3-minute integration of which is shown in Fig 4.10. Due to the fact that no separate flat-field observations were made during this observing run (see Section 4.7.3) the random structure present in the electronic noise, coupled with its appearance in all of the separate 3-minute integrations of 1012+008, made it impossible to construct a reliable flat-field for this object, and it is was therefore dropped from the modelling process.

The data for two more of the nine objects listed in Table 4.5 were of insufficient quality to successfully model the underlying host galaxies. In the case of 1202+281 this was simply due to the low integration time acquired (36 minutes) not allowing a good signal-to-noise detection of the host over a sufficiently large radius to reliably determine the scalelength. The final object to be rejected, 1307+085, was a victim of the partial cloud-cover experienced on the third night of the observing run. Once again the use of concurrent sky flat-fields made it impossible to accurately flat-field the images of this object.

The result of all of the technical difficulties experienced during this observing run

was that only four of the nine objects imaged actually yielded data of the high quality required by the two-dimensional modelling code. While this is obviously disappointing, it was fortuitous that the remaining four objects still allowed the main objectives of the run to be achieved. Three of the objects were allocated unreliable fits from the previous K–band imaging, and therefore presented a good test of the improvements to be gained from the increased resolution of tip-tilt imaging. In addition to this, the final object (1217+023), was considered to have a reliable model fit and therefore gave an opportunity to see if the modelling of the new data was consistent, or otherwise, with the previously obtained results.

4.7.5 The IRCAM3 Point Spread Function

A major drawback with the study of quasar host galaxies from the ground is the unstable nature of the instrument PSF. As was mentioned in Section 4.7.2, standard stars were observed before and after each individual jitter pattern, to provide measures of the PSF as close in time as possible. However, considering that the final deep quasar images are stacks of between 12 and 24 individual 3-minute frames, in some cases taken taken over two nights, there is no guarantee that any one of the PSF observations will be a good match to the final mosaic. In an effort to overcome this problem, further tip-tilt PSF observations were included from a more recent UKIRT observing run (Percival *et al.* 1999), producing a library of 65 high signal-to-noise PSF observations. The procedure for choosing the correct PSF to match a particular quasar mosaic was as follows.

Each of the 65 PSFs were normalized and tested against the core (central nine pixels) of the quasar image via the χ^2 statistic. The five individual PSFs which proved to be the best match to the quasar core were selected and allocated initially equal weighting, before being stacked to produce a composite PSF. The Downhill Simplex minimization routine described in Section 3.3.3 was then used to fix the optimal weighting to produced the minimum χ^2 between the composite PSF and the quasar core. The PSF produced at the end of this rather elaborate process was invariably a significantly better match, in terms of χ^2, than any one of the individual PSF observations. It is reassuring to note

Source	Type	Host	$\Delta\chi^2$	$r_{1/2}$ / kpc	K_{host}	K_{nuc}	b/a	L_{nuc}/L_{host}
0923+201	RQQ	Elliptical	27	8.6	13.98	12.48	0.87	3.98
0953+415	RQQ	Elliptical	14	8.4	15.18	12.72	0.73	9.62
1004+130	RLQ	Elliptical	276	8.5	13.92	12.90	0.85	2.55
1217+023	RLQ	Elliptical	187	7.7	14.13	13.62	0.84	1.59

Table 4.6: Results of the two-dimensional modelling of the IRCAM 3 data. Column 3 indicates the morphological type of the best fitting host galaxy. Column 4 gives the difference in χ^2 between the elliptical and disc host galaxy fits. Column 5 details the effective radius of the host galaxy ($r_e = r_{1/2}$ for ellipticals). Columns 6 & 7 list the integrated apparent magnitudes of the host and nuclear component respectively. Column 8 gives the axial ratio (b/a) for the best fit host. Column 9 converts the figures of columns 6 & 7 into a nuclear:host ratio.

that of the five best individual PSF matches selected, one was always the closest in time to the quasar observations. However, it is also worth noting that, in the majority of cases the best-fitting individual PSF was not observed the closest in time to the quasar observations, emphasizing that even with tip-tilt correction, the inherent variability of ground-based seeing is still the dominant factor to be considered in selecting the best PSF.

4.7.6 Results

The results from the two-dimensional modelling of the four quasars which did not suffer from image degradation are listed in Table 4.6. Surface-brightness profiles extracted from the two-dimensional model fits are shown in Fig 4.12 and Fig 4.13. Also shown in Table 4.7 are the results from the modelling of the new HST R–band imaging of the four objects. These results are identical to those presented in Section 4.1 and are repeated here simply for ease of comparison.

Source	Type	Host	$\Delta\chi^2$	$r_{1/2}$ / kpc	R_{host}	R_{nuc}	b/a	L_{nuc}/L_{host}
0923+201	RQQ	Elliptical	1733	8.2	17.22	15.66	0.98	4.23
0953+415	RQQ	Elliptical	91	7.1	18.15	15.19	0.86	15.39
1004+130	RLQ	Elliptical	501	8.2	16.93	15.02	0.94	5.78
1217+023	RLQ	Elliptical	2359	9.9	17.31	16.32	0.80	2.49

Table 4.7: Results of the two-dimensional modelling of the HST data. Column 3 indicates the morphological type of the best fitting host galaxy. Column 4 gives the difference in χ^2 between the elliptical and disc host galaxy fits. Column 5 details the effective radius of the host galaxy ($r_e = r_{1/2}$ for ellipticals). Columns 6 & 7 list the integrated apparent magnitudes of the host and nuclear component respectively. Column 8 gives the axial ratio (b/a) for the best fit host. Column 9 converts the figures of columns 6 & 7 into a nuclear:host ratio.

4.7.7 Host Morphologies

All four of the quasars are found to lie in elliptical host galaxies, just as they were from the HST imaging, despite 0923+201 and 0953+415 being radio-quiet. The morphological decision for 0953+415 is the least clear-cut, formally only 2σ, as expected considering that it has by far the largest L_{nuc}/L_{host}. As well as being in agreement with the HST modelling results, the morphology decisions for the new K-band images of 0953+415 and 0923+201 are fully consistent with the predictions of Taylor *et al.* (1996) that luminous RQQs are likely to have early-type host galaxies, with 0953+415 and 0923+201 being the most optically luminous RQQs in the full HST sample.

4.7.8 Scalelengths

An investigation of Tables 4.6 and 4.7 shows that the best-fit scalelengths from the two independent sets of data are in excellent agreement. In both wave bands the hosts are found to have large, and very similar scalelengths, spanning a range of less than 3 kpc.

The general result that these quasars are hosted by large galaxies with scalelengths of $r_e \simeq 10$ kpc is consistent with the conclusions of Taylor *et al.* (1996). However,

with the exception of 0953+415, the scalelength results presented here are not in good agreement on an individual object-by-object basis, differing by more than a factor of two in all cases. The reason for this most likely lies in the fact that, again with the exception of 0953+415, the best-fitting L_{nuc}/L_{host} from the modelling of the IRCAM 1 data are $2 \rightarrow 4$ times greater than those found using IRCAM 3. Given that an overestimate of the unresolved nuclear component will artificially lower the central surface-brightness of the best-fitting host-galaxy model, the requirement to match the host-galaxy flux at large radii will therefore lead to an inevitable overestimate of the host-galaxy scalelength. This conclusion is strengthened by a comparison of the HST scalelength results with the corresponding figures from Taylor *et al.* for all 33-objects in the HST sample. In the majority of cases there is a consistent bias in the previous K–band modelling towards finding large galaxies with a low central surface-brightness. The results presented in this chapter therefore point to a likely bias in the scalelengths previously determined for this sample, due simply to the need for sub-arcsec resolution to reliably de-couple the host and AGN components. In the absence of new tip-tilt imaging of the full HST sample, this clearly has implications for the accurate determination of the $R-K$ colours of the host galaxies. The adopted solution to this problem is fully described in Section 4.8.

If viewed in isolation it could appear of some concern that the best-fit scalelengths of all four host galaxies should be so similar, given that three of them have identical redshifts. At first sight this would raise the possibility of some area of the modelling, most likely a PSF artifact, unfairly biasing the determination of the host-galaxy scalelengths. However, this possibility can be firmly rejected for a number of reasons. Firstly, during the testing of the modelling code (Section 3.4) there was no such bias detected, with the code successfully discriminating between scalelengths in the range $5 \rightarrow 20$ kpc. Secondly, a comparison of the new K–band scalelength results with those from the HST R–band imaging shows the two to be in impressively close agreement, considering that they were independently derived from separate data-sets. The close agreement between the optical and infrared scalelengths derived for these four objects provides further reassurance that there is no correlation between scalelength and redshift, given that Fig 4.11 shows that no such correlation exists in the scalelengths determined for

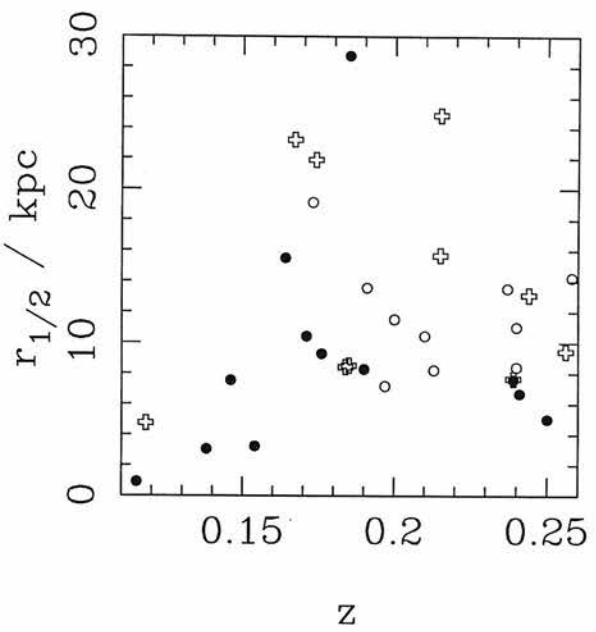

Figure 4.11: The $r_{1/2} - z$ distribution of the best-fitting host models of the RG (crosses), RQQ (filled circles) and RLQ (open circles) sub-samples.

the full HST sample (SR, p=0.52).

4.7.9 Host Luminosities

The integrated absolute K–band magnitudes of the four best-fitting host galaxy models are presented in Table 4.8. The absolute magnitudes have been calculated using k-corrections assuming a flat spectral index $\alpha = 0.0$ ($f_\nu \, \alpha \, \nu^{-\alpha}$). The calculation of the host luminosities in terms of $L^\star$ has been performed taking $M_K^\star = -24.6$ (Gardner *et*

Source	M_K	$L/L^\star$
0923+201	−26.21	4.3
0953+415	−25.48	2.2
1004+130	−26.75	7.1
1217+023	−26.54	5.9

Table 4.8: Luminosities for the four best-fitting host galaxies. Column 2 lists the absolute integrated K–band magnitudes. Column 3 restates the absolute magnitudes in term of $L^\star$.

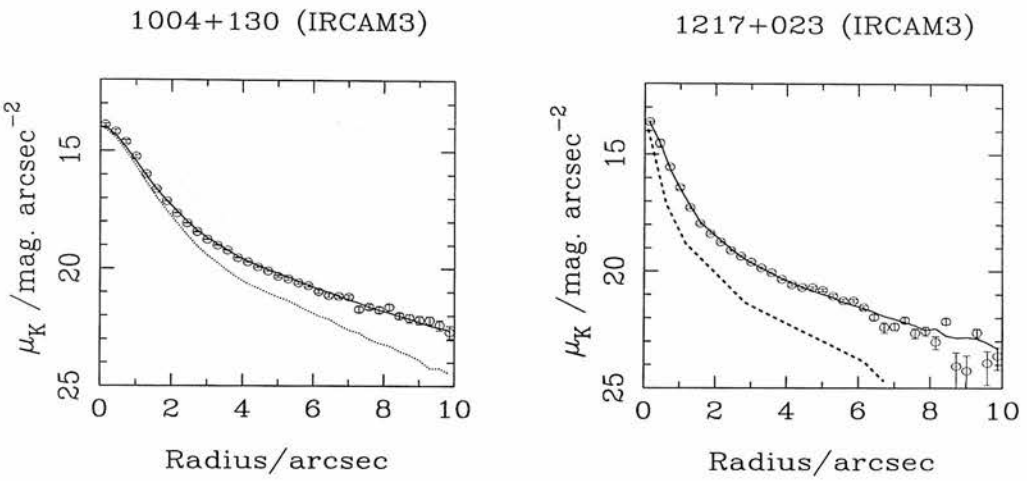

Figure 4.12: The surface-brightness profiles resulting from the two-dimensional modelling of two radio-loud quasars. Shown in the figure are the data (open circles), the best-fit model (solid line) and the best-fit nuclear component (dashed line).

al. 1997). Again it can be seen that these results confirm the findings of the HST R–band imaging, and the previous K–band imaging (Taylor *et al.* 1996), that the quasar hosts are all luminous galaxies with $L \geq 2L^*$. The fact that in this small group of objects the RLQs are substantially more luminous than the RQQs should not be taken as significant since, 1004+130 and 1217+023 are found to be brighter than average for RLQs from the R–band modelling, while 0953+415 has the largest L_{nuc}/L_{host} in the entire 33-object sample.

4.7.10 Discussion

Although the scope of this observing project was curtailed to some extent by the difficulties highlighted in Sections 4.7.2 & 4.7.4, it has still clearly shown the benefits to be gained by tip-tilt imaging in the near-infrared. With the telescope focusing problems at UKIRT solved, the active-optics system was successfully used to study more powerful quasars at $z \simeq 0.4$ in two subsequent observing runs in September 1997 and May 1998 (Percival, Miller, McLure & Dunlop 1999). In retrospect, perhaps the most important result of this observing run, in the context of this thesis, was the discovery of the likely bias in the scalelength figures from the previous modelling of this sample. While not

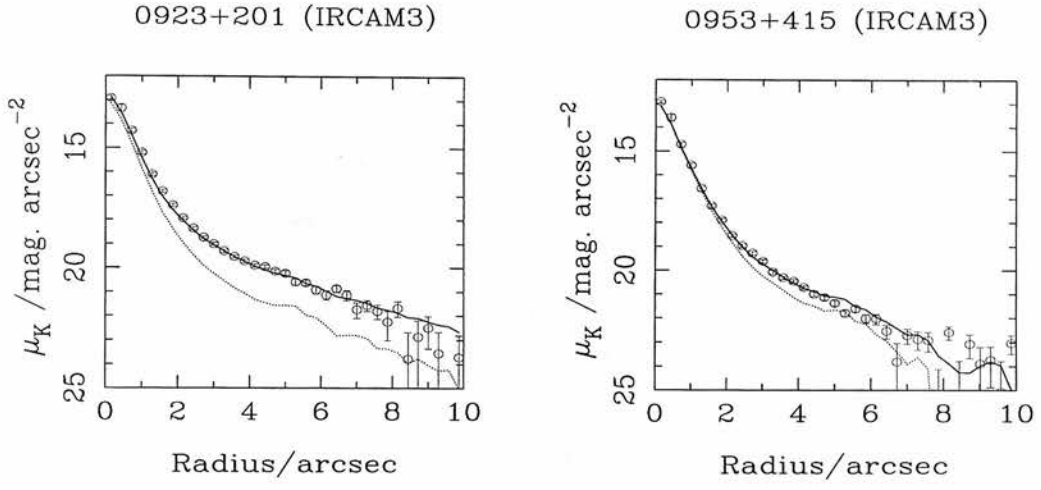

Figure 4.13: The surface-brightness profiles resulting from the two-dimensional modelling of two radio-quiet quasars. Shown in the figure are the data (open circles), the best-fit model (solid line) and the best-fit nuclear component (dashed line).

altering the central conclusions of the existing study, namely that the quasar hosts where large galaxies with $L \geq L_*$, it did allow the more accurate determination of the host galaxy colours discussed in the next section.

4.8 Colours

The original plan to produce the $R-K$ colours for the host galaxies was to simply use the integrated magnitudes from the HST and IRCAM 1 K–band model fits. However, it was quickly realised that there were two potentially serious problems associated with this strategy. The first of these concerns the determination of host morphology made from the two-dimensional modelling of the two data-sets. A comparison of the morphology determinations from the modelling of the new HST data (Tables 4.1 & 4.2), with those from the modelling of the K–band data (Taylor *et al.* 1996) shows that in a substantial number of case (13/33) the host was found to be a disc instead of the elliptical determination from the new HST modelling, although 8/13 of these cases were actually labelled as unreliable morphology determinations by Taylor *et al.* (1996). The problem posed by this is apparent when it is considered that the disc fits to the

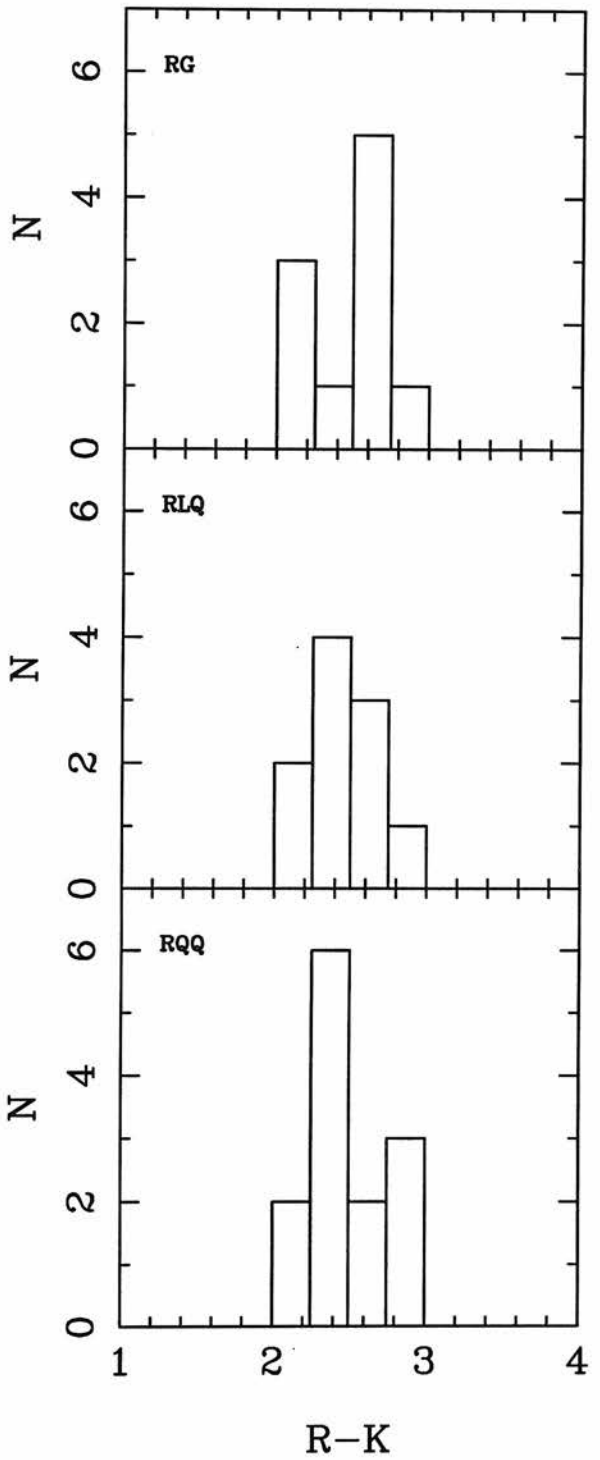

Figure 4.14: The rest-frame $R-K$ colours for the three host galaxy sub-samples. The three sub-samples can be seen to be consistent with each other, tightly distributed around a value of $R-K \sim 2.5$.

K–band data where $0.5 \rightarrow 1.0$ magnitudes fainter than the equivalent elliptical fits.

The second problem encountered in the host colour determination was the bias towards large scalelengths in the existing K–band modeling revealed by the tip-tilt imaging reported in the last section. Given that the integrated luminosity of the standard de Vaucouleurs $r^{1/4}$ law is proportional to $I_{1/2}r_e^2$, it is clear that scalelength errors of the order of ≥ 2 could bias the determined integrated K–band luminosity. There are two possible causes for the discrepancies in morphology and scalelength determination between the previous K–band study and the results presented in this chapter for the new R–band HST imaging. The first of these is the possibility that the level of sky background counts in the K- and R–band images has been systematically over- and underestimated respectively, which would certainly have the effect of producing a bias towards more disc-like hosts in the infrared modelling. However, although this could explain the differences in the morphological results from the two studies, it would also have the effect of biasing the HST elliptical host-galaxy fits to much larger scalelengths than the K–band elliptical host fits, the opposite of what is seen. The most viable explanation of the different findings would appear to be that the $\sim 1''$ seeing and coarse spatial resolution ($0.62''$/pix) of the K–band observations has resulted in the systematic overestimation of the unresolved nuclear component.

In retrospect this is as expected, given that the K–band PSFs were selected for modelling on the basis that they matched the flux in the central few pixels of the quasar images, a region inevitably contaminated by considerable galaxy emission because of the large pixel size. The result of this procedure will be a bias towards selecting PSFs which have slightly larger FWHM than the actual quasar observations, which in turn will bias the modelling to overestimating the nuclear component, underestimating the host galaxy central surface-brightess, and consequently overestimating the host scalelength. This scenario also naturally explains the K-band bias towards disc fits, given that the overestimate of the unresolved nuclear contribution will prevent the modelling code from recognising the different behaviour of disc and elliptical galaxy models at small radii.

Supporting evidence for this line of reasoning comes from a comparison of the best-

fit quasar L_{nuc}/L_{host} obtained from the K–band imaging and the new R–band results presented here. For 9/13 RQQ, and 9/10 RLQ, the best-fit K–band L_{nuc}/L_{host} is actually greater than the equivalent R–band figure, the opposite of what is expected considering the higher contribution of the host galaxy to the total flux with increasing wavelength. The suspicion that this effect is simply caused by poor resolution is further strengthened from the fact that, for the four objects successfully modelled from the new tip-tilt observations, all four have best-fit L_{nuc}/L_{host} smaller than their R–band equivalents.

Short of obtaining an entirely new set of K–band observations for the whole HST sample it is impossible to fully account for this problem. However, several steps were taken to minimize its impact on the calaculated host galaxy $R-K$ colours. Firstly, it was decided that the K–band luminosities should be based on the best-fitting model with the same morphology as the equivalent HST result, in order to counter the suspected bias towards disc fits. Secondly, the $R-K$ colours should be based on $12''$ diameter aperture photometry performed on both the HST and K–band model fits. The reasoning behind this decision had two separate aspects to it. Firstly, the model flux measured inside a diameter of $12''$ should be a reliable estimate of the host galaxy luminosity in this region, irrespective of any error in the best-fit scalelength. Secondly, considering that at the median redshift of the sample ($z = 0.2$) a radius of $6''$ corresponds to ~ 25 kpc, it can be seen that the adoption of a $12''$ software aperture will include galaxy light out to an average of $r \simeq 2.5r_e$ (cf. Tables 4.1 & 4.2). The result of this is that the $R-K$ colours derived from a $12''$ diameter aperture will be both reliable, and still sensitive to $\simeq 75$ % of the host-galaxy flux.

The results of the host galaxy $R-K$ calculations are listed in Tables 4.9 & 4.10, with absolute $R-K$ histograms for the separate sub-samples shown in Fig 4.14. The absolute colours have been calculated assuming the usual cosmology ($H_0 = 50, \Omega_0 = 1$), and spectral indices of $\alpha = 1.5$ & $\alpha = 0.0$ for the R- and K–bands respectively. Due to the absence of large nuclear components in the radio galaxies, the colours derived for this sub-sample are the most accurate, with typical uncertainties of the order of $\simeq 0.15$ mag. The colours of the quasar hosts are somewhat more uncertain, with a typical error of $0.3 \rightarrow 0.5$ magnitudes.

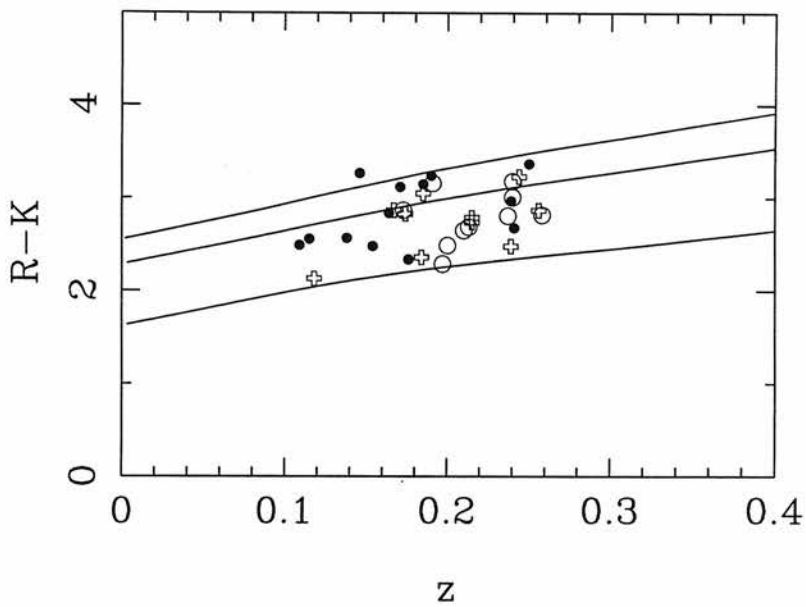

Figure 4.15: The apparent $R-K$ colours of the hosts (RGs = crosses, RLQs = open circles, RQQs = filled circles) plotted against redshift, compared with the colours predicted from simple k-correction of stellar populations with ages of 7, 10 and 13 Gyr (Guiderdoni & Rocca-Volmerange 1987). It is clear that the hosts of all 3 classes of powerful AGN have colours which are consistent with each other, and with that of mature stellar populations.

It is readily apparent from Fig 4.14 that the colour distributions of the three sub-samples are consistent with each other, with mean and median rest-frame colours of:

$$< R-K >= 2.48 \pm 0.05 \quad \text{median}=2.44 \quad \text{(All)}$$
$$< R-K >= 2.47 \pm 0.09 \quad \text{median}=2.56 \quad \text{(RG)}$$
$$< R-K >= 2.48 \pm 0.07 \quad \text{median}=2.46 \quad \text{(RLQ)}$$
$$< R-K >= 2.48 \pm 0.08 \quad \text{median}=2.41 \quad \text{(RQQ)}$$

In order to investigate the ages of the underlying stellar populations of the hosts galaxies, the apparent $R-K$ colours are compared with those predicted from k-correcting the 7, 10 and 13 Gyr stellar population models of Guiderdoni & Rocca-Volmerange (1987) in Fig 4.15.

Source	$M_R(host)$	$M_R(nuc)$	$(R-K)_{app}$	$(R-K)_{abs}$
RG				
0230−027	−23.55	-	2.08	2.16
0307+169	−23.96	−19.94	2.12	2.54
0345+337	−23.05	−19.63	3.62	2.88
0917+459	−24.20	−20.65	3.42	2.61
0958+291	−23.25	−21.70	1.94	2.74
1215+013	−22.85	−19.35	2.52	2.00
1215−033	−23.29	−17.87	2.56	2.11
1330+022	−23.70	−21.00	2.79	2.44
1342−016	−24.58	−18.35	2.56	2.58
2141+279	−24.09	−14.94	3.25	2.66
RLQ				
0137+012	−24.04	−23.53	2.82	2.44
0736+017	−23.58	−24.01	3.16	2.72
1004+130	−24.10	−25.70	3.01	2.66
1020−103	−23.36	−23.47	2.29	2.04
1217+023	−23.71	−24.40	3.18	2.83
2135−147	−23.37	−24.09	2.49	2.20
2141+175	−23.51	−24.52	2.69	2.41
2247+140	−23.80	−23.80	2.81	2.48
2349−014	−24.32	−24.00	2.87	2.59
2355−082	−23.62	−23.06	2.65	2.40

Table 4.9: Absolute magnitudes (M_R), and optical-infrared ($R-K$) colours of the best-fitting host galaxy and nuclear component for the RGs and RLQs. Columns 2 and 3 give the R-band absolute magnitudes (M_R) derived from the current modelling of the HST data, assuming a spectral index of $\alpha = 1.5$ (where $f_\nu \propto \nu^{-\alpha}$) for the galaxy and $\alpha = 0.2$ for the quasar. Columns 4 and 5 list the apparent and rest-frame $R-K$ colours of the host-galaxies respectively. The colours have been derived by combining 12-arcsec aperture R-band photometry from our HST-based models with the 12-arcsec aperture K-band photometry derived by Taylor *et al.* (1996), to minimize the uncertainty introduced by errors in constraining the galaxy scalelengths at K.

Source	$M_R(host)$	$M_R(nuc)$	$(R-K)_{app}$	$(R-K)_{abs}$
RQQ				
0052+251	−23.33	−24.39	2.48	2.29
0054+144	−23.62	−24.49	3.12	2.83
0157+001	−24.29	−23.70	2.84	2.57
0204+292	−23.30	−23.03	2.49	2.34
0244+194	−22.77	−23.24	2.34	2.07
0257+024	−23.32	−19.69	2.56	2.41
0923+201	−23.25	−24.57	3.24	2.96
0953+415	−22.82	−25.52	2.97	2.61
1012+008	−23.78	−23.95	3.15	2.11
1549+203	−22.26	−23.98	3.37	2.97
1635+119	−23.05	−21.54	3.27	2.42
2215−037	−23.52	−22.58	2.68	2.30
2344+184	−22.54	−20.30	2.57	2.36

Table 4.10: Absolute magnitudes (M_R), and optical-infrared ($R-K$) colours of the best-fitting host galaxy and nuclear component for the RQQs. Columns 2 and 3 give the R-band absolute magnitudes (M_R) derived from the current modelling of the HST data, assuming a spectral index of $\alpha = 1.5$ (where $f_\nu \propto \nu^{-\alpha}$) for the galaxy and $\alpha = 0.2$ for the quasar. Columns 4 and 5 list the apparent and rest-frame $R-K$ colours of the host-galaxies respectively. The colours have been derived by combining 12-arcsec aperture R-band photometry from our HST-based models with the 12-arcsec aperture K-band photometry derived by Taylor *et al.* (1996), to minimize the uncertainty introduced by errors in constraining the galaxy scalelengths at K.

It is striking how well the host galaxies are bracketed by the 7- and 13-Gyr models, with no objects predicted to be younger than 7-Gyrs at $z = 0.2$. Given that the look-back time to $z = 0.2$ is $\simeq 2$ Gyr, a figure which is relatively insensitive to adopted cosmology, Fig 4.15 shows that the host galaxies are consistent with being $9 \rightarrow 15$ Gyrs-old at $z = 0$, in good agreement with the ages typically determined for low-z ellipticals. Moreover, it can be seen that the predicted $z = 0$ colour of $R - K \simeq 2.5$ is perfectly consistent with the rest-frame host colours derived above. It is clear from this that the host galaxies of all three types of powerful AGN have optical-infrared colours consistent with old, passively evolving stellar populations.

Further, model-independent, support for this conclusion can be gained from a comparison of Fig 4.15 with the $R - K$ versus z plot of objects detected in the K-band survey of Glazebrook *et al.* (1995), which reached a depth of $K \simeq 17.3$. The host galaxy $R - K$ colours presented here track well the red envelope displayed by these K-band selected galaxies at comparable redshifts.

The host galaxy colours presented in this section are the first clear evidence that the hosts of all AGN, not just radio galaxies, have ages which are comparable to the oldest ellipticals known. The inevitable conclusion from this is that these galaxies, or at least their stellar populations, must have formed at high redshift ($z \geq 3$), a theme which is revisited in Chapter 6. The fact that the $R - K$ colours are so similar to passive ellipticals forces the further conclusion that any star-formation associated with AGN activity must either be dust enshrouded, confined to tidal features masked from the modelling, or possibly just sufficiently restricted to the nuclear regions of the host, in which case the flux would be attributed to the unresolved nuclear component. Large-scale secondary star-formation, widely distributed throughout the host galaxies is effectively ruled out by these results.

4.9 Comparison with Brightest Cluster Galaxies

Considering that the two-dimensional modelling results reported in this chapter indicate that the host galaxies of powerful AGN are both large and luminous, it is therefore of

interest to compare their properties with those of the Brightest Cluster Galaxies (BCG), the largest and most luminous galaxies known. A recent indication of the characteristic R–band luminosity of cluster galaxies, comes from the determination of the luminosity function for a sample of 20 Abell clusters in the redshift range $0.06 < z < 0.25$ by Gaidos (1997). The result of this study was that the cluster galaxy luminosity function could be well described by a Schechter function with a characteristic absolute magnitude of $M_R^* = -22.63 \pm 0.11$. A comparison with the mean absolute magnitude determined for the AGN host galaxies ($M_R = -23.5$) confirms that the hosts of powerful AGN typically have luminosities more than twice that of an L^* cluster galaxy, demonstrating that they are directly comparable to the very bright end of the cluster galaxy population. This conclusion is in good agreement with the findings of the K–band imaging of the HST sample, with Taylor *et al.* finding the mean luminosity of the host galaxies to be $< M_K >= -25.5 \pm 0.1$, a figure not inconsistent with the value of $< M_K = 25.9 \pm 0.3$ found for first-ranked cluster galaxies by Thaun & Puschell (1989).

Taken together, the K- and R–band results show that the luminosities of the host galaxies of the HST sample are comparable to those of galaxies populating the very bright end of the cluster galaxy luminosity function. An interesting question arising from this is to ask whether the host galaxies are directly comparable to first-ranked cluster galaxies, or whether they are drawn from lower down the cluster luminosity function. Strong circumstantial evidence that host galaxies are directly comparable to first-ranked cluster galaxies comes from a comparison of the host-galaxy Kormendy relation determined in this chapter, with that found for cD galaxies by Hamabe & Kormendy (1987) in the B–band:

$$\mu_{1/2} = 2.94 \log_{10} r_{1/2} + 20.75 \tag{4.7}$$

If a typical elliptical galaxy colour at $z = 0.2$ of $B - R = 2.4$ is assumed (Fukugita *et al.* 1995), then the Kormendy relation for all 33 objects in the HST sample presented in Section 4.5 becomes:

$$\mu_{1/2} = 2.90 \log_{10} r_{1/2} + 20.75 \tag{4.8}$$

which can be seen to be in excellent agreement with the Hamabe & Kormendy result.

In order to pursue the use of the Kormendy relation further, it was decided to compare the results presented in this chapter with those of the study of 83 Abell clusters by Schneider, Gunn & Hoessel (1983). An interesting feature of the Schneider, Gunn & Hoessel study is that they produced Kormendy relations for the first-, second- and third-ranked cluster galaxies, which are presented in Table 4.11 along with the corresponding mean scalelength figures.

There are two noteworthy aspects to the results presented in Table 4.11. Firstly, it can be seen that the Kormendy relations for the first-, second- and possibly third-ranked cluster galaxies are consistent with the Kormendy relation determined for the host galaxies in Section 4.5 (it is unclear from Schneider, Gunn & Hoessel (1983) what the errors on the Kormendy relation slopes actually are). This of course implies that the striking agreement with the cD-galaxy Kormendy relation noted above does not necessarily mean that the AGN host galaxies are exclusively drawn from first-ranked cluster galaxies. This point would seem to be strengthened by the mean scalelength results of Schneider, Gunn & Hoessel, which indicate that the AGN host-galaxy scalelengths are more comparable with second-ranked cluster galaxies than first-ranked. However, there is an added complication involved, in that, the 83 Abell clusters studied by Schneider, Gunn & Hoessel cover Abell classes $0 \rightarrow 4$, with a strong possibility that the scalelength figures are biased by the extremely large galaxies found at the centres of Abell clusters of class 3 & 4.

In an attempt to overcome this problem it was decided to use the results from a later paper in the same series of cluster studies (Hoessel & Schneider 1985), from which it was possible to construct a sample of 51 first-ranked cluster galaxies within the same redshift range as the HST sample ($0.1 < z < 0.26$), which could also be further sub-divided into their separate Abell classes. The application of the KS test to the scalelength distributions of the AGN host galaxies, and the 14 first-ranked cluster galaxies from Abell clusters of class 0 & 1, shows that the two are not significantly different (p=0.22). However, the extension of the Abell sample to include the first-ranked galaxies of Abell class 2 clusters (15 objects), shows the two distributions to

be different at the 2σ level (p=0.011). The suspicion that the mean scalelength figures presented in Table 4.11 are biased by the galaxies from the richest Abell clusters is confirmed by the lower mean scalelength for Abell classes 0 & 1 of $< r_e >= 20.9 \pm 4.7$, which is consistent with the mean AGN host-galaxy figure of $< r_e >= 12.2 \pm 1.0$, thanks mainly to the large range of scalelengths found by Hoessel & Schneider.

Considering the much smaller error on the mean host-galaxy scalelength, compared with the corresponding figure for the first-ranked cluster galaxies in Abell classes 0 & 1, an obvious question to ask is whether the wide range of scalelengths apparently displayed by the cluster galaxies is associated with some problem in the profile fitting used by Hoessel & Schneider, or whether it is an intrinsic feature of cluster galaxies which sets them apart from the AGN hosts. So that any sources of possible systematic error could be eliminated as much as possible, HST WFPC2 images of four Abell clusters with similar redshifts to the objects in the HST sample were retrieved from the HST archive facility [1]. Following the production of reduced images of comparable signal-to-noise to the host galaxy images, the four brightest galaxies in each cluster were identified and modelled in identical fashion to the AGN host galaxies. The results of the elliptical model fits to these 20 galaxies are presented in Table 4.12 & Table 4.13. The mean scalelength of all 20 HST cluster galaxies modelled is $r_{1/2} = 28.22 \pm 5.61$, more than a factor of two greater than found for the host galaxies, but still not formally inconsistent. An examination of Tables 4.12 & 4.13 clearly shows that the brightest two galaxies in each of the two richest (class 4) clusters are biasing the mean scalelength. If these four galaxies are excluded, the mean scalelength figure is reduced to $r_{1/2} = 17.33 \pm 2.59$, which differs from the mean AGN host-galaxy scalelength by less than 2σ, a result confirmed by the application of the KS test which returns a probability of p=0.065. The use of an identical procedure to model the cluster galaxies also has the advantage of providing integrated luminosities which can be compared to the derived host-galaxy magnitudes, with minimum danger of biasing due to systematic errors. Even with the inclusion of the four outlying, class 4, cluster galaxies, the mean absolute R–band magnitude is $M_R = -23.32 \pm 0.25$, some 0.2 magnitudes fainter than the average host galaxy value.

[1] http://archive.stsci.edu

Rank	Kormendy Relation	$< R_e >$
1	$\mu_{1/2} = 3.2 \log r_{1/2} + 18.3$	28.2 ± 1.1
2	$\mu_{1/2} = 3.3 \log r_{1/2} + 18.7$	8.5 ± 1.1
3	$\mu_{1/2} = 3.7 \log r_{1/2} + 18.7$	5.5 ± 1.1

Table 4.11: The results of the Schneider, Gunn & Hoessel study of the first-, second- and third-ranked galaxies in a sample of 83 Abell clusters. The results have been converted to the cosmology used throughout this thesis, and an elliptical galaxy colour of $g_r - R_c = 0.22$ assumed to convert from the original Gunn-r filter to the standard Cousins-R filter (Fukugita *et al.* 1995).

In summary, the evidence presented in this section shows that, in terms of luminosity and Kormendy relation, the host galaxies of powerful AGN appear to be indistinguishable from the brightest cluster galaxies. The evidence that AGN host galaxies have characteristic sizes which are directly comparable to first-ranked cluster galaxies is more ambiguous. A combination of the results from the study of Hoessel & Schneider, and the modelling of the HST cluster data, would suggest that in all but a few cases (eg. 1012+008, 0157+001, 2349-014, 0917+459) the host-galaxy scalelengths are typically a factor of two smaller than first-ranked cluster galaxies in the richest clusters (Abell $2 \rightarrow 4$). However, the same results also show that there is no strong evidence to suggest that the AGN host galaxies are not drawn from the same population as the first-ranked galaxies of poorer Abell clusters, of class 0 & 1. This result is of particular interest in reference to the FRII radio galaxy sub-sample, since it is traditionally thought that FRII sources avoid cluster environments (eg. Prestage & Peacock 1988). The question of radio galaxy environments has a crucial bearing on possible models for their evolution in the redshift range $0 < z < 1.0$, a subject which is investigated in Chapter 6.

In order to come to any definite conclusions on the environments of the quasars and radio galaxies in the HST sample, it will be necessary to reliably identify which of the apparent companion objects actually lie at the AGN redshifts. The question of how this may be achieved is discussed at the end of Chapter 6.

	Abell	Class	Abell	Class	Abell	Class
	2390	1	1689	4	2218	4
Galaxy	r_e/kpc	M_R	r_e/kpc	M_R	r_e/kpc	M_R
1	27.8	−24.52	75.8	−25.33	100.5	−25.51
2	21.2	−23.14	59.0	−24.70	51.9	−24.54
3	12.1	−22.99	18.7	−23.62	35.7	−23.68
4	4.1	−22.21	7.6	−23.50	28.8	−23.29

Table 4.12: The model results for the four brightest galaxies in three of the clusters obtained from the HST archive. The redshifts of the clusters are 0.23, 0.175 & 0.171 respectively. The images of A2390 and A1689 were taken through the F814 (I–band) filter, while the image of A2218 was taken through the F702W (wide R) filter. The conversion between I- and R-magnitudes has been performed assuming $R - I = 0.8$ (Fukugita *et al.*). The final reduced images had signal-to-noise comparable to the HST host galaxy data.

	Abell	Class	Abell	Class
	0118	0	0103	0
Galaxy	r_e/kpc	M_R	r_e/kpc	M_R
1	30.5	−22.65	24.9	−23.62
2	25.4	−22.50	3.4	−22.74
3	16.6	−21.47	7.6	−22.69
4	5.2	−21.14	7.6	−22.69

Table 4.13: The model results for the four brightest galaxies in the two class 0 Abell clusters obtained from the HST archive. The redshifts of the clusters are 0.11 & 0.19 respectively. The images of both clusters were taken through the F702W (wide R) filter. The conversion between I- and R-magnitudes has been performed assuming $R - I = 0.8$ (Fukugita *et al.*). The final reduced images had signal-to-noise comparable to the HST host galaxy data.

4.10 Interactions

It is often claimed in the literature (eg. Smith *et al.* 1986, Hutchings & Neff 1992, Bahcall *et al.* 1997) that morphological disturbance is a common feature of the host galaxies of powerful AGN. At first sight, the new R–band images presented in Appendix B show a relatively low occurrence of morphological disturbance, with only three objects (1012+008, 2349-014 & 0157+001) undergoing obvious, large-scale, interactions. However, as can be seen from the model-subtracted images, the removal of the best-fitting axisymmetric model for each host galaxy does reveal the presence of peculiarities such as excess flux, tidal tails and close companions, at lower surface-brightness levels. It is tempting to conclude from this that many of these AGN may have been triggered into action by recent interaction with companion objects. However, the true significance of the levels of interaction seen in the AGN host galaxies can only judged by comparison with an equally detailed investigation of the morphologies of a control sample of comparable, inactive galaxies. It was decided that the sample of twenty brightest cluster galaxies taken from the HST archive forms such a control sample.

With the range of redshifts covered by the four Abell clusters it was possible to construct 19 object pairs, consisting of one of the HST sample paired with a suitable control, drawn from the 20 cluster galaxies. Model-subtracted images of each of the galaxy pairs were then accessed in a blind test for the occurrence of four possible indicators of disturbance or interaction, i.e:

- Residual tidal/spiral arm features, Yes/No?
- Residual asymmetric flux, Yes/No?
- Residual symmetric flux, Yes/No?
- Companion object inside 10″ radius, Yes/No?

where it was not known, either the identity of the AGN, or which of the two objects in each of the pairs was active. The results of this process are shown in Table 4.14.

The one clear result of this test is that, taken as a group, the active galaxies of the

Object Type	Tidal/Spiral	Asymmetric Flux	Symmetric Flux	Companion
Active	5	8	5	7
Inactive	0	10	7	9

Table 4.14: The results of the blind test to determine any difference in the prevalence of features indicative of interaction or disturbance in the AGN sample (active) compared to inactive galaxies, using 20 BCG as a control sample (inactive). See text for description.

Object Type	Tidal/Spiral	Asymmetric Flux	Symmetric Flux	Companion
RQQ	6	5	1	2
RLQ	1	6	2	4
RQQ	0	4	2	3

Table 4.15: The results of the blind test to determine if any differences exist in the occurrence of features indicative of interaction or disturbance between the AGN sub-samples. See text for description.

HST sample display a greater occurrence of tidal/spiral arm features in their model-subtracted images than the control sample. There no suggestion that there is any significant difference between the two samples from the other three indicators tested for. It is noteworthy however, that of the six occurrences of tidal/spiral arms, only one of these (2349-014) is a radio-loud object. To test whether or not this indicates a inherent difference between the radio-loud and radio-quiet AGN, the blind test was repeated for all 33 HST objects, without control galaxies, but still keeping the identity of each AGN secret, in order to prevent any subconscious bias. The results of this test are presented in Table 4.15.

There are several features of the results presented in Table 4.15 which are worthy of comment. Firstly, it can be seen that there is no significant difference indicated between the RG and RLQ sub-samples, in keeping with much of the results presented in this chapter as a whole. Secondly, it would initially appear that there is a significant difference between the radio-loud objects and the RQQ sub-sample in terms of the occurrence of tidal/spiral arm features. However, an examination of which of the RQQs

are contributing to this result shows that four of them are the objects which have combined disc/bulge model fits. Therefore, if the comparison is restricted to include only those RQQs with single-component elliptical host galaxies, this apparent difference disappears. The results of these blind comparison tests would seem therefore, to support two separate conclusions. Firstly, the finding that there are no detectable differences between the elliptical AGN host galaxies and the BCG control sample provides further evidence that these two classes of object are directly comparable. Secondly, the apparently higher rate of occurrence of tidal/spiral arm features in the RQQ sub-sample is only the result of the previously determined fact that a minority of RQQ host galaxies, two of which are not actually true quasars, have substantial disc components, and is not a result of some inherent difference in interaction rates between radio-quiet and radio-loud objects.

4.11 Comparison with results in the Literature

A substantial number of the 23 quasars featured in the HST sample have been recently studied by a number of different authors, using both the HST and ground-based imaging. Considering that the host magnitude should be a reasonably well determined parameter, even with the wide variety of analysis methods employed, it was thought worthwhile to perform a comparison between the results of the different studies, and the results presented in this here. All host magnitudes have been converted to their equivalent apparent V-magnitude for ease of comparison, and are listed in Table 4.16.

4.11.1 Bahcall *et al.*

The host galaxy magnitudes in Table 4.16 have been taken from the final paper in the series published from the study of 20 powerful quasars in the redshift range $0.09 < z < 0.29$ (Bahcall *et al.* 1997). Given that magnitudes were quoted for two-dimensional fits using both disc and elliptical models, the values listed in Table 4.16 are those for the elliptical fits, to allow a fair comparison with the new R–band HST results. The general agreement between the host magnitudes for the eight quasars in common between the

	This Work	Bahcall	McLeod	Boyce	Kotilainen
source	m_v	m_v	m_v	m_v	m_v
0137+012	18.0	-	-	18.0	-
0736+017	16.9	-	-	-	17.2
1004+130	17.7	17.4	17.8	-	-
2135−147	18.0	17.9	-	-	-
2349−014	16.7	16.6	-	-	-
0052+251	17.5	17.0	17.4	-	-
0054+144	17.4	17.6	-	-	-
0157+011	16.4	-	16.6	-	-
0923+201	18.0	17.9	17.8	-	-
0953+415	19.0	18.6	18.3	-	-
1012+008	17.4	17.4	16.9	-	-
2215−037	18.3	-	-	18.4	-

Table 4.16: A comparison of the determined host magnitudes for the quasars from the HST sample which have recently been studied by other authors. All magnitudes have been converted to apparent V-magnitudes. The R–magnitudes from this work have been converted assuming $V - R = 0.8$. The F606W magnitudes of Bahcall *et al.* have been converted using the k-corrections quoted in Bahcall *et al.* (1997). The $H-$ magnitudes of McLeod & Rieke and Kotilainen *et al.* have been converted assuming the $V - H = 2.9$ colour quoted by McLeod & Rieke (1995b)

two samples is good, with a median difference of $V_{606} - V_{675} = -0.1$. By far the worst agreement is for 0052+251, where the Bahcall *et al.* figure is 0.5 magnitudes brighter than the host magnitude found here. However, considering that the majority of the host profile for 0052+251 is dominated by the disc component, this is perhaps not surprising. Indeed, the best-fit two-dimensional disc model presented by Bahcall *et al.* has a V-magnitude of 17.5, in perfect agreement with the best-fit disc/bulge model found here.

4.11.2 McLeod & Rieke

As with the Bahcall *et al.* results, the V-magnitudes of the hosts converted from the H–band results of McLeod & Rieke are in good overall agreement with the new HST R–band figures. Of the six quasars which are common to both samples, four of them have independently estimated visual magnitudes in agreement to ≤ 0.2 magnitudes. However, two objects (0953+415 & 1012+008) have luminosities estimated from the H–band results which are 0.7 and 0.5 magnitudes brighter than estimated from the R–band results presented here. It seems likely that the reason for this disagreement lies in the method of PSF-subtraction used by McLeod & Rieke prior to their modelling of the underlying host galaxies. The technique employed by McLeod & Rieke was to normalize a PSF-star to the flux in the central pixel of the quasar image, before a fraction (typically 0.8-0.9) was subtracted-off. The residual one-dimensional luminosity profile was then fitted with either a disc or elliptical galaxy model. With highly nuclear dominated quasars such as 0953+415 and 1012+008, it seems very probable that a much greater fraction than 0.8 or 0.9 of the central pixel flux is actually due to the unresolved nuclear component. As a result it would appear inevitable that the nuclear component was under-subtracted, leading to the anomalously bright host-galaxies magnitudes.

4.11.3 Boyce *et al.*

The results obtained for the two objects which the HST sample has in common with that studied by Boyce *et al.* compare very favourably. The difference in estimated V-magnitude for 2215-037 is only ~ 0.1 mag, with the difference for 0137+012 even smaller at ≤ 0.1 magnitude. Considering that this study was also performed on the HST with an filter (F702W) which also approximates the R–band filter, the close agreement is perhaps to be expected. The fact that the analysis performed by Boyce *et al.* , two-dimensional cross-correlation, is perhaps the most similar to the techniques employed here is also a factor.

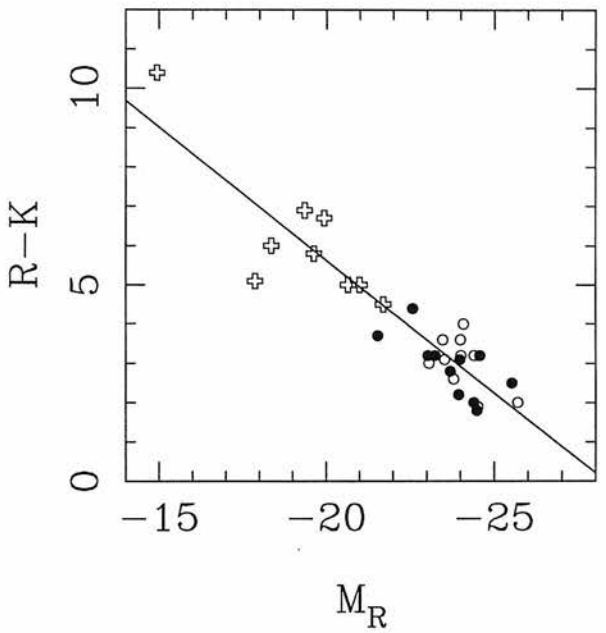

Figure 4.16: Plot of apparent $R-K$ colour versus absolute R-band luminosity of the fitted nuclear components of the objects in the HST sample. Shown in the plot are the RG (crosses), RLQ (open circles) and RQQ (filled circles) sub-samples. Also shown is the least-squares fit to the data which has a slope of 0.68 ± 0.05.

4.11.4 Kotilainen *et al.*

The estimated V-magnitudes obtained from the H–band imaging of 0736+017 by Kotilainen *et al.* and the new R–band results presented in this chapter do not agree particularly well, with the H–band result 0.5 magnitudes brighter than the new R–band figure. Obviously with only one object in common between the two samples it is impossible to say whether or not this is a systematic effect or not. However, the fact that the H–band estimate was obtained in $\sim 1''$ seeing will obviously have made the separation of nuclear and host light difficult.

4.12 Summary and Conclusions

In this chapter the wide variety of information that can be recovered from the two-dimensional modelling of the HST host galaxy data has been presented. Given the

quantity and detail of this information it would be easy for the overall picture to be lost. Fortunately two clear general results emerge. The first of these is that the host galaxy modelling results strongly support the orientation-based unification of RGs and RLQs. The scalelengths, luminosities, Kormendy relations, axial ratios and $R-K$ colours of the two samples have been shown to be basically identical. Given these results it seems clear that these two classes of AGN have host galaxies drawn from the same underlying distribution. However, it is noteworthy that the identical nature of the RG and RLQ host galaxy properties would also be predicted in a scenario where the two classes are linked by evolution. One way to differentiate between these two models is to examine the $R-K$ colours of the fitted RG nuclear components to determine whether the RGs are consistent with harbouring hidden quasar nuclei (see Fig 4.16). If it is assumed that the reddening of the RG nuclei obeys a $\Delta m \propto \lambda^{-1}$ law, as predicted by orientation-based unification, then the slope of the reddening vector which should connect the RGs and RLQs in Fig 4.16 can be calculated:

$$E(R-K) = A_R\left(1-\frac{A_K}{A_R}\right) \tag{4.9}$$

$$\Rightarrow E(R-K) = 0.70A_R \tag{4.10}$$

The slope of the least-squares fit in Fig 4.16 (solid line) is 0.68 ± 0.05, which corresponds to a dust reddening law of $\lambda^{-0.95\pm0.15}$. Furthermore, if the fitted R-band nuclear components of the RGs are de-reddened using a slope of 0.68, until each object has the mean colour of the RLQ nuclei ($R-K=3.0$), then the mean luminosity of the de-reddened RG nuclei is $M_R = -23.90 \pm 0.46$. It can be seen that this perfectly consistent with the previously determined mean nuclear luminosity of the RLQs, $M_R = -23.73 \pm 0.10$. Given the clean nature of this result, there seems little room for argument that the RG and RLQ sub-samples are not consistent with being composed of the same type of objects, viewed from different orientations.

The second, and perhaps more far-reaching conclusion, is that all of the separate results presented in this chapter indicate that the hosts of *all* powerful AGN at $z \sim 0.2$ are essentially normal, massive ellipticals. The evidence which has been presented to support this conclusion can be summarized as follows:

1. 31 of the 33 host-galaxies imaged have bulge-dominated host galaxies
2. All quasars with $M_V < -23.0$ have bulge-dominated hosts, irrespective of radio power
3. 30 of the 33 host galaxies having best-fit beta values in range $0.2 < \beta < 0.3$
4. All host galaxies have $L \geq L_*$, 25/33 have $L \geq 2L_*$
5. Mean $r_{1/2} = 12.23 \pm 1.00$ with a median of $r_{1/2} = 10.45$
6. Mean $M_R = -23.53 \pm 0.09$ with a median of $M_R = -23.52$
7. All three sub-samples consistent with Kormendy relation with slope ~ 3
8. All three sub-samples have axial ratios in range $0.8 < b/a < 0.9$
9. $R - K$ colours of all three sub-samples consistent with that expected of an old stellar population, formed at $z \geq 3$
10. Comparison with a redshift and luminosity matched sample of cluster galaxies shows no evidence that morphological disturbance occurs significantly more frequently in active galaxies

Chapter 5

AGN Black-Hole Masses

5.1 Introduction

The unambiguous conclusion of Chapter 4 was that all quasars brighter than $M_V = -23.0$ were located in otherwise normal, massive elliptical host galaxies. This conclusion suggests that, in combination with recently published work, the results of the HST host galaxy study could be used to estimate the masses of the black-holes which power the AGN phenomenon. Two recently published correlations between the properties of low redshift elliptical galaxies and the mass of their central black-holes have already been discussed in Chapter 1. The studies of Magorrian *et al.* (1998) and Franceschini *et al.* (1998) provide methods of estimating black-hole masses through correlations found with bulge luminosity and radio emission respectively. This chapter explores the application of these relations to the results of the two-dimensional modelling programme, with the aim of investigating what properties, if any, of the central black-holes of RGs, RQQs and RLQs may be linked to the origin of radio "loudness".

5.2 The Host Mass–Black-hole connection

The Magorrian *et al.* study used HST surface photometry and ground-based spectroscopy of a sample of 36 nearby galaxy bulges to investigate the distribution of their central black-hole masses. The technique employed by Magorrian *et al.* was to produce models which simultaneously matched both the galaxy surface-brightness profiles and velocity dispersions, producing combined fits for the ratio of the black-hole to the spheroidal bulge mass (M_{bh}/M_{sph}), and the galaxy mass-to-light ratio (Γ). Thirty of the thirty-six galaxies studied were found to require a massive dark object (MDO), assumed to be a supermassive black-hole, at the 95% confidence level. The best-fitting relations had the form:

$$M_{bh} = 0.006 M_{sph} \tag{5.1}$$

$$\log(\Gamma/\Gamma_{\odot}) = -1.11 + 0.18 \log(L/\mathrm{L}_{\odot}) \tag{5.2}$$

both of which have a large scatter associated with them. Five of the six galaxies which did not formally require a MDO were also consistent with these relations. The result that the masses of MDOs are linearly related to the masses of their host-galaxy bulge strengthens the conclusions of Kormendy & Richstone (1995), who found that $\geq 20\%$ of nearby bulges had a central MDO which obeyed a similar relation : $M_{bh} \simeq 0.003 M_{sph}$. It is also interesting to note that a mass-to-light ratio proportional to $M^{0.18}$ is in good agreement with the inferred relation of $\Gamma \propto M^{0.2}$, which is invoked to explain the tilt of the observed elliptical galaxy fundamental plane away from that predicted by homology and the virial theorem alone (eg. Faber *et al.* 1987).

Using the results of the Magorrian *et al.* study it is now possible to estimate the central black-hole mass of the HST host galaxies from the luminosity of their best-fitting model. Taking the absolute host R–band magnitude as m_R, the calculation proceeds as follows:

$$m_R - m_{\odot} = -2.5 \log(L_{host}/\mathrm{L}_{\odot}) \tag{5.3}$$

$$\Rightarrow (L_{host}/\mathrm{L}_{\odot}) = 10^{[(m_R - 4.3)/-2.5]} \tag{5.4}$$

where the absolute R–band magnitude of the Sun has been taken as 4.3.

$$(M_{sph}/\,\mathrm{M}_{\odot}) = (\Gamma/\Gamma_{\odot})\,(L_{host}/\,\mathrm{L}_{\odot}) \tag{5.5}$$

$$\Rightarrow (M_{sph}/\,\mathrm{M}_{\odot}) = (L_{host}/\,\mathrm{L}_{\odot})\left[0.08\,(L_{host}/\,\mathrm{L}_{\odot})^{0.18}\right] \tag{5.6}$$

$$\Rightarrow (M_{bh}/\,\mathrm{M}_{\odot}) = 0.006\,(L_{host}/\,\mathrm{L}_{\odot})\left[0.08\,(L_{host}/\,\mathrm{L}_{\odot})^{0.18}\right] \tag{5.7}$$

The results of applying the above relations to the model results presented in Chapter 4 to estimate galaxy spheroidal and black-hole masses for the objects in the HST sample are presented in Tables 5.1 & 5.2.

It is clear from Table 5.1 that the distributions displayed by the RGs and RLQs are once again in good agreement. With the application of the Kolmogorov-Smirnov (KS) test the two distributions are shown to be statistically indistinguishable (p=0.68). As expected following the discovery of a median difference of 0.4 magnitudes in their respective host galaxy luminosity, the black-hole mass distributions displayed by the RLQ and RQQ sub-samples appear to be incompatible. The non-linear nature of Eqn 5.7 has amplified the luminosity difference found in Chapter 4 to a now significant difference in the black-hole mass distributions (KS, p=0.004). Even after the removal of the two sub-luminous Seyfert-like objects (0257+024, 2344+184) the difference is still significant at the 2σ level (KS, p=0.015). The series of histograms shown in Fig 5.1 illustrate how the difference in host galaxy absolute magnitude propagates through to produce the significant difference in black-hole mass distributions. It was realised that the combination of these new black-hole mass estimates with the measured quasar nuclear R–band emission, could offer a possible insight into quasar black-hole accretion rates. In order to preform this comparison, some form of model of the relationship between matter accreted by the black-hole, and the subsequent radiation emitted, is

Source	$m_{sph}/10^{11}M_{\odot}$	$m_{bh}/10^{9}M_{\odot}$	M_R (Eddington)	L_{nuc}/L_{edd}
0230−027	10.8	6.5	-26.0	-
0307+169	16.9	10.2	-26.9	-
0345+337	6.3	3.8	-25.0	-
0917+459	22.2	13.3	-27.4	-
0958+291	8.8	5.3	-25.7	-
1215−033	8.2	4.9	-25.5	-
1215+013	5.1	3.0	-24.6	-
1330+022	12.8	7.7	-26.3	-
1342−016	33.2	19.9	-28.1	-
2141+279	19.5	11.7	-27.1	-
0137+012	18.5	11.1	-27.0	0.04
0736+017	11.2	6.7	-26.1	0.15
1004+130	19.7	11.8	-27.2	0.25
1020−103	8.8	5.3	-25.7	0.13
1217+023	12.9	7.7	-26.4	0.16
2135−147	8.9	5.4	-25.7	0.23
2141+175	9.5	5.7	-25.8	0.31
2247+140	14.2	8.5	-26.6	0.08
2349−014	25.0	15.0	-27.6	0.04
2355−082	11.7	7.0	-26.2	0.06

Table 5.1: The results of applying the Magorrian relations to the radio-loud objects. Columns two and three list the predicted galaxy spheroid mass and central black-hole mass respectively. Column 4 lists the predicted absolute R–band Eddington luminosity of the black-hole, assuming a simple accretion-disc model (see text). Column five gives the ratio of the predicted Eddington luminosity to the best-fitting nuclear model component. There are no entries in column 5 for the RGs since their nuclear emission is most likely dust-obscured.

Source	$m_{sph}/10^{11}M_{\odot}$	$m_{bh}/10^{9}M_{\odot}$	M_R (Eddington)	L_{nuc}/L_{edd}
0052+251	5.6	3.4	-24.8	0.69
0054+144	11.6	6.9	-26.2	0.21
0157+001	25.0	15.0	-27.6	0.03
0204+292	8.3	5.0	-25.5	0.10
0244+194	4.6	2.8	-24.5	0.31
0257+024	1.1	0.7	-21.8	0.14
0923+201	7.8	4.7	-25.4	0.47
0953+414	5.1	3.1	-24.6	2.33
1012+008	13.9	8.4	-26.5	0.10
1549+203	2.7	1.6	-23.4	1.71
1635+119	6.3	3.8	-25.0	0.04
2215−037	10.5	6.3	-26.0	0.04
2344+184	3.2	1.9	-23.8	0.04

Table 5.2: The results of applying the Magorrian relations to the radio-quiet objects. Columns two and three list the predicted galaxy spheroid mass and central black-hole mass respectively. Column 4 lists the predicted absolute R–band Eddington luminosity of the black-hole, assuming a simple accretion-disc model (see text). Column five gives the ratio of the predicted Eddington luminosity to the best-fitting nuclear model component.

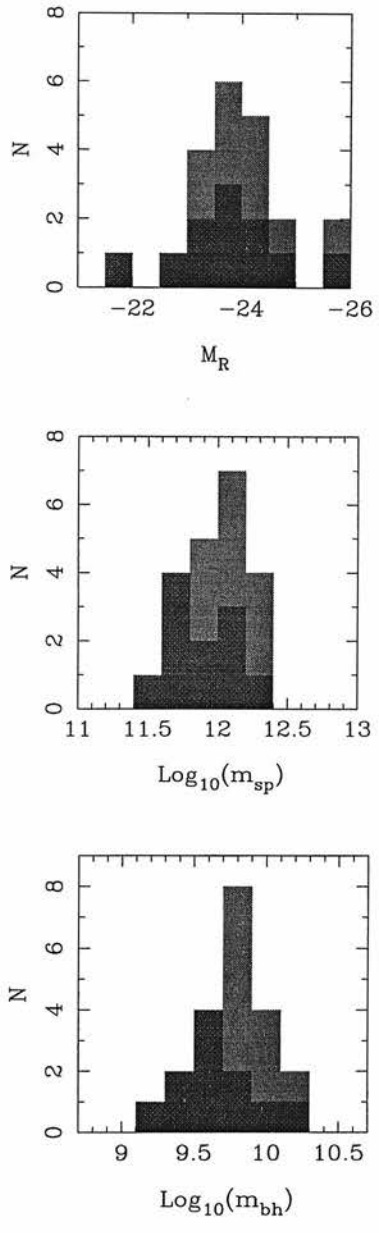

Figure 5.1: A sequence of histograms illustrating how a small difference in host galaxy luminosity between the RLQs and RQQs can produce a noticeable difference in estimated black-hole mass. Top histogram shows the absolute host galaxy luminosity distributions of the RQQs (black) and RLQs (grey) sub-samples. The middle histogram shows the distributions of the resulting galaxy spheroid mass using the mass-to-light ratio given by Magorrian *et al.* (1998). The bottom histogram shows the estimated central black-hole mass distributions as predicted by the Magorrian relation. The two Seyfert-like RQQ objects have been excluded from this figure.

required. This type of work is obviously a whole area of expertise in itself. However, considering that the fitted R–band nuclear component is the only spectral information available, and given the large uncertainties inherent to the Magorrian *et al.* relations, it was decided that the accretion disc model should be as simple as possible. For the purposes of this calculation it is assumed that the luminosity of the accretion disc is given by the Eddington formula for the balance between gravitational attraction and radiation pressure (Robson 1996):

$$L_{edd} = \frac{4\pi G M_{bh} m_p c}{\sigma_T} \tag{5.8}$$

where m_p is the proton mass, and σ_T is the Thomson scattering cross-section. If it is also assumed (albeit unrealistically) that the emission of the disc is described by a single-temperature blackbody function, it is then possible to assign an effective temperature to the disc through the relation:

$$L_{edd} = 2\pi R^2 \sigma^2 T_{\rm eff}^4 \tag{5.9}$$

where the factor of two arises from considering emission from both sides of the accretion disc. In order to calculate the effective temperature is is necessary to decide upon a characteristic radius to use in Equ 5.9. For this calculation the characteristic size has been chosen as three times the Schwarzschild radius (R_s), where R_s is given by :

$$\mathrm{R}_s = \frac{2GM_{bh}}{c^2} \tag{5.10}$$

With an estimate of the effective temperature of the disc, it is then possible to calculate the observed flux at a specific frequency according to:

$$S_\nu = I_\nu d\Omega \tag{5.11}$$

where $d\Omega$ is the solid angle of the disc as seen by the observer, given by:

$$d\Omega = \frac{\pi R^2}{(10\mathrm{pc})^2} \tag{5.12}$$

and I_ν is the Planck function given by:

$$I_\nu = \frac{2h\nu^3}{c^2} \left[\exp\left(\frac{h\nu}{kT}\right) - 1 \right]^{-1} \tag{5.13}$$

where h and k are the Planck and Boltzmann constants respectively. Taking the central wavelength of the R–band filter to be 6500Å (4.62×10^{14} Hz), it is then possible to convert the value given by Equ 5.13 into an absolute magnitude which can be directly compared to the fitted nuclear components presented in Chapter 4. Although this extremely simplistic model does not in any way realistically represent the physics of black-hole accretion discs, any relative difference detected between the RQQ and RLQ sub-samples is still of interest. The use of a simple model also has the advantage that any results produced can not be due to the fine tuning of a large number of free parameters. The estimated nuclear luminosities for the two quasar sub-samples are listed in column 4 of Tables 5.1 & 5.2, and compared with the measured nuclear luminosities in Fig 5.2.

Despite the large number of sources of potential scatter the results of this calculation appear remarkably sensible. As can be seen from Fig 5.2, the maximum luminosity produced by any quasar is comparable with the predicted Eddington limit, while the majority appear to be radiating at $\sim$ 10% of the Eddington luminosity. Two of the RQQ objects (0953+415, 1549+203) are required to be radiating at marginally super-Eddington rates to produce their observed nuclear luminosities, if allocated a black-hole mass as estimated from the Magorrian *et al.* relations. However, this is not unexpected, given that these objects have the highest measured L_{nuc}/L_{host} ratios in the whole HST sample. Since both are predicted to be super-luminous by a factor of only ~ 2, this can not be considered to be problem in light of the simplicity of the model, and the scatter in the Magorrian relation. Taken as a group there is a suggestion that the RQQs are radiating at a higher percentage of the Eddington limit than the RLQs, although, even including the two super-luminous objects, the difference is not formally significant (KS, p=0.29).

However, the correlation between observed M_R and predicted Eddington M_R is stronger (SR, p=0.22) than that found in Chapter 4 between the host-galaxy luminosity and the nuclear luminosity (p=0.51). If the two super-luminous RQQs are excluded from the correlation test then the result becomes marginally significant (p=0.06), although this is undoubtedly due to inclusion of the two Seyfert-like RQQs, with the correlation becoming weak (p=0.34) if these objects are also excluded from the test.

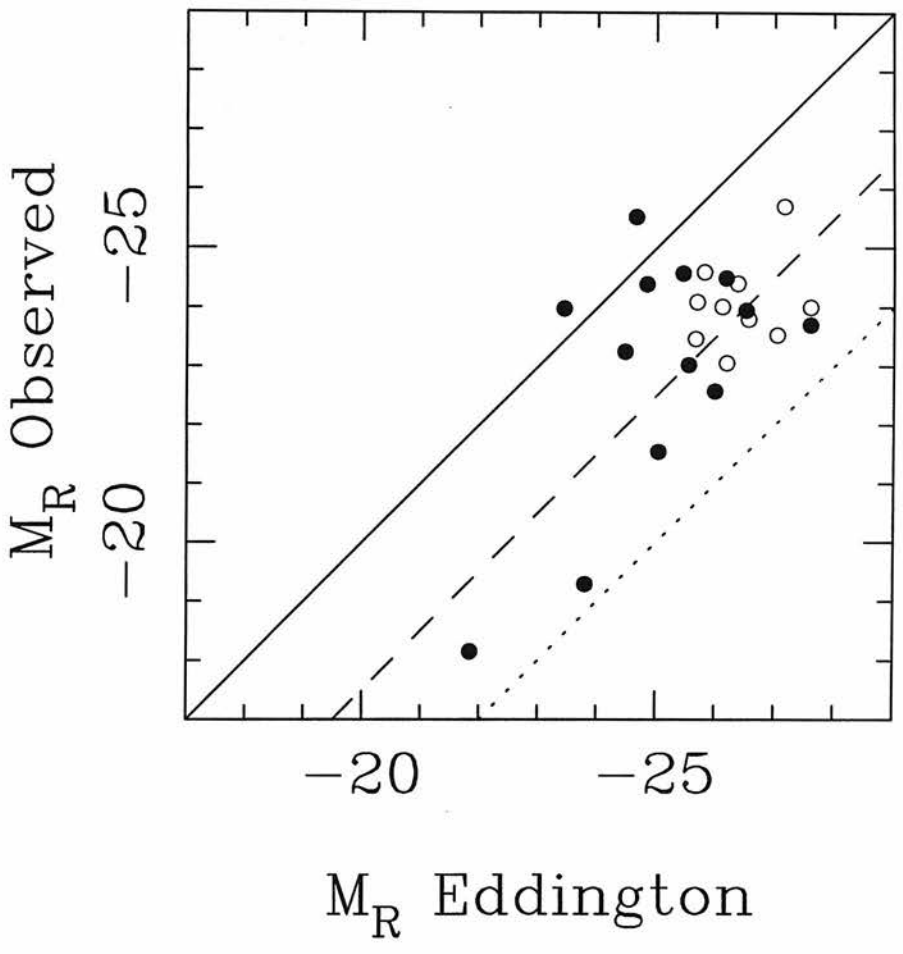

Figure 5.2: The observed absolute magnitude M_R of the nuclear component in each quasar plotted against the absolute magnitude which is predicted by assuming that each quasar contains a black hole of mass $m_{bh} = 0.006 m_{spheroid}$, and that the black hole is emitting at the Eddington luminosity (RLQs = open circles, RQQs = filled circles). The solid line shows where the quasars should lie if they were all radiating at their respective Eddington luminosities, while the dashed line indicates 10% of predicted Eddington luminosity, and the dotted line indicates 1% of predicted Eddington luminosity. The nuclear components of the radio galaxies are not plotted because all the evidence suggests they are substantially obscured by dust.

The distributions displayed by the RQQs and RLQs in Fig 5.2, combined with similar fitted nuclear components found in Chapter 4, suggests that, in both classes of quasar, the *optical* luminosity arises from a similar process of accretion onto a massive black hole, and that RLQs and RQQs of comparable absolute magnitude $M_R < -23.5$ are powered by black holes of comparable mass $M > 3 \times 10^9 \mathrm{M}_\odot$.

The results of this calculation can be regarded as providing independent evidence that the relation of Magorrian *et al.* still applies for large galaxy and black-hole masses. To re-state this result from the opposite angle, if it were believed that the Magorrian result held at large galaxy masses *a priori*, then the large black-hole masses of $\simeq 10^9$ required to produce quasar emission of $M_R < -23.5$, would require host galaxies with bulge masses of $> 5 \times 10^{11} \mathrm{M}_\odot$. The only Host galaxies capable of meeting this requirement are giant ellipticals with $L \simeq 2L^*$, exactly as was found from the modelling of Chapter 4.

5.3 The Radio Power–Black-hole connection

A second method of estimating galactic black-hole masses comes from the study of Franceschini *et al.* (1998). The sample of objects studied by Franceschini *et al.* consisted of thirteen nearby (≤ 30 Mpc, $H_o = 50$) galaxies taken from the literature, all of which have estimates for the central black-hole mass. Eleven of the thirteen objects were regarded as having reliable black-hole estimates, originating from high spatial resolution spectroscopy, with the estimates from gas kinematics and surface photometry of a further two objects considered as limits.

In order to look for correlations between the estimated black-hole masses and the host galaxy, Franceschini *et al.* investigated the emission of the host galaxy at optical, hard X-ray, far infrared (60μm) and radio wavelengths (5GHz). The results from this process successfully confirmed the strong correlation between galaxy bulge luminosity (B–band) and black-hole mass previously found by Kormendy & Richstone (1995), from whose sample 8 of the 13 black-hole estimates were taken, but failed to find significant correlations with either the X-ray luminosity or the far-infrared emission. The results

of the Franceschini *et al.* study which are of particular relevance to this chapter are the very tight relationships which were found between black-hole mass and both total and core radio emission. These empirical relations have the form:

$$\log P^{core}_{5GHz} = 2.73(\pm 0.59) \log M_{bh}/M_{\odot} - 2.87 \tag{5.14}$$

$$\log P^{tot}_{5GHz} = 2.66(\pm 0.29) \log M_{bh}/M_{\odot} - 0.875 \tag{5.15}$$

5.3.1 Total Radio Power

The Franceschini *et al.* data for black-hole mass and total 5GHz radio power have been re-plotted in Fig 5.3, along with their best-fitting relation (solid line). To investigate to what extent this relation is followed by the objects in the HST sample, the relevant data points (or upper limits) have been added to the figure. Unlike the study of Franceschini *et al.* , who had the advantage of high spatial resolution spectroscopy to estimate the black-hole mass, the value of m_{bh} used for the HST data had to be estimated from the application of the Magorrian *et al.* relations, as described above. The black-hole masses predicted from the application of the Franceschini total-radio power relation to the AGN in the HST sample are listed in column 2 of Tables 5.3 & 5.4.

There are several points worth mentioning with respect to Fig 5.3. Firstly, the location of the radio-loud AGN on this diagram can be seen as good circumstantial evidence that the black-hole estimates from the Magorrian relation are not physically unreasonable. Secondly, it can be seen from Fig 5.3 that there is an obvious bias towards the spheroid-based black-hole estimates being systematically smaller than predicted by the Franceschini relation. This is confirmed by an examination of the results presented in Table 5.3 & 5.4, which shows that the total-radio power black-hole estimator returns a larger value that the Magorrian relation for 18 of the 20 radio-loud HST objects. However, in the vast majority of cases this off-set is small, with the mean ratio of $m_{sph}/m_{5GHz} = 2.03 \pm 1.06$ suggesting that the two estimates could be well correlated. This possibility is investigated in Fig 5.4 which shows the two estimates plotted against each other. Initial application of the Spearman rank correlation test reveals only a weak

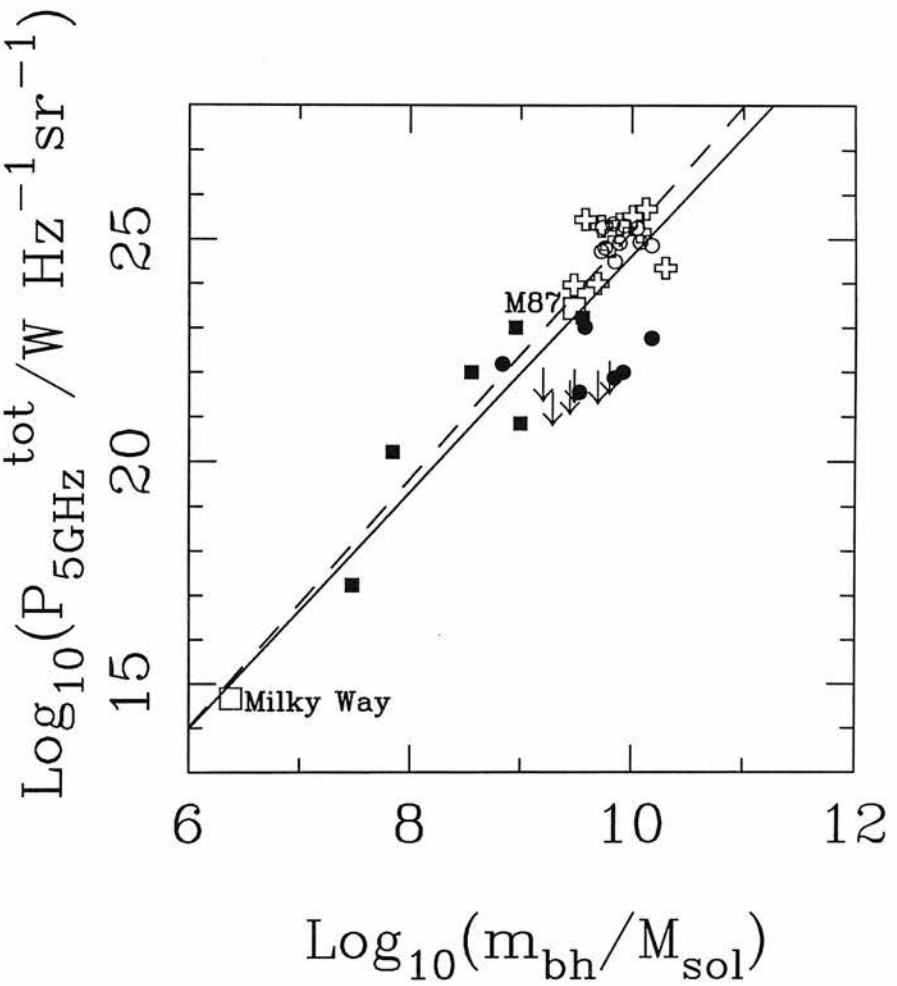

Figure 5.3: Total radio luminosity P_{5GHz}^{total} versus black-hole mass showing the data on low-redshift 'normal' galaxies from Franceschini *et al.* (1998), and the AGN from the HST sample (RGs = crosses, RLQs = open circles, RQQs = filled circles). The solid line is simply the best-fitting relation ($P \propto m_{bh}^{2.7}$) to the nearby galaxy data given by Franceschini *et al.*. The dashed line is a least-squares fit to a combined data-set of the Franceschini *et al.* objects and the radio-loud AGN from the HST sample (see text). For the nearby galaxies m_{bh} has been estimated directly from stellar dynamics, while for the AGN m_{bh} has been estimated from host-galaxy spheroid luminosity using the relations derived by Magorrian *et al.* (1998).

correlation (p=0.372). However, an investigation of Fig 5.4 shows that two of the radio galaxies (0345+337 and 1342-016) would appear to be biasing this result. This suspicion is confirmed with their exclusion from the test greatly increasing the significance of the correlation (p=0.037). Considering the large uncertainties involved in the extrapolation of black-hole mass from galaxy spheroidal luminosity, it can be seen as remarkable that these two independent estimates of black-hole mass typically agree to within a factor of two.

It is worth remembering at this point that the precise value of the slope of the Franceschini relation is based on a sample of only twelve objects, only seven of which have reliable black-hole estimates arising from high-resolution spatial spectroscopy. Consequently, the slope is not particularly well determined, as can be seen from the large 1σ errors quoted in Equ 5.14. The change in slope of the total-radio power relation required to fit the radio-loud AGN from the HST sample was determined by re-fitting a combined dataset consisting of the seven Franceschini *et al.* objects with firm black-hole mass estimates, and the twenty HST radio-loud objects. The least-squares fit to this dataset is:

$$\log P^{tot}_{5GHz} = 2.79(\pm 0.16) \log M_{bh}/M_{\odot} - 2.72(\pm 1.54) \tag{5.16}$$

and is plotted as the dashed line in Fig 5.3. It is clear that only a very small change in slope and normalization of the Franceschini total-radio power relation is required to bring it into full agreement with the black-hole estimates based on the host galaxy bulge luminosity. It is noteworthy that this altered relation still provides a good representation of the Franceschini *et al.* low-z inactive galaxy data.

A third point which is immediately obvious from Fig 5.3 is that the vast majority of the RQQs are producing substantially less radio emission than predicted by the Franceschini relation, if it is assumed that the black-hole masses estimated from host galaxy luminosity are accurate. The two RQQ sources which do appear to follow the total-radio power relation are 1635+119 and 0257+024, both of which were identified in the previous chapter as having total optical luminosities below that adopted as the quasar-Seyfert dividing line ($M_V = -23.0$). The first of these two RQQs, 1635+119,

has been identified by Kukula *et al.* (1998) as a so-called 'radio-intermediate' quasar, which displays radio luminosities well above that generally seen in RQQs, but still well below the radio power of true RLQs. It has been suggested that radio-intermediate quasars are the result of relativistic beaming of aligned radio-quiet sources (eg. Miller *et al.* 1993), although the de-projected size of the lobe structure detected in 1635+119 has led Kukula *et al.* to suggest that this source may be better described as a low luminosity RLQ. The second of the unusual RQQ sources, 0257+024, was found to have a combined disc/bulge host galaxy from the modelling described in Chapter 4. The reason for its position in Fig 5.3 would appear to be the low luminosity of the bulge component of the model host galaxy, raising the possibility that, for this source at least, the radio luminosity is more closely related to the total host galaxy luminosity than the luminosity of the bulge component.

Considering that the RGs and RLQs appear so consistent with the $P_{5GHz} : m_{bh}$ relation, it is of course inevitable that the majority of the RQQs should lie below it. However, the position of the RQQs on the $P_{5GHz} - m_{bh}$ plane shown in Fig 5.3 does suggest a possible correlation (albeit with a number of upper limits involved) between radio-luminosity and host-galaxy-derived m_{bh} within the RQQ sub-sample. The suggestion from this is that the radio luminosities of the RQQs might also be linked to black-hole mass via a relation of similar slope ($m_{bh}^{2.5-3.0}$), but with a normalization some two orders of magnitude lower. This situation would be consistent with the radio emission from RQQs scaling with black-hole mass in a similar way to that of radio-loud objects, but being restricted to a lower luminosity regime by some undetermined external factor.

The study of RQQ radio emission by Kukula *et al.* (1998) has shown that, where detectable, the radio emission from RQQs arises entirely from a compact core-like component. It was therefore decided that it was of interest to investigate whether the radio properties of RQQs can be linked to those of nearby galaxies if only compact radio emission is included.

Source	$m_{bh}/10^9 M_\odot$	$m_{bh}/10^9 M_\odot$	$m_{bh}/10^9 M_\odot$
0230−027	6.5	12.0	
0307+169	10.2	21.7	6.1
0345+337	3.8	20.4	23.5
0917+459	13.3	25.1	8.7
0958+291	5.3	17.9	11.5
1215−033	4.9	5.8	
1215+013	3.0	5.7	
1330+022	7.7	18.7	
1342−016	19.9	7.9	
2141+279	11.7	16.0	6.9
0137+012	11.1	17.3	18.5
0736+017	6.7	18.7	
1004+130	11.8	13.1	5.6
1020−103	5.3	11.0	
1217+023	7.7	12.9	
2135−147	5.4	17.5	12.6
2141+175	5.7	11.7	
2247+140	8.5	18.1	26.9
2349−014	15.0	12.3	14.6
2355−082	7.0	9.0	

Table 5.3: Three different estimates of the central black-hole mass of the radio-loud objects. Column 2 gives the black-hole mass estimate from the Magorrian relations. This information is identical to that provided in Table 5.1 and is included here for ease of comparison. Column 3 gives the black-hole mass estimate from the total $P_{5GHz} : m_{bh}$ relation of Franceschini *et al.* (1998). Column 4 gives the corresponding figure estimated from the core $P_{5GHz} : m_{bh}$ relation. The objects for which no core radio power black-hole estimate is given are those for which a reliable measure of the core luminosity could not be readily recovered from the literature.

Source	$m_{bh}/10^9 M_\odot$	$m_{bh}/10^9 M_\odot$	$m_{bh}/10^9 M_\odot$
0052+251	3.4	0.7	1.3
0054+144	6.9	0.9	1.7
0157+001	15.0	2.0	3.9
0244+194	2.8	<0.6	<1.1
0257+024	0.7	1.2	2.3
0923+201	4.7	<0.8	<1.4
0953+414	3.1	<0.8	<1.4
1012+008	8.4	1.0	1.9
1549+203	1.6	<0.8	<1.5
1635+119	3.8	2.5	4.8
2215−037	6.3	<0.9	<1.7
2344+184	1.9	<0.5	<0.9

Table 5.4: Three different estimates of the central black-hole mass of the radio-quiet objects. Column 2 gives the black-hole mass estimate from the Magorrian relations. This information is identical to that provided in Table 5.1 and is included here for ease of comparison. Column 3 gives the black-hole mass estimate from the total $P_{5GHz} : m_{bh}$ relation of Franceschini *et al.* (1998). Column 4 gives the corresponding figure estimated from the core $P_{5GHz} : m_{bh}$ relation.

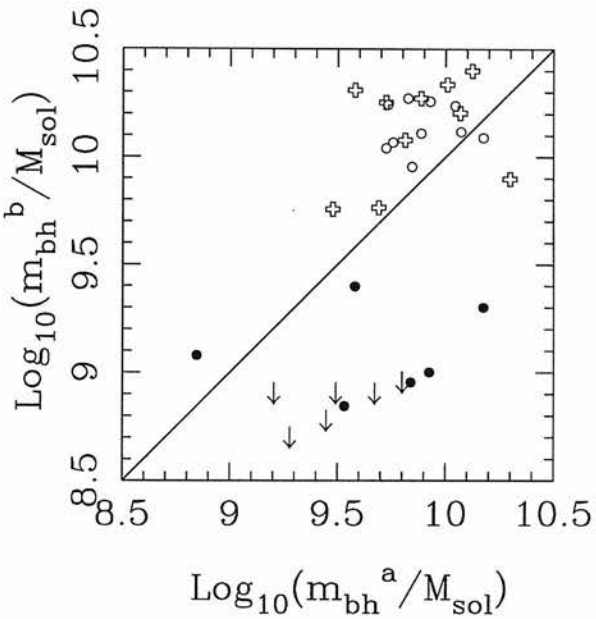

Figure 5.4: A comparison between of the black-hole masses predicted from host galaxy spheroidal luminosity via the Magorrian relations (m^a_{bh}) and those predicted from the P^{tot}_{5GHz} Franceschini relation (m^b_{bh}).

5.3.2 Core Radio Power

The Franceschini *et al.* data for black-hole mass and core-radio power have been re-plotted in Fig 5.5, along with the RQQs from the HST sample. For the RQQ objects the latest core-radio power detections and upper limits have been taken from Kukula *et al.* (1998). An investigation of the literature produced values for the core component of eight of the HST radio-loud objects (all lobe-dominated to minimize the impact of beaming), and these have also been plotted (Giovannini *et al.* 1988, Clarke *et al.* 1992, Lister & Gower 1994). The black-hole mass values for all of the HST objects have again been estimated from the host galaxy luminosity, via the Magorrian relations. The solid line shown in Fig 5.5 is not the best-fit relation found by Franceschini *et al.* (see Eqn 5.15) but instead has the form:

$$\log P^{core}_{5GHz} = 2.51(\pm 0.29) \log M_{bh}/M_{\odot} - 1.29(\pm 2.36) \qquad (5.17)$$

which has been calculated by re-fitting the Franceschini data with firm core detections,

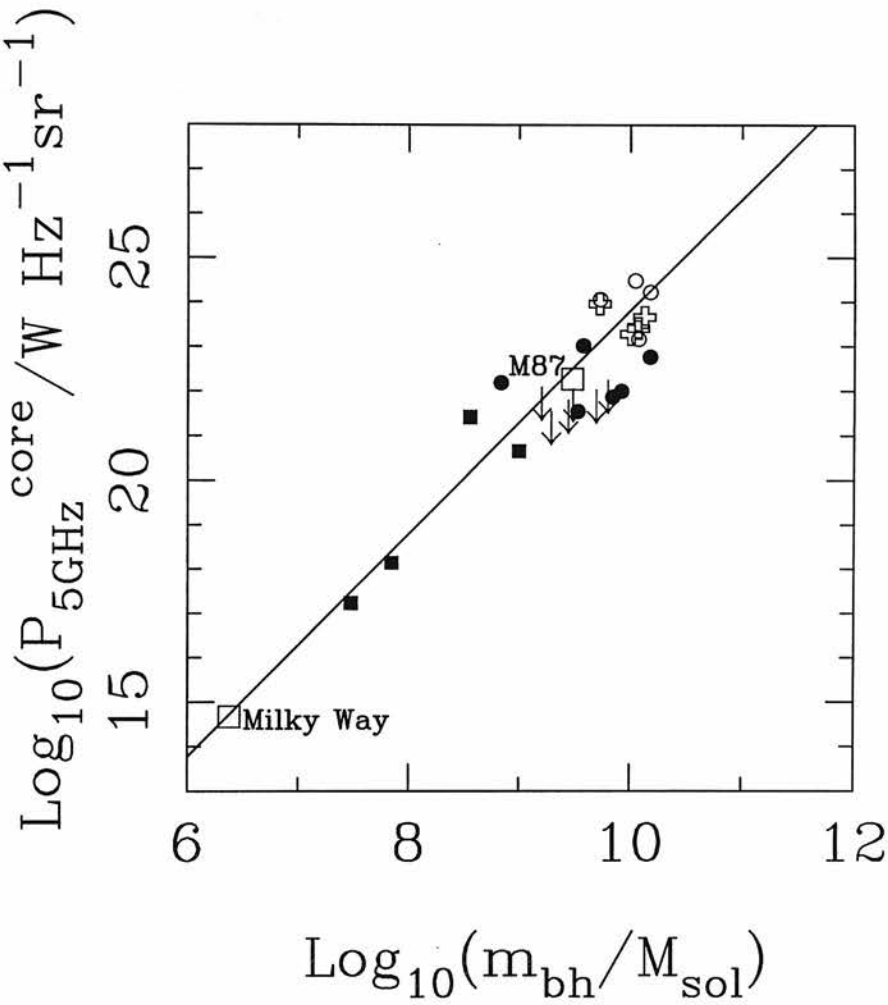

Figure 5.5: Core radio luminosity P^{core}_{5GHz} versus black-hole mass showing the data on low-redshift 'normal' galaxies from Franceschini *et al.* (1998), and the AGN from the HST sample (RGs = crosses, RLQs = open circles, RQQs = filled circles) for which a core reliable radio flux was available in the literature. The solid line is the relation $P \propto m_{bh}^{2.5}$ which was calculate from re-fitting the Franceschini *et al.* data while attributing all of the radio emission from M31 (after removal of very extended radio emission linked to star-formation) to the core (see text for discussion).

with the alteration that all of the radio emission from M31 (after removal of very extended radio emission linked to star-formation) has been attributed to the core. The reason for this change is that if M31 were placed at the median redshift of the HST sample ($z = 0.2$) then it would not be possible to perform a separation into core- and extended radio emission. It would appear to be the rejection of sources with only radio core limits, along with the different treatment of the radio emission of M31, that has led to the flatter relation between m_{bh} and P^{core}_{5GHz} found here. It can be seen however that the two relations are perfectly consistent within the relatively large errors. The results of applying this relation to estimate the black-hole masses of the HST objects with radio core detections are listed in column 4 of Tables 5.3 & 5.4.

There are several noteworthy aspects to Fig 5.5. Firstly, it is noticeable that M87 moves from the total-radio power relation in Fig 5.3, to the core-radio power relation in Fig 5.5, once its extended radio emission is removed, as do several of the radio-loud AGN. Secondly, as with total-radio power, there is a suggestion that the RQQs may follow a relation of similar slope to the Franceschini data. Obviously, with a large number of sources with only upper limits available this is entirely dependent on what the core luminosity of these sources actually are. If it is assumed that the core-radio luminosities of these RQQ objects lie at, or at least not significantly below, their present limits, the RQQ objects as a group do not display a significant correlation between core radio power and black-hole mass (SR, p=0.19). The imminent VLA observations of the six undetected RQQs should clarify this issue.

Adopting the position that it is at least possible that P^{core}_{5GHz} is a reasonable tracer of black-hole mass, Fig 5.4 shows a comparison between the black-hole estimates derived from P^{core}_{5GHz} and host galaxy spheroidal luminosity via the Magorrian relations. Applying the Spearmann rank correlation test confirms that the two estimates are highly correlated (p=0.0014), if the six RQQ limits are regarded as detections. However, the detection of a strong correlation relies crucially upon the inclusion of the undetected sources, a fact that is highlighted by their exclusion from the test reducing the correlation to a insignificant level (p=0.144).

Using the same simplistic accretion-disc model as described previously, Fig 5.7

shows a comparison of predicted Eddington nuclear luminosity with measured nuclear luminosity, identical to that shown in Fig 5.2 except that the black-hole masses of the RQQs have been estimated using the P^{core}_{5GHz} relation. The systematically lower black-hole masses predicted by the P^{core}_{5GHz} relation can be seen to lead to a clear separation of the RQQ and RLQ sub-samples. Using the core radio luminosity to estimate black-hole mass leads to the result that the majority of the RQQs are radiating at around the Eddington limit (the fact that one source lies an order of magnitude above the Eddington line in Fig 5.7 cannot be regarded as a serious problem considering the simplicity of the accretion-disc model, and the scatter in the P^{core}_{5GHz} relation), with the RLQs occupying the same region of the diagram as they did in Fig 5.2, radiating at $\sim 10\%$ of the Eddington limit. This then raises the possibility that, if the P^{core}_{5GHz} predictions are accurate, there may be a selection effect at work. The selection of optically-matched samples of RQQs and RLQs may in fact have selected lower mass ($\simeq 10^9 M_{\odot}$) black holes radiating close to the Eddington limit for comparison with higher mass ($\simeq 10^{10} M_{\odot}$) black holes radiating (in the optical) at around 10% of their Eddington luminosity. The viability of all three of the black-hole mass estimators considered in this chapter is discussed in the next section.

5.4 Discussion: The Origin of Radio-Loudness

The results presented in this chapter can be interpreted in two distinct ways depending on which of the three black-hole mass estimators are taken as being the more reliable. As far as the radio-loud objects are concerned, a comparison of columns 2, 3 & 4 of Table 5.3 confirms that essentially all routes of black-hole mass estimation lead to values of $m_{bh} \geq 10^{10} M_{\odot}$. However, for the RQQs, use of P^{core}_{5GHz} to estimate m_{bh} produces values typically more than a factor of two smaller than inferred from host-galaxy luminosity, and implies that *no* RQQ in the sample has a black-hole more massive than $m_{bh} = 5 \times 10^9 M_{\odot}$. The adoption of the P^{core}_{5GHz} relation as the black-hole mass predictor presents the prospect that the radio-loudness dichotomy may simply be due to the existence of a black-hole mass threshold which must be crossed to produce powerful, large-scale, radio emission. Contrary to this, if the host galaxy spheroidal luminosity is

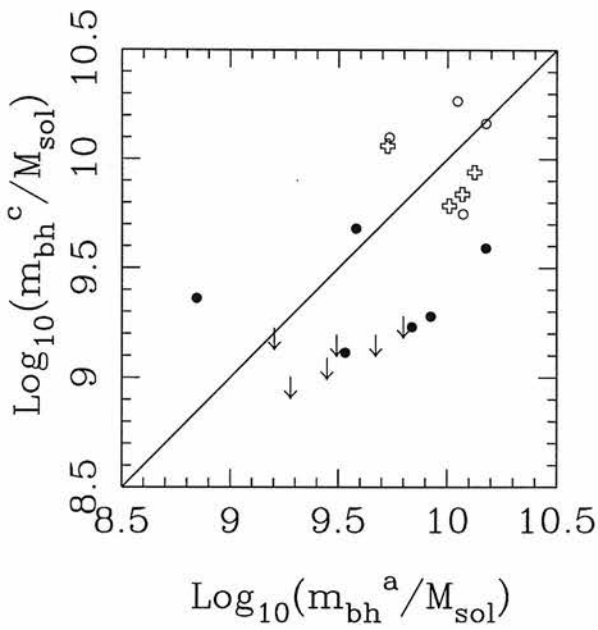

Figure 5.6: A comparison between of the black-hole masses predicted from host galaxy spheroidal luminosity via the Magorrian relations (m^a_{bh}) and those predicted from the P^{core}_{5GHz} Franceschini relation (m^c_{bh}).

assumed to be the better tracer of black-hole mass, the overlap in predicted RQQ and RLQ black-hole distributions would imply that some other physical parameter, such as black-hole angular momentum, must be invoked to explain the dichotomy.

In the picture where black-hole mass is the only parameter controlling the production of powerful radio emission the situation is deceptively simple. As described above, the implication of the adoption of the core radio emission as the black-hole estimator implies that a central black-hole mass of $m_{bh} \geq 10^{10} M_{\odot}$ is required to produce a radio-loud object; either quasar or FRII radio galaxy. The similarity in the optical properties of RQQs and RLQs can be explained in this scheme by the order-of-magnitude difference in black-hole masses being counter-balanced by the RQQs accreting material at a rate approximately an order-of-magnitude greater than the RLQs. A straightforward prediction of this model is that there should be a population of elliptical galaxies with similar luminosities to the RQQ host galaxies, but which do not produce quasar-like nuclear emission due to a greatly reduced accretion rate. At first sight M87 (and three other members of the Franceschini *et al.* sample) would appear to be exactly such an

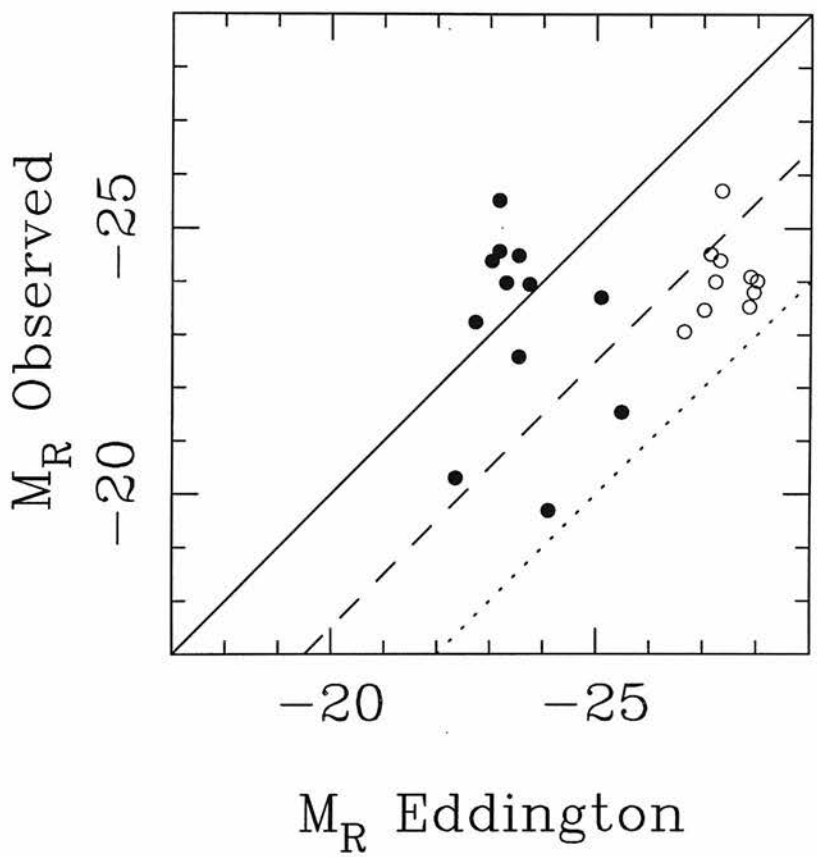

Figure 5.7: As Fig 5.2, but this time with Eddington M_R derived for the RQQs using the values of m_{bh} estimated from the P^{core}_{5GHz} relation. The values of m_{bh} for the RLQs has been estimated from the P^{tot}_{5GHz} relation, although for the RLQs the use of any of the three black-hole estimators discussed here leads to very similar results, as is confirmed by an investigation of Table 5.3.

object. The absolute R–band luminosity of M87 ($M_R = -23.43$), taking the figure of $M_B = -21.86$ quoted by Franceschini *et al.* and assuming a colour of $B - R = 1.57$ (Fukugita *et al.* 1995) , and radio luminosity are certainly typical of that displayed by the RQQ host galaxies. However, the example of M87 also serves to illustrate one of the major problems associated with the P^{core}_{5GHz} black-hole estimates, namely, why do the Magorrian and Franceschini relations produce consistent predictions for the radio-loud objects but, significantly different predictions for the radio-quiets?

The question which must be answered is why does galaxy spheroidal luminosity appear to accurately predict the black-hole mass of objects such as M87, and presumably those of the radio-loud AGN (independently confirmed by both radio luminosity correlations), while systematically over-estimating the black-hole mass of the RQQs by greater than an order-of-magnitude. Although it is a possibility that the Magorrian relations do not apply to the host galaxies of RQQs, it would seem to be somewhat unlikely. Given that the modelling results of Chapter 4 indicated that the hosts of RQQs and the radio-loud objects were basically identical in terms of luminosity, characteristic size and optical-infrared colour, some non-obvious mechanism would seem to be needed during the formation of RQQ hosts, to allow them to have a different relation between black-hole and host galaxy mass.

What then are the implications for the radio-loudness dichotomy if it is assumed that the black-hole estimates derived from the host galaxy luminosity are the most reliable? As was described in Section 5.2, there does seem to be a trend for the RLQs to have larger black-hole masses than their RQQ counterparts, just as with the core-radio luminosity black-hole mass estimates. Even with the exclusion of the two Seyfert-like RQQs, the median black-hole masses of $4.7 \times 10^9 M_\odot$ (RQQs) and $7.4 \times 10^9 M_\odot$ (RLQs) are substantially different, and are confirmed as such by the KS test (p=0.015). Indeed, an examination of the figures listed in Table 5.1 & 5.2 suggests a natural division between the two quasar classes at $\sim 7 \times 10^9 M_\odot$, with only 2/11 RQQs with black-hole masses greater than this value, compared to 6/10 RLQs. However, unlike the P^{core}_{5GHz} estimated black-hole masses, there is still considerable overlap between the two distributions, as can be seen in Fig 5.2. The Magorrian relations predicts 4/11 RQQs to have masses $\geq 5 \times 10^9 M_\odot$, in contrast to the P^{core}_{5GHz} estimates which predict *all*

RQQs to have masses $\leq 5 \times 10^9 M_{\odot}$.

The considerable overlap between the two quasar sub-samples in terms of black-hole mass is also apparent from the estimates of their respective accretion rates. Investigation of Tables 5.3 & 5.4 confirms that, based on the simple accretion model described in Section 5.2, both sub-samples are estimated to be accreting at a median rate of 14% of that required to produce the Eddington luminosity. Therefore, it seems that the black-hole mass estimates using the Magorrian *et al.* relations make it unlikely that there exists a simple black-hole mass threshold, beyond which the production of powerful radio emission is inevitable. Although the results do imply that the most massive black-holes are more likely to be found in radio-loud objects, if this were the whole story, several of the objects from the RQQ sub-sample would be expected to be producing powerful radio emission also. There is of course a possibility that these presently radio-quiet objects will eventually evolve to produce powerful radio jets, although, the large radio luminosities expected from the early stages of powerful jet production (eg. Kaiser *et al.* 1997), and the near unanimous finding that RQQ radio emission is compact in nature (eg. Kukula *et al.* 1998) suggests that this is not the normal course of events. Furthermore, the similarity of the predicted accretion rates for the two quasar sub-samples, combined with their near-identical best-fitting unresolved nuclear components (see Chapter 4), suggests that different accretion rates cannot be the cause of the bi-modal quasar radio luminosity distribution either. In conclusion, it appears that the most probable scenario is that some other physical parameter is required, in conjunction with black-hole mass, to explain the radio-loudness dichotomy. Is it possible that this extra physical parameter is the black-hole angular momentum?

A recent model proposed by Wilson & Colbert (1995) would appear to make several predictions about the properties of quasar host galaxies and black-hole masses which are consistent with the results presented here. The basic premise of this model is that a rapidly spinning supermassive black-hole is the prerequisite for the production of radio-loud objects (RG or RLQ), and that such black-holes are only produced via the coalescence of the central black-holes of two merging galaxies. In this model the energy-source for the production of powerful radio-jets comes from the extraction of mechanical energy from the spinning black-hole, and is not directly related to the

accretion of material (naturally explaining why the RQQs and RLQs were found to have similar accretion rates). Further assumptions of the model are that the mass of galactic black-holes are correlated to the mass of their host galaxies (as is implied by Magorrian *et al.*), and that elliptical galaxies are the result of mergers between galaxies of roughly equal mass. Based on these assumptions Wilson & Colbert predict the outcome of three types of merger:

1. Low mass-low mass galaxy mergers should produce low mass ellipticals with low-mass, rapidly spinning, black-holes.

2. Low mass-high mass mergers should result in high mass galaxies with high mass, low spin, black-holes. The remnant galaxy should retain the morphology of the high mass progenitor.

3. High mass-high mass mergers produce a high mass elliptical galaxy with a high-mass, rapidly spinning, black-hole. These are the rarest merger events and lead to the production of powerful radio sources.

This merger/black-hole spin model can be used to predict several observational properties of quasars which agree well with the findings of this chapter, and the results of the modelling performed in Chapter 4, i.e. :

- Only the most massive ellipticals should host quasars.
- Only a small fraction of quasars should be radio-loud.
- No reason for RQQs and RLQs to have different accretion rates.
- Possible overlap in RQQ and RLQ black-hole mass distributions still consistent with bi-modal radio luminosity distribution.

In conclusion, it would appear that the new HST R–band data for the sample of low-z AGN is most consistent with a picture where a combination of both black-hole mass and angular momentum is responsible for the production of powerful radio emission. However, the restrictions imposed by the small sub-sample sizes, and the availability

of only upper limits for nearly half of the RQQs, necessarily make these conclusions tentative. The determination of reliable host galaxy luminosities for larger numbers of quasars, coupled with new deeper radio observations of the undetected RQQs (see Chapter 7) should assist in clarifying this issue.

Chapter 6

The Evolution of 3CR Radio Galaxies from z=1

The results of the low-redshift HST host-galaxy survey clearly indicated that these objects are, in their global structural parameters at least, normal massive ellipticals. An interesting question arising from this work is, what form of evolution links these objects with their higher-redshift counterparts? This chapter examines this question by reporting on an investigation of the properties of an existing HST WFPC2 survey of powerful 3CR radio galaxies at $z \simeq 1$.

6.1 Introduction

It has been known since the early 1980's that the hosts of powerful radio galaxies display a tight relation between the K-band magnitude and redshift (Lilly & Longair 1984). In recent years it has been shown that, at least out to $z = 1$, essentially the same relation is followed by both the less powerful Parkes Selected Regions (PSR) and 6C radio galaxies (Dunlop *et al.* 1989; Eales *et al.* 1997) and by brightest cluster galaxies (Aragón-Salamanca *et al.* 1998, Collins & Mann 1997). When the K-band magnitudes of the 3CR galaxies are corrected for the expected effects of passive evolution of their

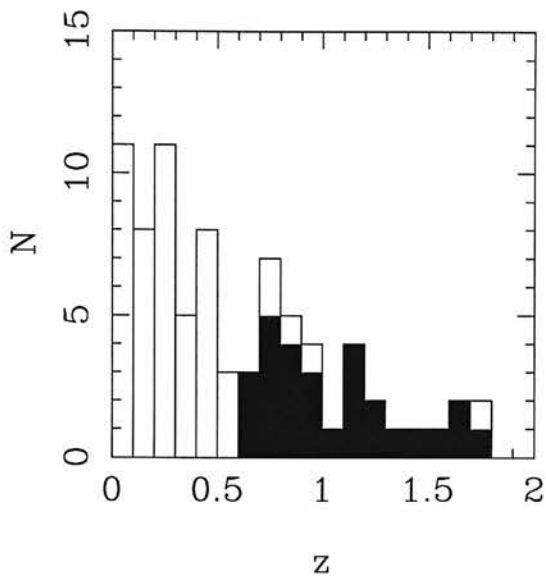

Figure 6.1: The redshift distribution of the complete 79 object FRII 3CR subsample (Laing *et al.* 1983). The shaded objects are those included in the Best *et al.* sample. Reproduced from Best *et al.* 1997.

stellar populations they appear to represent rather good standard candles from the present day out to redshift one and greater. Consequently, for many years it was widely accepted that the tightness of the $K-z$ relation for the 3CR radio galaxies could be most naturally explained by the most powerful radio galaxies having a rather well-defined mass, being formed at $z \gg 1$, and evolving basically passively thereafter.

However, this long-held view has recently been challenged in a series of papers by Best, Longair & Röttgering (1997,1998), hereafter BLR. Between 1994–1996 BLR undertook an extensive study of a virtually complete sample of 28 powerful FRII 3CR galaxies in the redshift range $0.6 < z < 1.8$ (see Fig 6.1). BLR obtained V and I–band HST images, J and K–band UKIRT images, and complimentary radio observations at 8.4 GHz with the VLA.

BLR made use of the four broad–band images they obtained for each of their sources to perform spectral synthesis fitting. The four broad–band fluxes were fitted by a simple two-component model consisting of an old stellar population and a power-law contribution which represented any possible aligned component. The stellar population SEDs were constructed from the models of Bruzual & Charlot (1993), and assumed a

1-Gyr burst of star formation at $z_{for} = 10$, with the stars evolving passively from that point onwards to the redshift of the particular 3CR galaxy. The assumed form of any possible nuclear/aligned emission was a power-law of the form $f_\nu \alpha \nu^{-0.4}$ which was used as a compromise between the likely contributions of quasar/starburst/dust scattered emission. The results of this fitting procedure (BLR 1998) show that the broad–band fluxes from these 3CR galaxies are fully consistent with that expected from an old passively evolving stellar population, as required in the traditional interpretation of the $K - z$ relation.

However, the results of the determination of the elliptical galaxy half-light radii (r_e) performed by BLR, combined with a summary of the literature concerning the environments of 3CR galaxies at high and low redshift, led BLR to challenge the traditional view of the $K - z$ relation. Using the method of fitting de Vaucouleurs templates to azimuthally averaged luminosity profiles, BLR produced best–fit scalelengths for 19 of their 28 objects (excluding 3C41 and 3C22 which have a large nuclear contribution (Leyshon & Eales 1998) not dealt with in the BLR fitting scheme). The results of this profile fitting revealed a mean scalelength of $r_e = 14.7 \pm 1.3$ kpc ($\Omega_0 = 1, H_0 = 50$). As pointed out by BLR this is significantly larger than the $r_e = 8.2 \pm 1$ kpc found to be typical of low redshift ellipticals by Schombert (1987), and only around a factor of two smaller than the average scalelength of low-z brightest cluster galaxies, $r_e = 32.7 \pm 1.1$ kpc, found by the same author. Combining this result with the $L \alpha r_e^{0.7}$ relation found by Kormendy (1977), and confirmed by the modelling results of the HST AGN sample presented in Chapter 4, BLR argue that even at $z = 1$ the hosts of 3CR radio galaxies are highly evolved massive systems, larger by a factor of two than their low-z counterparts.

Combining their determination of large scalelengths for the $z = 1$ 3CR galaxies with results from the literature concerning the environments of high redshift radio galaxies (see BLR 1998 for a review), BLR concluded that the passive appearance of the $K - z$ relation is a cosmic conspiracy. The general picture given by existing studies is that the environments of $z \simeq 1$ 3CR's are consistent with moderately rich clusters; galaxy–galaxy cross-correlation function measures are consistent with Abell class 0, or richer (Hill & Lilly 1991), while multi-colour imaging shows many companion objects

consistent with passively evolving coeval galaxies (Dickinson 1997). As pointed out by BLR, the same is not found in existing studies of the environments of low redshift 3CR's (Prestage and Peacock 1988), where it has been reported that these objects reside in fairly low-density environments and have smaller characteristic sizes and luminosities than their high-redshift counterparts (Lilly and Prestage 1987).

On the basis of the apparent redshift dependence of both 3CR galaxy size and cluster environment, BLR argued that the 3CR galaxies at $z = 0$ and $z = 1$ cannot be linked by a simple "closed-box" passive evolution scheme. In the picture favoured by BLR, the $K - z$ relation can be explained by the two 3CR galaxy samples having different dynamical evolutionary histories, but being observed at the points in their respective histories where they both contain a characteristic mass of stars; a few times $10^{11}\,M_{\odot}$. The $z \simeq 1$ 3CR galaxies would reach this mass first due to their location in a larger density peak producing strong merging between $z = 3 \rightarrow 1$. The 3CR galaxies at low-z would reach the characteristic mass later through merging within their weaker cluster environment between $z = 1$ and the present day, as is expected in many hierarchical galaxy formation models (Kauffmann 1999). The 3CR galaxies at $z = 1$ would obviously also grow through merger activity in this redshift range and would become the radio dormant BCG we see today at low redshift, radio activity having ceased presumably due to the lack of available gas to feed their central black-hole. This picture is both consistent and appealing, but it is motivated by confidence in the result that 3CR galaxy sizes differ substantially between $z = 1$ and $z = 0$, together with the unquestioning acceptance of environmental studies which now date back $10 - 15$ years.

It was a careful examination of the methods used by BLR in determining their scale-lengths which provided the original motivation for the work presented in this chapter. As mentioned above, scalelengths were presented by BLR for 19 of their 28 object sample (the images of the excluded 9 objects having poor signal-to-noise or suffering from extreme aligned emission). However, only 6 of these 19 scalelengths where actually determined from the high resolution HST imaging. The reason for this is that the one-dimensional profile fitting technique employed was unable to cope with the masking of significant contamination by companion objects or aligned emission. The

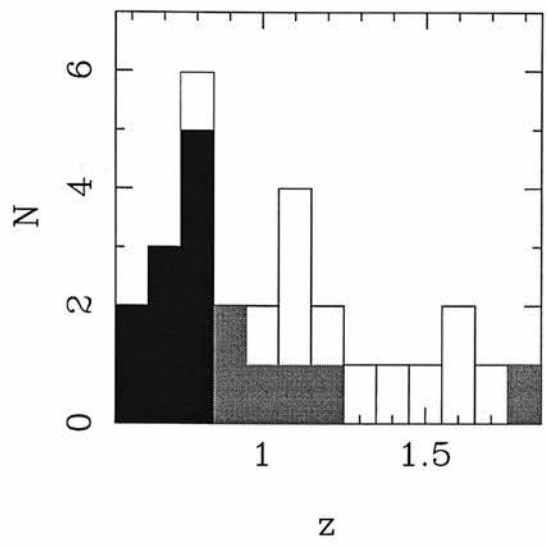

Figure 6.2: Histogram showing the redshift distribution of the virtually complete Best *et al.* sample. Objects shaded grey and black are objects which have been successfully modelled during this re-analysis. Objects shaded in black are members of the 10-object sub-sample.

majority of the scalelength information presented by BLR was in fact derived from the analysis of their K-band imaging data obtained at UKIRT. As reported by BLR, this imaging was obtained in $1''$ seeing conditions with typically 54 minutes of on-source integration which, considering the redshift range of the objects, leaves a relatively small amount of data which has both good signal-to-noise and is free from substantial seeing effects. The use of an analytical gaussian function to represent what has proven to be the extremely complicated IRCAM3 PSF (see Chapter 4) casts further doubt on the quoted scalelength values. Experience gained from the comparison of the modelling results of the $z \simeq 0.2$ AGN host galaxies with those previously obtained from typically $1''$ K-band imaging (Dunlop *et al.* 1993, Taylor *et al.* 1996) has demonstrated that the twin benefits of high resolution and a temporally stable PSF tend to combine to revise the best-fitting galaxy scalelength downwards (see Chapter 4). The main reason for this systematic trend appears to be that the high spatial resolution provided by HST allows the reliable identification of separate companion objects and their subsequent masking from the modelling process, preventing the inclusion of extra flux from biasing the scalelength determination to higher values. This effect is obviously only going to be strengthened at redshifts of $z \sim 1$ where the angular separation between companion objects and the target can easily be of the same order as the typical seeing experienced

during the BLR UKIRT observations.

Given these considerations it was felt worthwhile to re-examine the publically available HST data to determine whether the use of the full two-dimensional analysis utilised in the $z \simeq 0.2$ AGN host-galaxy programme would produce significantly different scale-length figures from those published by BLR.

6.2 Data Reduction

All the HST images taken of the 3CR galaxies in the 28-object BLR sample were obtained from the HST archive facility[1]. A detailed list of redshifts, filters and exposure times can be found in Table 1 of BLR (1997). An investigation of the shorter-wavelength exposures of each object (mainly F555W, F622W) confirmed that they were either of insufficient signal-to-noise to be useful, or dominated by emission aligned with the radio axis. Of the 28 objects in the sample, preliminary analysis of the I-band images revealed a total of 16 which could be successfully modelled with the two-dimensional technique. The observational parameters of these 16 objects are detailed in Table 6.1 and illustrated as part of the full sample in Fig 6.2 .

For each object there are two CR-SPLIT I-band exposures of unequal length available, together giving a typical exposure time of $\simeq$ 1800 seconds. The initial processing of the images, flat-fielding and bias removal, was carried out by the standard HST pipeline. The two exposures were then combined using the IRAF task CRREJ, which successfully removes cosmic ray events using a sophisticated sigma-clipping algorithm. The next step in the reduction process was the fitting of a plane to the image with the 3CR galaxy masked out, to accurately determine the sky background while allowing for any residual flat-fielding gradients that may have been present. The final step was the production of a two-dimensional mask for each source which eliminated any companion objects, or aligned emission, from the model-fitting process, as well as any regions of the image that could have been biased by scattered light from nearby bright stars. The advantage of being able to mask-out substantial areas of the image while still being

[1] http://archive.stsci.edu

Source	z	Filter	Exp Time/s	$r_{1/2}$/kpc	$\mu_{1/2}$	I_c	L_{nuc}/L_{host}
3C22	0.938	F814W	1400	5.9	22.3	19.8	0.306
3C34*	0.690	F785LP	1700	23.8	24.2	18.8	0.002
3C41*	0.795	F785LP	1700	6.3	22.2	19.7	0.170
3C49*	0.621	F814W	1400	15.0	23.0	18.9	0.000
3C65	1.176	F814W	1760	9.9	24.5	20.9	0.088
3C217	0.897	F814W	1700	5.8	22.0	20.1	0.007
3C226*	0.820	F785LP	1700	8.5	22.6	19.4	0.050
3c239	1.781	F814W	2200	10.8	23.5	19.7	0.041
3C247*	0.749	F814W	2400	25.2	24.1	18.6	0.025
3c252	1.105	F814W	1700	7.3	23.2	20.5	0.000
3C277.2*	0.766	F814W	2400	7.6	22.5	19.7	0.005
3C289	0.967	F814W	1800	18.0	24.9	20.0	0.063
3C337*	0.635	F814W	1400	6.4	22.5	19.8	0.055
3C340*	0.775	F785LP	1700	4.3	21.3	19.7	0.000
3C352*	0.806	F814W	1800	18.1	24.7	19.6	0.024
3C441*	0.708	F785LP	1700	10.9	22.7	19.1	0.023

Table 6.1: The results of the two-dimensional modelling of the 16-objects from the Best *et al.* $z \simeq 1$ 3CR sample which did not suffer from excessive aligned emission. Listed in column 5 are the fitted scalelengths in kpc, with the surface-brightness at that scalelength in Cousins I-magnitudes arcsec^{-2} given in column 6. Column 7 lists the integrated apparent I–band magnitude of the best-fit host galaxy with column 8 giving the ratio of the integrated luminosity of the best-fit nuclear component and host galaxy. Objects labelled with a * are members of the 10-object sub-sample.

able to run the model fitting in two-dimensions has allowed greater use to be made of the HST data than BLR.

6.2.1 Empirical PSF Determination

Simple radial surface-brightness plots for the 16 objects chosen for modelling reveals that there is sufficient signal-to-noise to allow fitting to a typical radius of $\simeq 4''$. It is therefore necessary to have a point spread function (PSF) to convolve the model galaxies with, which has good signal-to-noise out to at least this radius. Due to the synthetic PSFs produced by the TINYTIM software package (Krist 1998) being unable to reproduce the WFPC2's scattered light halo outside a radius of $\simeq 1.5''$, it is clear that an empirical PSF is required for the modelling of these data (see Chapter 3). A glance at Table 6.1 reveals that all of the exposures utilised here were imaged through either the F785LP or F814W filters. This required the acquisition of two relatively deep PSFs imaged with the correct filter/chip combination, which were also located close to the average chip position of the 3CR galaxies, in order to avoid the noticeable positional variation of the WFPC2 PSF. An interrogation of the HST PSF search tool [2] produced disappointing results, with all available PSFs either too faint or too small in angular extent.

Fortunately, two suitable stars were present on the exposures of 3C41 (F785LP) and 3C239 (F814W). Due to the need for sufficient depth in the PSF wings, both of these stars had saturated cores in even the shortest exposures. To overcome this problem a modified version of the PSF re-sampling technique described in Chapter 3 was implemented. Both PSFs were only saturated within a radius of $\leq 0.3''$ of their core, well inside the radius where TINYTIM can accurately reproduce the empirical PSF. Making use of this, the two PSFs had their core replaced with the equivalent TINYTIM model, the relative scaling being determined by matching the flux in an annulus between $0.4'' < r < 0.7''$. Another advantage of this approach is that due to TINYTIM's ability to produce model PSFs at up to 50 times oversampling, sub-pixel centring of the PSF can be matched to that of the galaxies to an accuracy of $\leq 0.005''$.

[2] http://www.stsci.edu/instruments/wfpc2/

Source	z	$\mu_{1/2}$	M_{I_C}
3C34	0.690	21.7	−24.9
3C41	0.795	19.4	−24.5
3C49	0.621	20.5	−24.5
3C226	0.820	19.7	−24.9
3C247	0.749	21.2	−25.4
3C277.2	0.766	19.5	−24.4
3C337	0.635	19.9	−23.7
3C340	0.775	18.5	−24.4
3C352	0.806	21.1	−24.7
3C441	0.708	20.1	−24.7

Table 6.2: The absolute magnitudes and characteristic surface-brightness of the 10-object sub-sample ($H_0 = 50, \Omega_0 = 1$)

6.3 Modelling

The modelling of these objects proceeded in an identical fashion to that of the $z \simeq 0.2$ AGN sample, described in Chapter 4. Each object was modelled with both a standard Freeman disc template and de Vaucouleurs $r^{1/4}$ profile, with no *a priori* assumptions being made about position angle, axial ratio or any possible central point-source contribution. Prior to the modelling of each source a maximum radius, outside of which pixels would be excluded due to insufficient signal-to-noise, was determined by an examination of the one-dimensional surface-brightness profile. The median value for this outer radius was $4''$, corresponding to a physical radius of 33 kpc at the median redshift of $z = 0.8$ ($H_0 = 50, \Omega_0 = 1$). This is reasonably well matched to the outer radius of $12''$ (50 kpc) used for each of the radio galaxies in the $z = 0.2$ AGN sample, ensuring that the same physical region of the galaxy light distribution is under investigation in both redshift regimes. The modelling technique strongly preferred a $r^{1/4}$ host galaxy for all 16 objects analysed. The quality of the fits was good, with no significant residual flux.

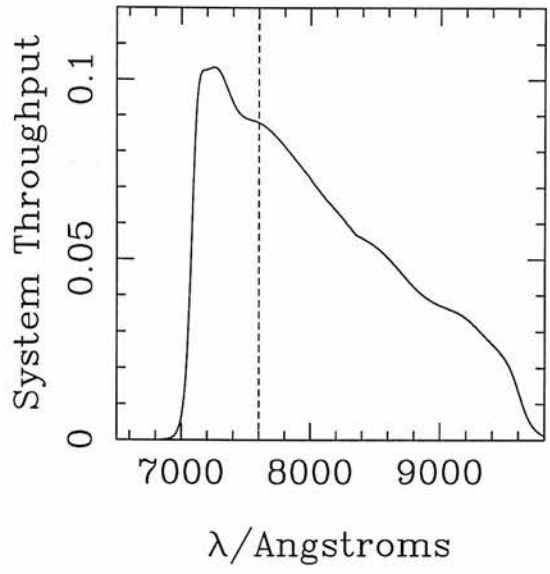

Figure 6.3: The F814W filter profile including the system response and quantum efficiency of WFPC2. Also shown is the location of the 4000Å break of an elliptical galaxy spectrum observed at a redshift of $z = 0.9$

6.4 Results

In this section the scalelength, absolute luminosity and Kormendy relation results from the two-dimensional modelling of the $z \simeq 0.8$ objects are presented. Due to the significant effect that choice of cosmology can have on angular diameter, cosmological dimming and look-back time over this redshift range, results are given for a range of possible cosmologies. Four different representative scenarios are considered featuring two values of H_0 (50,70), together with both open ($\Omega_0 = 0.1$) and flat ($\Omega_0 = 1$) geometry.

The results from the modelling of all 16 HST objects are presented in Table 6.1. The main conclusions reached from this modelling work are based largely on the results for a 10-object sub-sample. The sub-sample consists of the low-redshift end of the BLR sample and is illustrated in Fig 6.2. The remaining 6 objects ($z \geq 0.9$) have been excluded from the following analysis due to the incursion of the 4000Å break into the HST F814W filter. The throughput of the F814W filter is shown in Fig 6.3 complete with the system response and CCD quantum efficiency. As can be seen from this Figure,

Ω_0	H_0	median r_e / kpc	$< r_e >$ / kpc
1	50	9.7	12.6 ± 2.3
1	70	8.2	9.3 ± 1.6
0.1	50	11.5	14.8 ± 2.7
0.1	70	8.2	10.6 ± 1.9

Table 6.3: The scalelength results from the two-dimensional modelling of the $z \simeq 0.8$ sub-sample. Columns one and two detail the choice of cosmology. Column three gives the median scalelength values for the 10-objects in the sample. Column four gives the corresponding mean values together with the standard error.

for objects with redshifts $z \geq 0.9$ this filter will bridge the 4000Å break, meaning that it can no longer be assumed that the detected flux has originated from the dominant old stellar population. Given that the alignment effect in radio galaxies is stronger in the rest-frame UV than at longer wavelengths it is to be expected that these objects are contaminated by a significant aligned component. The 10-object sub-sample has the advantage of having a tight redshift distribution with a mean of 0.74 ± 0.07 and a median of 0.76, which is well matched by the distribution of the 10 radio galaxies studied at low-z, with its mean redshift of 0.20 ± 0.04 and median of 0.20. This allows a direct comparison between the two samples without the added complication of allowing for significant evolutionary effects within the samples themselves.

6.4.1 Scalelengths

The results of the determination of galaxy half-light radius (r_e) for the 10-objects in the $z \simeq 0.8$ sub-sample are presented in Table 6.3. Two features of this table are immediately obvious. Firstly, it is clear that regardless of cosmology the derived half-light radii are remarkably consistent, with both the mean and median values displaying a range of only 4 kpc. Secondly, the mean scalelength is systematically larger than the median in all four cosmologies, consistent with the suggestion from Fig 6.4 that the distribution of scalelengths from the full 16-object sample, and indeed the 20 radio-loud AGN at $z \simeq 0.2$, has a substantial tail toward high values.

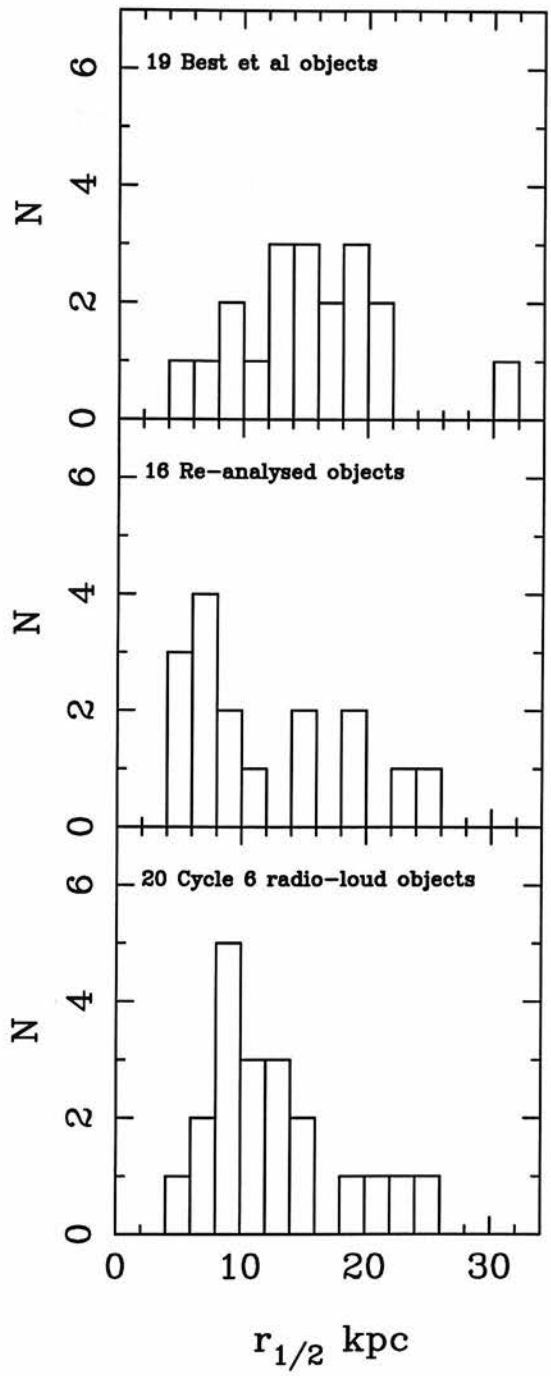

Figure 6.4: A comparison of the distribution of scalelengths derived from the modelling of the $z \simeq 0.8$ 3CR galaxies with that obtained by Best *et al.* Also shown is the distribution of scalelengths obtained for the 10 radio galaxies and 10 radio-loud quasars in the HST $z \simeq 0.2$ AGN host-galaxy programme. All three histograms assume $H_0 = 50, \Omega_0 = 1$

Given that the scalelength results obtained by BLR are quoted assuming $H_0 = 50, \Omega_0 = 1.0$ it is straightforward to investigate what differences exist between their scalelength determinations and those presented here. Due to the fact that most of the BLR scalelength information is derived from their K–band observations rather than the HST images, it is not the case that they have published a scalelength value for each of the objects re-modelled in this paper. In order to perform a comparison between the two sets of results it has been necessary to simply base the BLR figures on the 8-objects from our 10-object sub-sample for which they have derived a scalelength value.

Assuming $H_0 = 50, \Omega_0 = 1.0$ the mean scalelength of the 10-object sample is $r_e = 12.61 \pm 2.26$ kpc with a median of 9.70 kpc. The corresponding BLR-derived values for 8 of these 10 objects are $r_e = 15.15 \pm 2.71$ kpc with a median of 14.95 kpc. Given the small number statistics that are available, and the inherent difficulty in constraining galaxy scalelengths, the median is probably the more robust measure of the typical scalelength. Using the median it can be seen from these figures that the one-dimensional analysis technique employed by BLR has systematically overestimated the characteristic size of the 3CR galaxies by $\approx 50\%$.

In order to check that the use of these two cut-down samples was not overtly biasing the results, a comparison was also performed between the full 16-object sample and the 12-objects from this sample for which there is also a BLR-derived scalelength figure available. The mean scalelength of the 16-object sample is $r_e = 11.48 \pm 1.59$ kpc with a median of 9.20 kpc. The corresponding BLR-derived values for 12 of these objects are $r_e = 15.66 \pm 1.91$ kpc with a median of 15.45 kpc. It can be seen from this that the use of the expanded samples strengthens the conclusion that the BLR scalelengths are overestimated, with the median BLR scalelength being $\approx 70\%$ greater than the two-dimensional modelling results presented here.

6.4.2 Absolute Magnitudes

The absolute Cousins I-band magnitudes for the $z \simeq 0.8$ and $z \simeq 0.2$ sub-samples are listed in Table 6.4 for the four different cosmologies. The values shown are calculated

Ω_0	H_0	z	Median M_I	$< M_I >$
1.0	50	0.2	-24.52	-23.45 ± 0.16
1.0	50	0.8	-24.60	-24.62 ± 0.13
1.0	70	0.2	-23.69	-23.72 ± 0.16
1.0	70	0.8	-23.87	-23.89 ± 0.13
0.1	50	0.2	-24.54	-24.55 ± 0.16
0.1	50	0.8	-24.98	-25.07 ± 0.18
0.1	70	0.2	-23.80	-23.81 ± 0.16
0.1	70	0.8	-24.25	-24.24 ± 0.13

Table 6.4: The absolute I-band magnitudes of the two 10-object radio galaxy sub-samples. Column four gives the median figures with column five listing the corresponding mean figures complete with standard error.

from integrating the best-fit de Vaucouleurs profile to infinite radius in order to be consistent with the results for the low-z AGN hosts . As was pointed out in Section 6.2, the objects comprising the sub-sample were imaged through two separate HST filters; F814W and F785LP. The F814W filter is a member of the standard HST filter set and closely mimics the Cousins I-band filter. As a result, it was decided to convert all of the integrated apparent magnitudes to their equivalent Cousins I-band value. The 5 objects from the sub-sample imaged with the F814W filter had no correction applied to them since the similarity of the F814W and Cousins I-band filters is such that for elliptical galaxies the difference in magnitude is expected to be less than 0.05 in all cases. This level of photometric accuracy is substantially greater than is possible in the face of the uncertainties in determining the host magnitudes.

The throughput for the F785LP filter is significantly different from that of the Cousins I-band filter. The conversion from magnitudes obtained through this filter to Cousins I-band magnitudes is therefore more complicated. The original strategy to overcome this problem was to make use of the one object from the 16-object sample (3C239) for which there are exposures in both filters available with comparable signal-to-noise. However, this object has the highest redshift, $z = 1.781$, of all of the 28 objects in the BLR sample and subsequently the two images were too faint to get a

reliable conversion. In addition to this, 3C239 has a highly distorted morphology in the HST images (BLR 1997), making it unclear whether a conversion factor obtained from this object would be applicable to the mostly undistorted objects in the sub-sample. In light of this, the method used to convert the F785LP fluxes for each host to the equivalent F814W figure, and hence Cousins I-band magnitude, was to predict the count rates R_{object} ($e^{-1}s^{-1}\mathrm{pixel}^{-1}$) of a source of apparent visual magnitude V in the two filters using the filter ratios of Holtzman *et al* 1995.

The cosmology-independent k-corrections for each object, produced by the blueward shifting of the I-band filter along the galaxy spectrum with increasing redshift, were calculated from the figures presented for a burst-elliptical galaxy by Rocca-Volmerange & Guiderdoni (1988). Given that the predictions produced by different spectral synthesis codes can differ significantly (Charlot *et al.* 1996) it was considered worthwhile to make an independent check of the validity of these k-corrections. Due to the restriction of this analysis to the 10-object sub-sample, for which the images sample galaxy light long-ward of the 4000Å break, it is possible to estimate the necessary cosmological k-corrections by modelling the galaxy spectrum as a power-law of the form $f_\nu \alpha \nu^{-\alpha}$, where α is the spectral index. The value of α appropriate for radio galaxies imaged in the I-band was estimated to be $\alpha \simeq 2$ from a typical old ($\geq$ 12Gyr) elliptical galaxy spectrum. This is in good agreement with the value of $\alpha = 1.82$ needed to reproduce the k-corrections of Rocca-Volmerange and Guiderdoni (1988). The question of whether the absolute magnitudes presented in Table 6.4 are substantially different from the results previously obtained for the $z = 0.2$ radio galaxies is addressed within Section 6.5.

6.4.3 The Kormendy Relation

Given that the hosts of the 10 radio galaxies within the sub-sample are well fitted by a standard de Vaucouleurs galaxy template, it is interesting to see whether the parameters obtained from these fits produce a Kormendy relation comparable to that followed by low-z inactive ellipticals (and the hosts of the $z = 0.2$ AGN, see Section 4.5). The $\mu_{1/2}$ values required to construct the Kormendy relation have been corrected

$\mu_{1/2} = 3.51_{\pm 0.36} \log r_{1/2} + 16.53_{\pm 0.38}$	$\Omega_0 = 1.0$	$H_0 = 50$
$\mu_{1/2} = 3.51_{\pm 0.36} \log r_{1/2} + 17.05_{\pm 0.33}$	$\Omega_0 = 1.0$	$H_0 = 70$
$\mu_{1/2} = 3.51_{\pm 0.38} \log r_{1/2} + 16.28_{\pm 0.42}$	$\Omega_0 = 0.1$	$H_0 = 50$
$\mu_{1/2} = 3.51_{\pm 0.38} \log r_{1/2} + 16.80_{\pm 0.37}$	$\Omega_0 = 0.1$	$H_0 = 70$

Table 6.5: The best-fitting Kormendy relations for the 10 $z \simeq 0.8$ 3CR galaxies under four different choices of cosmology.

for the cosmological dimming of surface-brightness according to:

$$\frac{I_1}{I_2} = \frac{(1+z_2)^{3+\alpha}}{(1+z_1)^{3+\alpha}} \tag{6.1}$$

where a value of $\alpha = 1.8$ has been assumed. The resulting $\mu_{1/2} - r_{1/2}$ relation for the four cosmologies are shown in Table 6.5. It is clear from this that the choice of cosmology makes no significant difference to the slope of the Kormendy relation (as expected given the small redshift range of the objects), and that in all cases this slope is consistent with that of $\simeq 3$ displayed by inactive low-z ellipticals (Kormendy 1977).

It is worth noting that the $r_{1/2}$ and $\mu_{1/2}$ parameters from the one-dimensional modelling of BLR failed to produce a $\mu_{1/2} - r_{1/2}$ relation which was consistent with the expected slope of $\simeq 3$. The modelling results of BLR had the $z \simeq 1$ 3CR galaxies lying along a constant luminosity slope of 5, exactly as is expected when the galaxy luminosities have been well determined but the scalelengths have not been constrained (Abraham *et al.* 1992). The fact that the relation presented above is consistent with the Kormendy relation, within the errors, can therefore be taken as further evidence that the two-dimensional modelling has been much more successful in constraining the scalelengths of the sub-sample objects. The possibility of using the Kormendy relations derived above to test for the effects of passive or dynamical evolution is explored in section 6.5.3.

Ω_0	H_0	median r_e / kpc	$< r_e >$ / kpc
1	50	11.3	13.8 ± 2.2
1	70	8.1	9.8 ± 1.6
0.1	50	11.9	14.4 ± 2.3
0.1	70	8.5	10.3 ± 1.6

Table 6.6: The scalelength results from the two-dimensional modelling of the $z \simeq 0.2$ sub-sample. Columns one and two detail the choice of cosmology. Column three gives the median scalelength values for the 10-objects in the sample. Column four gives the corresponding mean values together with the standard error.

6.5 Comparison with low-redshift Radio Galaxies

6.5.1 Scalelengths

The derived median and mean scalelengths for the 10-source $z \simeq 0.2$ radio galaxy sample from the low-z AGN host-galaxy study are presented in Table 6.6. A comparison of these results with those presented for the $z \simeq 0.8$ sub-sample in Table 6.3 shows the two groups of galaxies to have very similar characteristic scalelengths. The poorest agreement between the two sets of results is for the $\Omega = 1.0$, $H_0 = 50$ cosmology. However, even in this case the figures are consistent to within the errors. In the other three cosmologies the median and mean scalelengths for the two samples are virtually identical, differing by ≤ 0.5 kpc in all cases. The similarity between the scalelength distributions of the two sub-samples is confirmed by an application of the Kolmogorov–Smirnov (KS) test. For the two $\Omega_0 = 1.0$ cosmologies the KS test returns a probability of 0.68 that the two samples are drawn from the same underlying distribution. This conclusion is even stronger in the $\Omega_0 = 0.1$ cosmologies where the KS test returns a probability of 0.97 that the two distributions are the same. Therefore, contrary to the results of BLR, no evidence has been found that the galaxies comprising the $z \simeq 0.8$ sub-sample are systematically larger than their $z \simeq 0.2$ counterparts.

6.5.2 Absolute Luminosity

In order to allow a direct comparison of the characteristic luminosities of the low- and high-redshift radio galaxy sub-samples, and thereby look for any evidence of significant merger activity, it is first necessary to correct for the different filters and the expected passive evolution of the stellar populations. To achieve this it was decided to convert the $z \simeq 0.2$ R-band magnitudes to their I-band equivalents, and then to predict the brightening of the stellar population between $z = 0.2$ and $z = 0.8$ due to passive evolution alone. The present-day colour of an elliptical galaxy formed at high redshift ($z \geq 3$) has been taken as $R - I = 0.7$ (Fukugita *et al.* 1995). The corrections to be made for the effects of passive evolution have been calculated using the synthetic galaxy spectral models of Jimenez *et al.* (1996) using the chosen set of four possible cosmologies. Several different galaxy formation redshifts were considered to investigate their effects on the resulting correction. A comparison between the predicted amount of I-band passive evolution between $z = 0.2$ and $z = 0.8$ and the difference in median absolute luminosity of the two samples is presented in Table 6.7.

It is immediately clear from these results that the difference in absolute I-band luminosity between the $z \simeq 0.2$ and $z \simeq 0.8$ samples is inconsistent with the amount of passive evolution predicted by the stellar synthesis models within the two Einstein-de Sitter cosmologies. This is still true even in the $\Omega_0 = 1$ model which allows present-day ellipticals to be as old as possible ($z_{for} = 10, H_0 = 50$); this model still requires 2.5 times more magnitudes of passive evolution than is seen in the data.

Adoption of either of the open cosmologies results in a measured difference in absolute luminosity of $\simeq 0.5$ mags between the two galaxy samples (columns 3 & 4). As can be seen from Table 6.7, this luminosity difference is formally consistent with the expected passive evolution in both open cosmologies, for all alternative formation redshifts. However, it is interesting to note from Table 6.7 that the $H_0 = 70, \Omega_0 = 0.1$ cosmology clearly provides the best match between the data and the spectrophotometric model predictions. In this cosmological picture the model predictions are perfectly consistent with the data for all star formation redshifts of $z \geq 4$, in good agreement with recent discoveries of old stellar population ellipticals at redshifts of $z = 1.5 \rightarrow 2$

Ω_0	H_0	ΔM_{med}	ΔM_{mean}	ΔM_{model}		
				$z_{for}=10$	$z_{for}=5$	$z_{for}=3$
1	50	0.17	0.18±0.16	0.52	0.60	0.70
1	70	0.17	0.18±0.16	0.63	0.60	0.56
0.1	50	0.52	0.44±0.16	0.26	0.24	0.46
0.1	70	0.43	0.45±0.16	0.38	0.51	0.64

Table 6.7: The results of the tests to determine the influence of different cosmology and formation redshift upon the amount of passive evolution expected between $z = 0.8$ and $z = 0.2$. Columns one and two list the cosmological parameters for each test. Column three lists the amount of evolution required to reconcile the median of the two absolute magnitude distributions. Column four gives the corresponding mean figures complete with standard errors. Columns 5-7 list the amount of passive evolution between $z = 0.2$ and $z = 0.8$ predicted by the spectrophotometric modelling for three galaxy formation redshifts. (The apparently anomalous trend displayed by the $\Omega_0 = 1, H_0 = 70, z_{for} = 3$ model is due to the fact that even at $z = 0.2$ a galaxy is only 6 Gyr old, and remains relatively bright at I.)

(Dunlop *et al.* 1996, Spinrad *et al.* 1997, Stiavelli *et al.* 1999).

6.5.3 Kormendy Relation

If the two samples of radio galaxies can truly be linked by a single population of passively evolving ellipticals it is to be expected that they should follow Kormendy relations which are identical except for a simple vertical shift in surface-brightness. After making the appropriate surface-brightness corrections (Section 6.4.3) and $R \rightarrow I$-band filter transformation (Section 6.5.2) the least-squares fit to the Kormendy relations formed by the $z \simeq 0.2$ radio galaxies are shown in Table 6.8.

It can be seen from this that, as for the $z \simeq 0.8$ galaxies, the choice of cosmology makes little difference to the slope of the Kormendy relation, although the normalization does change significantly. It is also apparent that the low-z objects appear to

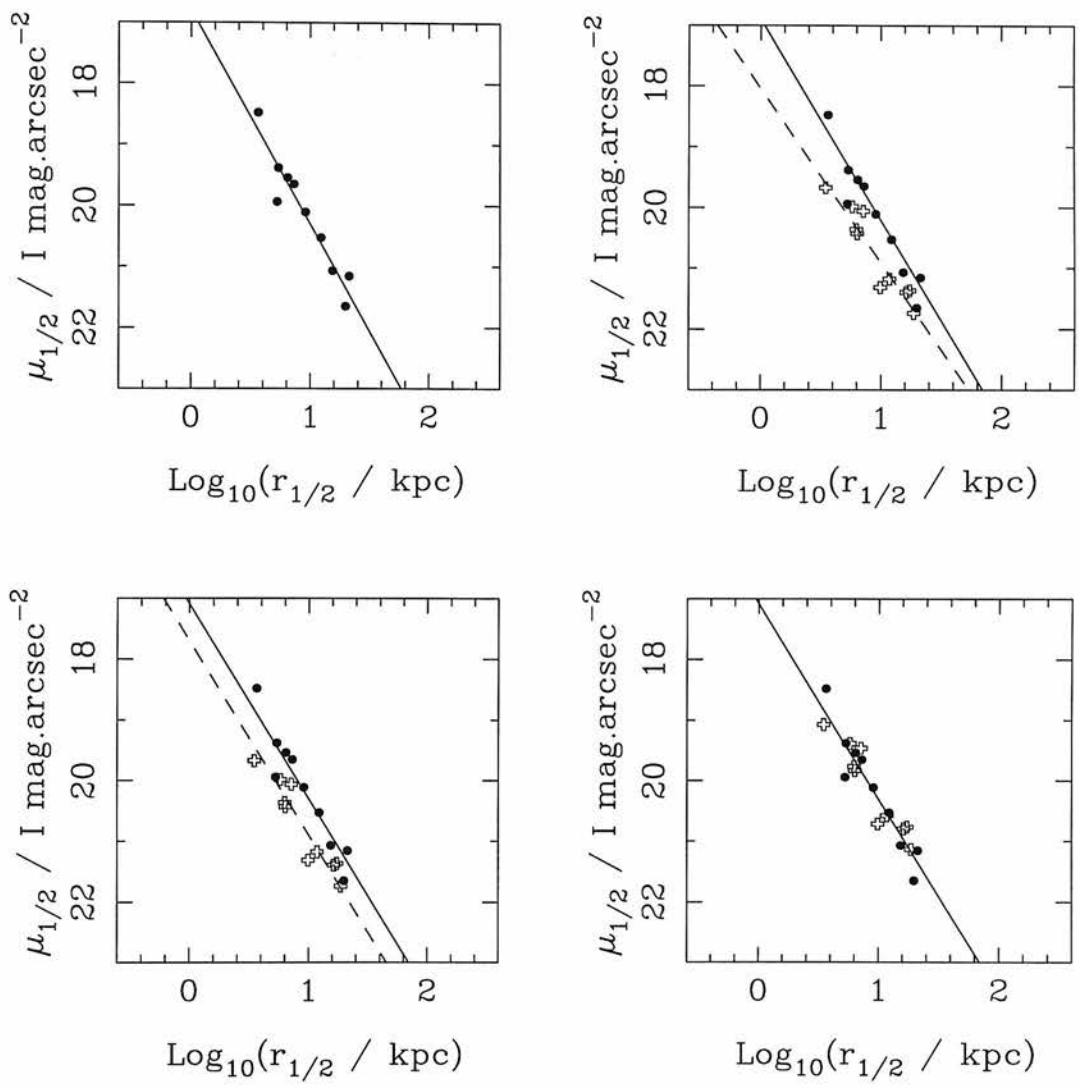

Figure 6.5: Shown in the top-left panel is the Kormendy relation followed by the $z \simeq 0.8$ sub-sample which has a best-fit slope of 3.5. In the top-right panel the $z \simeq 0.2$ radio galaxies (crosses) have been added along with their best-fit relation of slope 2.9 (dashed line). In the bottom-left panel both galaxy sub-samples are shown with the best-fit relation forced to have a intermediate slope of 3.20. The bottom right figure shows the best-fit Kormendy relation (slope=3.21) produced by brightening the surface-brightness of the $z \simeq 0.2$ galaxies by 0.6 magnitudes.

$\mu_{1/2} = 2.86_{\pm 0.34} \log r_{1/2} + 17.66_{\pm 0.38}$	$\Omega_0 = 1.0$	$H_0 = 50$
$\mu_{1/2} = 2.86_{\pm 0.34} \log r_{1/2} + 18.08_{\pm 0.33}$	$\Omega_0 = 1.0$	$H_0 = 70$
$\mu_{1/2} = 2.85_{\pm 0.34} \log r_{1/2} + 17.61_{\pm 0.42}$	$\Omega_0 = 0.1$	$H_0 = 50$
$\mu_{1/2} = 2.85_{\pm 0.34} \log r_{1/2} + 18.03_{\pm 0.37}$	$\Omega_0 = 0.1$	$H_0 = 70$

Table 6.8: The best-fitting Kormendy relations for the 10 $z \simeq 0.2$ radio galaxies under four different choices of cosmology.

follow a substantially flatter relation, with a slope of 2.9 instead of 3.5, although clearly both values are consistent with the expected slope $\simeq 3$ (due to the fairly substantial formal error in the fitted slope, which is predominantly a result of the small sample size and lack of dynamic range). To facilitate a fair comparison of the high- and low-z radio galaxy Kormendy relations, the least-squares fitting was repeated with an enforced intermediate slope of 3.20 . If it is indeed the case that these two galaxy populations can be linked by passive evolution alone then the vertical shift required to reconcile the Kormendy relations should be in good agreement with both that required to match the absolute magnitudes, and the passive evolution predictions of the stellar synthesis modelling. To explore what range of vertical magnitude shifts that are allowed by the data, least-squares fits were performed (with fixed slope=3.20) not only with the best estimate of r_e for each galaxy, but with the scalelengths of the $z \simeq 0.8$ sub-sample shortened and lengthened such that the KS test showed its scalelength distribution to differ from that of the $z \simeq 0.2$ sub-sample at the 1σ level. The results of this process are presented in Table 6.9. A comparison of the figures from Table 6.9 with those of Table 6.7 shows that in the $\Omega_0 = 1.0$ models considered here it is only possible to reconcile the luminosity evolution predicted by the Kormendy relations with that predicted by the spectral modelling and the absolute magnitude distributions, separately. In these cosmologies it is impossible to force both alternative measures of the amount of luminosity evolution, and the predictions of the spectral modelling, into agreement. In contrast, the $\pm 1\sigma$ predictions from the Kormendy relations in the $\Omega_0 = 0.1$ cosmolo-

Ω_0	H_0	$\Delta M(-1\sigma)$	ΔM	$\Delta M(+1\sigma)$
1.0	50	-0.24	0.43	0.56
1.0	70	-0.24	0.44	0.58
0.1	50	0.18	0.60	0.84
0.1	70	0.19	0.60	0.84

Table 6.9: The amount of luminosity evolution predicted by forcing both galaxy sub-samples to lie on a Kormendy relation with slope 3.2. Column four lists the implied vertical shift required to over-lay the Kormendy relations of the two samples using the best-fit scalelengths of Table 6.1 converted to the appropriate cosmology. Columns 3 and 5 list the vertical shift implied by shifting the best-fit scalelengths left(-1σ) and right($+1\sigma$) until the scalelength distributions of the two sub-samples differ at the 1σ level.

gies comfortably bracket the offsets given in Table 6.7, thus leaving both alternative measures of the luminosity evolution in excellent agreement.

In theory, the Kormendy relations for the low and high-z sub-samples presented here offer an opportunity to constrain both cosmology and the prevalence of merger activity. However, in practise the effects of these are very closely coupled. For example, the results presented here can be reproduced either by pure passive evolution since $z \simeq 0.8$ in an open Universe, or by modest growth ($\simeq 20\%$ growth in scalelength & luminosity) since $z \simeq 0.8$ in an Einstein-de Sitter Universe. Despite this inherent degeneracy, either very strong growth ($\geq 50\%$) from mergers, or the apparent negative growth claimed by Best *et al.* can be strongly excluded.

6.6 Conclusion

The results from a thorough re-examination of the BLR HST images of a sample of $z \sim 1$ 3CR radio galaxies has been presented. It has been shown that, contrary to the published results of BLR, in terms of scalelength, absolute magnitudes and Kormendy relation there are no significant differences between $z \sim 0.8$ and $z \sim 0.2$ 3CR radio galaxies. The two populations appear to be fully consistent with being comprised of

old stellar populations formed at high redshift and evolving passively thereafter.

It is obviously true that the fact that both the high and low-redshift radio galaxies have absolute luminosities consistent with pure passive evolution can easily be reconciled with the involvement of some dynamic evolution. In the dynamical model this simply requires that the proto-galactic clumps which merge to produce the final galaxies were formed reasonably coevally. The results presented here do not then require that these radio galaxies must have formed in a monolithic collapse at a single redshift. However, they do suggest strongly that the vast majority of merger activity within this population of massive ellipticals must have been completed before $z \simeq 1$. Although this is difficult to achieve with standard $\Omega_0 = 1$ hierarchical clustering models it is not necessarily inconsistent with semi-analytical galaxy formation models in a $\Omega_0 = 0.3, \Lambda = 0.7$ cosmology, where as much as 70% of present day ellipticals can already be in place by $z \simeq 1$ (Kauffman & Charlot 1999).

The crucial question still to be answered is whether or not it can be proven that a significant difference in cluster environment does exist between the two populations. If it can be shown that this is definitely the case then the argument forwarded by BLR that we are observing the effects of dynamical evolution producing the characteristic mass required for powerful radio emission at the two different epochs remains tenable, despite the fact it cannot be detected via a significant difference in scalelengths. However, as was discussed in Section 6.1, while there have been numerous surveys carried out recently tackling the environments of high-z radio sources, the work on the low-z environments looks to be subject to possible systematic error. This suspicion is further strengthened by the comparison of the $z \simeq 0.2$ radio galaxy sub-sample with bright cluster galaxies performed in Chapter 4, which showed the low-z radio galaxies to have luminosities, scalelengths and numbers of apparent companion objects apparently consistent with Abell clusters of class $0 \rightarrow 1$.

In an attempt to disentangle the radio galaxy environment problem, more near-infrared observations of the low-z radio galaxies and quasars from the HST sample are planned, to compliment the complete set of B–band optical CCD images for this sample obtained at the INT in 1992 (Taylor 1995) which cover an angular area of

$\sim 4''$ square. These images would be well complimented by observations using the recently commissioned UFTI camera on UKIRT. UFTI is a near-infrared camera using a 1024×1024 HgCdTe array which is sensitive from $1 \rightarrow 2.5\ \mu m$. Each pixel is $0.091''$ square giving a total field of view of $92''$. Using a simple mosaic technique the relatively wide-field of UFTI could be used to provide sensitive K-band observations well matched in area coverage to the existing B–band images. This combined dataset would give the opportunity to produce $B - K$ colours for all objects in the field, sufficient to perform number counts of the potential companion objects consistent with being at the same redshift as the target.

If it transpires that there is no significant difference in 3CR environments at high and low-z, then a much simpler picture of powerful radio galaxy evolution emerges. Combined with the scalelength evidence presented here, this would suggest that the host galaxies of powerful radio sources are basically the same sort of objects at *all* redshifts from $z = 0 \rightarrow 1$. In this picture the fall-off in 3CR radio power over this redshift range would simply be due to the progressively smaller amount of gas available to feed the central engine. Present day BCGs in this scenario have the potential to be powerful radio sources but are dormant due to not having been involved in a recent gravitational interaction with which to trigger gas in-fall, or simply to having exhausted all their available gas.

Chapter 7

Conclusions and Further Work

7.1 Conclusions

In the opening chapter of this thesis several key questions relating to the study of AGN host galaxies were identified as having been left unanswered by previous research. The opening section of this final chapter returns to these questions, to assess what progress has been made through the work on the HST imaging study. The second section describes several further conclusions which have been reached as a result of the related work on AGN black-hole masses and the evolution of 3CR radio galaxies. The final section of this chapter describes work which is planned, or in progress at the time of submission, which represents the logical next step in AGN host-galaxy research.

7.1.1 Morphology and Luminosity

The long-running debate over the possible existence of a host-galaxy morphological dichotomy between RLQs and RQQs has been effectively settled by this work. All of the RG, and all of the quasars with total luminosities of $M_V < -23.0$, have been shown to have host galaxies whose luminosity is bulge-dominated. The two RQQ sources with disc-dominated host galaxies have been found to have luminosities below the adopted Seyfert/quasar divide of $M_V = -23.0$. With the exclusion of these two sources, 10/10

RG, 10/10 RLQ and 9/11 RQQ have host galaxies which are well described by a single-component $r^{1/4}$ surface-brightness distribution. Furthermore, the match between the host galaxies and the standard $r^{1/4}$ law has been found to be sufficiently close that modelling with β left as a free parameter has shown 30/33 hosts to have β values in the range $0.2 < \beta < 0.3$.

The AGN hosts have been found to have much larger luminosities than average galaxies, with *all* hosts having $L \geq L^{\star}$, and 25/33 having $L \geq 2L^{\star}$ (taking $M_R^{\star} = -22.1$ from Lin *et al.* 1996). The host galaxy luminosities of the RG and RLQ sub-samples are basically identical, with median values of $M_R = -23.63$ and $M_R = -23.67$ respectively. In contrast, the luminosities of the RQQ sub-sample are found to be typically 0.4 magnitudes fainter than the radio-loud objects, a difference which is significant at the 2σ level. The difference in host luminosity found between the RQQs and RLQs reflects the trend seen in the results of other host galaxy studies, although is around a factor of two smaller than typically claimed (eg. Smith *et al.* 1986, Bahcall *et al.* 1997). The nuclear components of the RQQ and RLQ sub-samples have also been found to be basically identical, after the exclusion of the two Seyfert objects, with median values of $M_R = -23.97$ and $M_R = -24.01$ respectively. Unlike previous optical studies, but in agreement with the previous K-band imaging of this sample, no correlation has been found between host galaxy and unresolved nuclear luminosity, suggesting that in powerful AGN, the scatter in both the relationship between host galaxy and black-hole mass, and the black-hole accretion rate, are swamping any underlying correlation.

7.1.2 Characteristic Sizes and The Kormendy Relation

One of the specific aims of the HST host-galaxy study was to exploit the high resolution of HST to determine accurate host-galaxy scalelengths. There is good reason to be confident that this objective has been successfully realised. Evidence from the extensive programme of simulations described in Chapter 3, combined with the first reliable determination of the optical host-galaxy Kormendy relation, shows that the well known degeneracy between scalelength and characteristic surface-brightness has been successfully broken.

The average half-light radii of all of the AGN in the HST sample is large, with the median value of $r_e = 10.5$ kpc, more than three times the figure found to be typical of inactive ellipticals by Capaccioli *et al.* (1992). As with host luminosity, the scalelengths of the RG and RLQ sub-samples are found to be in excellent agreement, with median figures of $r_{1/2} = 11.27$ and $r_{1/2} = 11.28$ respectively. The median scalelength of the RQQs is $\sim 20\%$ smaller than that of the RLQs, although the difference in the mean figures is negligible. Taken as a whole, the scalelengths of the AGN in the HST sample are strongly correlated with luminosity, obeying a relation of the form $L \propto r^{0.75}$, in good agreement with the corresponding relation of $L \propto r^{0.70}$ found for inactive ellipticals by Kormendy (1977).

Perhaps the most significant result from the two-dimensional modelling programme has been the successful determination of the host galaxy $\mu_{1/2} - r_{1/2}$ fundamental plane projection, or Kormendy relation. The Kormendy relations determined for each of the AGN sub-samples are perfectly consistent with each other, and the relation of slope ~ 3 found for normal inactive elliptical galaxies by Kormendy (1977). Two further conclusions follow from this result. Firstly, the formation process of the host galaxies of powerful AGN must be sufficiently similar to that of normal inactive elliptical galaxies that the form of the fundamental plane is not effected. Secondly, it must be assumed that whatever level of morphological disturbance is experienced by the host galaxies of the HST sample, it is not seriously effecting the dominant mature stellar populations that the HST imaging study was specifically designed to be sensitive to.

7.1.3 Colours

The combinations of the new R-band modelling results with those obtained from both the IRCAM 1 and IRCAM 3 K-band imaging, has allowed the first reliable determination of optical-infrared colours for a statistically significant sample of powerful AGN host galaxies. The $R - K$ colours of the AGN hosts are tightly distributed around a rest-frame value of $R - K = 2.5$, with no detectable difference in colour between the three sub-samples. Through comparison with the elliptical-galaxy spectral models of Guiderdoni & Rocca-Volmerange (1987), it has been shown that a rest-frame colour of

$R - K = 2.5$ is perfectly consistent with that expected for a $\sim$ 14 Gyr-old passively evolving elliptical galaxy, in good agreement with the ages typically determined for very low-z inactive ellipticals. The conclusion arising from this is that the host galaxies, or at least their stellar populations, must have formed at high redshift ($z \geq 3$). The finding that the colours of AGN hosts are no different from those of normal ellipticals is in contrast to the often quoted result that AGN host galaxies are somewhat bluer than normal (eg. Véron-Cetty & Woltjer 1990).

The nuclear $R-K$ colours of the radio galaxy sub-sample were found to be perfectly consistent with those of dust reddened RLQ nuclei. The fitted slope of the reddening vector of 0.68 ± 0.05 is basically identical to the expected value of 0.70 for a λ^{-1} reddening law. Furthermore, the mean de-reddened nuclear luminosities of the RG sub-sample, $M_R = -23.90 \pm 0.46$, is in good agreement with the corresponding value for the RLQs, $M_R = -23.73 \pm 0.10$.

7.1.4 Interactions and Morphological Disturbances

The model-subtracted images presented in Appendix B provide an excellent opportunity to quantify the frequency, and magnitude, of the morphological disturbances which are often claimed to be a feature of AGN host galaxies. The initial impression given by the model-subtracted images is that evidence for recent interaction is widespread, with many of the AGN displaying some level or asymmetric flux residuals, or tidal arm features. However, comparison of the images with those of a luminosity- and redshift-matched sample of bright cluster galaxies has shown that the evidence for enhanced interaction in the AGN host galaxies is ambiguous. While it was found that there was evidence to suggest that spiral/tidal features were more common in the AGN model-subtracted images, it was also demonstrated that this signal was almost entirely due to the four RQQ objects, which were previously identified as having combined disc/bulge hosts. The exclusion of these four objects, two of which lie below the adopted quasar/Seyfert luminosity divide, effectively removes any evidence of a difference between the host galaxies and the cluster members. Furthermore, if these four RQQs are excluded, no evidence is found for a difference in the rate of occurrence of

interaction indicators between the three AGN sub-samples. It would therefore appear that, if galaxy interactions or mergers are necessary for the triggering of the AGN phenomenon, the timescale for the dissipation of the signatures of these interactions must typically be considerably shorter than the lifetime of the nuclear activity.

7.2 Further Conclusions

The results of the $z \sim 0.2$ AGN host galaxy imaging study led naturally to two related investigations which were fully described in Chapters 5 & 6. The main conclusions arising from this work are briefly summarized below.

7.2.1 AGN Black-hole Masses

The host-galaxy luminosities determined from the HST modelling programme were combined with the AGN total- and core-radio luminosities in Chapter 5 to investigate the distribution of AGN black-holes masses, using the correlations recently published by Magorrian *et al.* (1998) and Franceschini *et al.* (1998). The results of this investigation were relatively clear-cut in terms of the radio-loud AGN, with all three black-hole mass estimators predicting that the central black-holes of the RG and RLQ sub-samples have masses of $\sim 10^{10}\mathrm{M}_{\odot}$. Using a simple accretion disc model to predict the R-band magnitudes of the radio-loud black-holes, as estimated from the Magorrian relation, showed the majority of the radio-loud objects to be radiating at $\sim 10\%$ of the Eddington limit. A interesting result which follows on from this is that the largest host galaxies in the HST sample could comfortably produce quasars with luminosities of $\mathrm{M}_R \sim -28$, comparable with the most luminous quasars found at high redshift.

The situation with respect to the black-hole masses of the RQQs is not so clear. If the Magorrian relation is used as a black-hole estimator then, although the predicted RQQ black-hole masses are typically smaller than their radio-loud counterparts, there is still considerable over-lap between the two distributions. However, in contrast, the adoption of either of the two radio luminosity estimators leads to predicted RQQ black-

hole masses which are on average a factor of two smaller than those of the radio-loud objects, with no RQQ predicted to harbour black-holes of mass $\geq 5\times10^{9}M_{\odot}$. There are two prospects raised by this result. The first is that it could simply be the requirement to cross a black-hole mass threshold of $\sim 10^{10}M_{\odot}$ which is the cause of the radio-loudness dichotomy. The second is that in deliberately selecting luminosity-matched RLQ and RQQ samples, it is possible that a sample of RQQs with low-mass black-holes radiating at a substantial fraction of the Eddington limit may have been selected for comparison with a sample of RLQs with high-mass black-holes radiating at only a few percent of the Eddington limit. Further confusion is added to the situation due to the current non-detection of six of the RQQs1 at 5GHz. At the time of writing a new set of sensitive VLA observations of these objects has recently been obtained which promises to clarify the situation.

If host galaxy luminosity *is* adopted as the most reliable black-hole mass estimator, via the Magorrian relation, then the results presented in Chapter 5 suggest that an extra physical parameter, possibly black-hole angular momentum, is required to explain the radio-loudness dichotomy. Many of the determined properties of the AGN host galaxies and black-hole mass distributions, are explained qualitatively by the combined black-hole merger/spin model proposed by Wilson & Colbert (1995).

7.2.2 The Evolution of 3CR Radio Galaxies

One of the obvious areas of interest connected to the low-z AGN host galaxy study is how the properties of these host galaxies are related to their higher redshift counterparts. In the context of quasars this issue is addressed by two projects, described in the next section, which together investigate the evolution of quasar hosts in the redshift range $0.4 < z < 4.0$.

With respect to radio galaxies, the evolution of the hosts of powerful radio sources was investigated in Chapter 6, with the modelling of WFPC2 data for a sample of 3CR radio galaxies in the redshift range $0.6 < z < 1.8$, originally obtained by Best, Longair & Röttgering (1997, 1998). Contrary to the previous claims, the results for a

10-object sub-sample showed that the scalelength distribution of the 3CR radio galaxies at $z \sim 0.8$ is indistinguishable from that found for the $z \sim 0.2$ radio galaxy sample in Chapter 4. Furthermore, it proved possible to determine the Kormendy relation for this $z \sim 0.8$ sub-sample, which was also found to be indistinguishable from that displayed by the $z \sim 0.2$ radio galaxies if one allowed for purely passive luminosity evolution. The modest level of passive evolution implied between $z = 0.2 \rightarrow 1.0$ was shown to be perfectly consistent with that predicted by spectrophotometric galaxy models if a high formation redshift ($z \geq 4$) and a low density Universe are assumed.

Taken as a whole, the results of Chapter 6 show there to be no evidence that a significant amount of dynamical evolution is occurring in the powerful radio galaxy population in the redshift range $0 < z < 1$. The implication is that the traditional passive evolution interpretation of the radio galaxy $K-z$ relation remains acceptable. The one remaining piece of evidence that the $z = 0$ and $z = 1$ radio galaxies can not form a uniform population of passively evolving ellipticals, comes from the widely accepted "fact" that $z \sim 1$ 3CR sources inhabit more clustered environments, comparable to Abell class $0 \rightarrow 1$ clusters, while low-z 3CR sources avoid cluster environments. However, as was found in Chapter 4, there appears good circumstantial evidence that the radio galaxies in the HST sample, as well as the quasars, are in fact consistent with the brightest cluster galaxies of Abell clusters of class $0 \rightarrow 1$. The planned near-infrared environment study of the HST sample, described at the end of Chapter 6, should resolve this apparent contradiction.

7.3 Further Work

At the time of writing there are several observational projects of direct relevance to the work of the thesis which are already underway, or have been approved for telescope time. The aims and preliminary results of these projects are briefly described below.

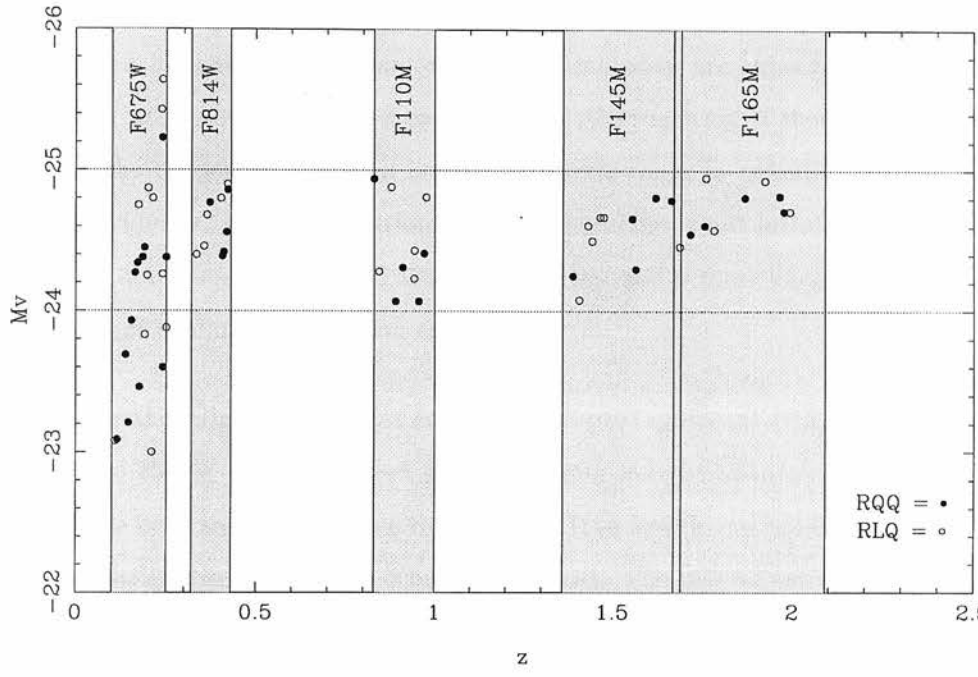

Figure 7.1: The redshift-luminosity distribution of the combined WFPC2/NICMOS sample showing the RQQs (filled circle) and RLQs (open circles) and the appropriate filters. The F814W, F110M and F165M filters approximate the standard I, J and H-bands. The redshift $z \sim 1.5$ redshift sample was eventually dropped due to orbit restrictions. The F675W sample is also shown to illustrate how these objects will provide the low-z baseline against which any cosmological evolution will be measured. Figure courtesy of Marek Kukula.

7.3.1 The Cosmological Evolution of Quasar Host Galaxies

The study of the evolution of quasar host galaxies over cosmologically significant timescales represents the logical next step in host galaxy research with HST. This section describes a project to use the HST WFPC2 and NICMOS (near-infrared camera and multi-object spectrometer) instruments to image the hosts of luminosity-matched quasar samples over the redshift range $z = 0.4 \rightarrow 2.0$.

The specific aim of the project is to search for evidence in the host galaxies to indicate whether pure luminosity evolution (LE), or luminosity-dependent density evo-

lution (LDDE), are the major contributors to the dramatic decline in quasar numbers from $z = 2$ to the present day. If LE of long-lived quasars is the dominant evolutionary factor, then high redshift quasars of similar luminosity are expected to inhabit lower luminosity hosts then their low-z counterparts. Alternatively, if there is little difference found in the properties of quasar hosts over a wide range in redshift, this can be taken as good evidence that the evolution in quasar numbers is not intimately related to the physics of active nuclei, such as gas accretion rates, and is more likely due to the general cosmological evolution of massive structures.

One of the original diagrams from the accepted proposal (P.I. James Dunlop) is reproduced in Fig 7.1, and shows how luminosity-matched samples of 5 RQQs and 5 RLQs have been selected in three redshift bins (the fourth $z \sim 1.5$ bin shown in Fig 7.1 was eventually dropped due to orbit restrictions). The careful choice of filters ensures that the same rest-frame region of the spectrum (≥ 4000Å) is studied in each bin, and that the images are not contaminated by strong emission lines. It can be seen from Fig 7.1 that, together with the $z \sim 0.2$ study, the new observations will provide a redshift baseline stretching from $z = 0$ to $z = 2$.

At the time of writing the observations of the $z = 1$ and $z = 2$ quasars have been obtained, while the $z = 0.4$ WFPC2 observations are scheduled for imminent completion. The analysis of the new NICMOS data is at a preliminary stage, and the raw results from the modelling of the $z = 1$ images are presented here only because of there relevance to the $z = 1$ 3CR study reported in Chapter 6. No attempt will be made to discuss the complex reduction of HST NICMOS images, a process in which the author had no involvement (described by Kukula *et al.* 2000).

Preliminary Results

The results from the two-dimensional modelling of the F110M (J–band) $z \sim 1$ sample are shown in Table 7.1. In all cases the modelling procedure found the host galaxy to be significantly better fitted by an early-type galaxy model, and it is these parameters which are listed in Table 7.1. If a reasonable colour of $I - J = 0.8$ is assumed for $z \sim 1$

Source	Type	z	$r_{1/2}$/kpc	$\mu_{1/2}$	J_{host}	J_{nuc}	L_{nuc}/L_{host}	b/a
pks0938	RLQ	0.943	4.3	21.10	19.49	19.81	2.29	0.75
4c02	RLQ	0.976	10.4	21.62	19.32	17.61	4.82	0.25
mc2112	RLQ	0.878	17.4	23.14	18.18	18.97	0.48	0.98
3c422	RLQ	0.942	17.0	22.88	18.29	17.90	1.43	0.75
pks0440	RLQ	0.844	13.0	22.71	18.84	18.47	1.41	0.61
bvf262	RQQ	0.970	4.6	21.56	19.85	19.24	1.76	0.74
bvf247	RQQ	0.890	11.9	22.83	18.88	20.14	0.31	0.83
bvf225	RQQ	0.910	17.1	23.78	20.11	17.91	7.61	0.31
sgp5-46	RQQ	0.955	3.9	21.65	20.10	19.46	1.79	0.88
sgp2-47	RQQ	0.830	-	-	-	18.33	-	-

Table 7.1: The results of the modelling of the $z \sim 1$ quasars imaged with NICMOS through the F110M filter. The properties of the F110M filter are sufficiently close to the standard J-band that the apparent magnitudes listed in columns 5 & 6 have simply been listed as J-band magnitudes. The host galaxy of sgp2-47 was not detected at a significantly better χ^2 level than the best-fitting unresolved nuclear component.

elliptical galaxies (Fasano *et al.* 1999), then the mean absolute I–band luminosity of the quasar hosts is $M_I = -24.59 \pm 0.21$. This can be seen to be in excellent agreement with the corresponding value of $M_I = -24.62 \pm 0.13$ determined for the $z \sim 0.8$ radio galaxies in Chapter 6. In addition to the host luminosities, the 3CR galaxies and the $z \sim 1$ quasars also display similar scalelength distributions, with mean values of $r_{1/2} = 11.0 \pm 1.8$ and $r_{1/2} = 12.6 \pm 2.3$ respectively. Although the fact that there are only 5 RLQs and 4 RQQs modelled at $z \sim 1$ makes it impossible to come to any firm conclusions, it is also of interest that the mean scalelengths of $r_e = 12.4 \pm 2.1$ (RLQ) and $r_e = 9.4 \pm 2.7$ (RQQ) are both compatible, and display the same trend for the RQQs to be smaller, that was found for the low-z AGN sample.

Considering that the redshift distributions of the 10-object 3CR galaxy sub-sample and the new $z \sim 1$ quasar sample are similar, it is possible to investigate whether their Kormendy relations are compatible, without the need to make surface-brightness k-corrections. It can be seen from Fig 7.2 that the two sub-samples display perfectly

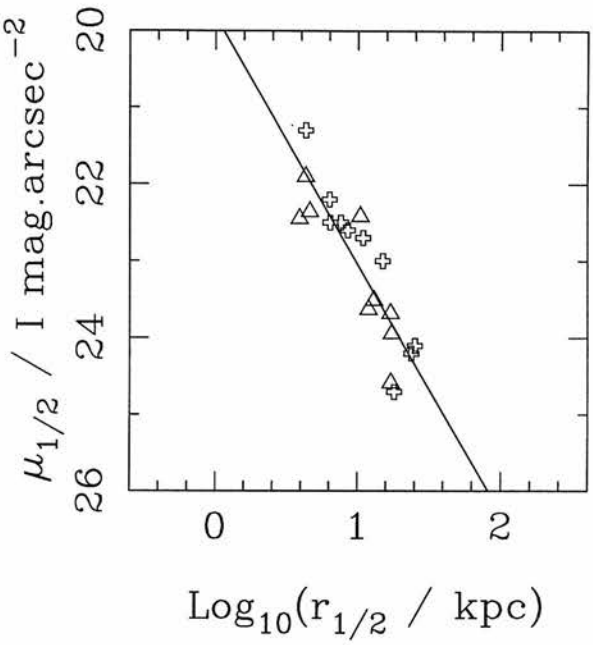

Figure 7.2: The apparent I-band Kormendy relation followed by the $z \sim 1$ quasars imaged with NICMOS (triangles), and the $z \sim 0.8$ 3CR radio galaxies imaged with WFPC2 (crosses). The solid line is a least squares fit to the combined sample, and has a slope of 3.23. An elliptical galaxy colour of $I - J = 0.8$ has been assumed.

consistent Kormendy relations, with a I–band best-fit for the two samples taken as a whole of :

$$\mu_{1/2} = 3.23_{\pm 0.42} \log r_{1/2} + 19.82_{\pm 0.4} \tag{7.1}$$

where again, a colour of $I-J = 0.8$ has been assumed. Given that the results of Chapter 6 indicate that the properties of the $z \sim 0.8$ 3CR radio galaxies are no different from those of the $z \sim 0.2$ AGN host galaxies, the clear implication is that the host galaxies of powerful AGN at $z \sim 1$ are essentially identical to their $z \sim 0.2$ counterparts in terms of host luminosity, scalelength and Kormendy relation. Although the J–band NICMOS results are only preliminary, there are two conclusions which are suggested even at this early stage. Firstly, if the formation of the host galaxies of powerful AGN is to be explained within the framework of hierarchical clustering models, the results to date require that this process must have been completed before $z = 1$. Secondly, the evidence available at present is more consistent with LDDE than pure LE, suggesting

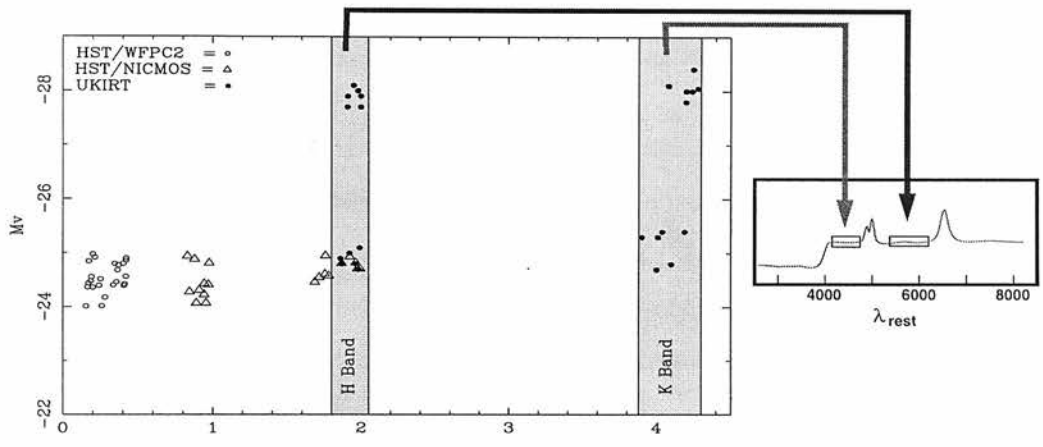

Figure 7.3: A plot of the $M_V - z$ plane showing the location of the two $z = 2$ and $z = 4$ samples chosen for imaging with UKIRT (shaded regions). Also shown are the three samples already imaged with a combination of HST WFPC2 and NICMOS. The idealised quasar spectrum shown in the figure is included to emphasis the point that the samples and filters have been specifically chosen to ensure line-free images that always sample the host-galaxy light long-ward of the 4000Å break. Figure courtesy of Marek Kukula.

that $z = 2$ is an important epoch not just for quasars, but for galaxy formation in general.

7.3.2 The Host Galaxies of the Highest Luminosity Quasars

In a project designed to build upon the NICMOS imaging study described above, telescope time has been successfully applied for (P.I. James Dunlop) to undertake K-band imaging of quasar hosts out to redshift $z = 4$ on UKIRT. The main figure from the successful proposal is reproduced in Fig 7.3, from which it can be seen that there are two separate aspects to the programme. Firstly, two samples of quasars have been selected at $z = 2$ and $z = 4$ which lie in the same $-24 < M_V < -25$ luminosity range as the objects in the NICMOS study. The result of this is that the new UKIRT data, in combination with the $z \sim 0.2$ and combined WFPC2/NICMOS programmes, will allow the evolution of quasar host galaxies to be studied from $z = 0.2 \rightarrow 4.0$. Therefore, the completion of the three projects will trace the evolution of the hosts of constant

luminosity quasars from the present day, through the peak of quasar activity at $z \sim 2$, right back to the first appearance of quasars at $z \sim 4$.

The second feature of the UKIRT programme illustrated by Fig 7.3 is that two further samples have been selected at $z = 2$ and $z = 4$ which have absolute luminosities comparable with the most luminous quasars known ($M_V = -28$). This will not only allow us to determine if these super-luminous objects are also located in the most luminous host galaxies, but will also allow the separate investigation of the effects of redshift and luminosity upon host-galaxy evolution.

7.3.3 AGN Black-hole Estimators

Given the somewhat different implications of the use of the Magorrian *et al.* (1998) and Franceschini *et al.* (1998) black-hole mass estimators for the radio-loudness dichotomy, it is obviously desirable to have a third, independent, black-hole mass estimator. Such a method has recently received renewed publicity through the work of Laor (1998), who used the FWHM of quasar Hβ emission lines as a direct indicator of the gravitational potential in the central few parsecs of the active nucleus. Combined with the, admittedly tentative, assumptions that the broad-line clouds are both virialized, and are situated at a radius from the central black-hole which scales as $R \propto L_{bol}^{1/2}$, where L_{bol} is the quasar bolometric luminosity, it is then possible to estimate the black-hole mass.

Using this method, Laor produced a host-galaxy/black-hole mass correlation in reasonable agreement with the Magorrian *et al.* result, using the host-galaxy luminosities of the quasars studied by Bahcall *et al.* (1997). However, application of the same method using the host-galaxy luminosities for the HST sample studied here, and Hβ FWHM measurements taken from the literature, fails to reproduce the claimed correlation. The strong suspicion arising from this is that the Laor result could be biased by the host luminosity-nuclear luminosity correlation known to be present in the Bahcall *et al.* results, but completely absent from the results presented in Chapter 4.

The situation is made more complicated at present due to the discovery that quoted

Hβ values in the literature can differ by as much as a factor of two for individual objects. In order to settle the issue of whether or not Hβ FWHM measurements can be used as a black-hole mass estimator, telescope time has been successfully applied for to obtain Hβ measurements for all of the objects in the HST sample at the INT, and is scheduled for December 1999.

The importance of the study of quasar host galaxies at high redshift is illustrated by the interesting agreement between the results of the black-hole mass investigation of Chapter 5, and the peak comoving number density of quasars between $z \sim 2$ and $z \sim 3$. Both the Magorrian and Franceschini black-hole mass estimators suggest a separation in typical black-hole mass between the RLQ and RQQ populations, with an apparent dividing line at around $9.5 \times 10^{10} M_{\odot}$. The black-hole mass function determined by Franceschini *et al.* (1998) predicts a number density of black-hole of mass $\geq 9.5 \times 10^{10} M_{\odot}$ of $\sim 10^{-5}$ Mpc^{-3}, in good agreement with a recent estimate of the peak comoving number density of quasars, also 10^{-5} Mpc^{-3} (Taylor *et al.* 1996: Warren, Hewett & Osmer 1995), if it is assumed that approximately 50% of quasars are obscured by dust in the UV-optical. Correspondingly, given that RLQs make up $\simeq 5\%$ of the total quasar population, the estimated number density of RLQs at $z \simeq 2$ will be $\sim 10^{-7}$ Mpc^{-3}, again in good agreement with the predictions of the Franceschini *et al.* black-hole mass function.

7.4 The Wider Context of Host Galaxy Studies

It seems clear that the numbers quoted above are sufficiently similar to be consistent with a large fraction of, if not *all*, massive elliptical galaxies at $z \simeq 2$ harbouring active quasars. In light of this, it would seem that the study of quasar host galaxies has a central role to play in tracing the formation and evolution of massive ellipticals.

Appendix A

Surface-Brightness Profiles

Surface-brightness profiles for each of the 33 objects in the AGN sample. Each plot shows the azimuthally-averaged data (open circles), the azimuthally-averaged best-fit two-dimensional model after convolution with the PSF (solid line) and the azimuthally-averaged best-fit unresolved nuclear component after convolution with the PSF (dotted line).

The Radio Galaxy 0230−027

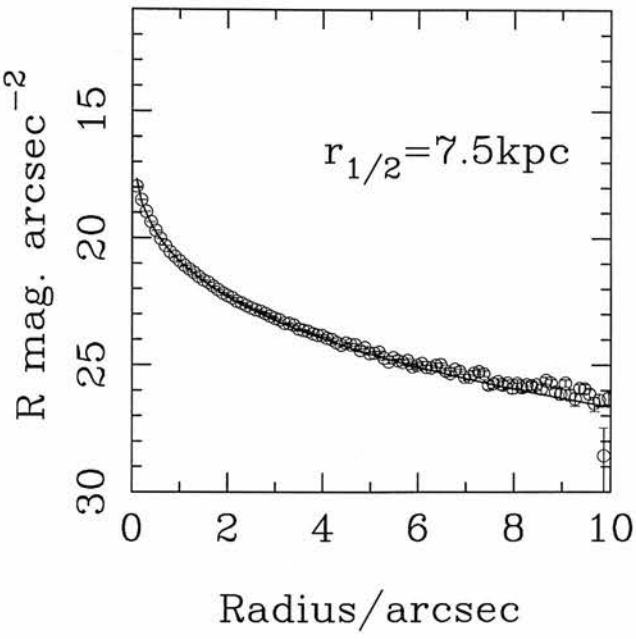

The Radio Galaxy 0307+169

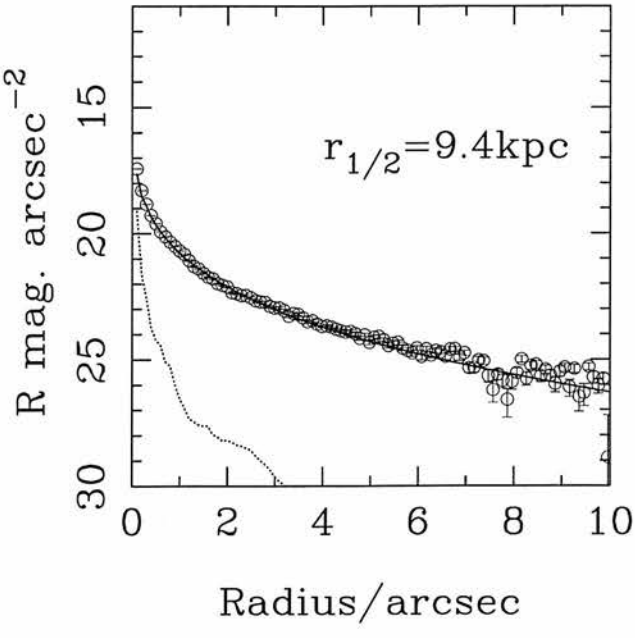

The Radio Galaxy 0345+337

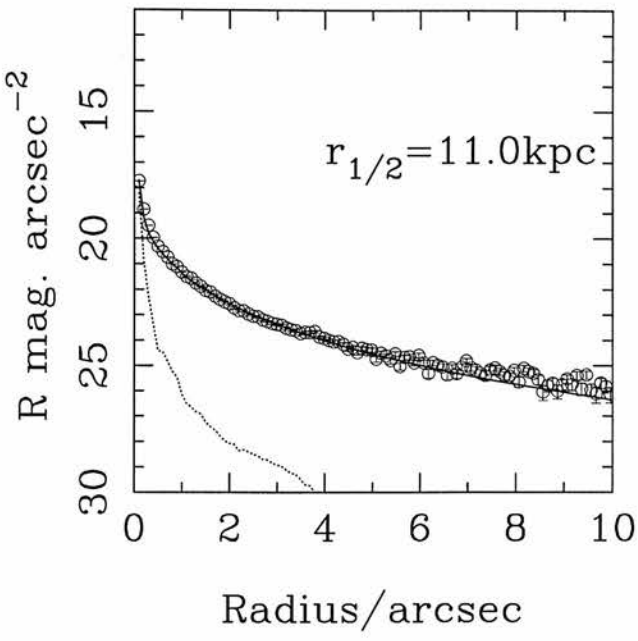

The Radio Galaxy 0917+459

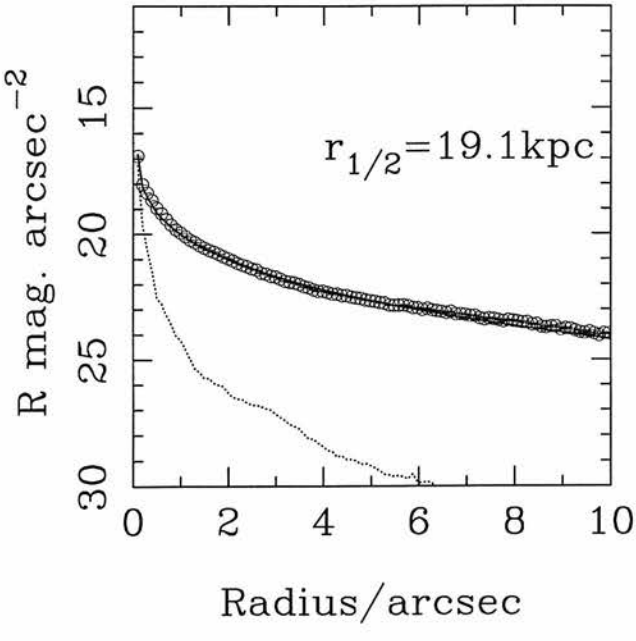

The Radio Galaxy 0958+291

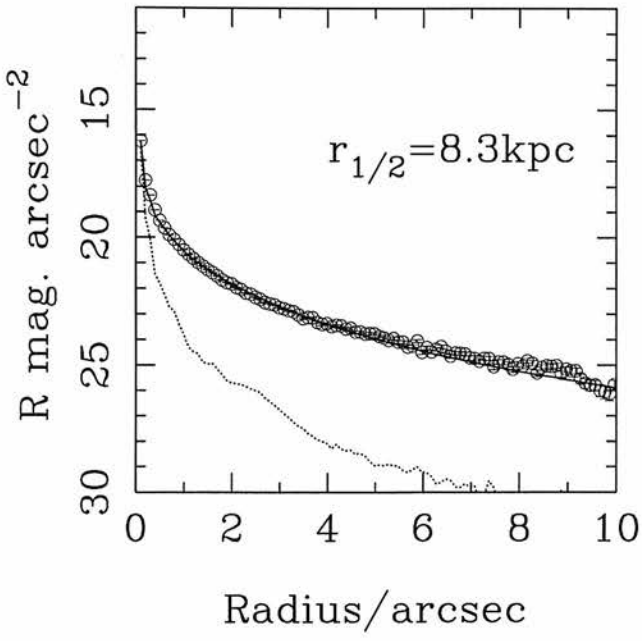

The Radio Galaxy 1215−033

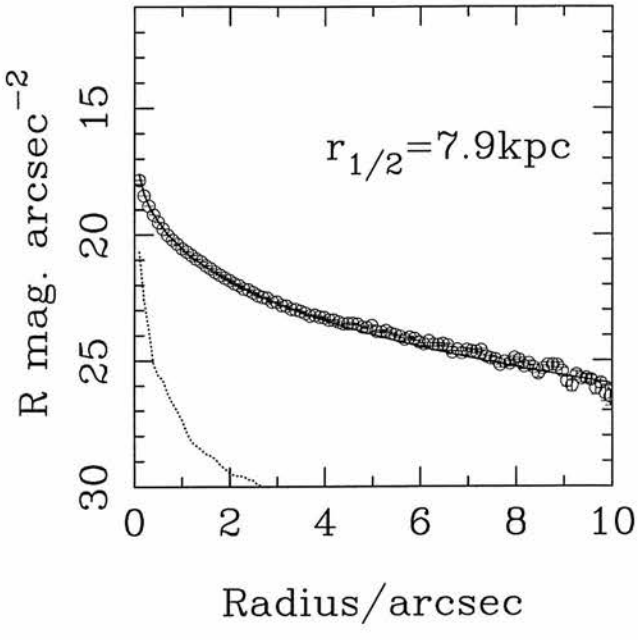

The Radio Galaxy 1215+013

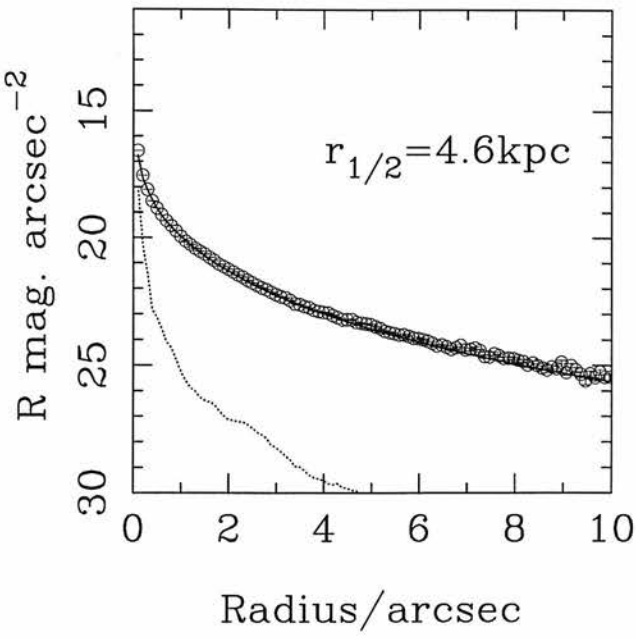

The Radio Galaxy 1330+022

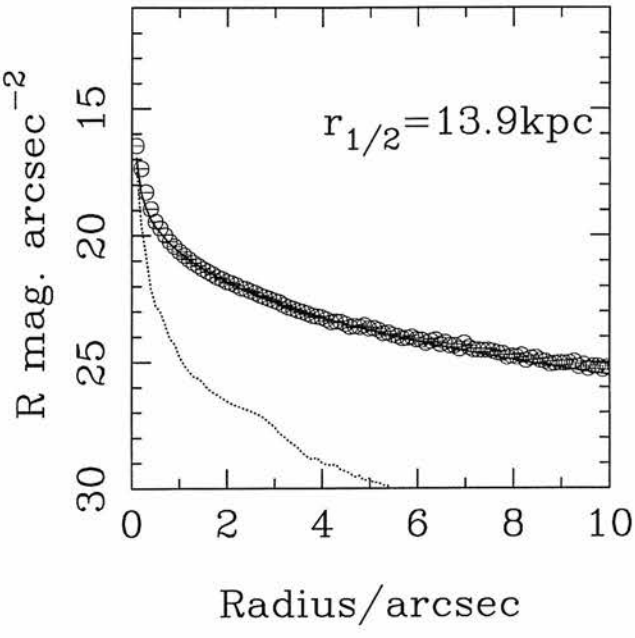

The Radio Galaxy 1342−016

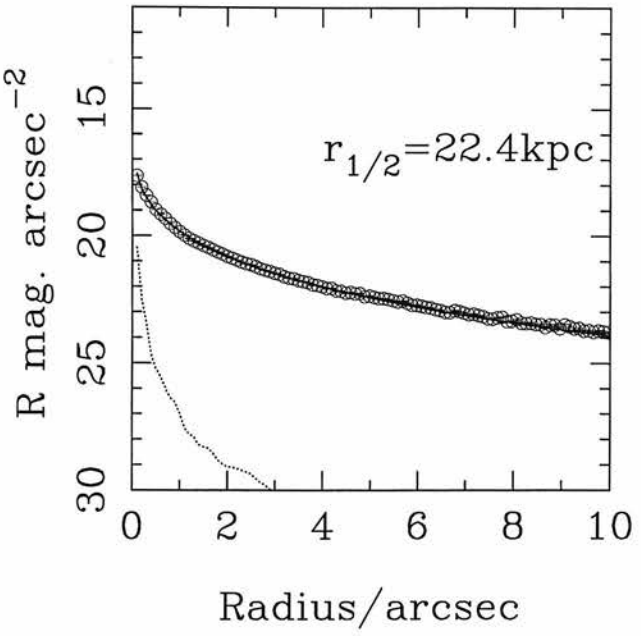

The Radio Galaxy 2141+279

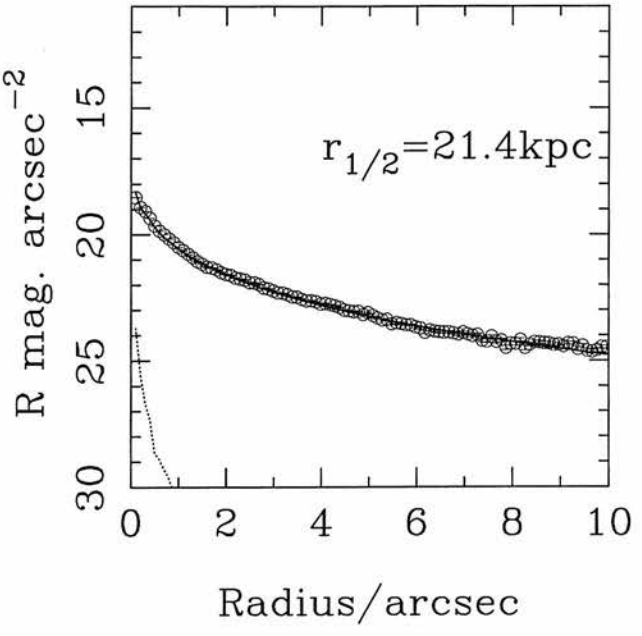

The Radio Loud Quasar 0137+012

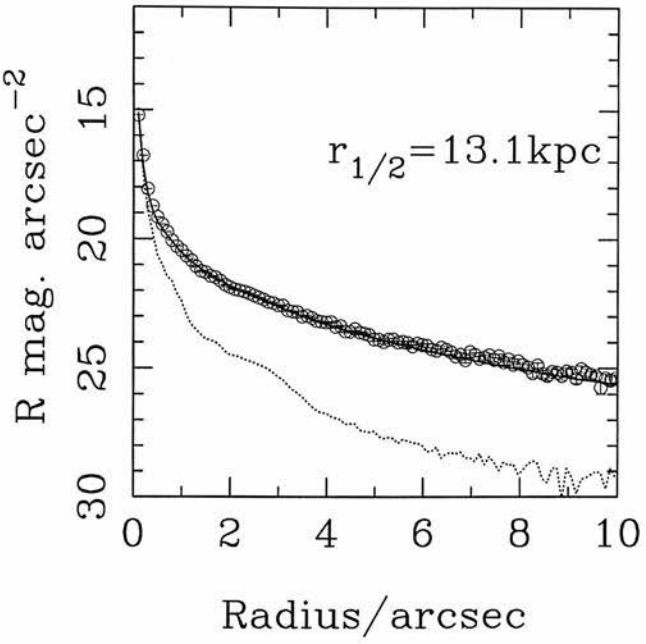

The Radio Loud Quasar 0736+017

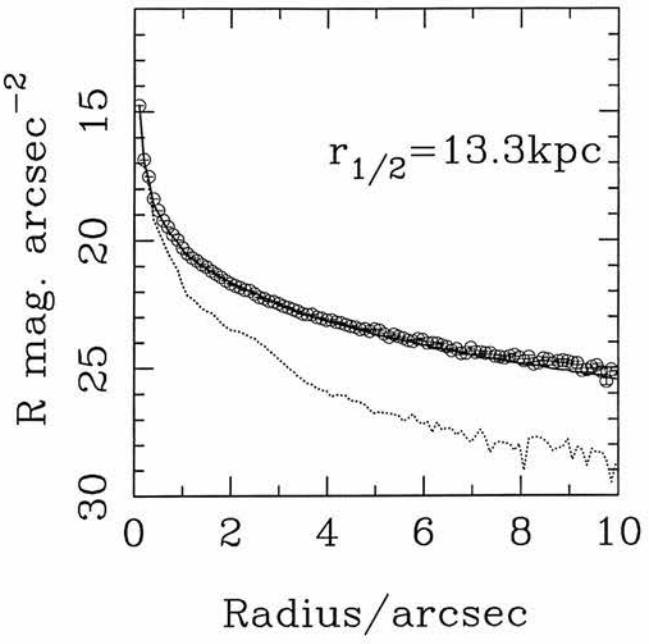

The Radio Loud Quasar 1004+130

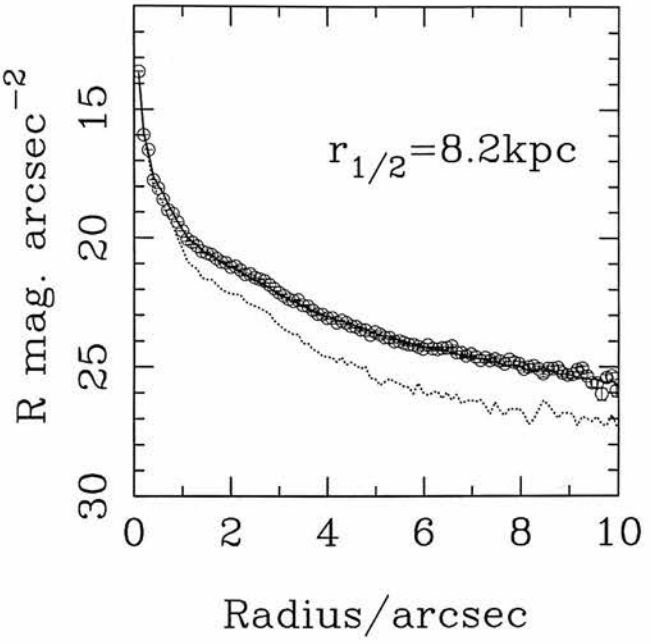

The Radio Loud Quasar 1020−103

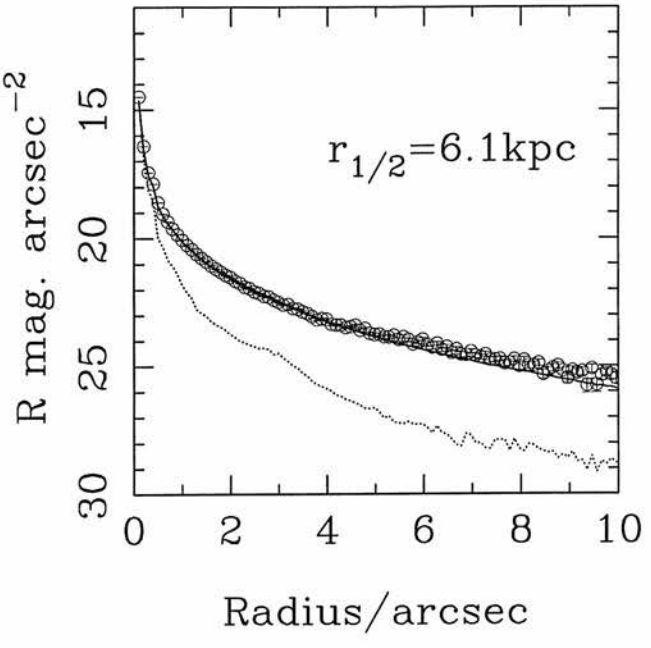

The Radio Loud Quasar 1217+023

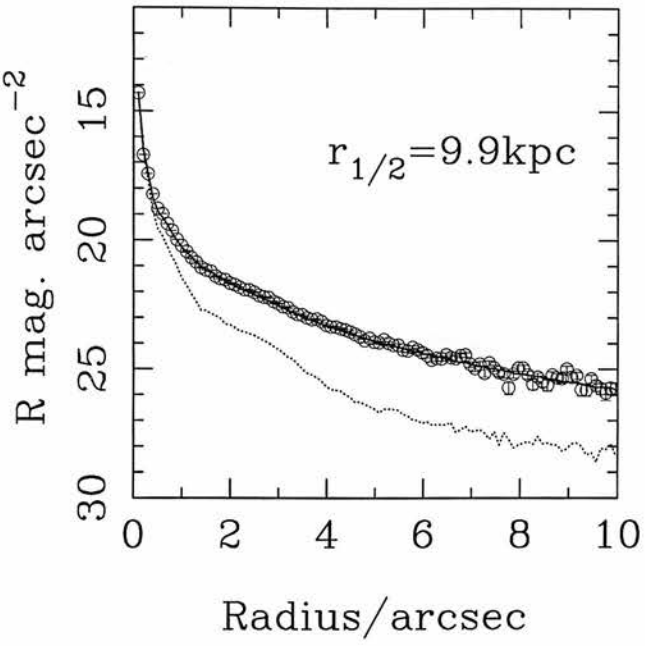

The Radio Loud Quasar 2135−147

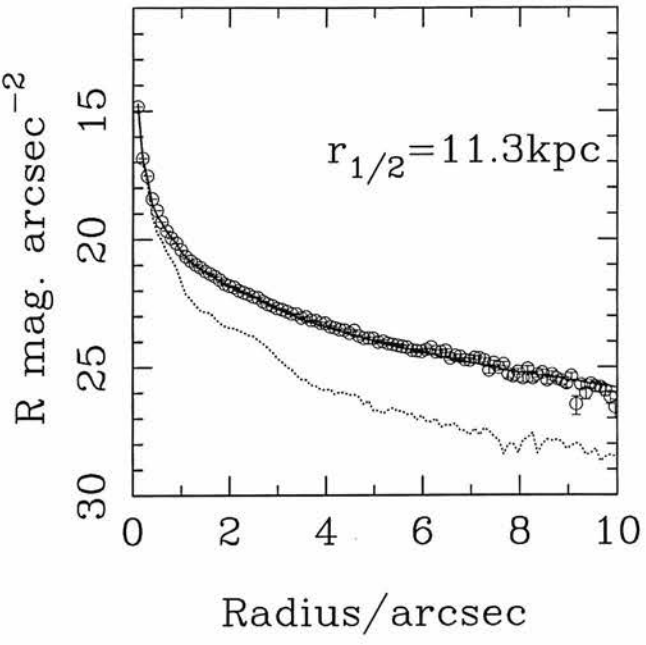

The Radio Loud Quasar 2141+175

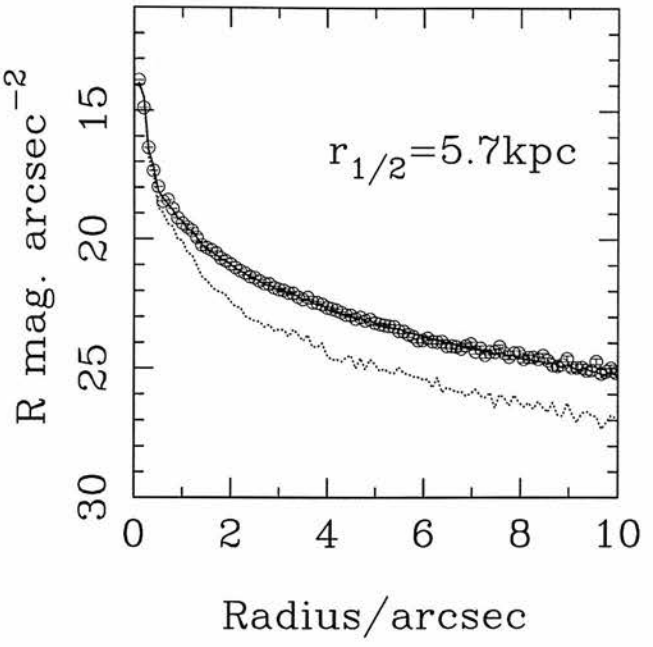

The Radio Loud Quasar 2247+140

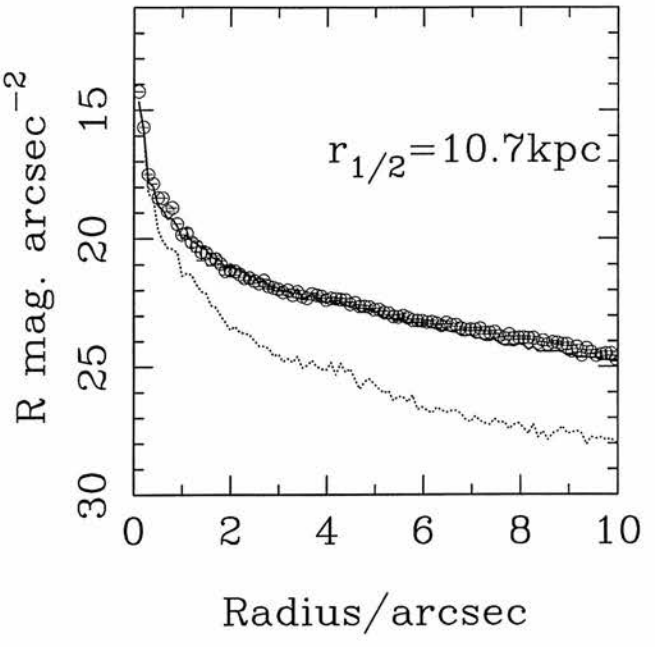

The Radio Loud Quasar 2349−014

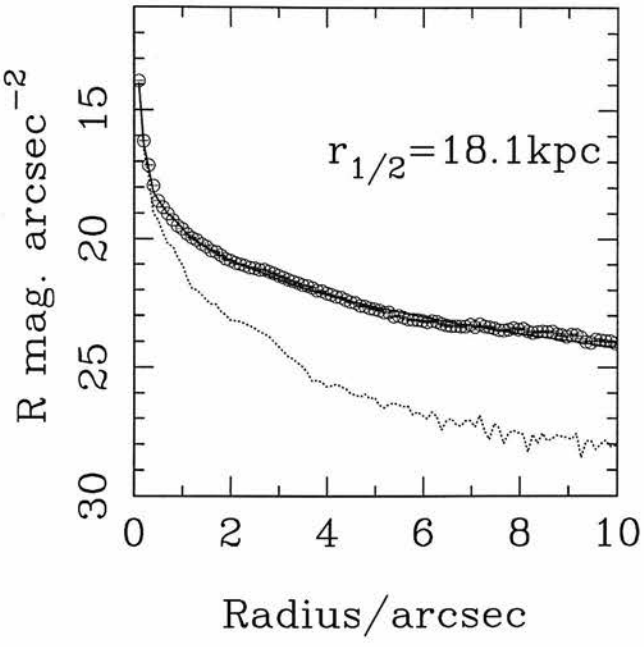

The Radio Loud Quasar 2355−082

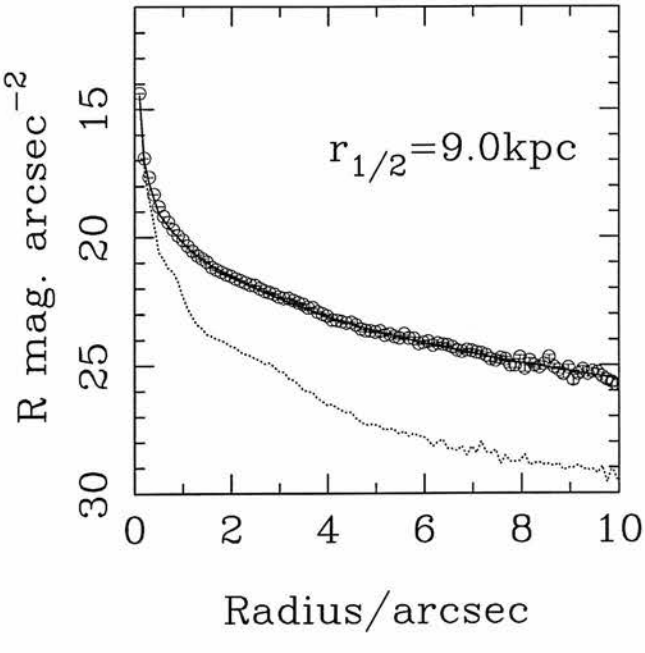

The Radio Quiet Quasar 0052+251

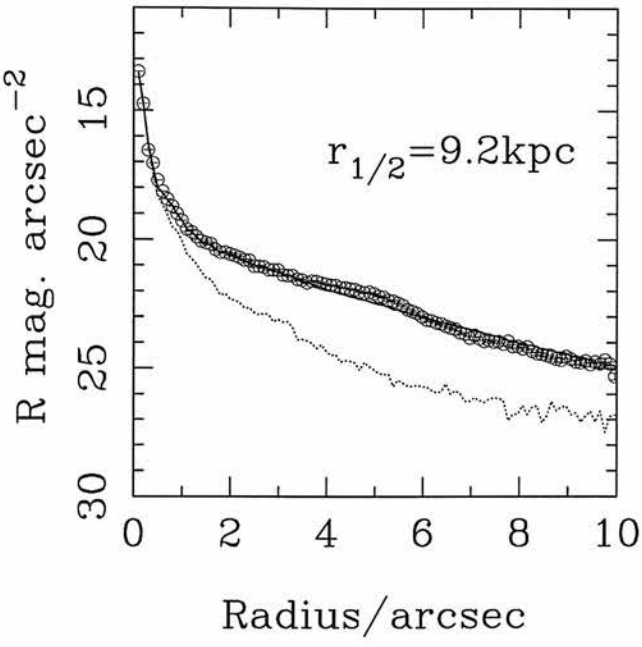

The Radio Quiet Quasar 0054+144

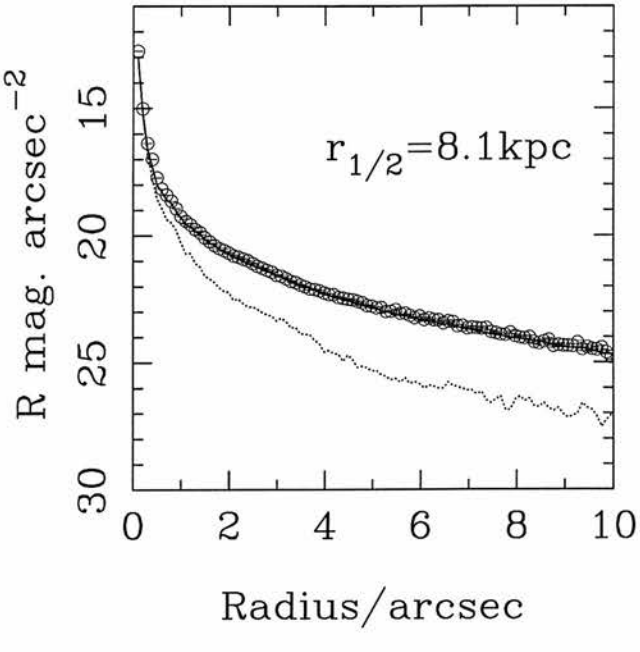

The Radio Quiet Quasar 0157+001

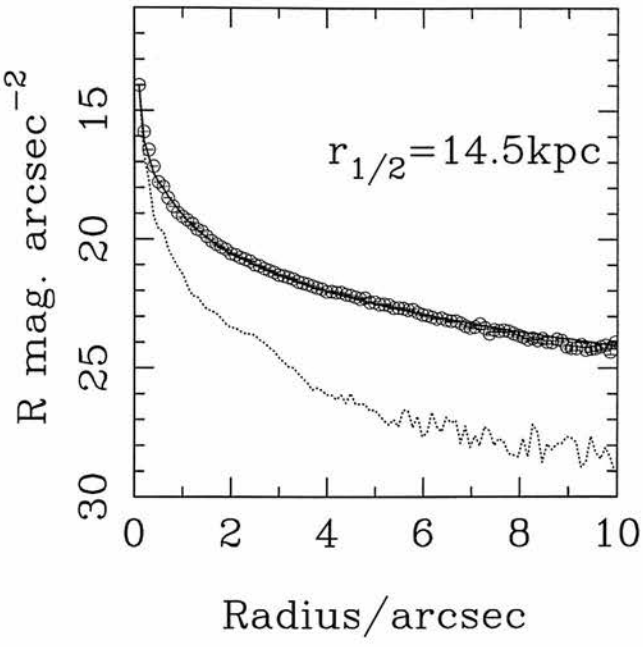

The Radio Quiet Quasar 0204+292

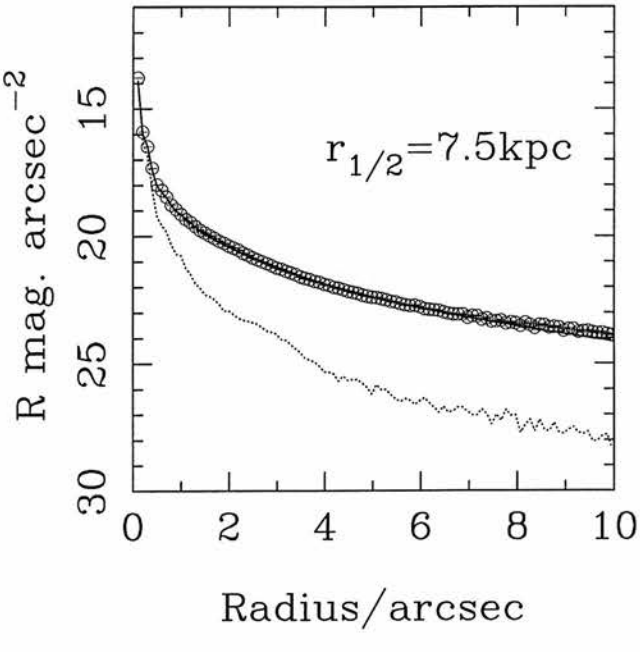

The Radio Quiet Quasar 0244+194

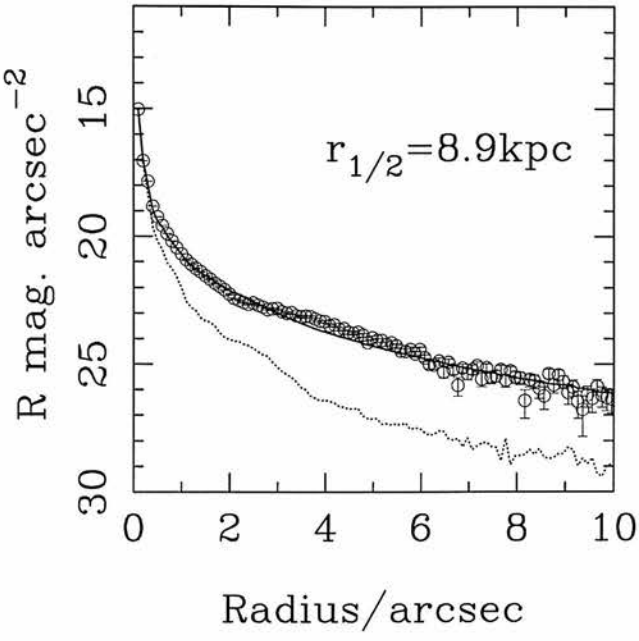

The Radio Quiet Quasar 0257+024

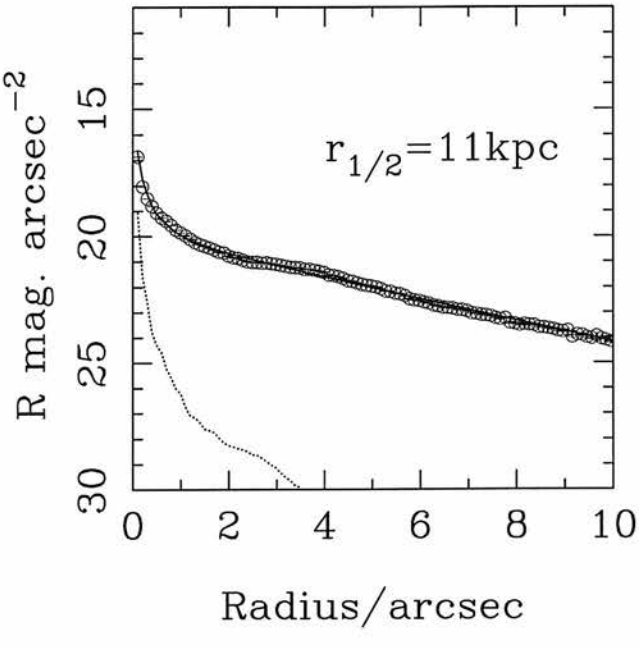

The Radio Quiet Quasar 0923+201

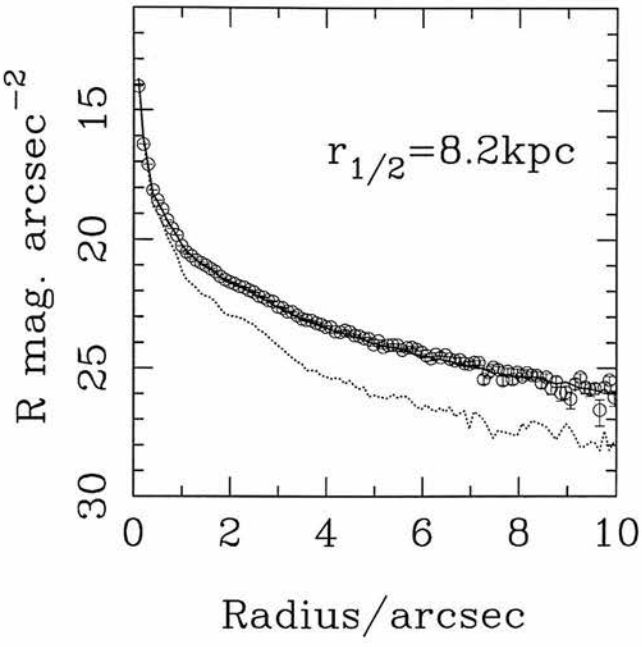

The Radio Quiet Quasar 0953+415

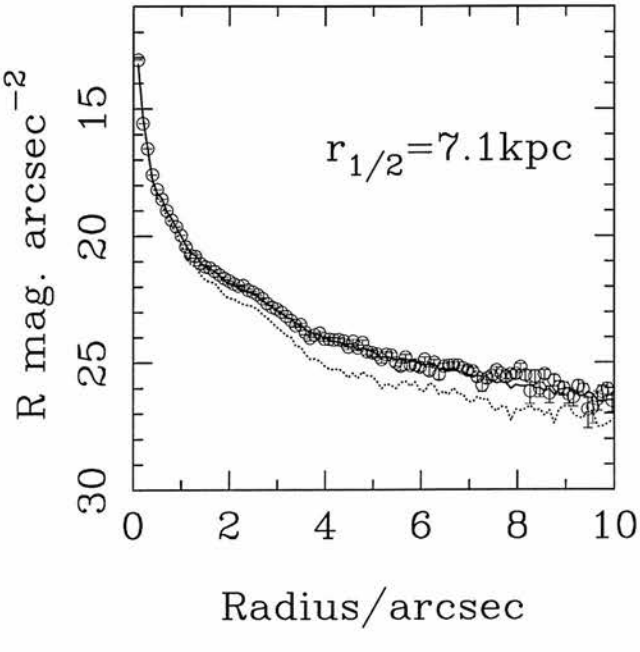

The Radio Quiet Quasar 1012+008

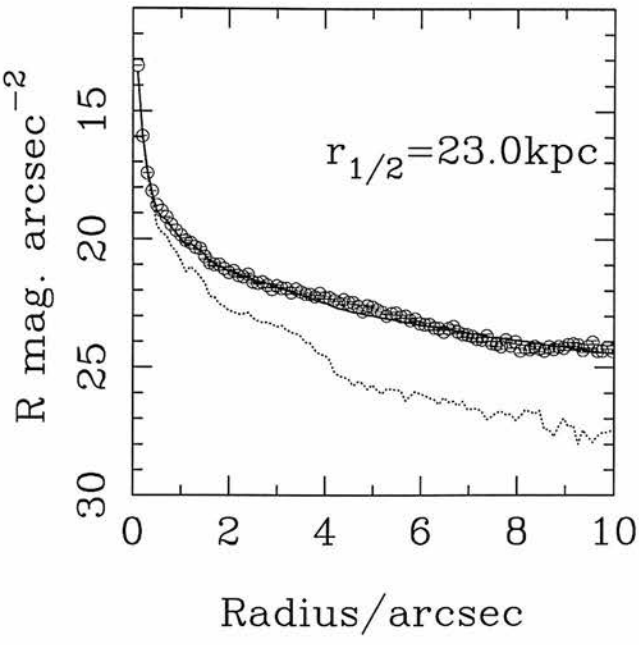

The Radio Quiet Quasar 1549+203

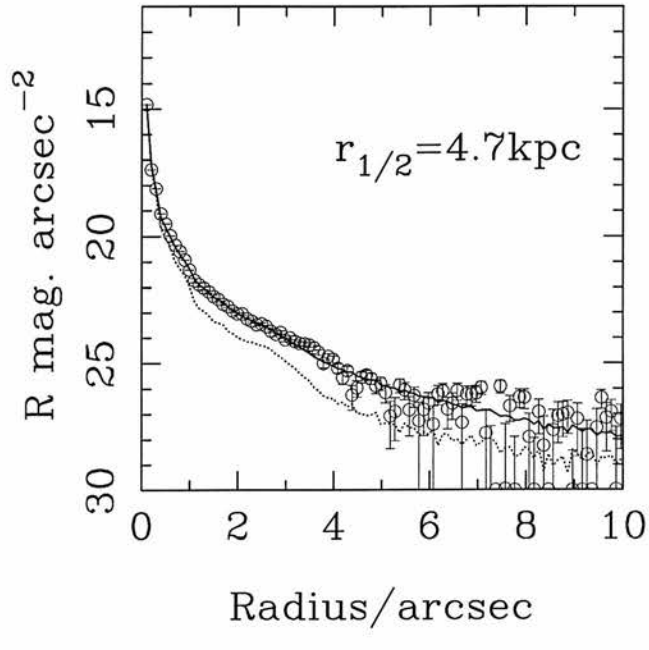

The Radio Quiet Quasar 1635+119

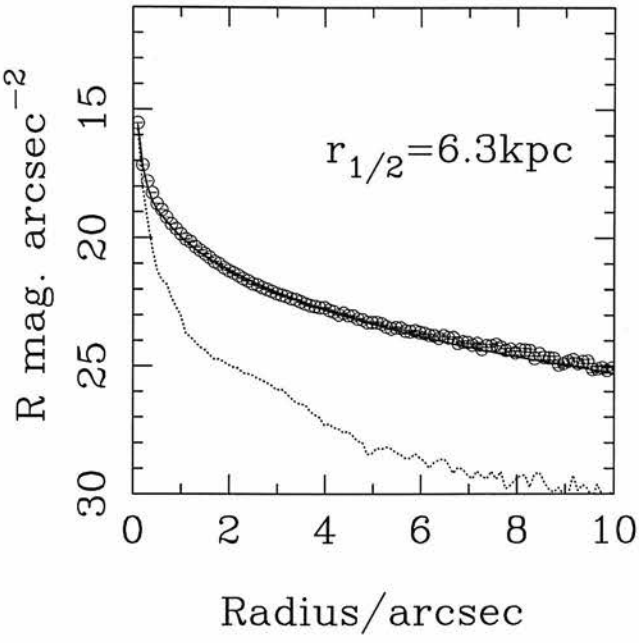

The Radio Quiet Quasar 2215−037

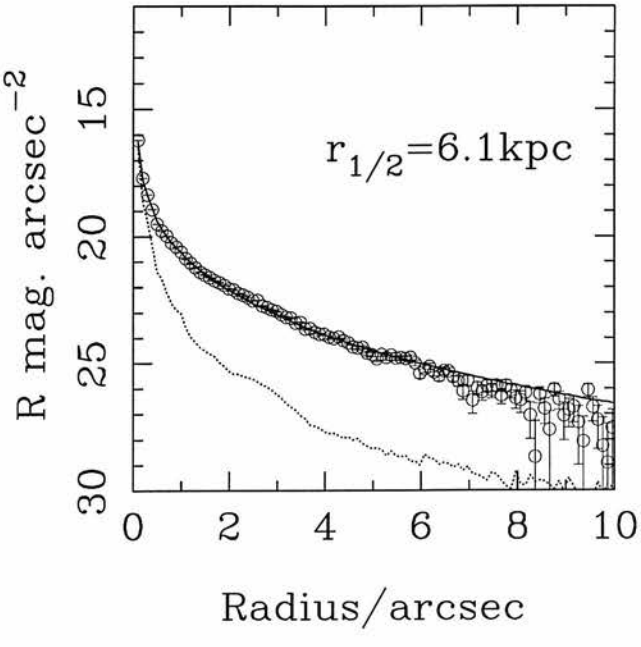

The Radio Quiet Quasar 2344+184

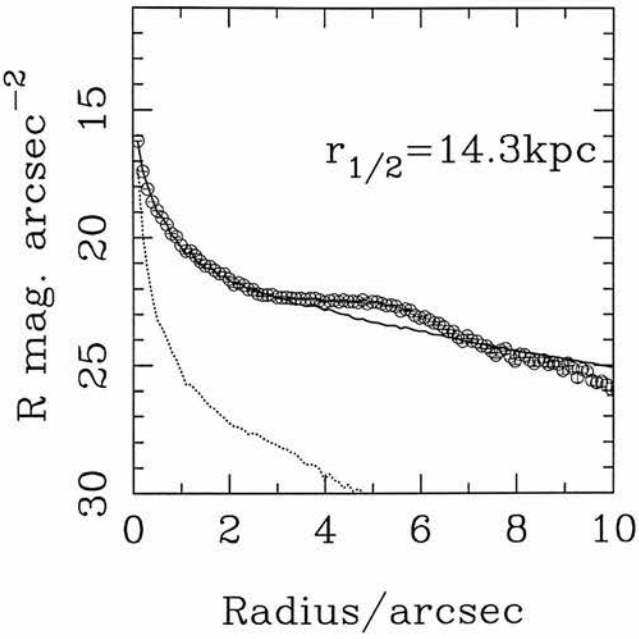

Appendix B

HST Images and Models

The R–band images, two-dimensional model fits, and model-subtracted residual images of each of the 33 objects in the AGN sample. A combined greyscale/contour image of the final reduced F675W R-band image of each AGN is shown in the top left panel (panel A) of each, which shows a region 12.5 $\times$ 12.5 arcsec centred on the target source. The surface-brightness of the lowest contour level is indicated in the top-right corner of the panel with the greyscale designed to highlight structure close to this limit. Higher surface-brightness contours are spaced at intervals of 0.5 mag.arcsec^{-2}, and have been superimposed to emphasize brighter structure in the centre of the galaxy/quasar. Panel B in each figure shows the best-fitting two-dimensional model, complete with unresolved nuclear component (after convolution with the empirical PSF) contoured in an identical manner to to panel A. Panel C shows the best-fitting host galaxy as it would appear if the nuclear component were absent, while panel D is the residual image which results from subtraction of the full two-dimensional model (in panel B) from the raw R-band image (in panel A), in order to highlight the presence of morphological peculiarities such as tidal tails, interacting companion galaxies, or secondary nuclei. All panels are displayed using the same greyscale.

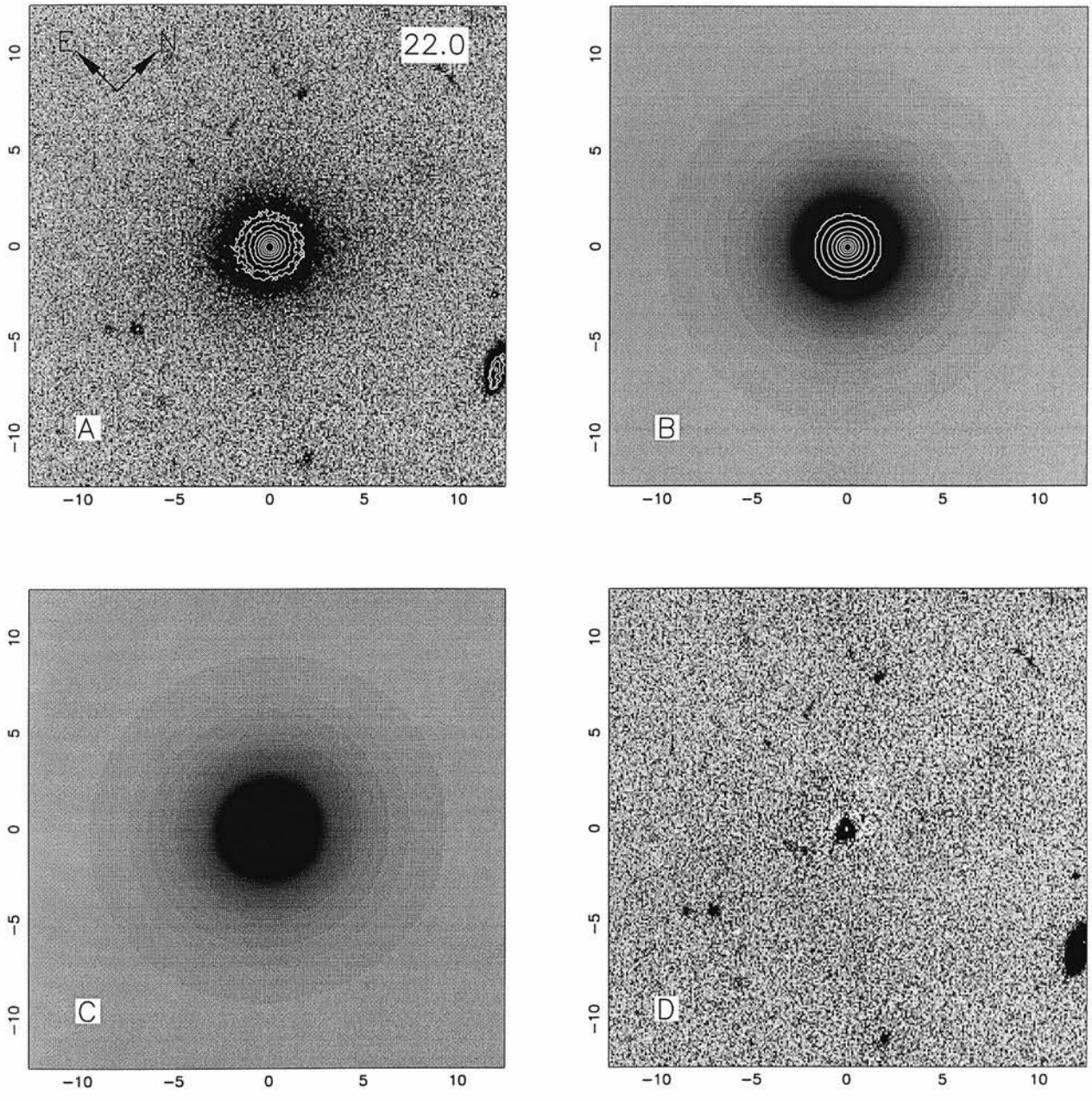

Figure B.1: The radio galaxy 0230−027

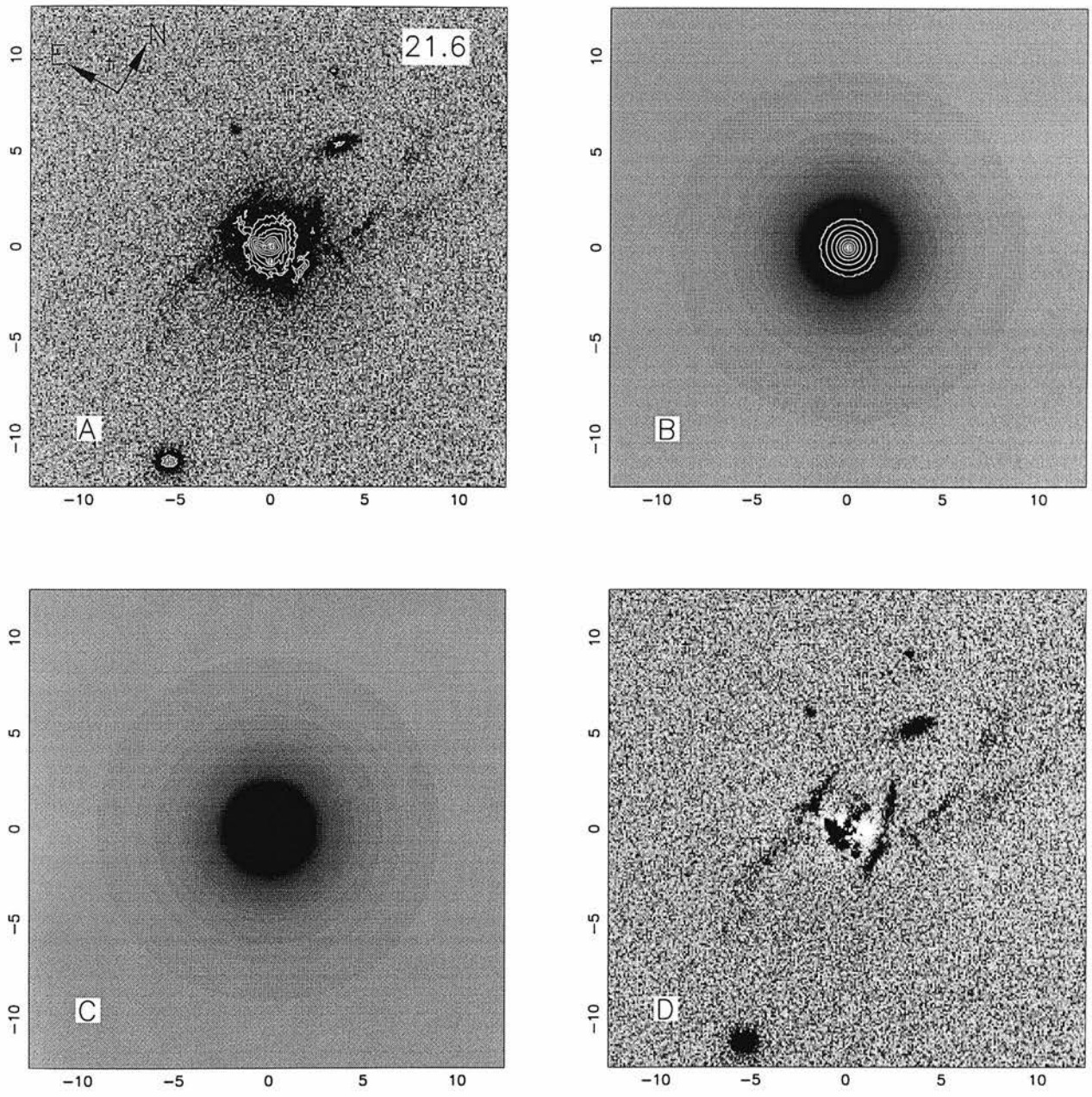

Figure B.2: The radio galaxy 0307+169

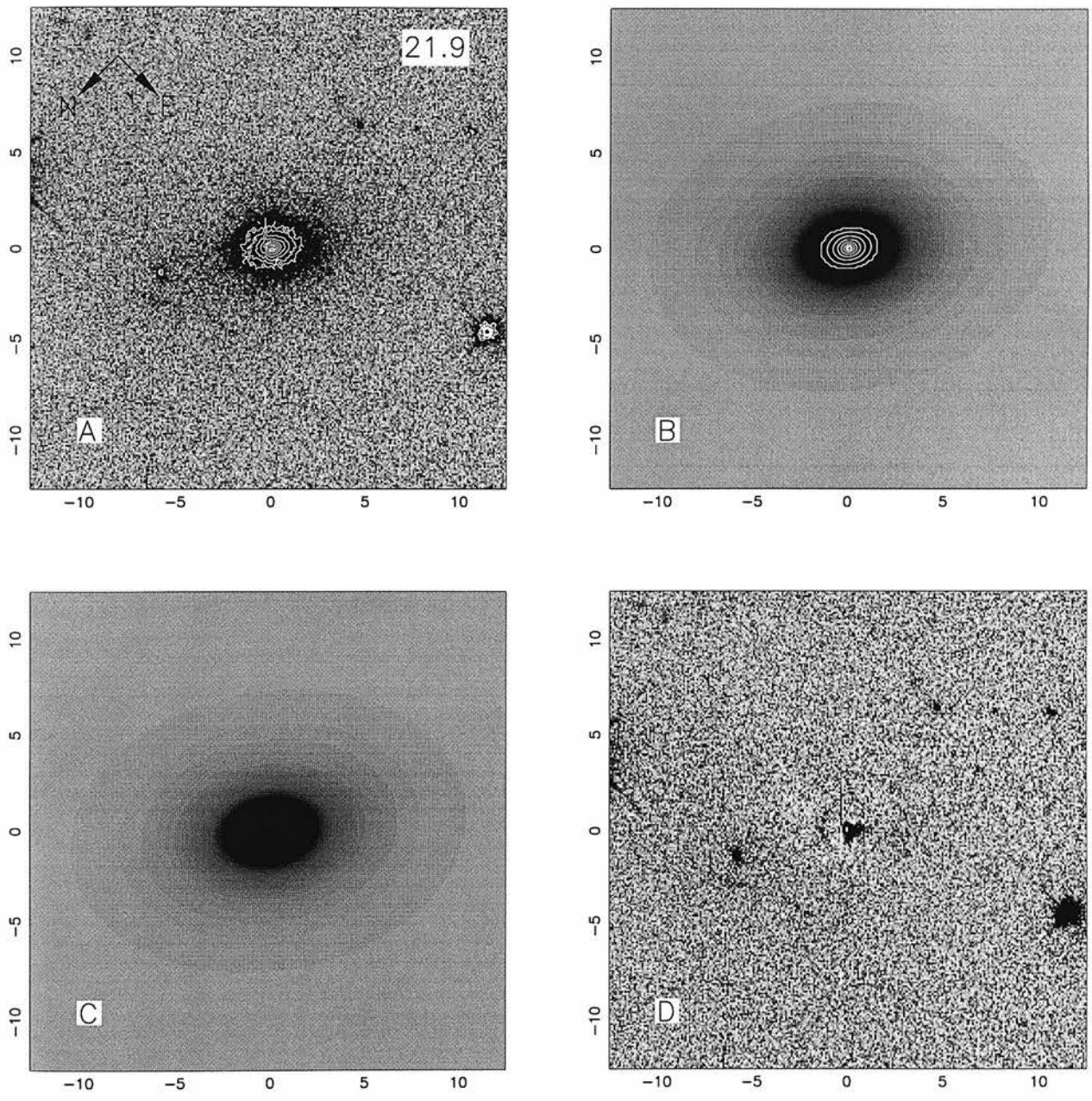

Figure B.3: The radio galaxy 0345+337

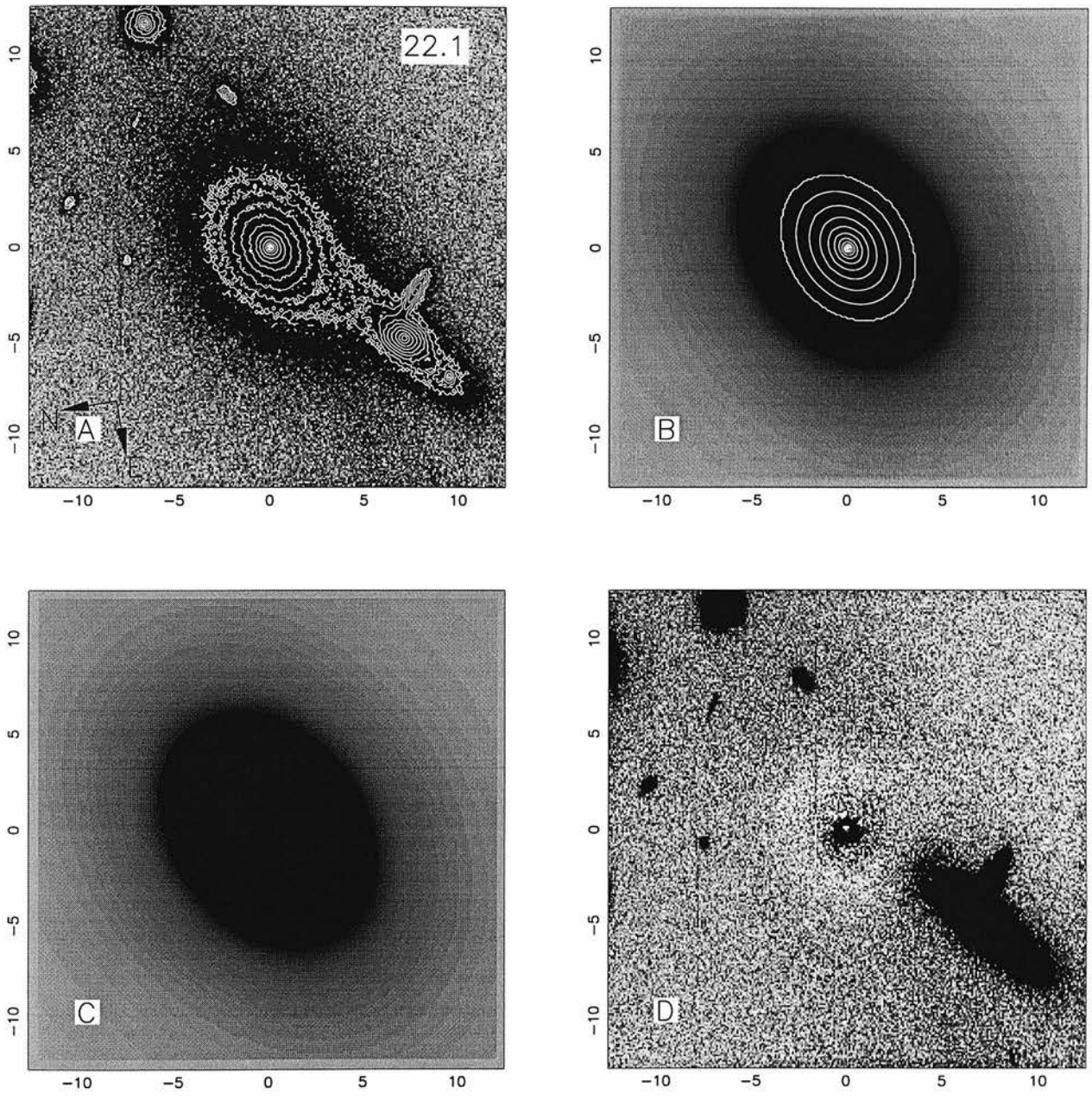

Figure B.4: The radio galaxy 0917+459

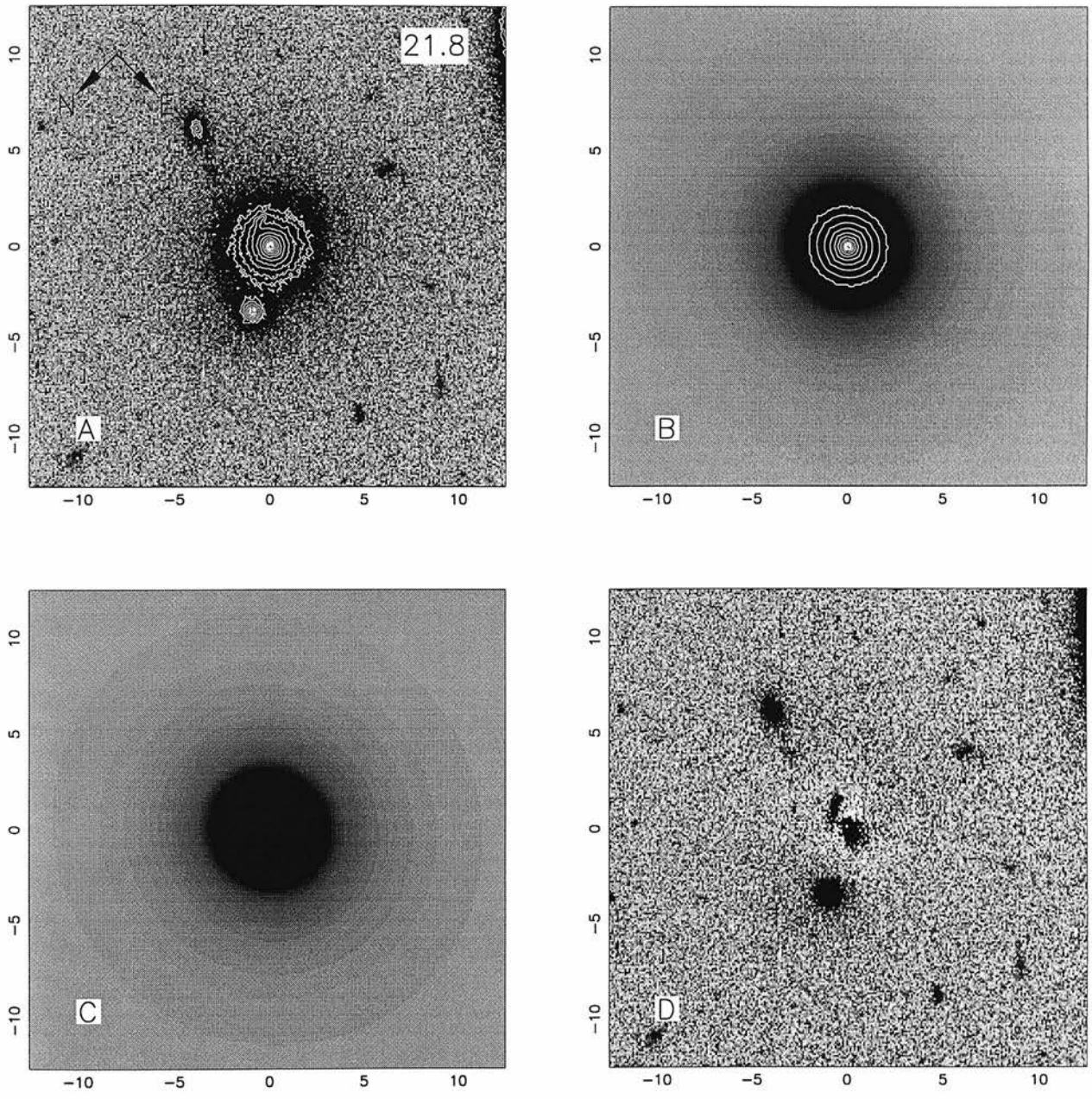

Figure B.5: The radio galaxy 0958+291

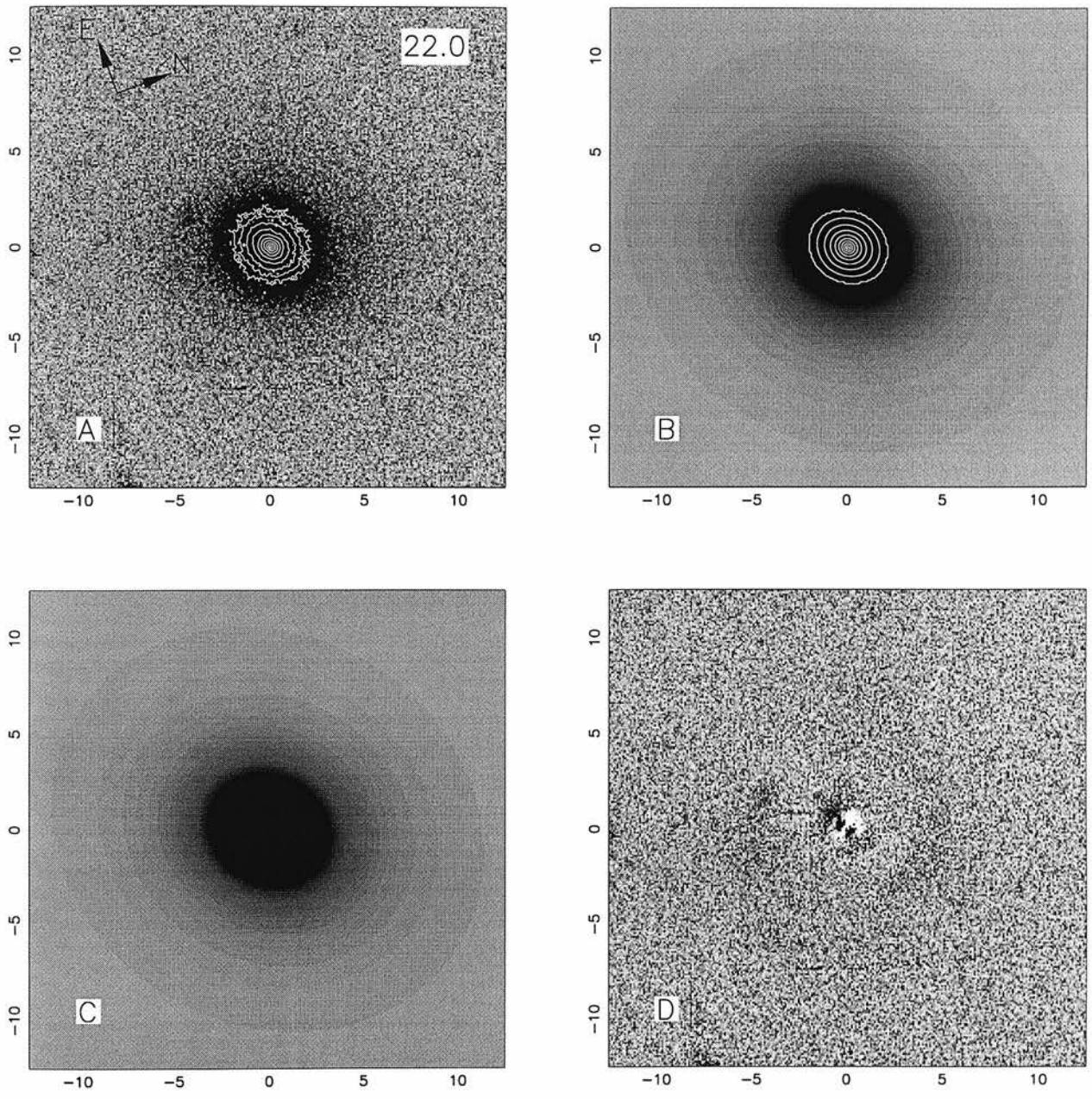

Figure B.6: The radio galaxy 1215−033

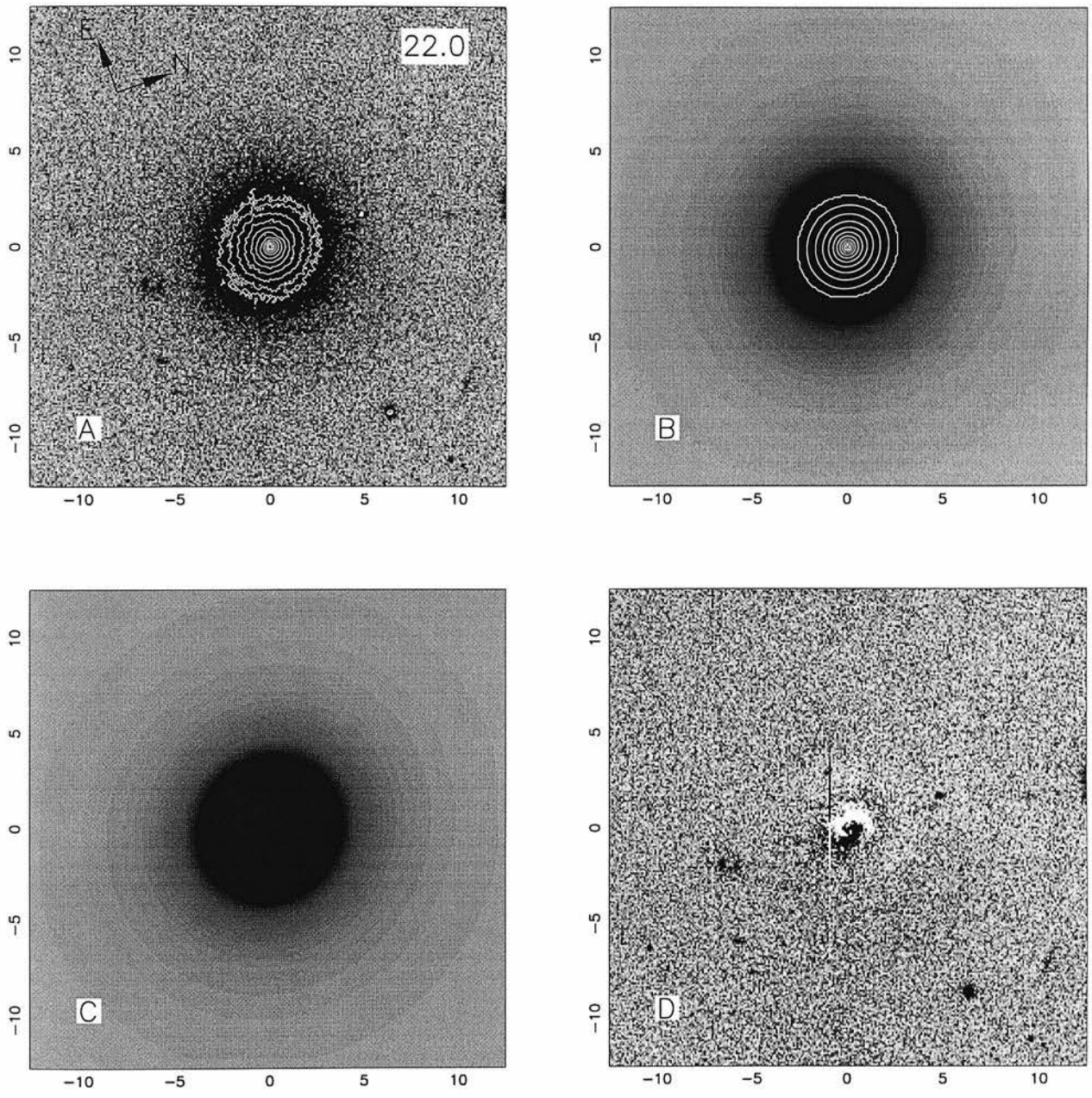

Figure B.7: The radio galaxy 1215+013

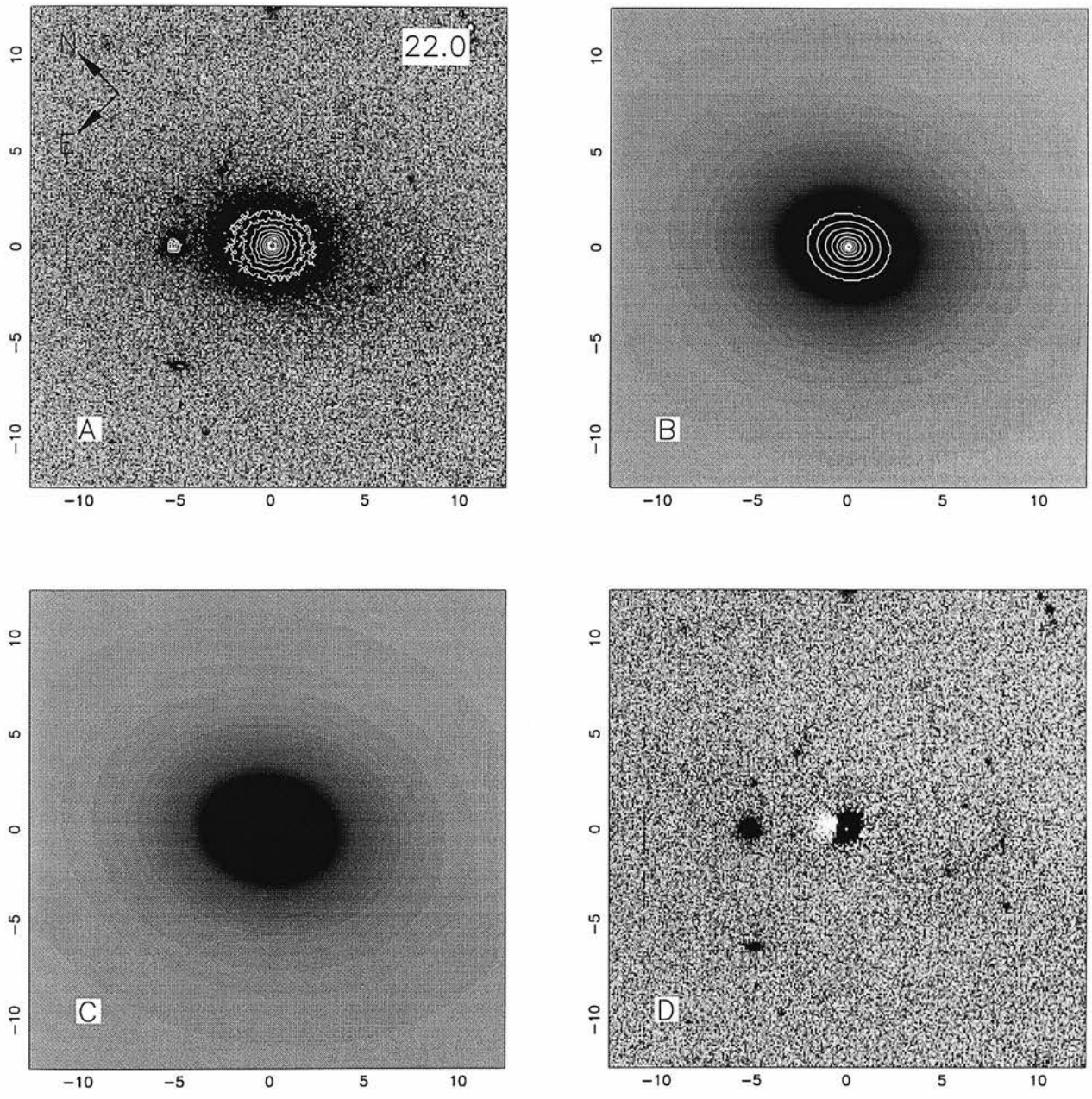

Figure B.8: The radio galaxy 1330+022

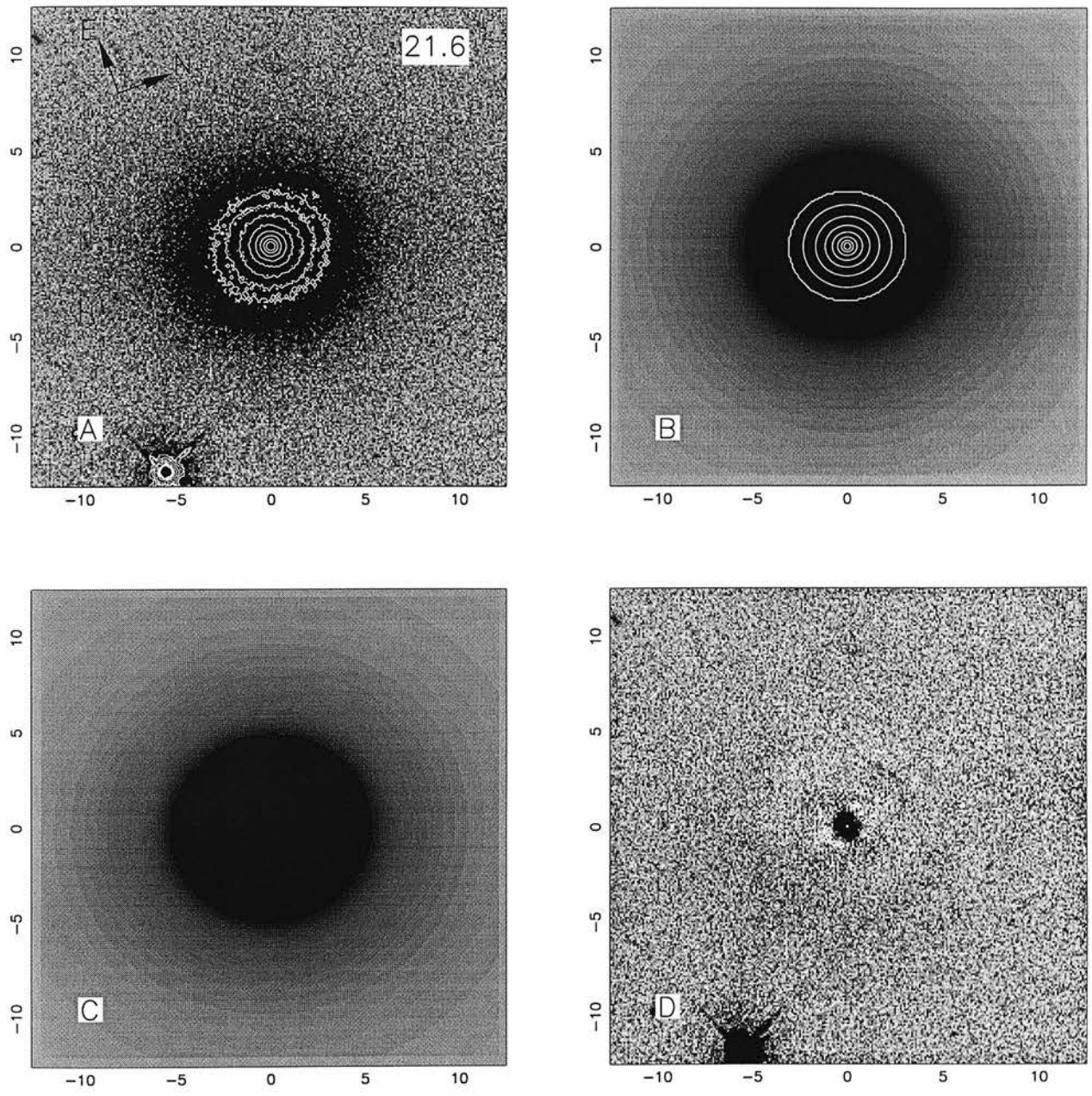

Figure B.9: The radio galaxy 1342−016

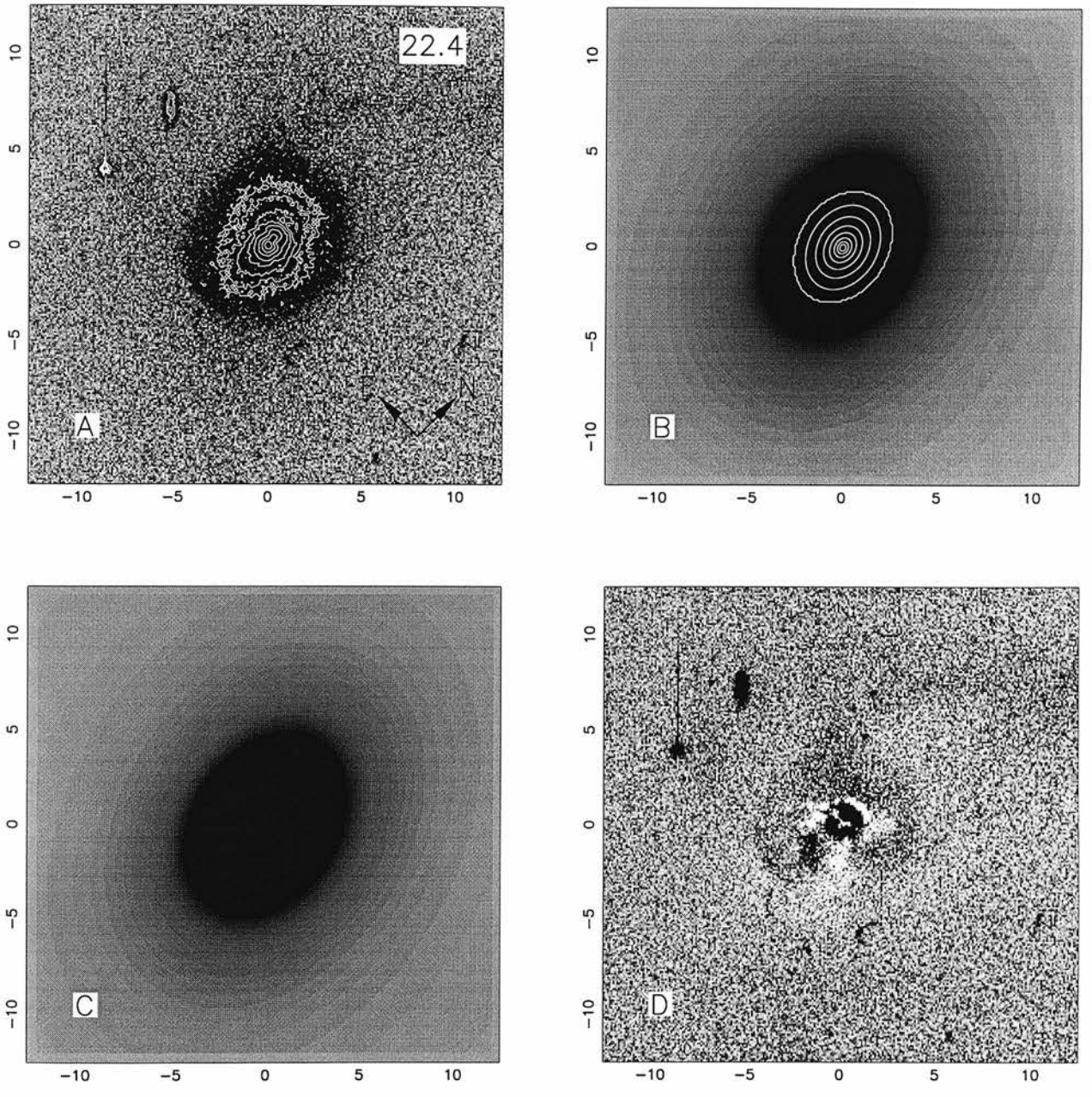

Figure B.10: The radio galaxy 2141+279

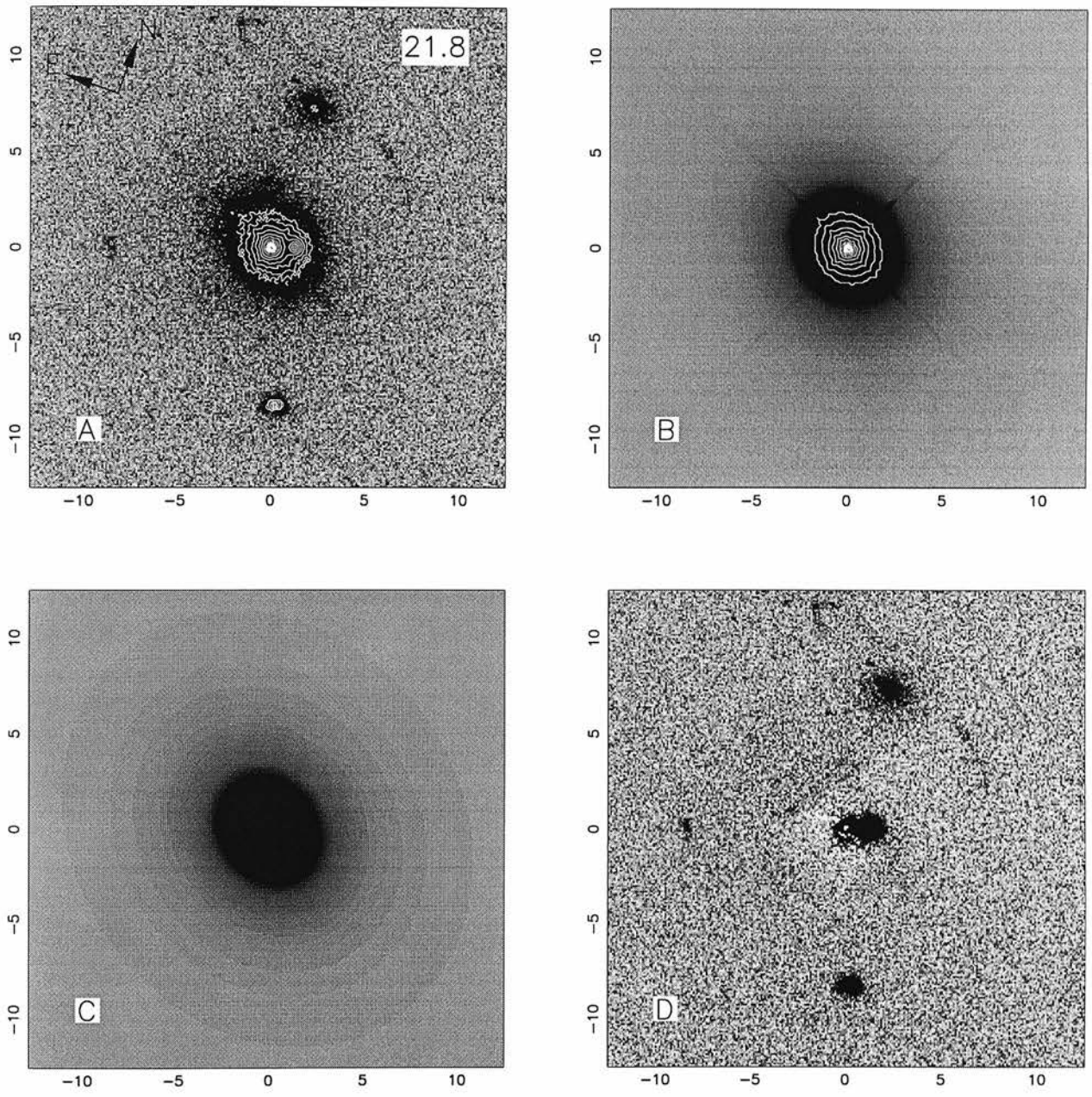

Figure B.11: The radio-loud quasar 0137+012

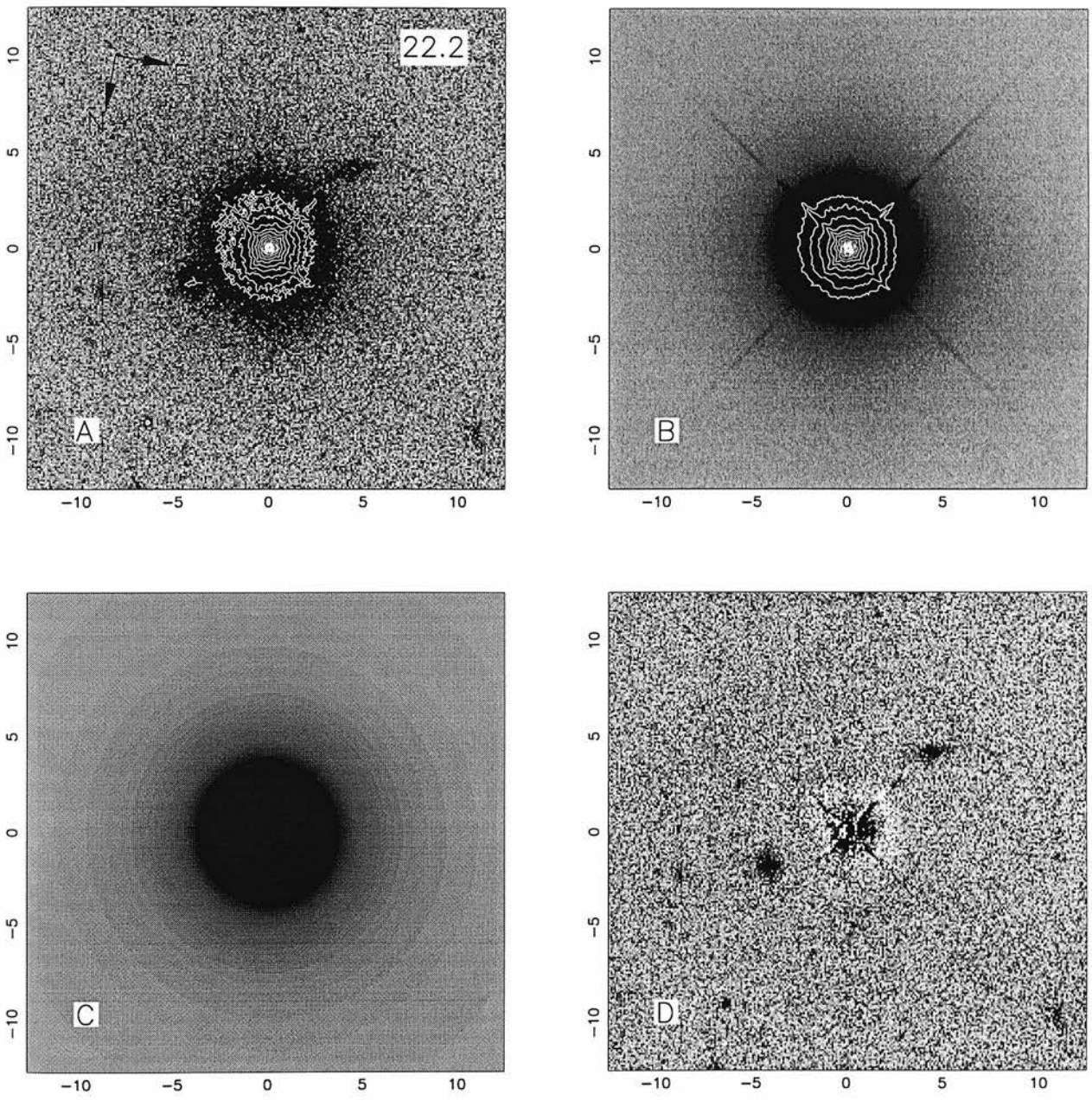

Figure B.12: The radio-loud quasar 0736+017

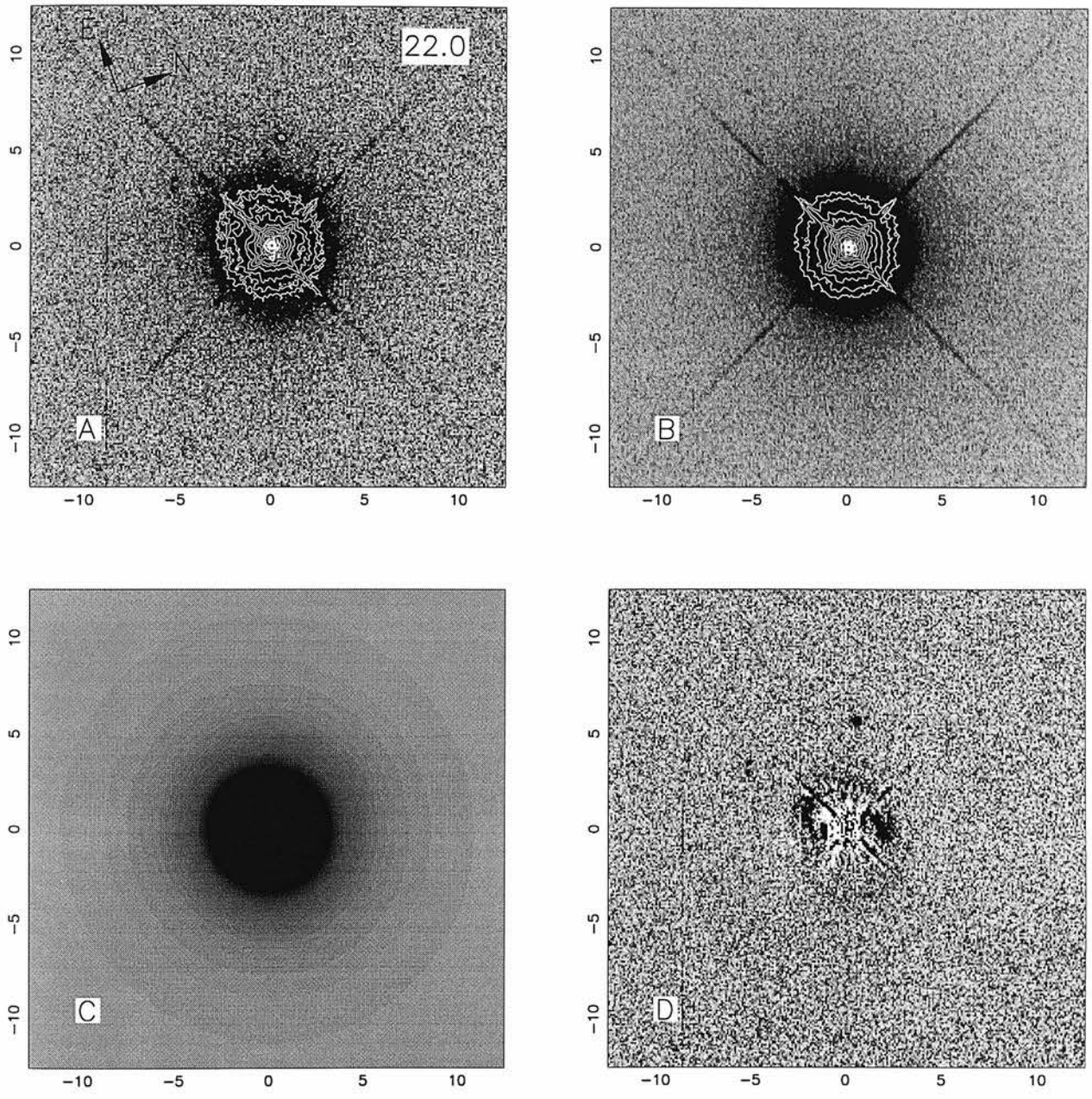

Figure B.13: The radio-loud quasar 1004+130

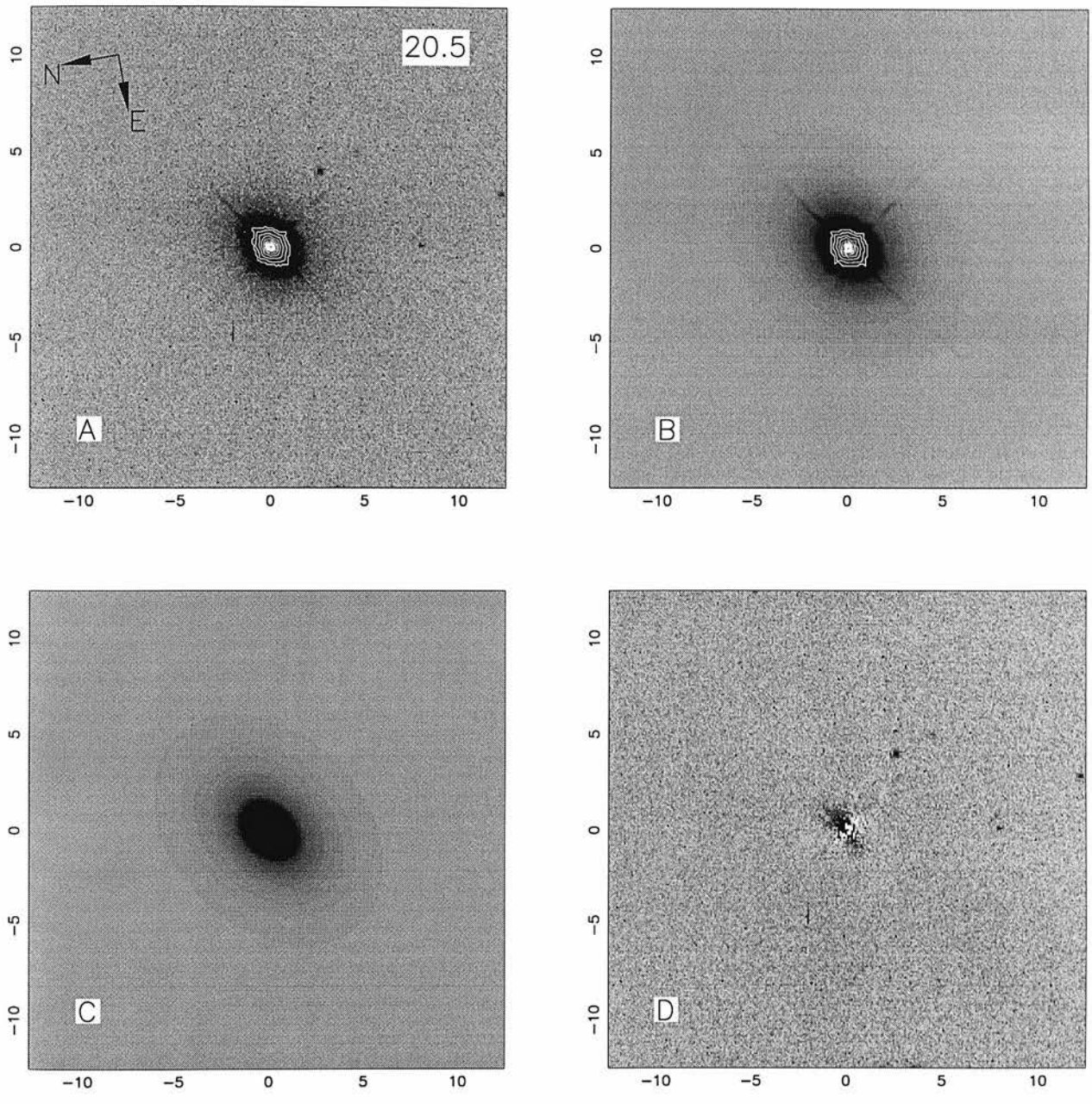

Figure B.14: The radio-loud quasar 1020−103

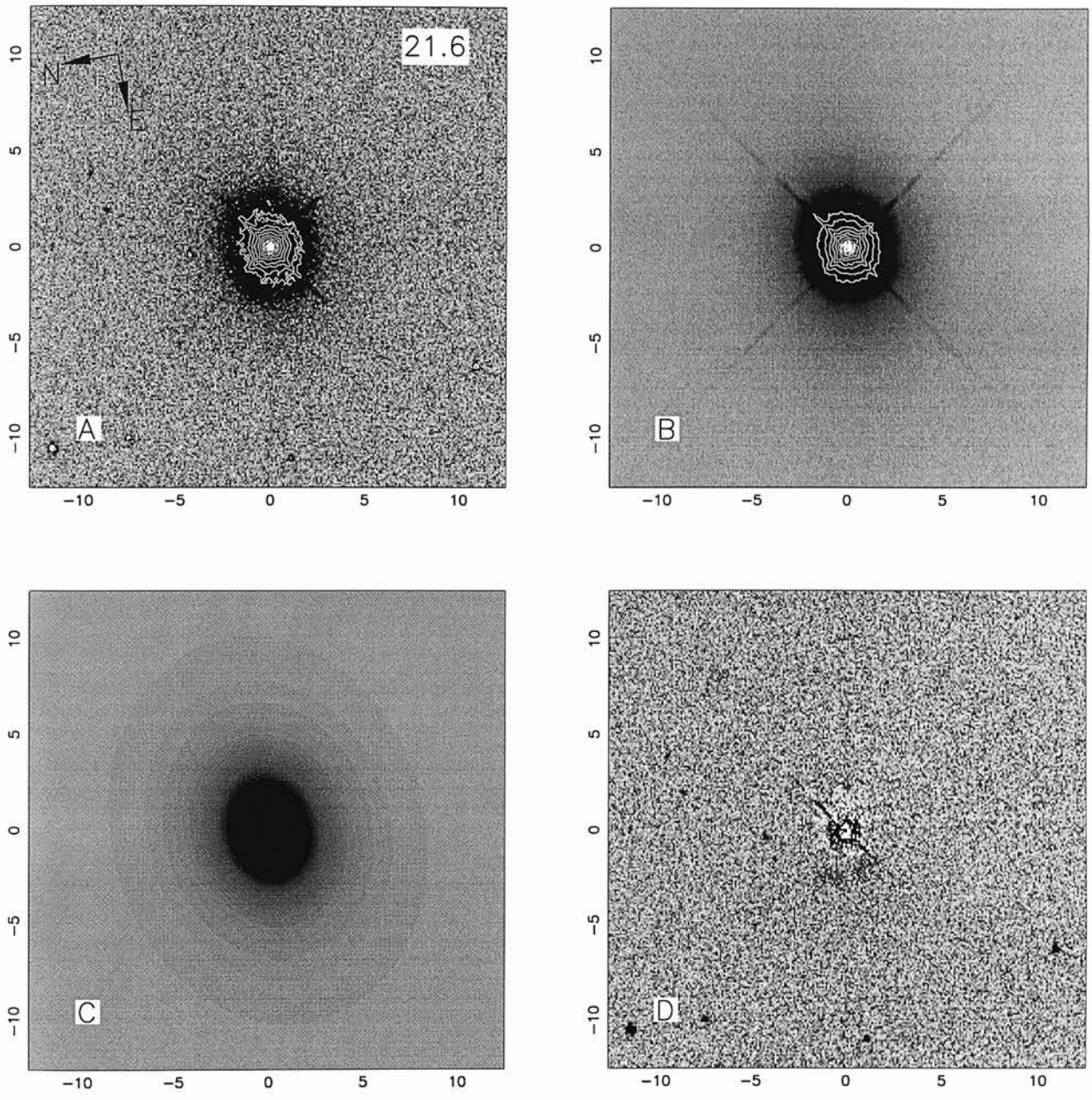

Figure B.15: The radio-loud quasar 1217+023

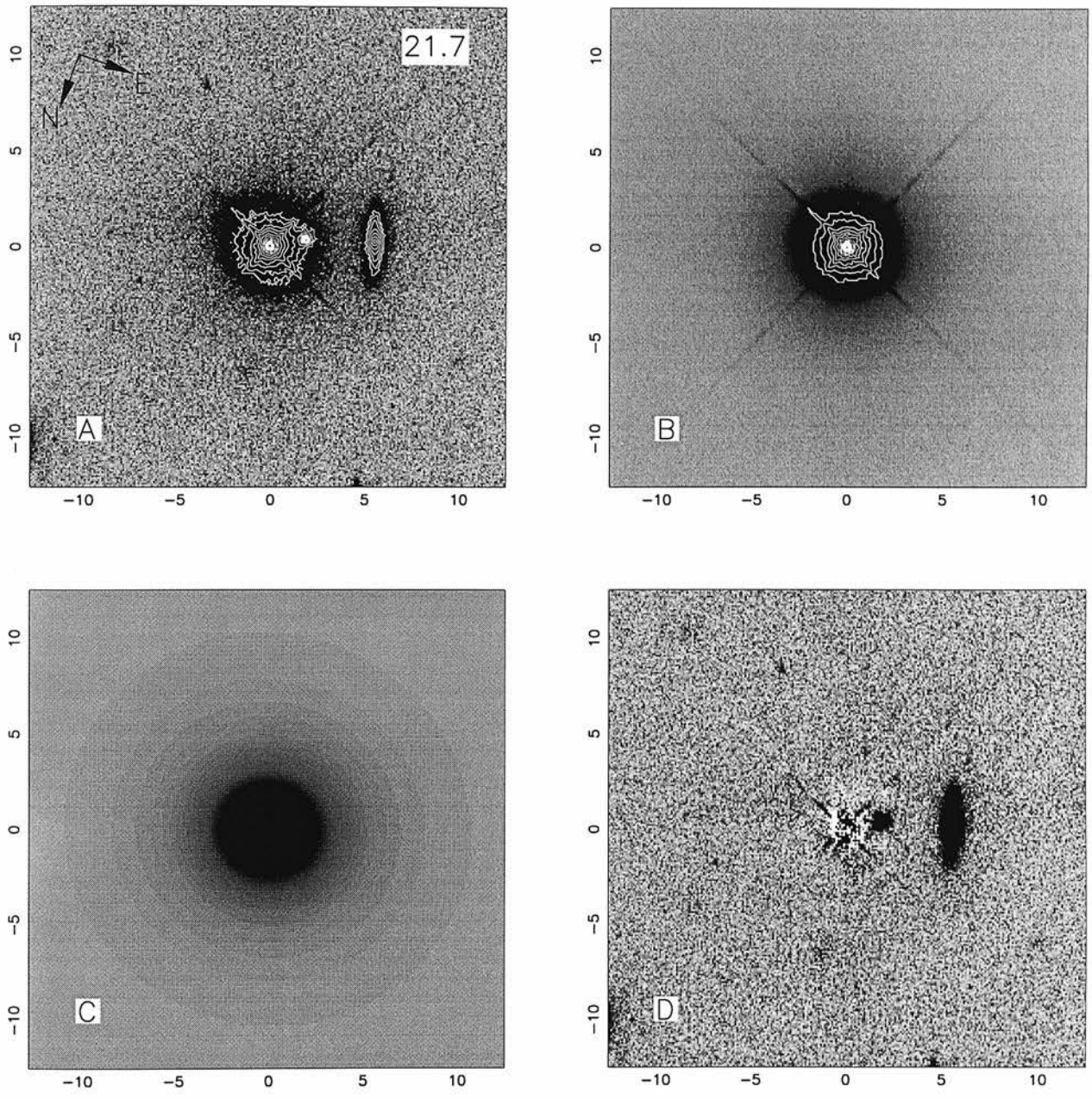

Figure B.16: The radio-loud quasar 2135−147

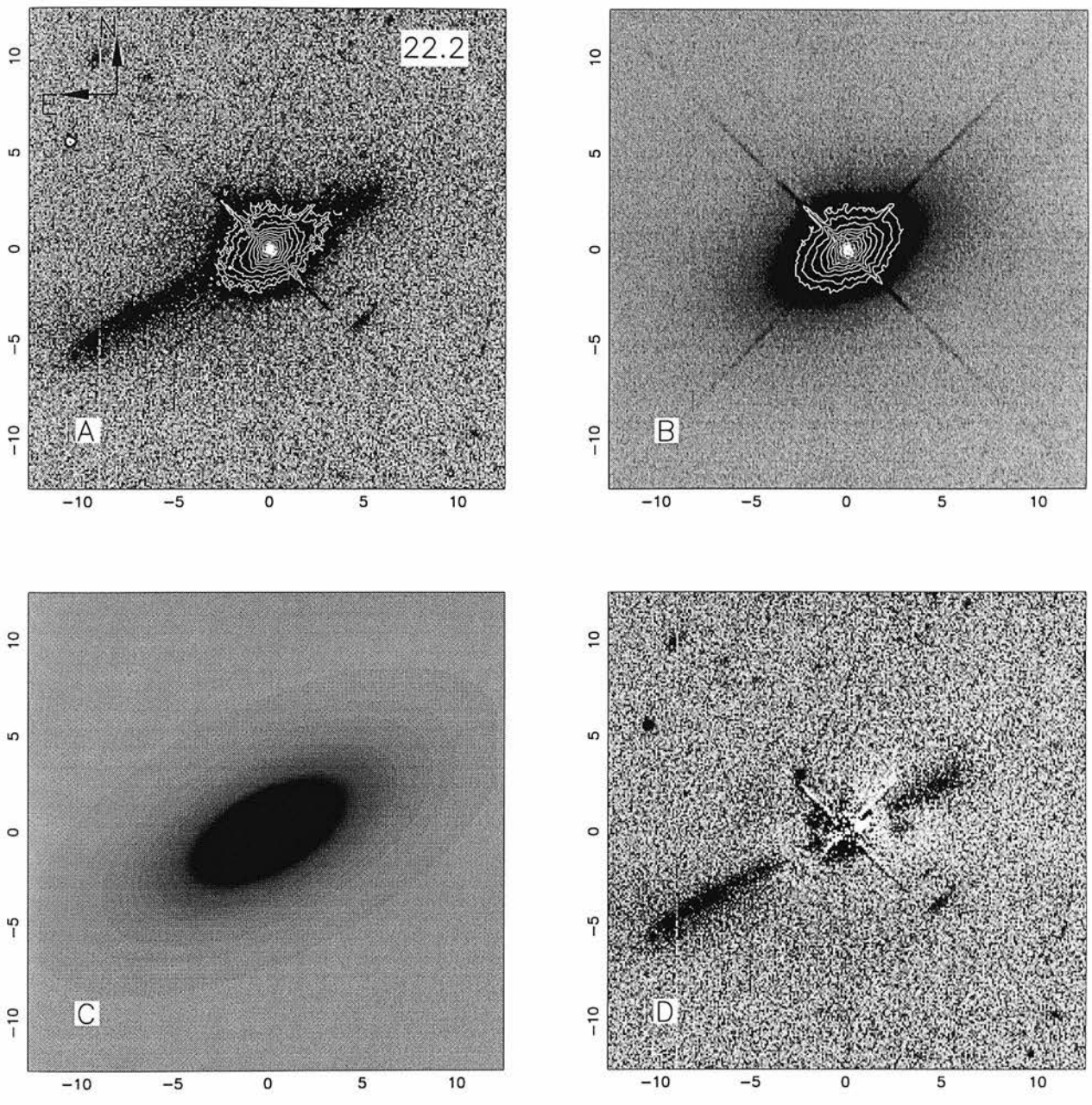

Figure B.17: The radio-loud quasar 2141+175

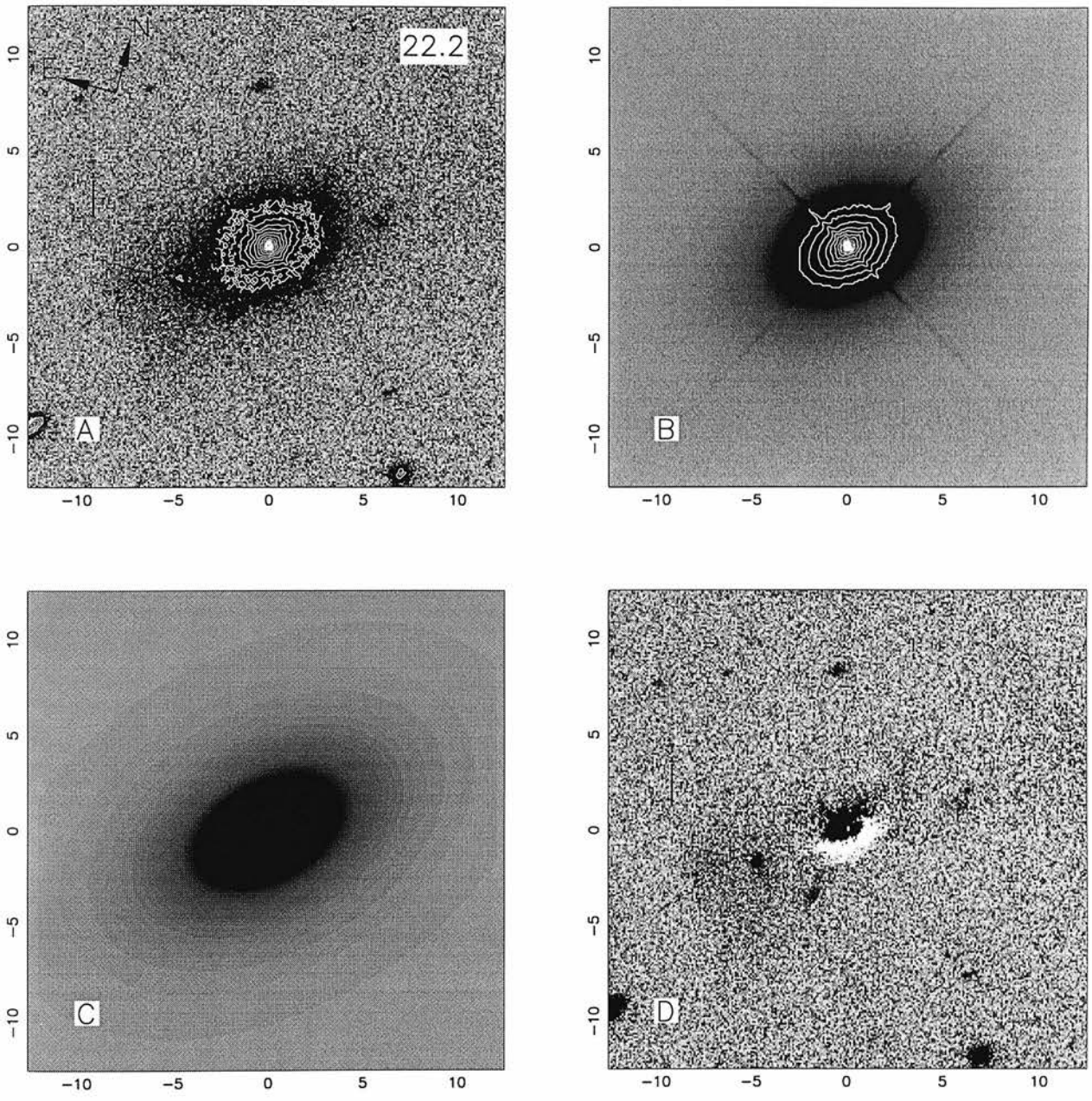

Figure B.18: The radio-loud quasar 2247+140

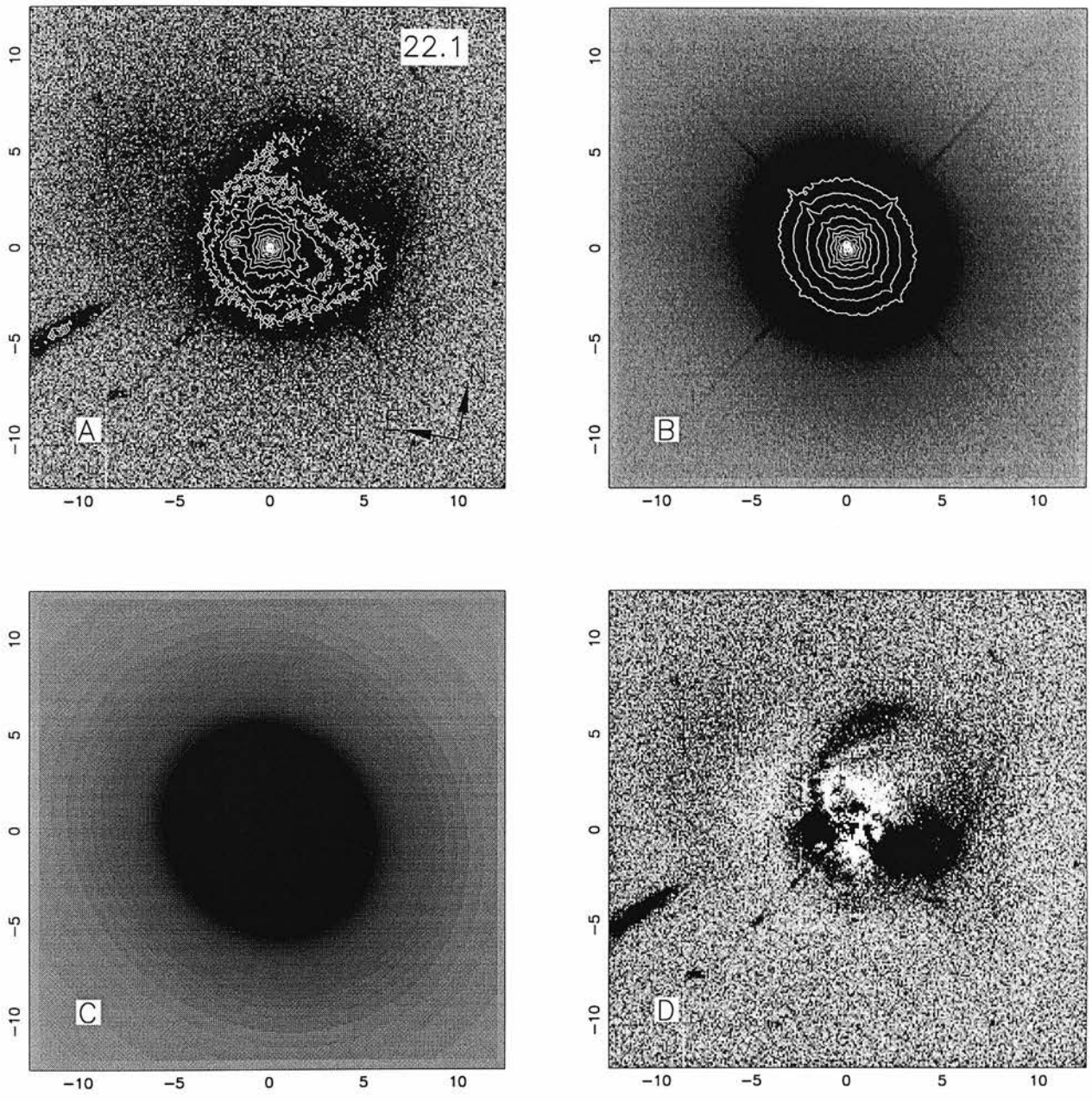

Figure B.19: The radio-loud quasar 2349−014

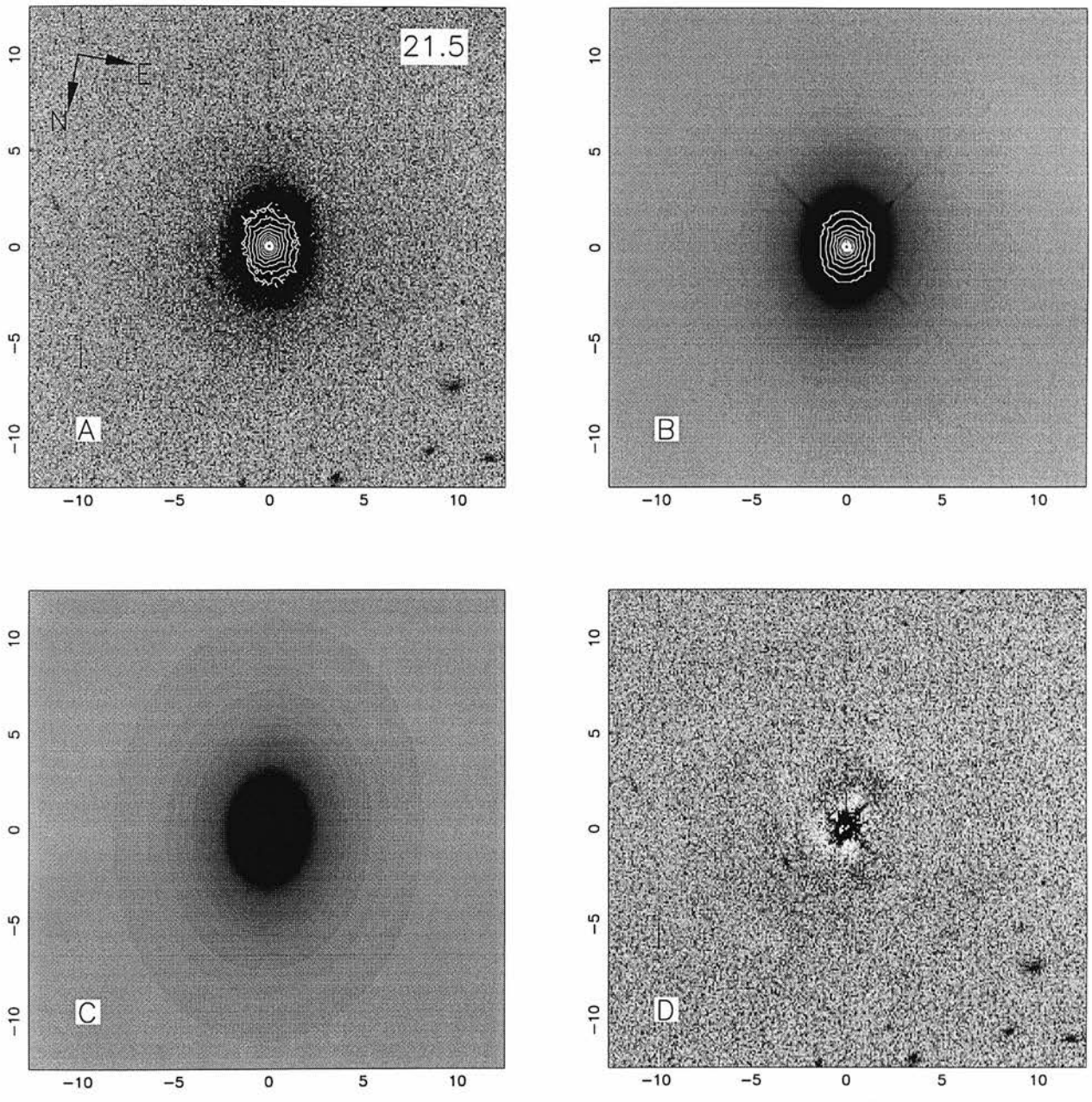

Figure B.20: The radio-loud quasar 2355−082

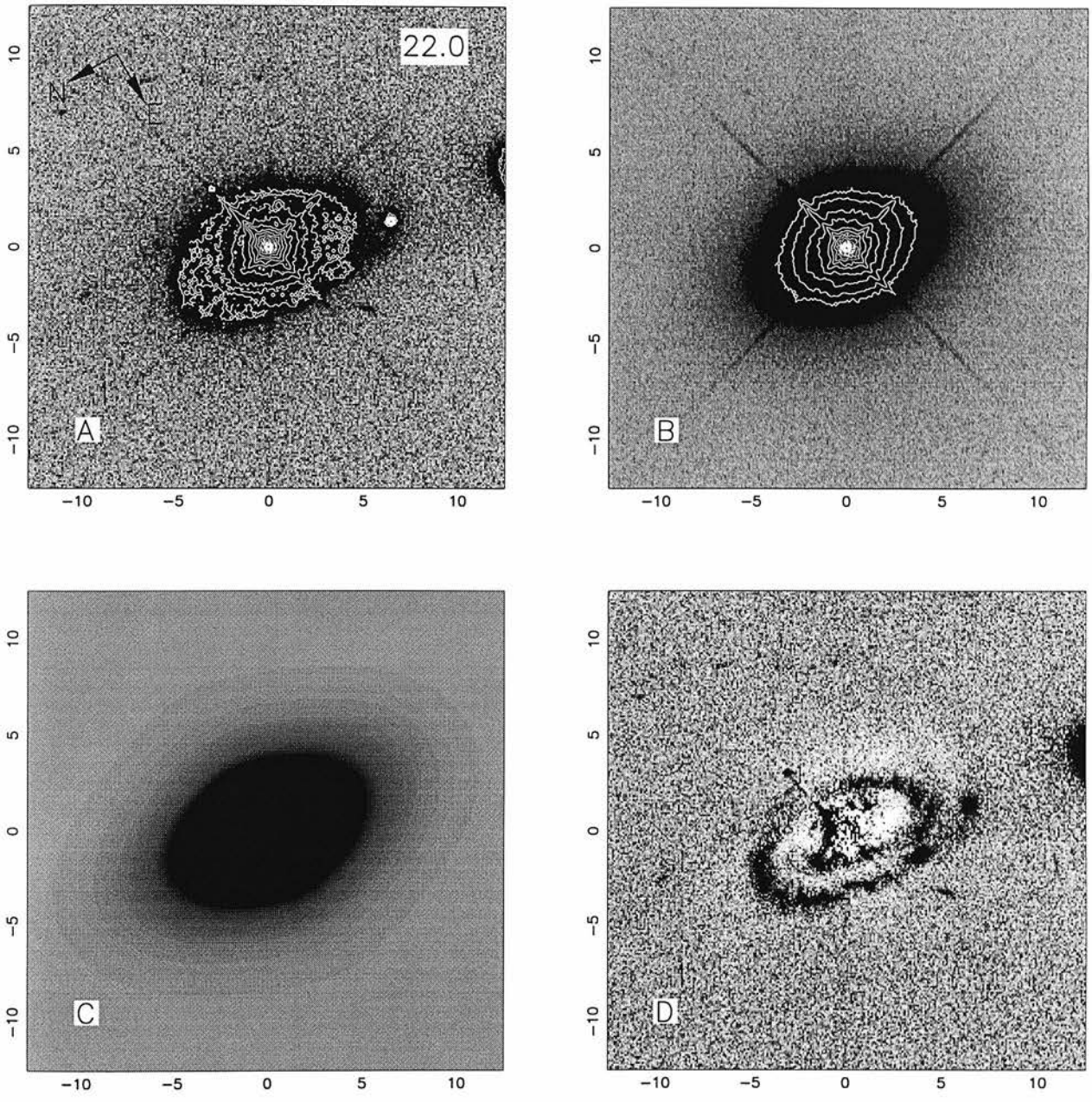

Figure B.21: The radio-quiet quasar 0052+251

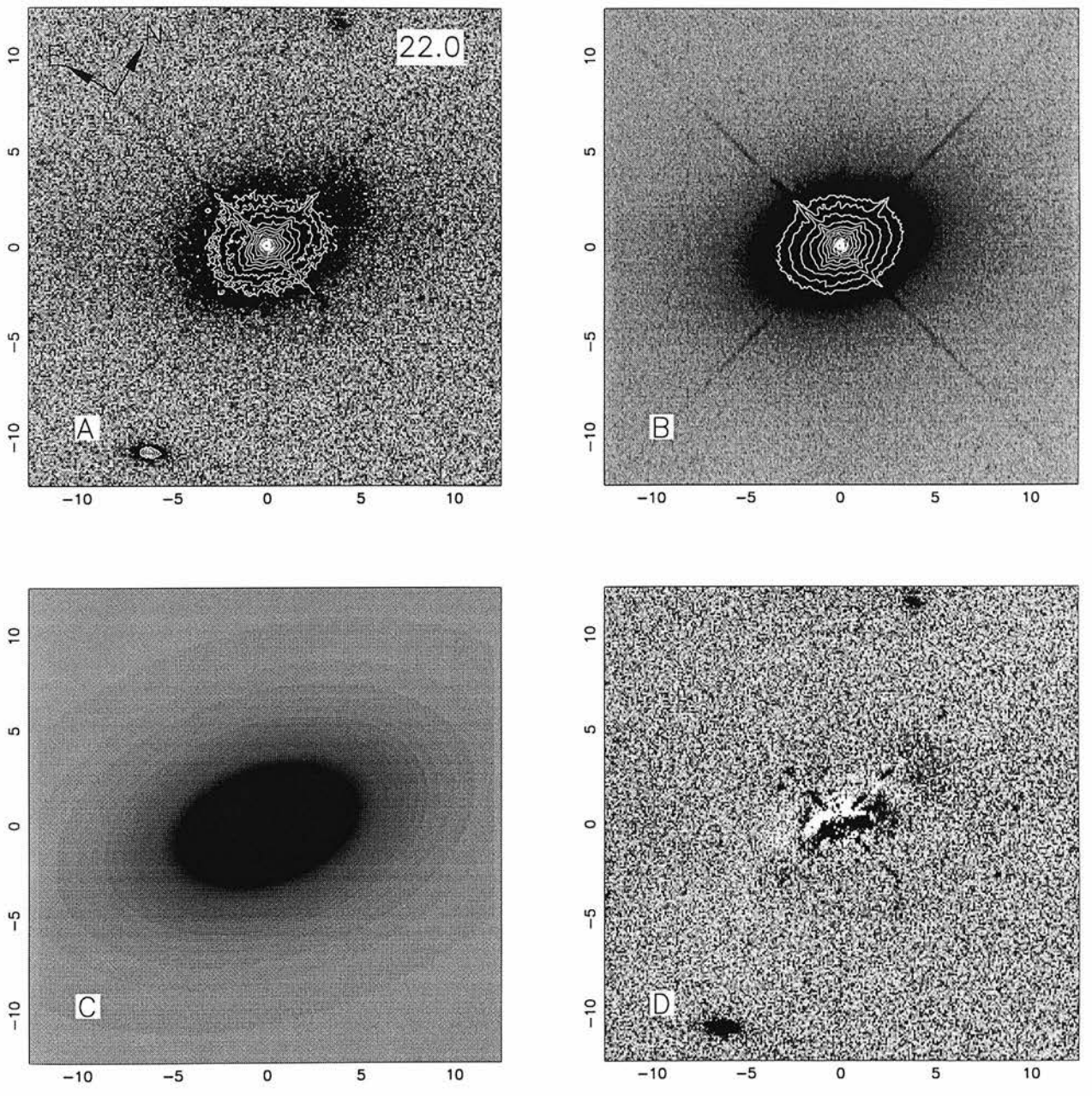

Figure B.22: The radio-quiet quasar 0054+144

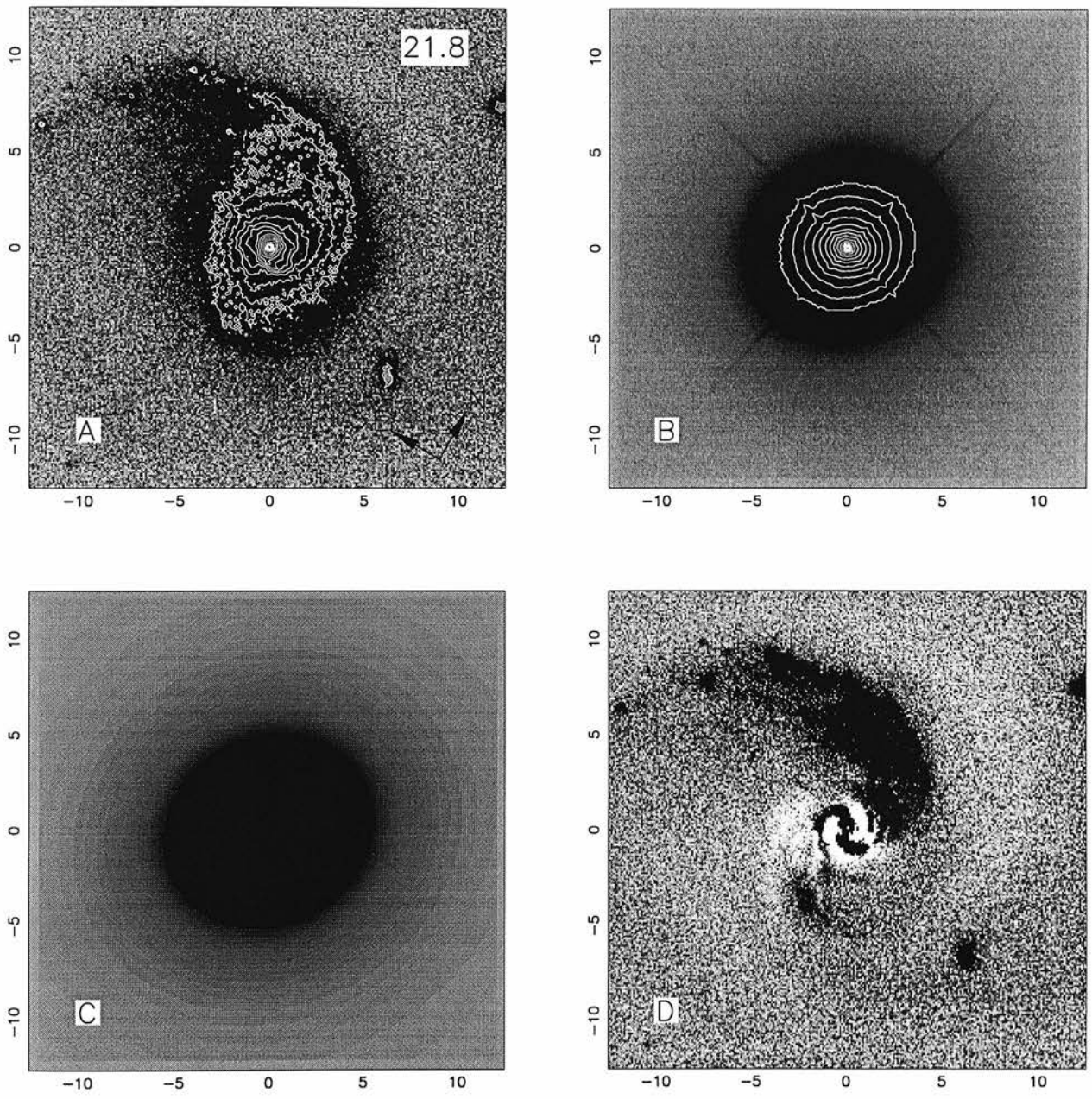

Figure B.23: The radio-quiet quasar 0157+001

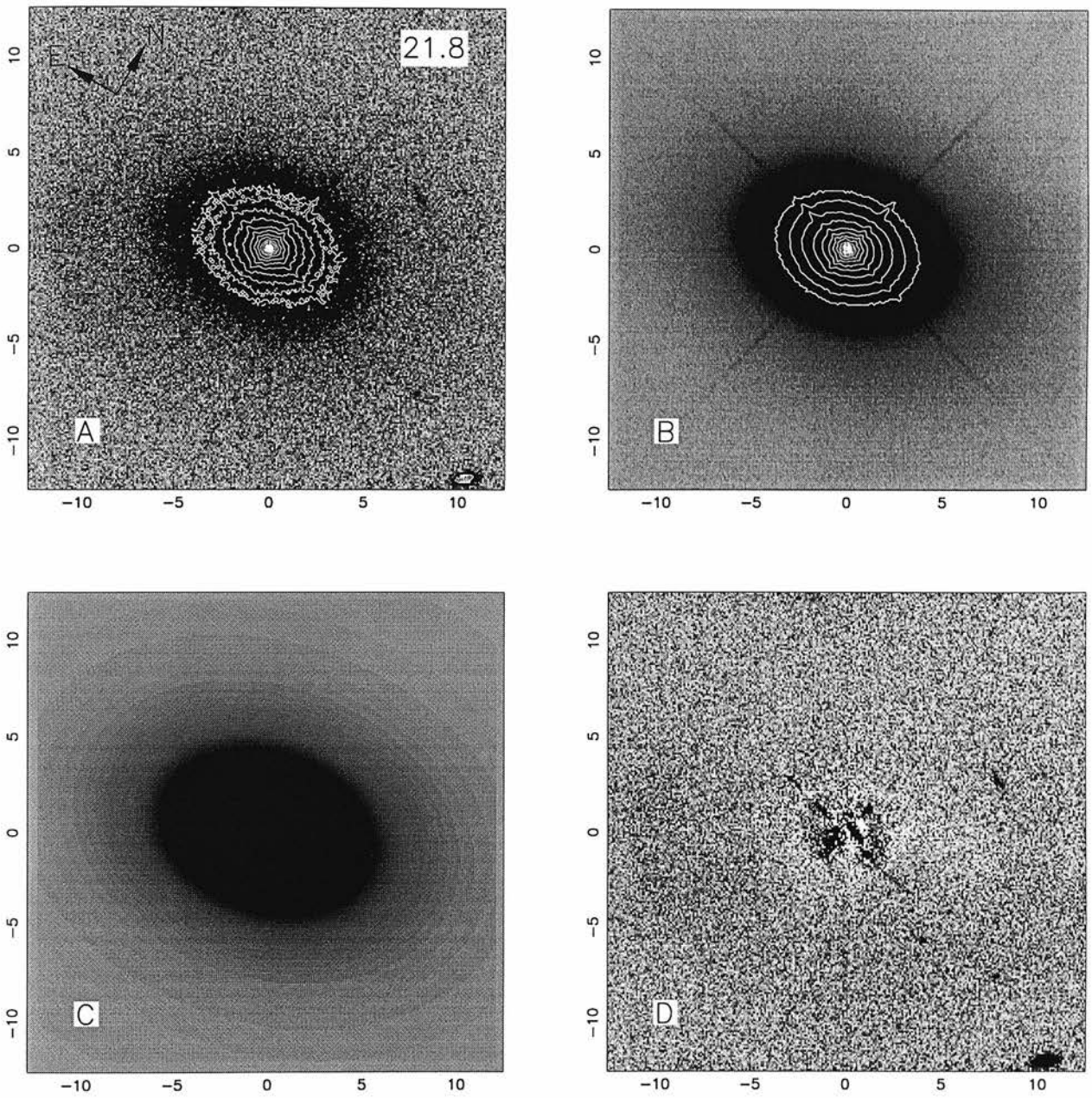

Figure B.24: The radio-quiet quasar 0204+292

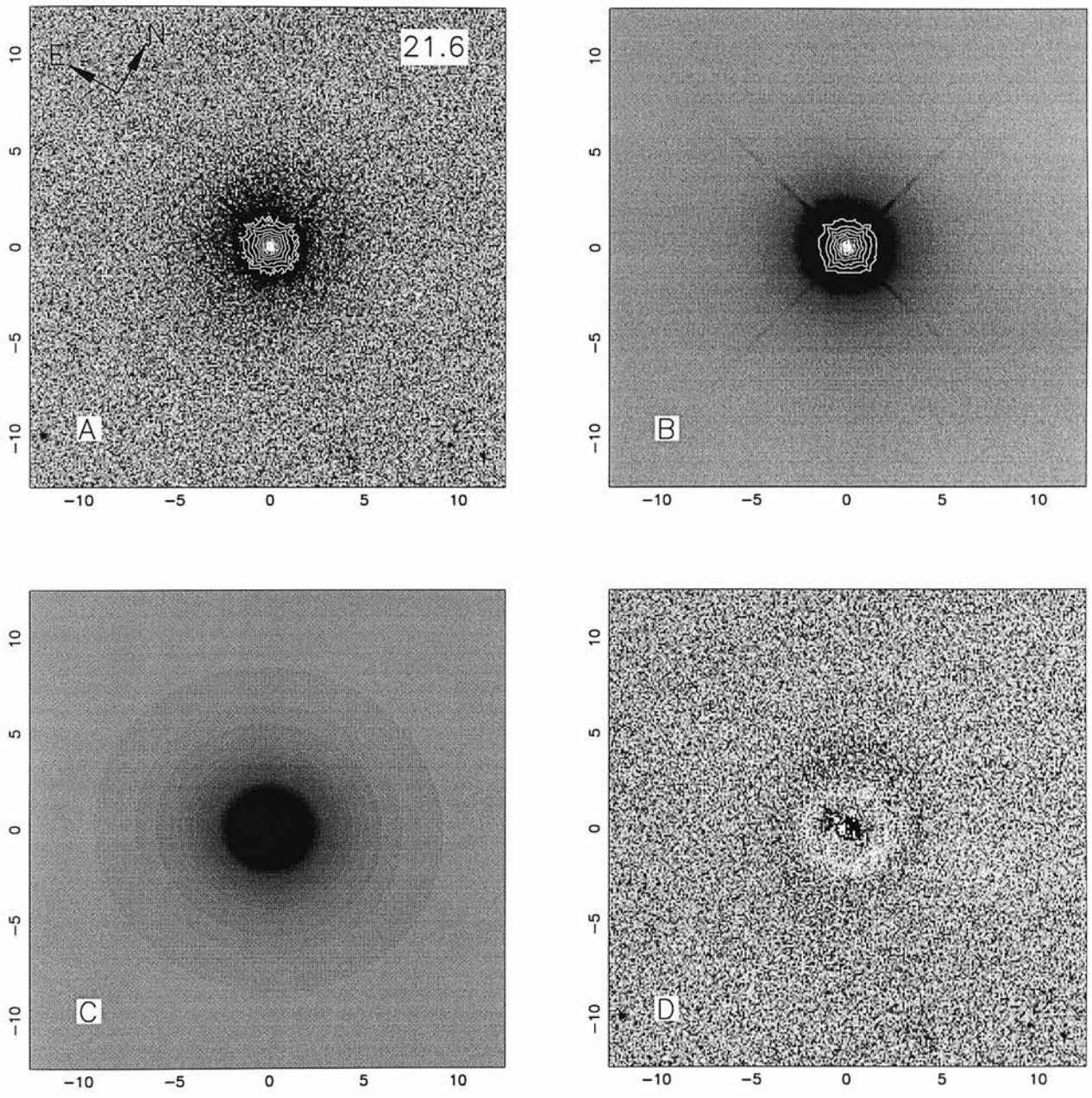

Figure B.25: The radio-quiet quasar 0244+194

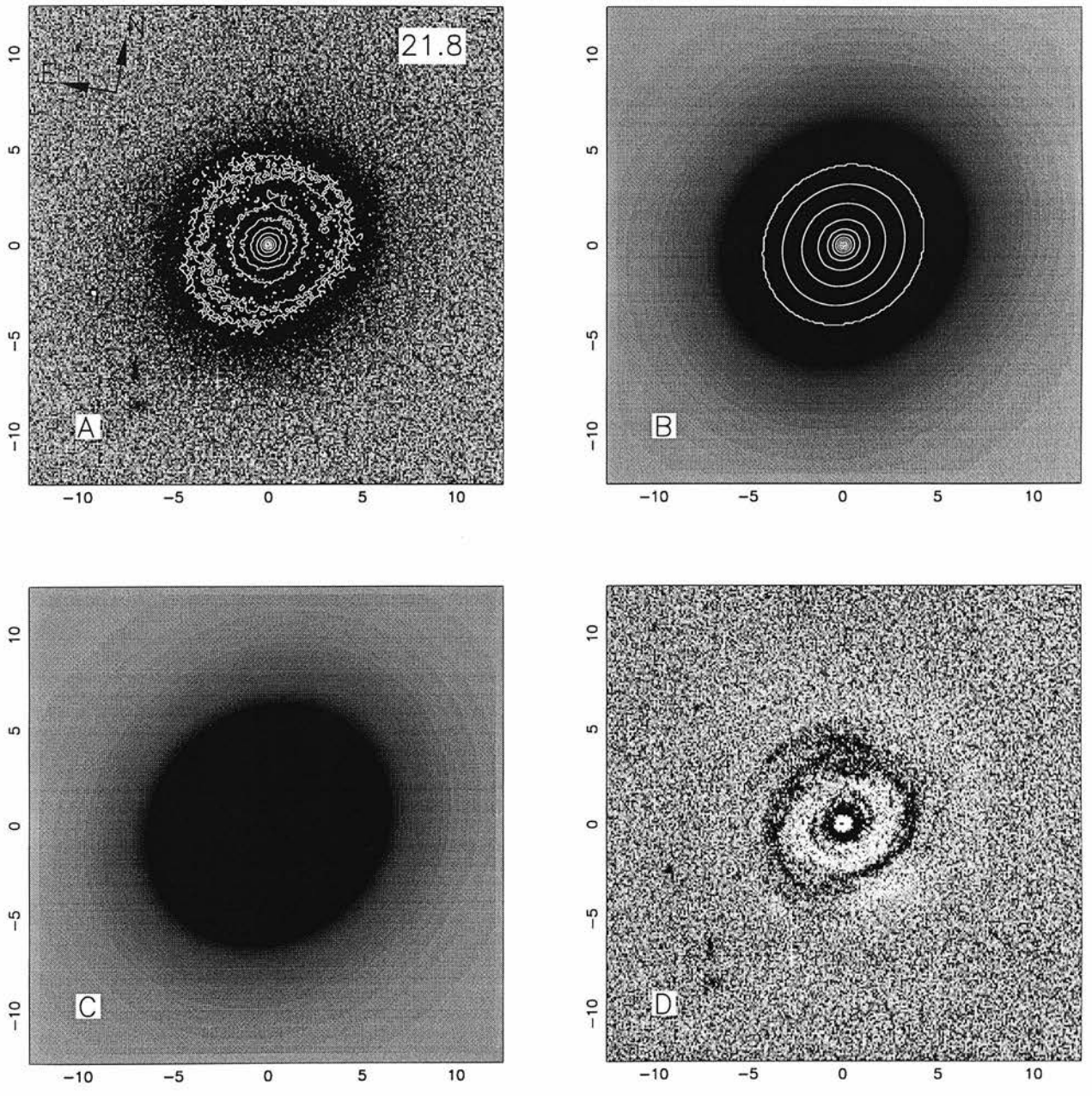

Figure B.26: The radio-quiet quasar 0257+024

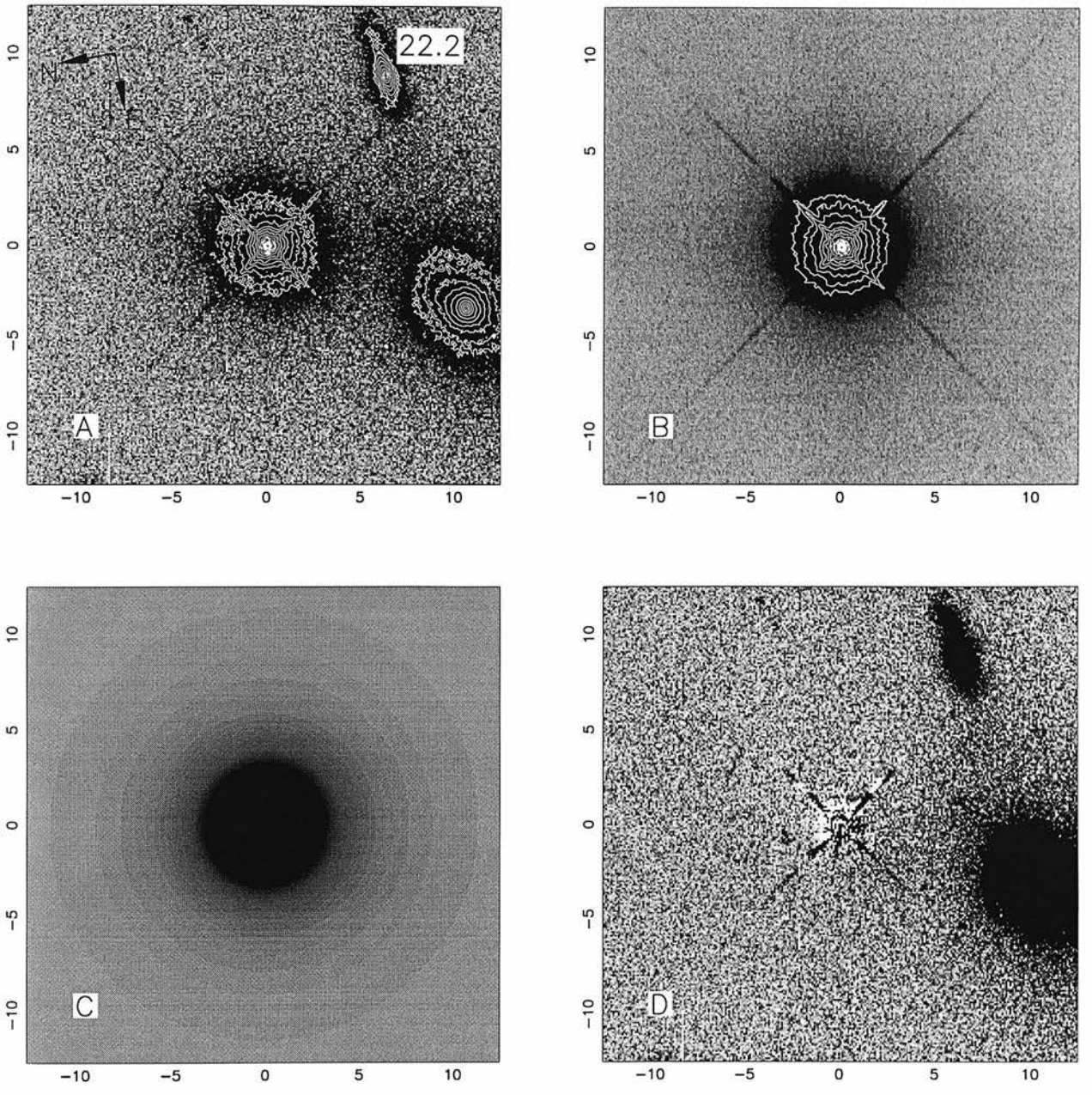

Figure B.27: The radio-quiet quasar 0923+201

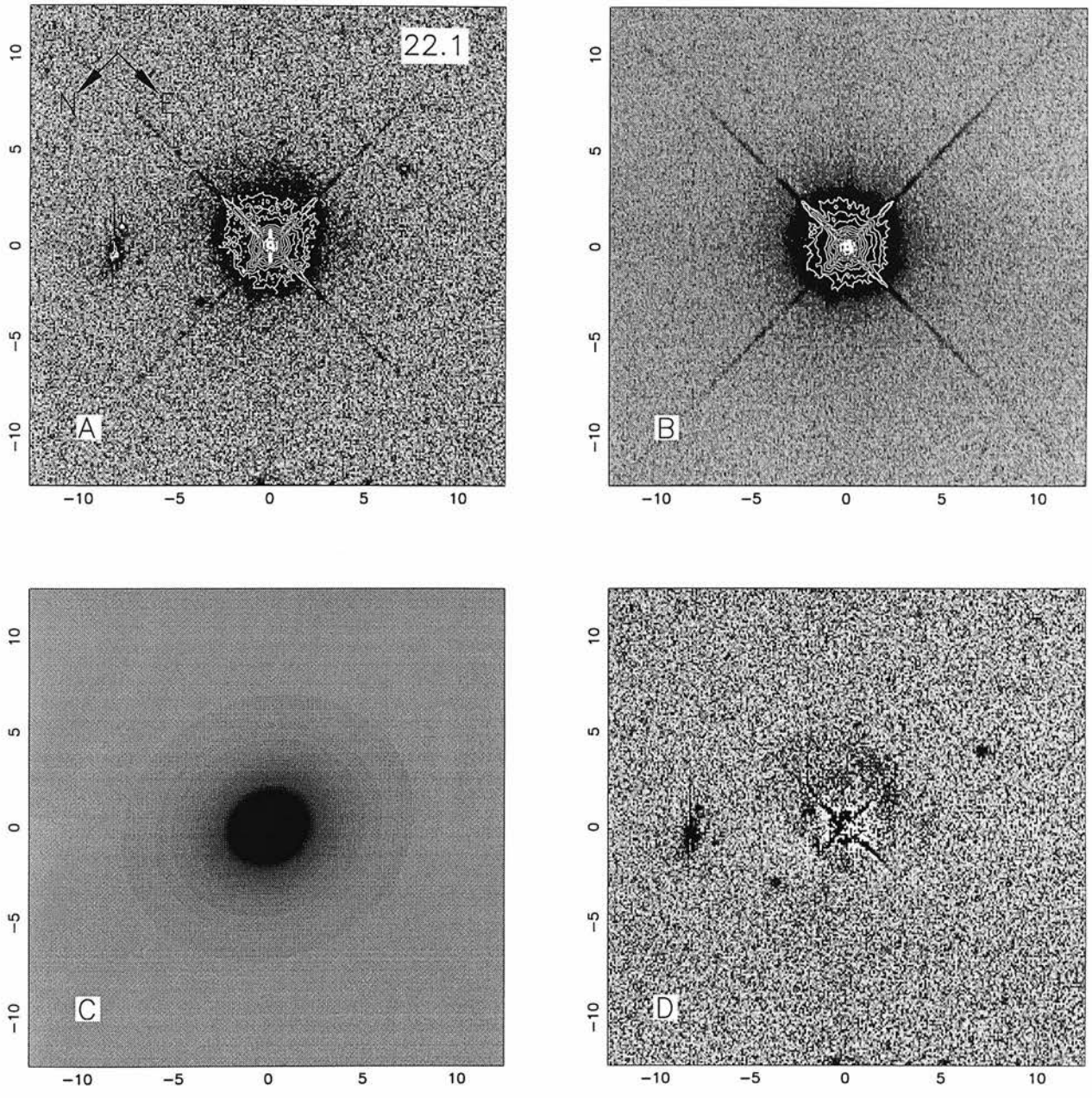

Figure B.28: The radio-quiet quasar 0953+415

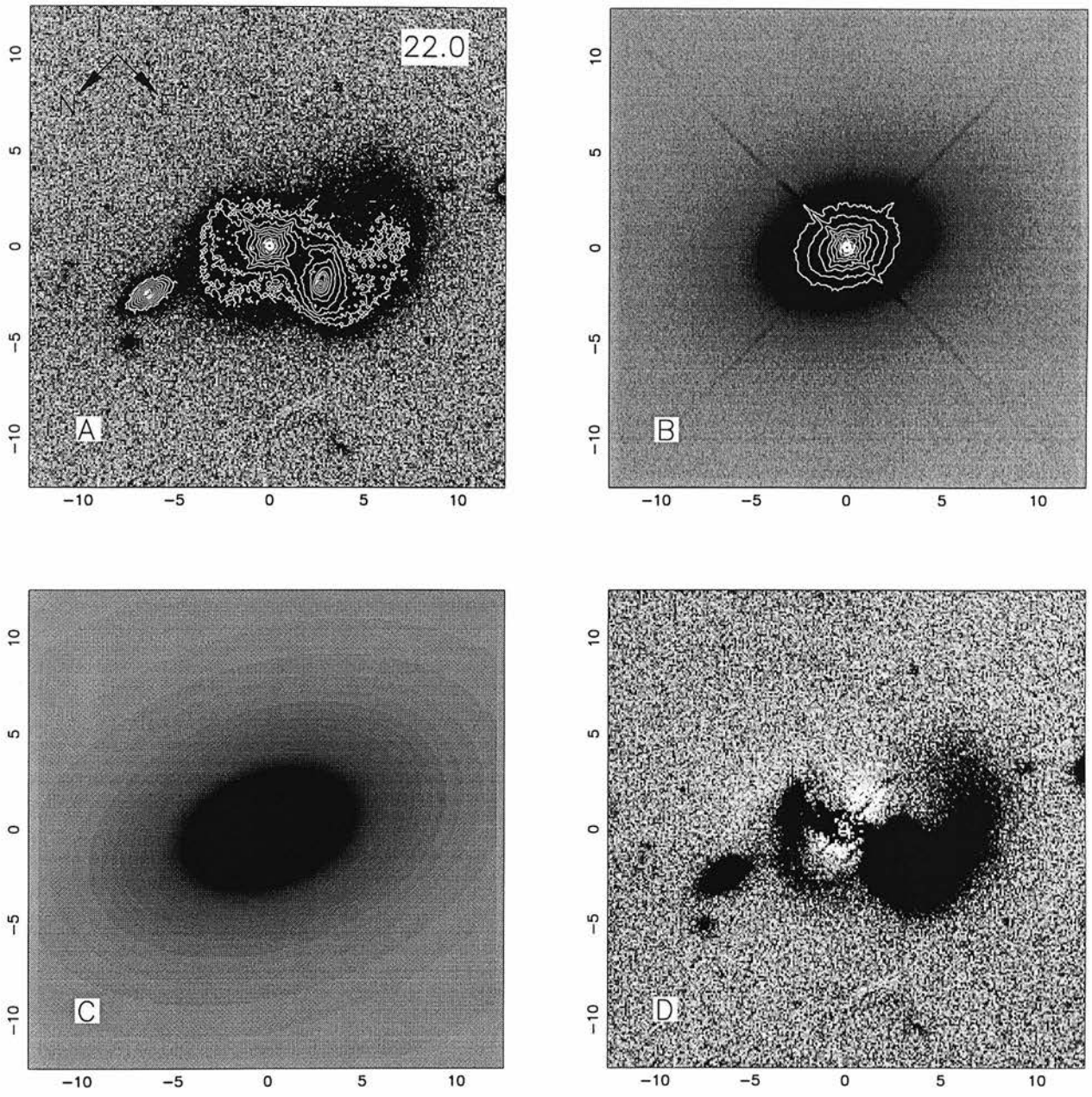

Figure B.29: The radio-quiet quasar 1012+008

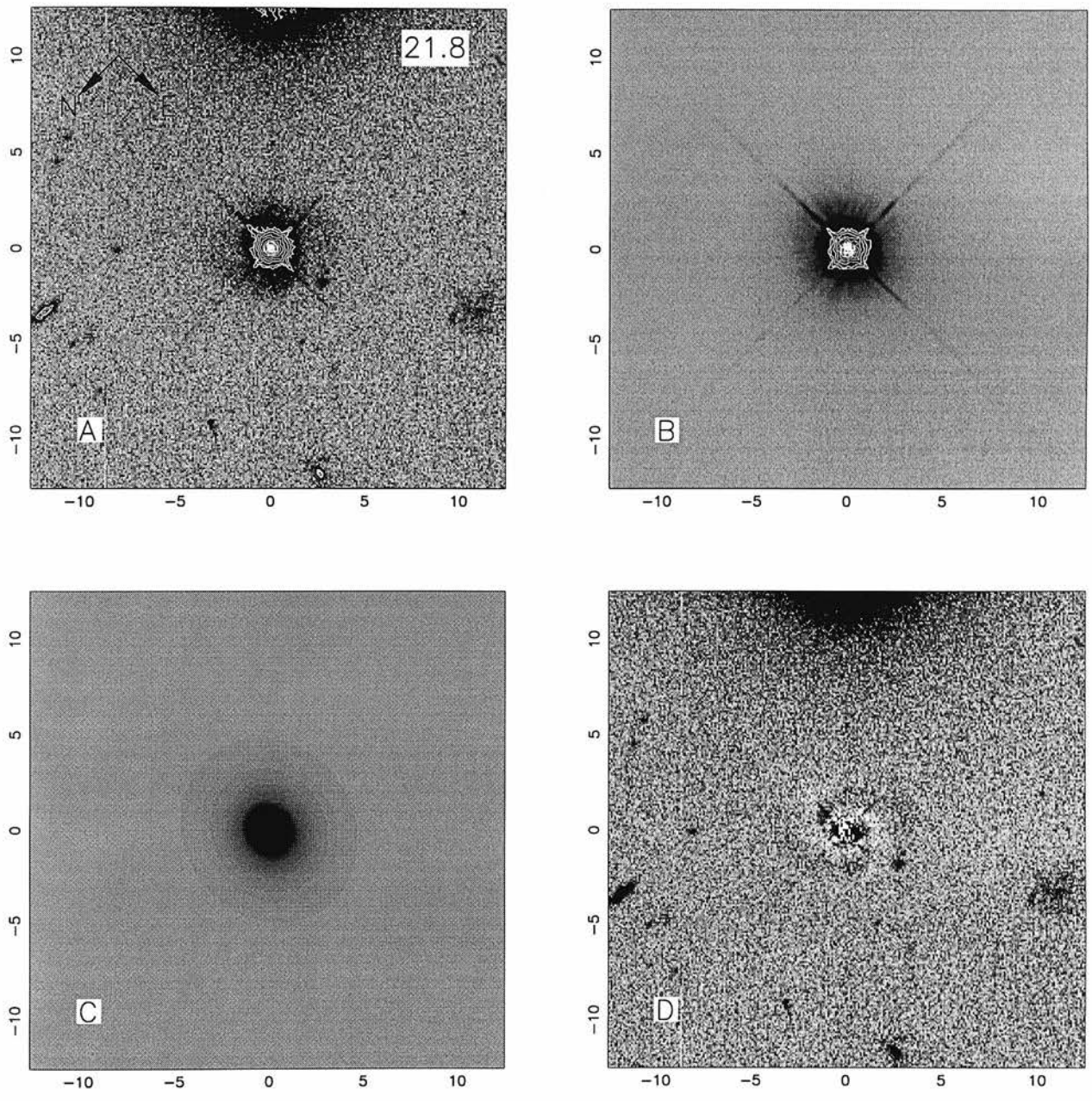

Figure B.30: The radio-quiet quasar 1549+203

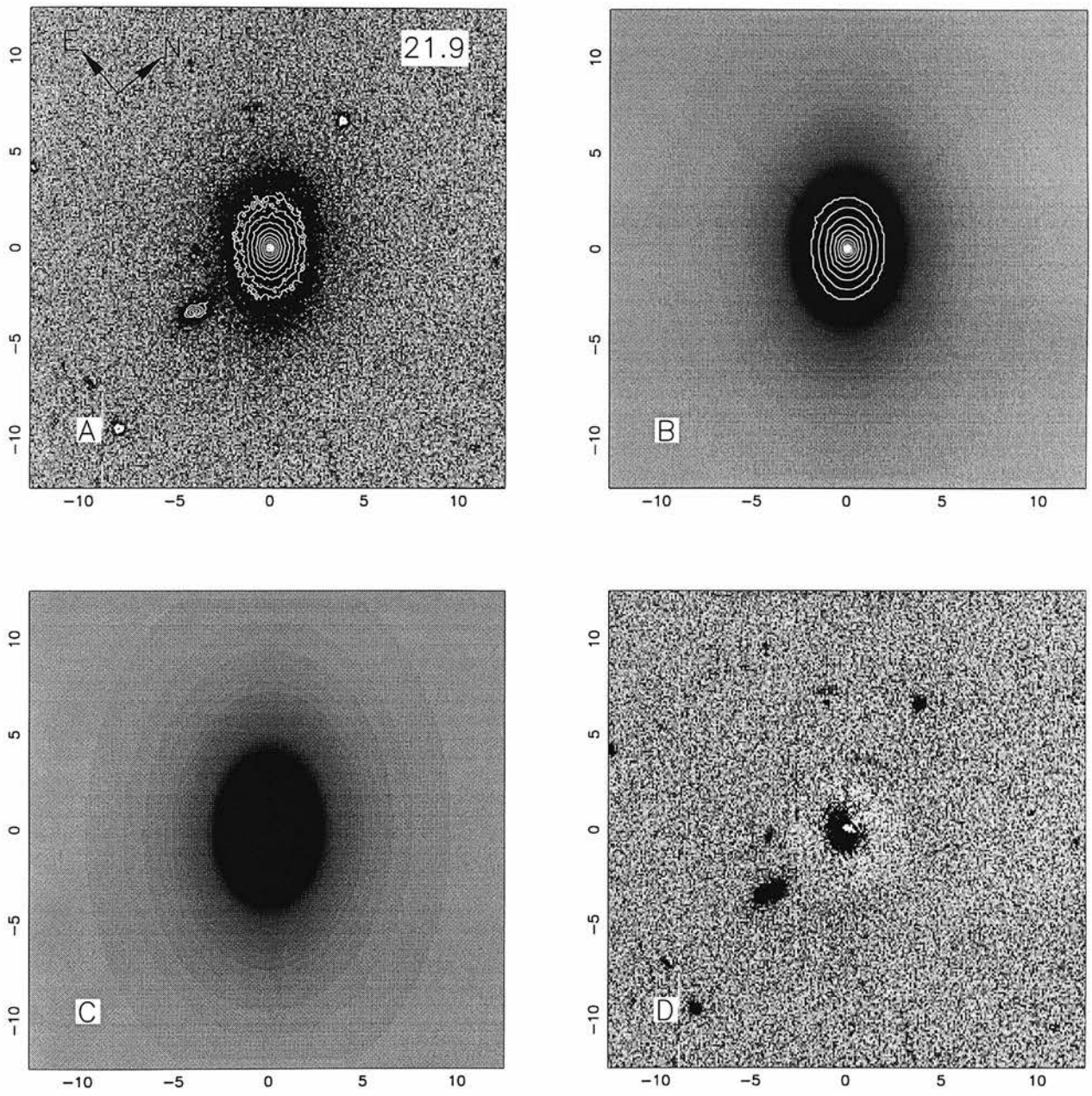

Figure B.31: The radio-quiet quasar 1635+119

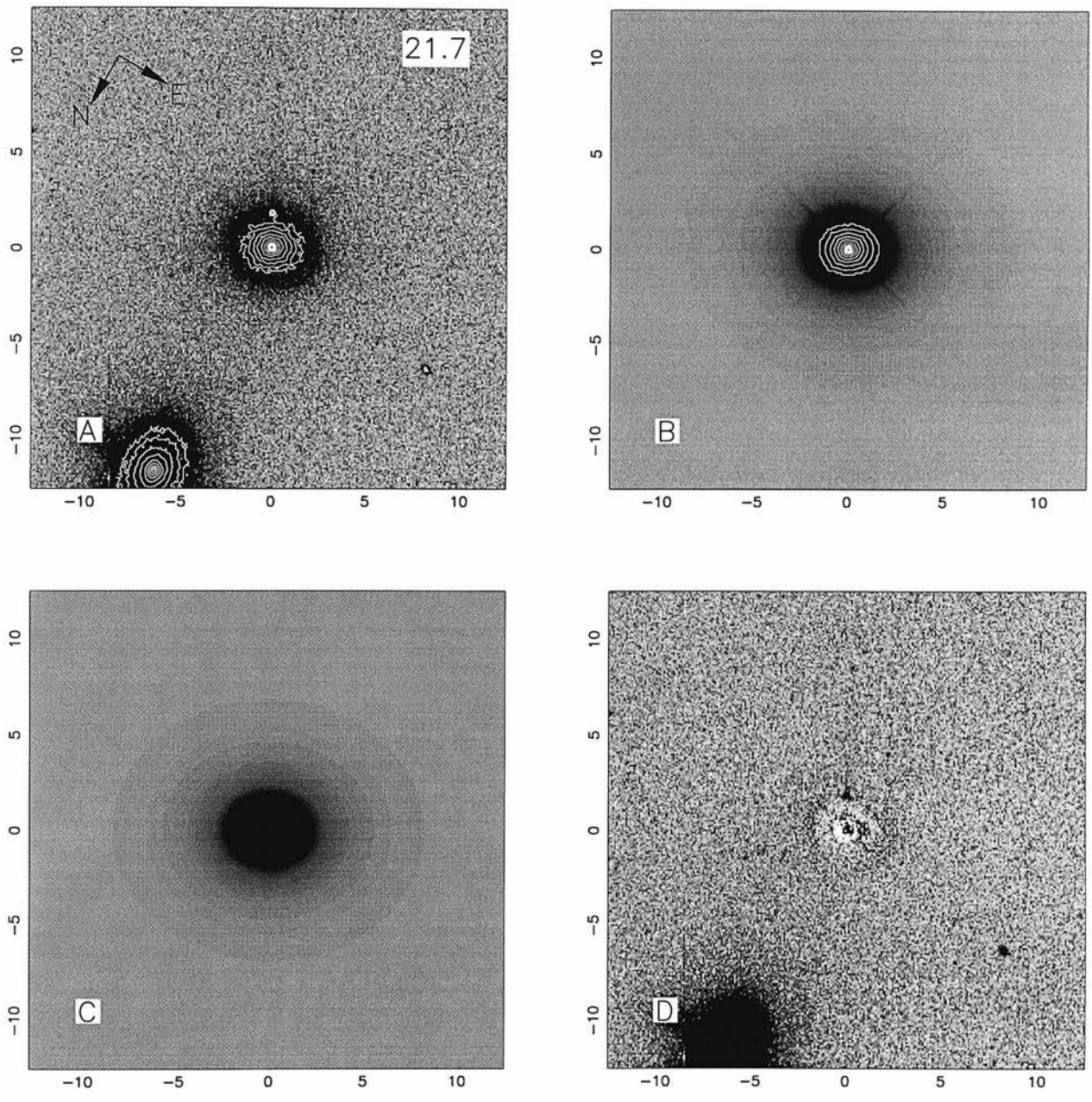

Figure B.32: The radio-quiet quasar 2215−037

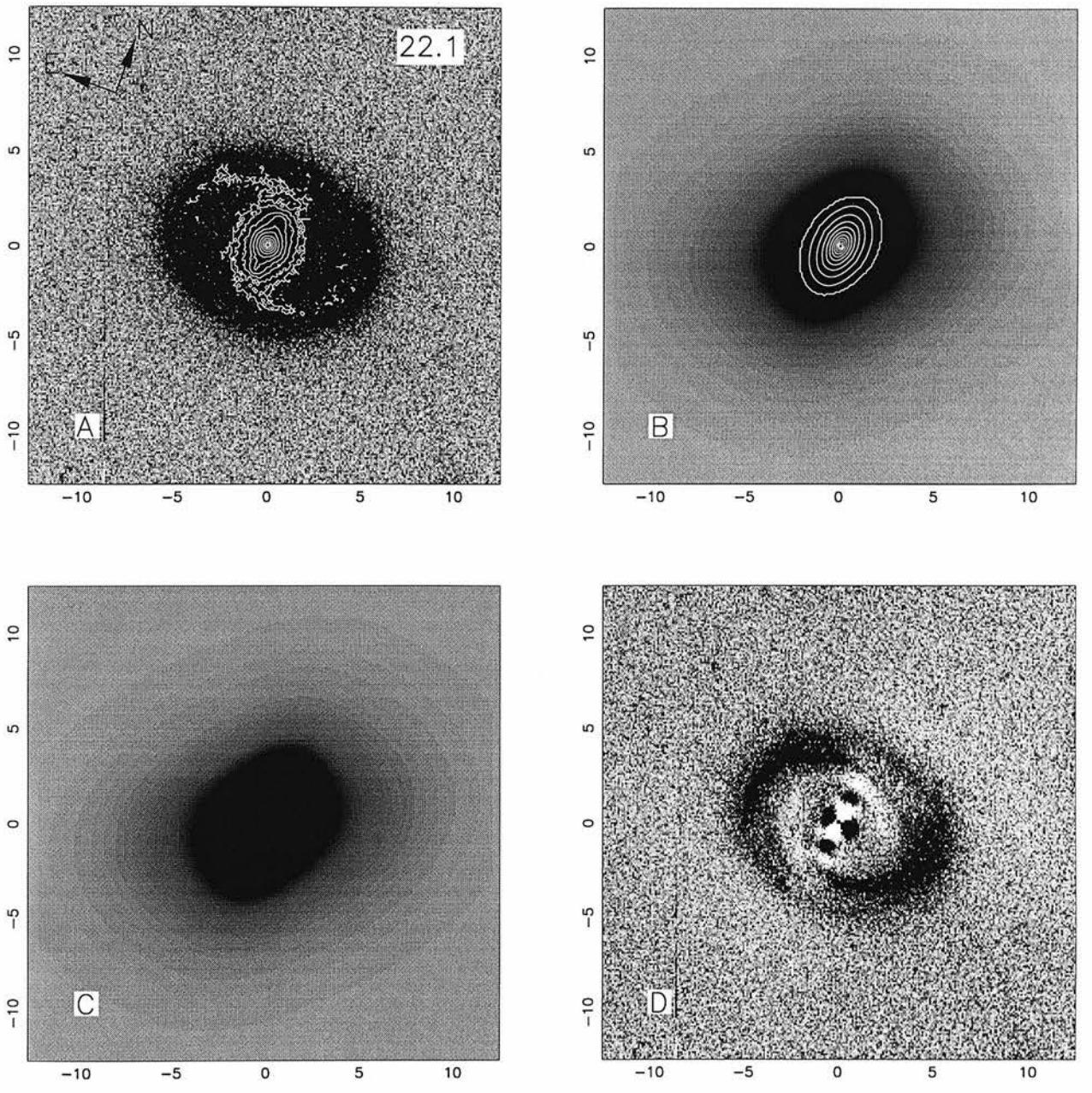

Figure B.33: The radio-quiet quasar 2344+184

Appendix C

A Comparative HST Host Galaxy Imaging Study

This appendix includes the text of the recently published MNRAS paper, "A comparative HST imaging study of the host galaxies of radio-quiet quasars, radio-loud quasars and radio galaxies: Paper 1". Some of the material presented in Chapters 2, 3, 4 & 5 appears in this paper, although the results presented in the paper are restricted to only 19 of the 33 objects in the HST AGN sample.

Mon. Not. R. Astron. Soc. **308**, 377–404 (1999)

A comparative *HST* imaging study of the host galaxies of radio-quiet quasars, radio-loud quasars and radio galaxies – I

R. J. McLure,[1] M. J. Kukula,[1,2] J. S. Dunlop,[1] S. A. Baum,[2] C. P. O'Dea[2] and D. H. Hughes[2]

[1]*Institute for Astronomy, University of Edinburgh, Blackford Hill, Edinburgh EH9 3HJ*
[2]*Space Telescope Science Institute, 3700 San Martin Drive, Baltimore, MD 21218, USA*

Accepted 1999 March 22. Received 1999 March 22; in original form 1998 October 20

ABSTRACT

We present the first results from a major *HST* WFPC2 imaging study aimed at providing the first statistically meaningful comparison of the morphologies, luminosities, scalelengths and colours of the host galaxies of radio-quiet quasars, radio-loud quasars and radio galaxies. We describe the design of this study and present the images that have been obtained for the first half of our 33-source sample. We find that the hosts of all three classes of luminous AGN are massive elliptical galaxies, with scalelengths $\simeq 10$ kpc, and $R-K$ colours consistent with mature stellar populations. Most importantly, this is first unambiguous evidence that, just like radio-loud quasars, essentially all radio-quiet quasars brighter than $M_R = -24$ reside in massive ellipticals. This result removes the possibility that radio 'loudness' is directly linked to host galaxy morphology, but is however in excellent accord with the black hole/spheroid mass correlation recently highlighted by Magorrian et al. We apply the relations given by Magorrian et al. to infer the expected Eddington luminosity of the putative black hole at the centre of each of the spheroidal host galaxies we have uncovered. Comparison with the actual nuclear R-band luminosities suggests that the black holes in most of these galaxies are radiating at a few per cent of the Eddington luminosity; the brightest host galaxies in our low-z sample are capable of hosting quasars with $M_R \simeq -28$, comparable to the most luminous quasars at $z \simeq 3$. Finally, we discuss our host-derived black hole masses in the context of the radio luminosity:black hole mass correlation recently uncovered for nearby galaxies by Franceschini et al., and consider the resulting implications for the physical origin of radio loudness.

Key words: black hole physics – galaxies: active – galaxies: photometry – quasars: general – infrared: galaxies.

1 INTRODUCTION

Studies of the host galaxies of active galactic nuclei (AGN) may hold the key to answering several important questions about these still poorly understood objects. Such questions include (i) what is the physical origin of radio loudness?, (ii) by what mechanisms are galactic nuclei triggered into activity (e.g. Smith & Heckman 1990; Hutchings & Neff 1992)?, (iii) which classes of AGN can be unified via orientation effects (Peacock 1987; Barthel 1989; Urry & Padovani 1995)?, (iv) which classes of AGN can or cannot be unified via time evolution (e.g. Ellingson, Yee & Green 1991), and (v) how does the recently inferred relation between black hole mass and galaxy bulge mass (Magorrian et al. 1998) extend to high masses? Furthermore, by defining the parameter space occupied by AGN hosts, important constraints can be derived on the fraction of the galaxy population which might contain a dormant AGN, constraints which need to be satisfied by any physical model which endeavours to explain the cosmological evolution of active galaxy populations (Small & Blandford 1992; Haehnelt & Rees 1993; Dunlop 1997; Silk & Rees 1999).

Determining the properties of the hosts of relatively low-luminosity AGN such as Seyfert nuclei has proved relatively straightforward since the advent of CCD detectors, and their properties are now reasonably well established (e.g. MacKenty 1990). However, studying the properties of quasar host galaxies presents a far more serious challenge due to the combination of their larger cosmological distances, and much higher nuclear:host luminosity ratios. Initial attempts to image quasar hosts from the ground did achieve a limited degree of success and led to a reassessment of long-held views and suppositions about galaxies

with powerful nuclear activity (e.g. Smith et al. 1986; Véron-Cetty & Woltjer 1990). In particular, they overturned the notion (arrived at by analogy with Seyferts) that radio-quiet quasars would be found only in spiral galaxies (e.g. Véron-Cetty, Woltjer & Roy 1991). However, the potential of ground-based observations of quasar hosts is fundamentally limited by atmospheric seeing, and effective *optical* studies have generally proved to be extremely difficult to carry out from the ground. This is unfortunate, because a clear understanding of both the differences and similarities between the host galaxies of the three main classes of *powerful* active galaxy – radio-quiet quasars (RQQs), radio-loud quasars (RLQs) and radio galaxies (RGs) – is obviously of fundamental importance in any attempt to unify or relate the various manifestations of the AGN phenomenon.

One way to reduce the distorting influence of the nuclear light is to observe at near-infrared (NIR) wavelengths where the nuclear:host luminosity ratio can be minimized (Dunlop et al. 1993). The advantages of this approach are demonstrated to good effect by McLeod & Rieke (1994a,b), who observed a sample of Seyfert galaxies and nearby quasars in the H band and found that, despite the large scatter in host properties for AGN of low luminosity, for high-luminosity quasars there appears to be a minimum host H-band luminosity which increases with nuclear power (McLeod & Rieke 1995a). Successful NIR imaging of quasar hosts has also been carried out by Kotilainen & Ward (1994), Hutchings & Neff (1997) and Carballo et al. (1998).

We have also exploited this fact, while at the same time attempting to minimize cosmological distance, via an extensive K-band imaging study of the hosts of matched samples of RQQs, RLQs and RGs in the redshift range $0.1 \leq z < 0.35$ (Dunlop et al. 1993; Taylor et al. 1996). This infrared study was successful in that, unlike previous ground-based optical studies, it proved possible to determine reliably the morphological type of a substantial fraction (>0.5) of the quasar hosts. Moreover, the use of properly matched samples allowed us to demonstrate that the hosts of all three classes of powerful AGN were large ($\geq$10 kpc), luminous ($> 2L^*$) galaxies, and that the hosts of RLQs and RGs were statistically identical, consistent with unified models. We also found that at least some of the RQQs appeared to lie in elliptical rather than disc-like galaxies, and there was a suggestion in our data that the probability of an RQQ having an elliptical host is an increasing function of quasar luminosity (a tendency also noted by McLeod & Rieke 1995b). However, we were unable to prove that this effect was significant, due to the fact that the morphologies of the hosts of the more luminous RQQs in our sample remained ambiguous with the limitations of ground-based seeing. This drawback, coupled with the desirability of obtaining reliable optical–infrared colours for all the host galaxies in our AGN sample led us to undertake a complementary R-band imaging study of this same sample with WFPC2 on the *HST*. Here we report the first results of this, the most detailed *HST* study to date of the host galaxies of quasars and radio galaxies.

While the observed nuclear:host luminosity ratio of a quasar is inevitably much higher at R than at K, the high spatial resolution offered by *HST* allows the nuclear contamination to be confined to the central regions of the host galaxy image, thus enhancing the prospects of reliable determination of host galaxy morphology, luminosity and scalelength. This resolution advantage has previously been explored in a number of pilot *HST* studies of small samples of quasars (Bahcall, Kirkhados & Schneider 1994, 1995a,b,c; Hutchings et al. 1994; Disney et al. 1995; Hutchings & Morris 1995), although it comes with the price that the nucleus inevitably saturates in any *HST* image of sufficient depth to produce a useful image of the underlying host. As a result, it has proved difficult to perform accurate subtraction of the nuclear contribution, which is still vitally important for the reliable determination of host galaxy properties (Hutchings 1995). A second problem with some previous *HST* studies has been the use of filters which have included strong emission lines, making it difficult to discern which host galaxy features can be reliably attributed to starlight (Bahcall et al. 1995a). A third problem has been the use of the wide V-band filter, which fails to sample properly the dominant stellar population of the host (at $\lambda_{\rm rest} > 4000$ Å) for $z > 0.25$ (Bahcall et al. 1994). A fourth problem has been the unavailability of an accurate point spread function (PSF) of sufficient depth to investigate the contribution of the quasar nucleus at large radii (>3 arcsec) due to the problem of scattered light within WFPC2.

As described in more detail below, our new 34-orbit *HST* R-band study of the hosts of RQQs, RLQs and RGs has been designed to overcome these problems, and it differs from previous *HST* studies of quasar hosts in five important ways. First, we are imaging statistically comparable samples of each class of AGN. Second, we already possess deep infrared images of all our targets, which will allow the first meaningful study of the optical–infrared colours of quasar hosts. Third, we have used the F675W R-band filter, and restricted the redshift range of our targets, in order to ensure that the images are always uncontaminated by emission lines, and we always sample the rest frame emission of the host galaxy longward of the 4000-Å break. Fourth, we have devoted an orbit of our *HST* observing programme to assembling an accurate PSF of sufficient dynamic range to define accurately the contribution of the quasar nucleus out to an angular radius $r > 10$ arcsec. Fifth, we have developed and applied a two-dimensional modelling procedure which allows us to extract reliably the morphology, luminosity and size of the host galaxies from our images, without requiring us to make asumptions a priori about the values of these parameters (which contrasts with the analysis of Bahcall et al. 1994 as highlighted by McLeod & Rieke 1995b and Bahcall et al. 1997).

The results presented here from the first year of this study demonstrate the importance of these five improvements. In particular, whereas most previous *HST* studies have tended to highlight the fact that many quasar hosts display a wide range of morphological peculiarities, our study is already revealing a surprising degree of similarity and homogeneity in the spatial distribution and age of the dominant stellar populations in the hosts of these powerful AGN.

The layout of the paper is as follows. In Section 2 we summarize the main properties of the matched RG, RLQ and RQQ samples which are the subject of this *HST* study, and then in Section 3 we give details of the observations, image reduction and PSF determination. In Section 4 we present the images, list and summarize the results of applying our host-galaxy modelling procedure to these data, and provide brief notes on the images of each of the 19 AGN observed to date in the context of previous observations. In Section 5 we discuss the main implications of the trends uncovered by the initial results of this study, and in Section 6 we summarize our principal conclusions. Unless otherwise stated, $\Omega_0 = 1$ and $H_0 = 50\,{\rm km\,s^{-1}\,Mpc^{-1}}$ are assumed throughout, and we convert previously published scalelengths and luminosities to this cosmology for ease of comparison.

2 THE SAMPLE

The full sample selected for *HST* imaging consists of 33 objects (10 RLQs, 13 RQQs and 10 RGs) selected from the slightly larger statistically matched samples which were imaged in the NIR by Dunlop et al. (1993) and Taylor et al. (1996). Full details of these samples can be found in these papers. The key point is that the RLQ and RQQ subsamples were selected to be statistically indistinguishable in terms of optical luminosity and redshift, while the RLQ and RG subsamples were selected to be indistinguishable in terms of radio luminosity, radio spectral index and redshift. Note that, following the radio observations of Kukula et al. (1998), we now possess either a radio detection or a strong upper limit on radio luminosity for all the RQQs in our sample, making it possible to quantify their 'radio quietness', and hence explore the extent to which this can be related to any properties of the host galaxy (see Section 5).

The original combined sample comprised a total of 40 objects (12 RGs, 13 RLQs and 15 RQQs) with $0.1 < z < 0.35$, but for this *HST* study we have restricted the redshift range in order to avoid [O III] emission entering the blue end of the F675W filter. This results in the slightly smaller subsamples described above, without compromising their statistical compatibility. The 19 objects which have been observed during the first year of this study, and for which we present the data in this first paper, are listed in Table 1, along with the dates on which they were observed with the *HST*.

3 OBSERVATIONS

3.1 Detector and filter choice

Observations were made with the Wide Field & Planetary Camera 2 (WFPC2) (Trauger et al. 1994) on the *Hubble Space Telescope* (*HST*) using the F675W filter. The filter spans 877 Å in the wavelength range 6275.5–7152.5 Å, roughly equivalent to standard R band, and thus excludes both [O III] λ5007 and Hα emission for redshifts $0.1 \leq z \leq 0.25$ (a wider filter, though providing greater throughput, would have allowed our images to become contaminated by line emission which could mask, or at least be confused with, the underlying stellar continuum of the host galaxy).

Table 1. Observing dates for the objects presented in this paper.

Object	*HST* Archive designation	Type	Observing date
GRW+70D5824	PSF-STAR	STAR	Aug 07 1997
0958+291	3C234.0	RG	Jun 11 1997
0345+337	3C93.1	RG	Feb 16 1998
0917+459	3C219	RG	Mar 25 1998
2141+279	3C436	RG	Apr 27 1998
2247+140	PKS2247+14	RLQ	Jun 25 1997
2141+175	OX169	RLQ	Jul 01 1997
0137+012	PHL1093	RLQ	Jul 04 1997
2349−014	PKS2349−01	RLQ	Jul 05 1997
1004+130	PKS1004+13	RLQ	Nov 28 1997
0736+017	PKS0736+01	RLQ	Feb 06 1998
0953+415	PG0953+415	RQQ	Jun 02 1997
0054+144	PHL909	RQQ	Jun 27 1997
2344+184	2344+184	RQQ	Jun 28 1997
0244+194	0244+194	RQQ	Jun 29 1997
0157+001	0157+001	RQQ	Jun 30 1997
0257+024	US3498	RQQ	Jul 04 1997
1635+119	MC1635+119	RQQ	Feb 19 1998
0923+201	PG0923+201	RQQ	Mar 12 1998
1012+008	PG1012+00	RQQ	Mar 12 1998

WFPC2 consists of four detectors, each comprising 800×800 pixels: three WF chips, each with a pixel scale of 100 mas; and one PC chip, with a pixel scale of 45 mas. Although the PC chip offers smaller pixels and correspondingly better sampling of the instrument PSF, it is ultimately less sensitive to low-surface-brightness emission than the WF chips, even when the pixels are binned up, and we therefore opted to use the larger detectors. Target sources were centred on the WF2 chip, which was chosen for its marginally better performance over the period immediately prior to our observations.

3.2 Observing strategy and image reduction

Observations of the target quasars and radio galaxies were carefully tailored to ensure that the maximum amount of information could be derived from the final images. In both cases, deep, sensitive images of the galaxies are clearly desirable, but for the quasars such exposure times inevitably entail saturation of the central source, allowing no independent measure of PSF normalization.

Slightly different strategies were therefore used for the quasar and radio galaxy samples. For the quasars, exposures of 5, 26 and 3×600 s were taken. The short exposures guaranteed that at least one unsaturated image of the quasar would be obtained, thus ensuring an accurate measure of the central flux density. The three 600-s exposures each provided a 3σ surface-brightness sensitivity $\mu_R = 23.8$ mag arcsec^{-2} (per pixel), and their comparison facilitated reliable cosmic ray removal using standard IRAF tasks. With azimuthal averaging, the combined 1800-s deep image of each quasar allows extended emission to be traced reliably out to a surface brightness level $\mu_R > 26$ mag arcsec^{-2}.

For the radio galaxies there was little danger of saturation, and so short exposures were not required. Three 700-s exposures were therefore obtained for each radio galaxy. Any remaining time in the orbit was filled with an exposure of flexible length (usually 40 to 100 s).

The sources discussed in this paper – constituting approximately half of our sample – were all observed between 1997 June and 1998 April (see Table 1 for exact dates). Calibration was carried out using the standard pipeline.

3.3 Determining the point spread function

The form of the WFPC2 point spread function (PSF) depends critically on both the position on the chip and the spectral energy distribution (SED) of the target source. These effects are well understood and can be included in software to produce accurate synthetic PSFs. However, despite providing an excellent fit over the central few arcseconds, the synthetic PSFs produced by packages such as TINYTIM deviate from the empirical WFPC2 PSF at larger radii ($\geq$2 arsec). This is due to scattering within the camera. Since the scattered light shows complex structure which is not uniform, and which is also wavelength- and position-dependent, it cannot easily be modelled.

We therefore devoted one orbit of our allotted *HST* time to constructing a deep, unsaturated stellar PSF using the F675W

filter, with the star centred on exactly the same part of the WF2 chip as the target objects.

The star chosen was GRW +70D5824, a white dwarf of spectral type DA3 and apparent magnitude $V = 12.77$. Since it also serves as a UV standard star for WFPC2, the position and spectrum of this object are extremely well determined (Turnshek et al. 1990). No stars of a comparable brightness lie within 30 arcsec, ensuring that the stellar PSF is not contaminated by PSFs or scattered light from neighbouring objects. The $B-V$ colour of the PSF star is 0.09, sufficiently similar to the neutral colours ($B-V \simeq 0$) typical of our quasar sample to provide a reasonable match to a quasar SED over the wavelength range of the F675W filter.

In order to obtain both unsaturated images of the PSF core *and* deep images of the wings, a series of exposures was carried out with durations of 0.23, 2, 26 and 160 s. After 0.23 s the central pixel of the stellar image reaches approximately 10 per cent of its saturation value (assuming that the star is perfectly centred). This is the shortest practical exposure length – in exposures of less than 0.23 s the PSF would be compromised by the shutter flight time. Subsequent exposure durations were carefully staggered to ensure that the star never saturated beyond the radius at which the wings of the PSF in the previous, shorter exposure became lost in the noise. This allowed us to build up a composite PSF of very high dynamic range by splicing together annuli from successively deeper exposures.

The brightest quasar in our sample has an apparent magnitude of $V = 15.15$, more than 2 mag fainter than the PSF star. We were therefore able to ensure that the deepest stellar image probed much further into the wings of the PSF than even the longest quasar exposure.

Each exposure also used a two-point dither pattern to improve the sampling of the PSF (which is significantly undersampled by the 0.1-arcsec pixel scale of the WF chips).

Thus the stellar PSF is designed to match the PSFs of the target quasars as closely as possible in terms of depth, position on the detector, and SED. However, we note that we cannot account for time-dependent variations in the PSF using this method. These variations are due to changes in the telescope focus and include contributions from several sources. Of these, the most significant for our observations is the short-term (intra-orbit) variability ('breathing') due to temperature fluctuations in the telescope's environment. However, with the relatively large pixel scale of the WF chips the effect on the amount of flux falling on the central pixel of a point source is likely to be only a few per cent at most.

4 RESULTS

4.1 Images

The images, two-dimensional model fits, and model-subtracted residual images are presented in Appendix A in Figs A1–A19. A grey-scale/contour image of the final reduced F675W *R*-band image of each AGN is shown in the top-left panel (panel A) of each Fig. A1–A19, which shows a region 12.5×12.5 arcsec^2 centred on the target source. The surface brightness of the lowest contour level is indicated in the top-right corner of the panel, with the grey-scale designed to highlight structure close to this limit. Higher surface-brightness contours are spaced at intervals of 0.5 mag arcsec^{-2}, and have been superimposed to emphasize brighter structure in the centre of the galaxy/quasar. Panel B of each figure shows the best-fitting two-dimensional model, complete with unresolved nuclear component (after convolution with the empirical PSF) contoured in an identical manner to panel A. Panel C shows the best-fitting host galaxy as it would appear if the nuclear component were absent, while panel D is the residual image which results from subtraction of the full two-dimensional model (in panel B) from the raw *R*-band image (in panel A), in order to highlight the presence of morphological peculiarities such as tidal tails, interacting companion galaxies, or secondary nuclei. All panels are displayed using the same grey-scale.

4.2 Modelling results

Full details of the two-dimensional modelling procedure which we have used to determine the properties of the host galaxies are presented elsewhere, along with the results of extensive tests of its ability to reclaim the true properties of a wide range of host-galaxy:nucleus combinations at different redshifts (McLure et al. 1999). In brief, the modelling procedure is a development of that used by Taylor et al. (1996), and here we have used two distinct versions of this procedure to determine the host-galaxy properties from our *HST* images. For both versions an accurate high-dynamic-range PSF and an accurate error frame for each quasar image are essential for the extracton of robust results (see McLure et al. for details).

In the first version the host-galaxy morphology is constrained by determining how well the data can be reproduced *assuming* that the host galaxy is *either* an elliptical galaxy (described by a de Vaucouleurs $r^{1/4}$ law) or an exponential disc. The remaining five parameters (host-galaxy position angle, host-galaxy axial ratio, host-galaxy scalelength, host-galaxy luminosity and nuclear luminosity) are then varied until, when convolved with the PSF, the model best fits the data as determined by χ-squared minimization (note that it is not assumed a priori that the radio galaxies have a negligible nuclear component). Then, if one assumed galaxy morphology yields a significantly better fit than the other, we can say that the galaxy is *better* described by a de Vaucouleurs law or by an exponential disc. The results of applying this procedure to the *HST* images are given in Table 2. The striking feature of these results is that all of the host galaxies except those of the two lowest luminosity RQQs are better described as elliptical galaxies, and that, with only one exception (the heavily nuclear dominated RQQ 0953+415), this difference is statistically very significant. One-dimensional luminosity profiles extracted from the best-fitting de Vaucouleurs or exponential models are compared with the data in Fig. 1.

In the second version we have removed the need to assume that the host galaxy can be described by either a pure $r^{1/4}$ law or exponential disc, and allow a sixth parameter β [where the luminosity profile of the galaxy is given by $I(r) \propto \exp(-r^{\beta})$] to vary continuously. Thus, $\beta = 1$ should result if the galaxy is best described by a pure exponential disc, and $\beta = 0.25$ should result if the galaxy really does follow a pure de Vaucouleurs law, but *all* values of β are available to the program to improve the quality of the model fit. The impressive results of applying this procedure to the *HST* images are given in Table 3 and illustrated in Fig. 2. One remarkable feature of these results (see Fig. 2) is that for 16 out of the 19 objects, the preferred β parameter for the host galaxy is in the range $0.18 < \beta < 0.3$, in excellent agreement with a pure de Vaucouleurs law. Perhaps most surprisingly, given pre-existing prejudices, this is true for six out of the nine RQQs in the current

Table 2. The outcome of attempting to model the AGN host galaxies as either an exponential disc or a de Vaucouleurs spheroid. The preferred host-galaxy morphology is given in column 2, with the $\Delta\chi^2$ between the chosen and alternative model given in column 3. In column 4, $r_{1/2}$ is given irrespective of the chosen host morphology. Column 5 lists $\mu_{1/2}$ in units of R mag arcsec^{-2}. Columns 6 and 7 list the integrated apparent magnitudes of the host galaxy and fitted nuclear component converted from F675W to Cousins R band, while column 8 gives the ratio of integrated galaxy and nuclear luminosities. Columns 9 and 10 give the axial ratio and position angle of the best-fitting host respectively.

Source	Host	$\Delta\chi^2$	$r_{1/2}$/kpc	$\mu_{1/2}$	$R_{\rm host}$	$R_{\rm nuc}$	$L_{\rm nuc}/L_{\rm host}$	b/a	PA/°
RG									
0345+337	Elliptical	2349	11.0	23.1	18.0	21.1	0.06	0.70	99
0917+459	Elliptical	33245	19.1	23.0	16.1	19.4	0.05	0.76	36
0958+291	Elliptical	7793	8.3	22.0	17.1	18.5	0.27	0.95	45
2141+279	Elliptical	8530	21.3	23.4	16.7	25.6	0.0003	0.74	148
RLQ									
0137+012	Elliptical	5093	13.1	22.6	17.2	17.3	0.8	0.85	35
0736+017	Elliptical	8909	13.3	22.9	16.9	16.2	1.9	0.97	13
1004+130	Elliptical	501	8.2	21.5	16.9	15.0	5.8	0.94	29
2141+175	Elliptical	1381	3.7	20.3	17.2	16.0	3.2	0.55	118
2247+140	Elliptical	8092	10.7	22.4	17.2	16.9	1.3	0.63	118
2349−014	Elliptical	13463	18.1	22.7	15.9	16.0	0.9	0.89	45
RQQ									
0054+144	Elliptical	6050	8.1	21.7	16.6	15.5	2.7	0.61	108
0157+001	Elliptical	12826	7.9	20.9	15.8	16.2	0.72	0.83	97
0244+194	Elliptical	2744	8.9	22.7	17.5	16.8	1.9	0.92	77
0257+024	Disc	15361	10.1	21.5	15.9	19.5	0.04	0.89	134
0923+201	Elliptical	1733	8.2	22.1	17.2	15.7	4.2	0.98	141
0953+415	Elliptical	91	7.1	22.4	18.2	15.2	15.4	0.86	115
1012+008	Elliptical	1056	23.0	23.8	16.6	16.2	1.5	0.64	109
1635+119	Elliptical	34765	6.3	21.6	16.8	18.1	0.3	0.69	179
2344+184	Disc	22348	8.8	22.7	17.2	19.2	0.2	0.79	146

subsample. Moreover, the only two RQQs which appear to have a significant disc component are the two least-luminous RQQs in this subsample. The clear implication is that *all* bright quasars, with $M_R < -23.5$ reside in massive ellipticals, irrespective of their radio power. Such a result has been hinted at before (Disney et al. 1995; Taylor et al. 1996), but this is the first time it has proved possible to demonstrate unambiguously that this is the case.

4.3 Notes about individual objects

Here we provide a brief discussion of the *HST* image of each object presented in this paper, with reference to other recent *HST* and ground-based data. A more detailed description of each object, together with our existing K-band images, can be found in Dunlop et al. (1993) and Taylor et al. (1996). Sources are listed by IAU name, with alternative names given in parenthesis. Radio luminosities or upper limits at 5-GHz have been calculated assuming $H_0 = 50\,{\rm km\,s^{-1}\,Mpc^{-1}}$ and $\Omega_0 = 1$. Note that following the deep VLA radio observations of RQQs undertaken by Kukula et al. (1998), radio detections or strong upper limits are now available for all the RQQs in the current sample.

4.3.1 The radio galaxies

0345+337 (3C 93.1, 4C +33.08, B2 0345+33, NRAO 0146, DA 113, OE +376)

[$z = 0.244$, $\log_{10}(L_{5\,\rm GHz}/{\rm W\,Hz^{-1}\,sr^{-1}}) = 25.45$]

The results of our modelling of this object, shown in Fig. A1, reveal the host to be a large elliptical galaxy, with $r_{1/2} = 11$ kpc. The strong preference for a elliptical host is confirmed by the variable-beta modelling, which yields $\beta = 0.249$. The unresolved central point source is weak, making up ≈6 per cent of the integrated flux in the best-fitting model. The model-subtracted image shows some low-level residual flux unaccounted for by the symmetrical host template.

The embedded companion detected 6 arcsec NW of the main galaxy in our K-band image is seen as clearly separated in the new R-band image. The other companion detected to the SE at K is again detected here, together with several other faint companion objects. The two steep-isophote companions are confirmed to be foreground stars from our *HST* image.

At high resolution in the radio this is a compact steep-spectrum source having a diameter of ≈ 0.4 arcsec (Akujor et al. 1991).

0917+459 (3C 219, 4C +45.19, NRAO 0320, DA 266, LHE 249, OK +430)

[$z = 0.174$, $\log_{10}(L_{5\,\rm GHz}/{\rm W\,Hz^{-1}\,sr^{-1}}) = 25.69$]

A disc host for this radio galaxy is excluded by our model fitting with a high level of confidence. As shown in Figs A2 and 1(b), the host is a large elliptical, $r_{1/2} = 19$ kpc, with a very weak, unresolved nuclear component. The variable-beta model again chooses an almost perfect de Vaucouleurs template, with $\beta = 0.229$. This galaxy has been recently imaged with *HST* in a snapshot survey of 3CR radio galaxies (De Koff et al. 1996), through the F702W (wide R) filter. De Koff et al. suggest that there may be an interaction with the large galaxy to the SE. However, our model-subtracted image provides little direct evidence for any interaction.

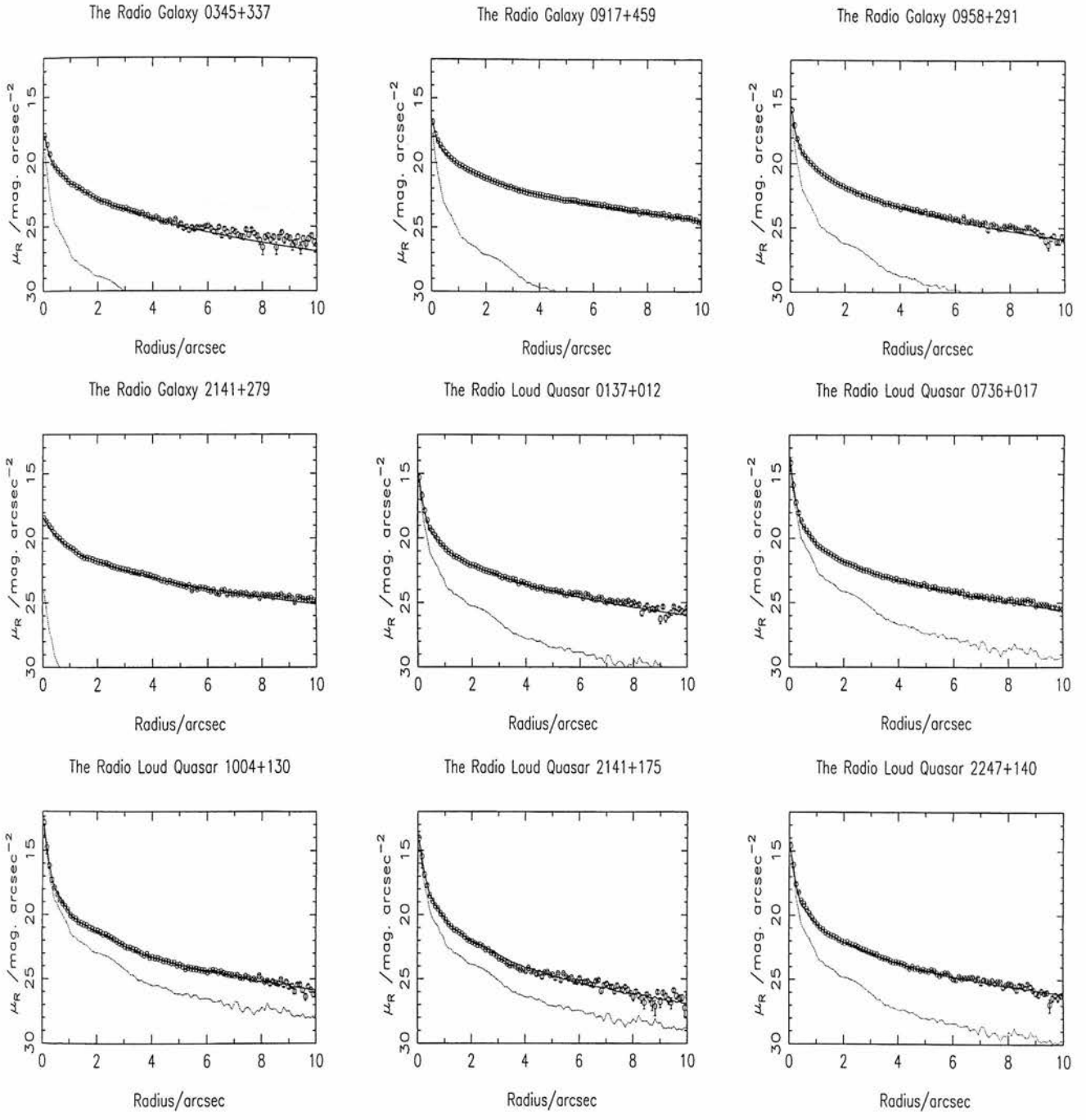

Figure 1. A comparison of the azimuthally averaged luminosity profiles derived from the images with those produced by the two-dimensional modelling. Each plot shows the azimuthally averaged image data (open circles), the azimuthally averaged best-fitting model after convolution with the PSF (solid line) and the azimuthally averaged best-fitting unresolved nuclear component after convolution with the PSF (dotted line).

This galaxy is clearly situated in a cluster, with a large number of companion objects detected at R and in our previous K-band image. In the radio this is a classical double source whose position angle is anticorrelated with the optical and NIR position angles.

0958+291 (3C 234.0, 4C +29.35, IRAS F09589+2901, B2 0958+29, NRAO 0343, CSO 0031, OL +200, DA 280, CTD 064, CTA 049)

[$z = 0.185$, $\log_{10}(L_{5\,\mathrm{GHz}}/\mathrm{W\,Hz^{-1}\,sr^{-1}}) = 25.30$]

As shown in Figs A3 and 1(c), the host is extremely well fitted by an elliptical galaxy template, with $r_{1/2} = 8.3$ kpc, and a disc host is formally excluded. This result is supported by the variable-beta model, which yields another virtually perfect de Vaucouleurs model ($\beta = 0.253$). This galaxy has a rather more luminous unresolved component, which contributes nearly 30 per cent of the integrated flux. 3C 234.0 was also included in the *HST* snapshot survey (De Koff et al. 1996), where features were detected emanating to the east and west of the galaxy nucleus. The large tidal arm

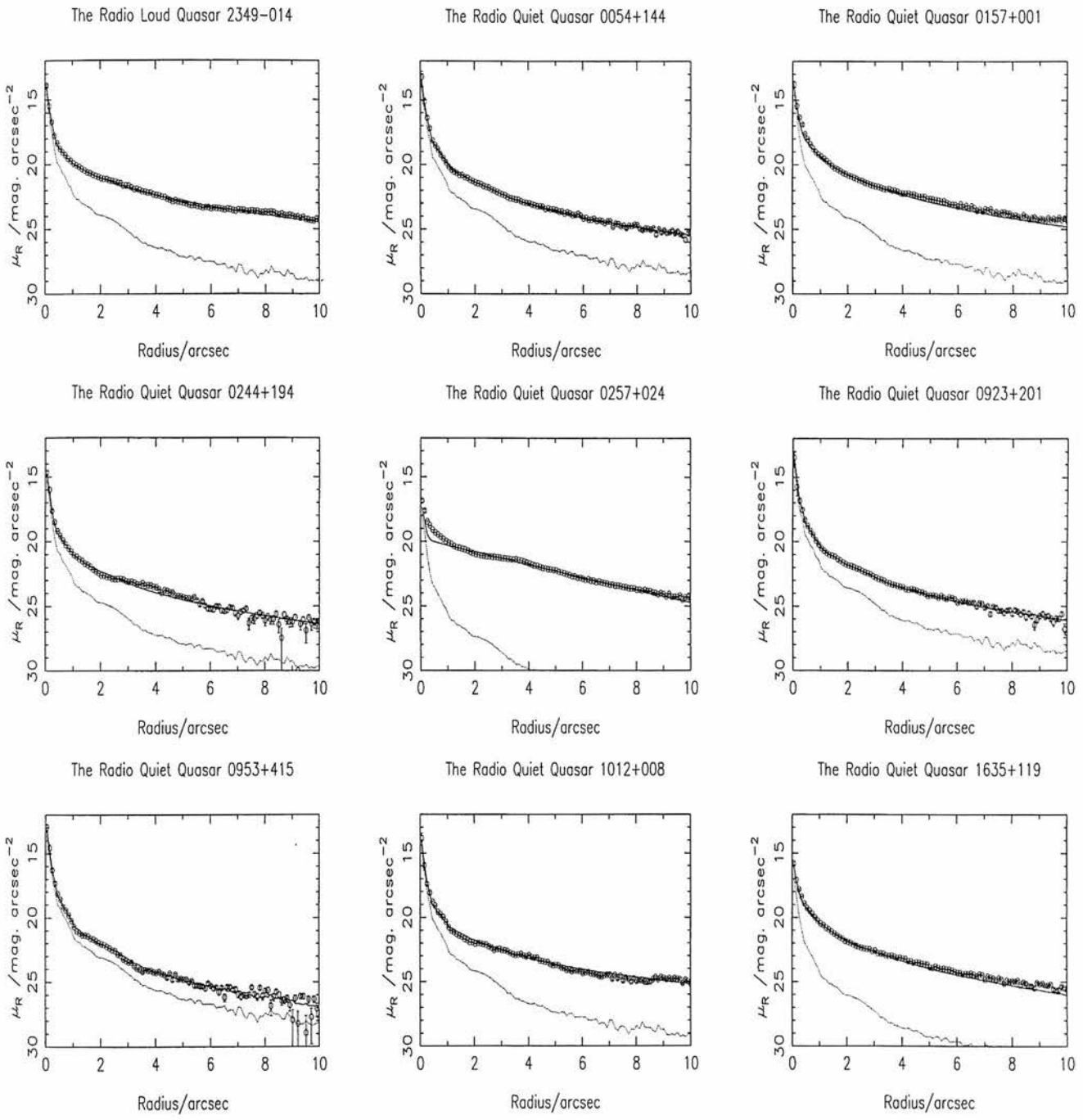

Figure 1 – *continued*

to the west of the nucleus is easily visible in the contour plot in Fig. A3, and is dramatically highlighted in the model-subtracted image. A fainter counterarm to the east of the nucleus is also present, although it is not easily discerned in this grey-scale image.

Numerous companion objects are detected in our *R*-band image, in agreement with the ground-based images of Hutchings, Johnson & Pyke (1988) through the same filter. Recent work by Young et al. (1998) has led to the detection of broad Hα in both total and polarized flux, consistent with our discovery of significant nuclear emission at *R*. In the radio 3C 234 is a classical double FRII source (Leahy, Pooley & Riley 1986).

2141+279 (3C 436, 4C +27.47, B2 2141+27B, NRAO 0665, CTD 132, DA 559, CTA 096)

[$z = 0.215$, $\log_{10}(L_{5\,\mathrm{GHz}}/\mathrm{W\,Hz^{-1}\,sr^{-1}}) = 25.17$]

A large elliptical host galaxy ($r_{1/2} = 21$ kpc) is strongly favoured for this object, with the variable-beta model again yielding an almost perfect de Vaucouleurs law ($\beta = 0.246$), with an insignificant central point source contribution (see Figs A4 and 1d). As can be seen in panel D of Fig. A4, a secondary nucleus lies approximately 0.6 arcsec from the centre of the host galaxy, and

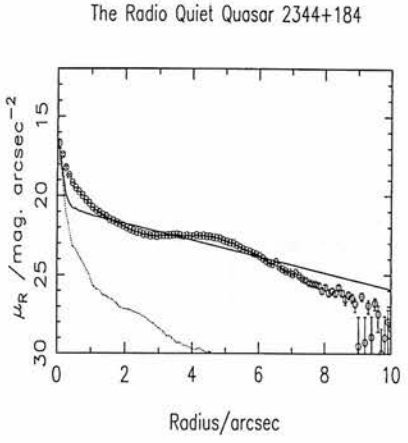

Figure 1 – *continued*

Table 3. The outcome of the variable-β modelling. Column 2 lists the host morphology of the best-fitting 'fixed β' model (results of which are given in Table 2). The best-fitting values for the β profile parameter are given in column 3. The $\Delta\chi^2$ of column 4 quantifies the improvement in fit between this variable-β model and the best-fitting disc or elliptical model. As with Table 2, columns 5 and 6 give the integrated apparent magnitudes of the host galaxy and nuclear component converted to the Cousins R filter. Column 7 lists the ratios of nuclear and integrated host luminosity.

Source	Host	β	$\Delta\chi^2$	$R_{\rm host}$	$R_{\rm nuc}$	$L_{\rm nuc}/L_{\rm host}$
RG						
0345+337	Elliptical	0.249	1.8	18.0	21.1	0.06
0917+459	Elliptical	0.229	263.6	16.0	19.4	0.04
0958+291	Elliptical	0.253	16.0	17.1	18.5	0.27
2141+279	Elliptical	0.246	2.2	16.7	26.1	0.0002
RLQ						
0137+012	Elliptical	0.185	126.3	17.0	17.4	0.72
0736+017	Elliptical	0.193	238.6	16.8	16.2	1.64
1004+130	Elliptical	0.253	4.7	16.9	15.0	5.83
2141+175	Elliptical	0.280	23.0	17.3	16.0	3.44
2247+140	Elliptical	0.249	16.6	17.2	16.9	1.31
2349−014	Elliptical	0.258	9.6	16.0	16.0	0.93
RQQ						
0054+144	Elliptical	0.251	2.9	16.6	15.5	2.75
0157+001	Elliptical	0.238	133.2	15.8	16.2	0.68
0244+194	Elliptical	0.220	47.4	17.5	16.8	1.80
0257+024	Disc	0.754	2850.7	15.9	19.5	0.04
0923+201	Elliptical	0.299	44.0	17.3	15.7	4.60
0953+415	Elliptical	0.266	8.8	18.2	15.2	15.8
1012+008	Elliptical	0.377	101.6	16.8	16.2	1.81
1635+119	Elliptical	0.183	549.6	16.7	18.3	0.23
2344+184	Disc	0.428	1043.8	17.0	19.2	0.12

this can be clearly seen in the model-subtracted image, along with some asymmetrical residual flux and several faint companion objects. The radio source has an FRII morphology (McCarthy, van Breugel & Kapahi 1991).

4.3.2 *The radio-loud quasars*

0137+012 (PKS 0137+012, PHL 1093, 4C 01.04, OC 062, UM 355)

Radio-loud; $[z = 0.258,\ \log_{10}(L_{5\,\rm GHz}/{\rm W\,Hz^{-1}\,sr^{-1}}) = 25.26]$

The modelling results for this object show the host galaxy to be a large elliptical ($r_{1/2}$=13 kpc) which contributes over half of the integrated flux at R (Fig. 1e). The variable-beta model fit is close to elliptical ($\beta = 0.185$), but it does provide a significantly better fit than a pure de Vaucouleurs law. The contour plot in Fig. A5 clearly shows a close companion object (separation $\approx$1.0 arcsec), which was not resolved in our K-band image. This object was masked out during the model fitting and can clearly be seen in the subtracted image. 0137+012 was one of four objects imaged with the PC camera on *HST* by Disney et al. (1995) using the F702W filter. Using a two-dimensional cross-correlation modelling technique, they also found the host to be a large early-type galaxy. The slightly larger scalelength ($r_{1/2} \simeq 22$ kpc)[1] and fainter host magnitude obtained by their modelling technique is most likely to be due to their use of a synthetic PSF. For a more detailed discussion of the problems associated with two-dimensional modelling and the WFPC PSF see McLure et al. (1999). In the radio the quasar is an FRII source of diameter 42 arcsec with a strong core (Gower & Hutchings 1984a).

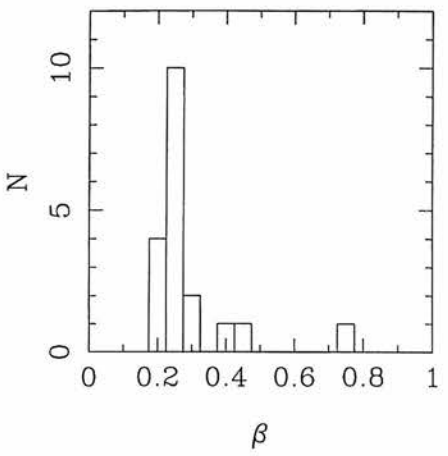

Figure 2. The distribution of β values which results from fitting luminosity profiles of the form $\exp(-r^{\beta})$ to the host galaxies and allowing β to vary as a free parameter in the model fitting. As can be seen from the histogram, 16 of the 19 AGN have host galaxies which follow near-perfect de Vaucouleurs profiles (McLure et al. 1999).

0736+017 (PKS 0736+01, OI 061)

Radio-loud; $[z = 0.191,\ \log_{10}(L_{5\,\rm GHz}/{\rm W\,Hz^{-1}\,sr^{-1}}) = 25.35]$

An elliptical host galaxy is again strongly preferred for this quasar, with a disc host formally excluded (Figs. A6 and 1f). As with 0137+012, the variable-beta modelling confirms the generally spheroidal nature of the host ($\beta = 0.1933$), but it does provide a statistically significant improvement over the pure de Vaucouleurs model. The companion object seen to the south of the quasar, first detected in our K-band image (Dunlop et al. 1993), is not obvious in our new *HST* image shown in Fig. A6. The large area of low-surface-brightness nebulosity to the NE of the quasar which was present in our K-band image is also missing from this R-band image, casting doubt on its reality. At radio wavelengths this quasar is a compact (0.013 arcsec) flat-spectrum source (Gower & Hutchings 1984b; Romney et al. 1984).

1004+130 (PKS 1004+13, PG 1004+130, 4C 13.41, OL 107.7)

Radio-loud; $[z = 0.240,\ \log_{10}(L_{5\,\rm GHz}/{\rm W\,Hz^{-1}\,sr^{-1}}) = 24.94]$

[1] Converted to our cosmology.

As can be seen from the contour plot in Fig. A7 this quasar is a highly nuclear-dominated object in the *R* band. The preferred host galaxy is again an elliptical, although due to the high $L_{\rm nuc}/L_{\rm host}$ ratio the preference is less clear-cut than for most of the other objects. The best-fitting host is fairly large ($r_{1/2} = 8$ kpc) and luminous, although the unresolved nuclear component contributes ≈85 per cent of the integrated flux (Fig. 1g). The results of the variable-beta modelling strongly support the choice of an early-type host ($\beta = 0.253$). 1004+130 is one of the quasars which has also been imaged at the *HST* in the *V* band by Bahcall et al. (1997). They also find the host to be best described by an early-type galaxy, although with a somewhat smaller scale length ($r_{1/2} = 5.8$ kpc). They suggest that there is some sort of structure close into the quasar nucleus. This is beautifully illustrated by our model-subtracted image; two spiral-arm-type features can be clearly seen on either side of the quasar nucleus. The subtracted image also reveals one companion object to the NE, together with two fainter companions to the east. In the radio this quasar is an FRII source of diameter 9 arcmin with a weak core (Miley & Hartsuijker 1978).

2141+175 (OX 169, MC3)

Radio-loud; $[z = 0.213,\ \log_{10}(L_{5\,\rm GHz}/\rm W\,Hz^{-1}\,sr^{-1}) = 24.81]$

Our *R*-band image of this complex object shown in Fig. A8 reveals the two extended filaments to the SE and NW previously detected by Smith et al. (1986) and Heckman et al. (1986). The best-fitting host galaxy is a moderate-sized elliptical with $r_{1/2} = 4$ kpc (Fig. 1h), with the variable-beta modelling producing a very similar fit. This quasar has been previously imaged with the *HST* with the F702W filter by Hutchings et al. (1994), who also concluded in favour of an $r^{1/4}$ law but fail to provide any quantitative information on the scalelength of the host galaxy. The model-subtracted image shows the NW filament to be more extended than previously thought, stretching to more than half the length of the SE filament. The hypothesis that the two extensions are composed of old stars (Stockton & Farnham 1991) is supported by their prominence in our existing *K*-band image (Dunlop et al. 1993), and in this emission-line free *HST* image. Also revealed by subtraction of the best-fitting model is a previously undetected companion ≈3 arcsec to the NE of the quasar. In the radio, 2141+175 is a compact (<4 arcsec) flat-spectrum source (Feigelson, Isobe & Kembhavi 1984).

2247+140 (PKS 2247+14, 4C 14.82, OY 181)

Radio-loud; $[z = 0.237,\ \log_{10}(L_{5\,\rm GHz}/\rm W\,Hz^{-1}\,sr^{-1}) = 25.31]$

This radio-loud quasar can be seen to be elongated in the NW/SE direction in Fig. A9, as previously reported by Hutchings et al. (1988) and Dunlop et al. (1993). The host galaxy is unambiguously elliptical, with a best-fitting scale length of 11 kpc (Fig. 1i). This preference is again impressively confirmed by the best-fitting beta value of $\beta = 0.249$. The subtracted image reveals two new companion objects embedded in the residual flux of the SE elongation. The quasar is a compact steep-spectrum radio source (van Breugel, Miley & Heckman 1984).

2349-014 (PG 2349-014, PKS 2349-01, PB 5564)

Radio-loud; $[z = 0.173,\ \log_{10}(L_{5\,\rm GHz}/\rm W\,Hz^{-1}\,sr^{-1}) = 24.86]$

The *R*-band image of this quasar presented in Fig. A10, shows it to be undergoing an extensive interaction. 2349-014 is included in the sample of Bahcall et al. (1997) (see also Bahcall et al. 1995a), and we confirm their detection of a compact close companion at ≈2 arcsec separation to the east. Bahcall et al. claim that there is no clear evidence for a normal host galaxy centred on the quasar, although they comment that the mean radial profile is well matched by a de Vaucouleurs law. The results of our two-dimensional modelling do not support this. Model-fitting after masking of the most prominent areas of asymmetric nebulosity produces a good match with a large elliptical host galaxy of scalelength $r_{1/2} = 18$ kpc (Fig. 1j). The variable-beta parameter modelling produces a near identical fit ($\beta = 0.258$). The subtracted image highlights the massive tidal arm feature to the north of the quasar and extensive nebulosity to the west. The source of this interaction would appear to be the nearby compact companion. In agreement with Bahcall et al., our new *R*-band data provides little evidence for interaction with the large galaxy to the SE. In the radio this quasar is an FRII source of diameter 53 arcsec with a strong core (Antonucci 1985).

4.3.3 The radio-quiet quasars

0054+144 (PHL 909)

Radio-quiet; $[z = 0.171,\ \log_{10}(L_{5\,\rm GHz}/\rm W\,Hz^{-1}\,sr^{-1}) = 21.87]$

The host galaxy of this radio-quiet quasar (Fig. A11) is extremely well described by an elliptical template with $r_{1/2} = 8$ kpc, and a disc host is formally excluded (Fig. 1k). The variable-beta modelling again strongly supports this unambiguous choice, settling on a value of $\beta = 0.251$. This object was also imaged with the *HST* at *V* by Bahcall et al. (see Bahcall et al. 1996), and in this case they also found the best-fitting host to be an early-type galaxy. In their *V*-band image Bahcall et al. claim not to detect the extended emission towards the western companion galaxy (off this frame) which was reported in Dunlop et al. (1993). However, the model-subtracted image presented here clearly shows considerable residual luminosity in the direction of the western companion, in agreement with the *K*-band data.

0157+001 (PG 0157+001, Mkn 1014)

Radio-quiet; $[z = 0.163,\ \log_{10}(L_{5\,\rm GHz}/\rm W\,Hz^{-1}\,sr^{-1}) = 22.87]$

This spectacular object can clearly be seen to be undergoing massive tidal disruption (Fig. A12). The bright companion object detected at the end of the NE tidal arm in our previous *K*-band image is again detected here, but lies just off the edge of the frame shown in Fig. A12. Also detected in the *R*-band is a faint counter arm to the west, embedded within which are two further bright companion objects. The underlying host galaxy is best described by a bright elliptical galaxy $r_{1/2} = 8$ kpc (Fig. 1l), with the variable-beta modelling choosing a near-perfect elliptical host ($\beta = 0.238$). The full extent of the tidal disruption is revealed by the model-subtracted image. This is the most radio-luminous of the 'radio-quiet' quasars in our sample, and its radio morphology is similar to that found in several radio-loud quasars with an unresolved core accompanied by a secondary component ≈2 arcsec west of the nucleus (Miller, Rawlings & Saunders 1993; Kukula et al. 1998).

0244+194 (1E 0244+1928)

Radio-quiet; $[z = 0.176,\ \log_{10}(L_{5\,\rm GHz}/\rm W\,Hz^{-1}\,sr^{-1}) < 21.43]$

The host of this radio-quiet quasar is well described by an large

elliptical galaxy with $r_{1/2} = 9$ kpc (Fig. A13). The variable-beta modelling provides a slightly improved fit with a value of $\beta = 0.220$. The model-subtracted image, shown in Fig. A13, is very clean and shows no obvious signs of any interaction.

0257+024 (US 3498)

Radio-quiet; $[z = 0.115,\ \log_{10}(L_{5\,\mathrm{GHz}}/\mathrm{W\,Hz^{-1}\,sr^{-1}}) = 22.19]$

The host of this radio-quiet quasar is dominated by a disc component with a best-fitting scalelength of $r_{1/2} = 10$ kpc (Fig. 1n). The model-subtracted image in Fig. A14 shows a ring of emission at ≈4 arcsec radius. Also revealed is substantial residual flux in the inner ≈2 arcsec where the host galaxy is bulge-dominated. This feature can also be clearly seen in the luminosity profile shown in Fig. 1(n). As a result of the central bulge, the variable-beta model chooses a substantially lower value of beta (0.75), and offers a significantly better χ^2 fit than a pure exponential disc. Nevertheless, this transpires to be the most disc-dominated host galaxy in the quasar sample observed to date.

0923+201 (PG 0923+201, Ton 1057)

Radio-quiet; $[z = 0.190,\ \log_{10}(L_{5\,\mathrm{GHz}}/\mathrm{W\,Hz^{-1}\,sr^{-1}}) < 21.66]$

This radio-quiet quasar is a member of a small group of galaxies. The two large galaxies in Fig. A15 to the SE and SW are at the same redshift as the quasar (Heckman et al. 1984), and 0923+201 was thought to be possibly interacting with these (Hutchings, Janson & Neff 1989). However, our two-dimensional modelling provides little evidence for any obvious interaction. The host is extremely well matched by a standard elliptical template (Fig. 1o), with the variable-beta model also choosing an approximately de Vaucouleurs model ($\beta = 0.3$). The subtracted image is very clean and symmetrical, but with perhaps a suggestion of more residual flux in the direction of the SE companion.

0953+415 (K438−7, PG 0923+415)

Radio-quiet; $[z = 0.239,\ \log_{10}(L_{5\,\mathrm{GHz}}/\mathrm{W\,Hz^{-1}\,sr^{-1}}) < 21.69]$

This radio-quiet quasar is the most heavily nuclear-dominated object in the sample. This can be seen immediately by its stellar-like appearance in the grey-scale of Fig. A16. The best-fitting host is a medium-sized elliptical of scalelength $r_{1/2} = 7$ kpc (Fig. 1p). However, due to the faintness of the host relative to the unresolved nuclear component, we are unable to exclude a disc host with a high level of confidence. Despite this, we are still able to constrain the relative luminosity of the AGN and host components, since both the alternative host models yield similar values. 0953+415 is another object which was imaged with the *HST* in *V* by Bahcall et al. (1994, 1997). From their *V*-band image Bahcall et al. were unable to clearly detect a bright host galaxy centred on the quasar. It seems likely that this inconsistency arises primarily from the procedure used by Bahcall et al. to subtract the PSF. As can be seen from the luminosity profile shown in Fig. 1(p), the unresolved AGN component dominates to a radius of only ≈2 arcsec. Normalization of the PSF in a annulus between 1 and 3 arcsec (as performed by Bahcall et al. 1997) will therefore lead to a substantial over-subtraction. Tests on our own data show that this effect is more than sufficient to explain the non-detection by Bahcall et al. The model-subtracted image reveals a tidal arm feature to the SW, along with up to four possible companion objects.

1012+008 (PG 1012+008)

Radio-quiet; $[z = 0.185,\ \log_{10}(L_{5\,\mathrm{GHz}}/\mathrm{W\,Hz^{-1}\,sr^{-1}}) = 22.00]$

This radio-quiet quasar is another dramatically interacting object which was also imaged in the *V*-band byBahcall et al. (1997). In the grey-scale of Fig. A17 the quasar is seen together with two companion galaxies to the north and east. The best-fitting host is a large elliptical with $r_{1/2} = 23$ kpc (Fig. 1q), a result supported by the variable-beta modelling result ($\beta = 0.377$). We note that, using two-dimensional modelling, Bahcall et al. (1997) concluded that the host was a disc galaxy with $r_{1/2} = 10.8$ kpc (after conversion to our adopted cosmology); however, Bahcall et al.'s best fit to the one-dimensional profile of this galaxy is an elliptical with $r_{1/2} = 24.5$ kpc, in excellent agreement with our result (this perhaps indicates that there is a problem with the method of two-dimensional modelling implemented by Bahcall et al.). From the model-subtracted image shown in panel D it is clear that the eastern companion is definitely interacting, with the northern companion perhaps also involved.

1635+119 (MC 2)

Radio-quiet; $[z = 0.146,\ \log_{10}(L_{5\,\mathrm{GHz}}/\mathrm{W\,Hz^{-1}\,sr^{-1}}) = 23.02]$

The host of this radio-quiet quasar is best-matched by a moderate-sized elliptical ($r_{1/2} = 6$ kpc) with a disc host being formally excluded (Fig. 1r). The model-subtracted image in Fig. A18 shows residual luminosity around the core of the quasar, unaccounted for by the standard elliptical template. This is confirmed by the variable-beta modelling, which shows a statistically significant improvement in the quality of fit with a beta parameter of $\beta = 0.184$. The model-subtracted image also shows numerous companion objects in this field.

2344+184

Radio-quiet; $[z = 0.138,\ \log_{10}(L_{5\,\mathrm{GHz}}/\mathrm{W\,Hz^{-1}\,sr^{-1}}) < 21.18]$

The modelling of this object presented here must still be regarded as preliminary. The raw *R*-band image presented in Fig. A19 shows this quasar to be residing in a disc galaxy with clearly evident spiral arms. A two-dimensional disc template of scalelength $r_{1/2} = 9$ kpc can reasonably reproduce the total luminosity of the object, but is obviously unable to cope with the spiral arms. As can clearly be seen from both the luminosity profile (Fig. 1s) and model-subtracted image, the inner ≈2 arcsec are dominated by a bulge with a different position angle from the main disc. A two-component model must therefore be adopted in order to properly analyse this quasar host.

5 DISCUSSION

A complete discussion of our results is not appropriate until all the sources in our matched samples have been observed. However, the initial results presented above suggest the emergence of several potentially important trends which deserve comment at this stage. Furthermore, since the majority of RQQs in our sample have in fact been observed, this interesting subsample of objects is already approaching completion, and we can draw some fairly robust conclusions regarding the nature of the RQQ population.

Table 4. Absolute magnitudes (M_R), and optical–infrared ($R-K$) colours of the best-fitting host galaxy and nuclear component for each AGN. Columns 2 and 3 give the R-band absolute magnitudes (M_R) derived from the current modelling of the *HST* data, assuming a spectral index of $\alpha = 1.5$ (where $f_\nu \propto \nu^{-\alpha}$) for the galaxy and $\alpha = 0.2$ for the quasar. Columns 4 and 5 list the $R-K$ colours of the host galaxy and nuclear component respectively. These colours were derived by combining 12-arcsec aperture R-band photometry from our *HST*-based models with the 12-arcsec aperture K-band photometry derived by Taylor et al. (1996), to minimize the uncertainty introduced by errors in constraining the galaxy scalelengths at K.

Source	M_R(host)	M_R(nuc)	$(R-K)_{\rm host}$	$(R-K)_{\rm nuc}$
RG				
0345+337	−23.05	−19.63	3.23	5.32
0917+459	−24.20	−20.65	2.83	4.49
0958+291	−23.25	−21.70	3.03	3.97
2141+279	−24.09	−14.94	3.02	9.85
RLQ				
0137+012	−24.04	−23.53	2.81	3.15
0736+017	−23.58	−24.01	3.15	2.73
1004+130	−24.10	−25.70	2.96	2.22
2141+175	−23.51	−24.52	2.53	1.97
2247+140	−23.80	−23.80	2.81	2.60
2349−014	−24.32	−24.00	2.86	3.64
RQQ				
0054+144	−23.62	−24.49	3.14	1.32
0157+001	−24.29	−23.70	2.94	2.82
0244+194	−22.77	−23.24	2.54	2.72
0257+024	−23.32	−19.69	2.70	4.66
0923+201	−23.25	−24.57	3.36	2.66
0953+415	−22.82	−25.52	2.84	2.59
1012+008	−23.78	−23.95	3.78	1.72
1635+119	−23.05	−21.54	3.27	3.23
2344+184	−22.54	−20.30	3.11	4.66

5.1 Host-galaxy luminosities and morphologies

The most striking initial result of this study is that our observing strategy, combined with modelling incorporating a high-dynamic-range PSF, has enabled us not only to detect easily all of the host galaxies observed to date, but also to determine unambiguously the morphological type of the host in virtually every case (see Tables 2 and 3, and Figs 1 and 2). This represents a major improvement on previous *HST*-based quasar-host studies, which in some cases have actually struggled to detect any host galaxy emission (Bahcall et al. 1994, 1997), leading the authors to conclude that some quasars lie in low-luminosity host galaxies. Our results to date (which include imaging of several of the quasars also imaged by Bahcall et al.) indicate that such conclusions were erroneous. In contrast, as detailed in Table 4 and illustrated in Fig. 3, we confirm the basic result of our ground-based K-band study that *all* the quasars in our sample lie in host galaxies with luminosities $\geq 2L^*$ (see the notes on 0953+415 in Section 3 for a detailed discussion of the most likely explanation for Bahcall et al.'s struggle to detect this host galaxy). A similar result with regard to host luminosities has recently been reported from the *HST* imaging of LBQS quasars at $z > 0.4$ by Hooper, Impey & Foltz (1997) (although in this work no attempt was made to identify the morphological type of the hosts of these slightly higher redshift quasars).

As hoped, these *HST* images have enabled us to improve substantially on our K-band study in terms of discerning the morphological type of the hosts. All of the radio galaxies and RLQ hosts we have observed to date can be unambiguously classified as massive elliptical galaxies, with scalelengths in the range 6–23 kpc, consistent with unification of RGs and RLQs via orientation effects. Perhaps more unexpectedly, all except the two least-luminous RQQs are also found to lie in massive ellipticals, placing on a firm statistical footing the tentative result reported by Disney et al. (1995) and Taylor et al. (1996) that luminous RQQs lie in massive ellipticals, despite the fact that the less-luminous, radio-quiet Seyfert galaxies are predominantly disc-dominated. Thus, whatever the true physical origin of radio loudness, it is clearly not simply a consequence of the morphological type of the host galaxy. A particularly striking feature of this result is the extent to which a pure $r^{1/4}$ law provides an essentially perfect description (apart from obvious tidal tails and secondary nuclei) of the hosts of 16 out of the 19 AGN observed in our sample to date.

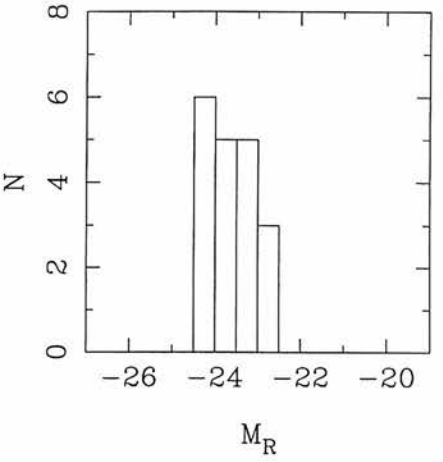

Figure 3. The distribution of (integrated) R-band absolute magnitudes (M_R) displayed by the best-fitting host galaxies. The adopted fiducial integrated absolute magnitude M_R^* corresponding to an L^* galaxy is $M_R^* = -22.2$, which is derived from the most recent determination of M_R^* by Lin et al. (1996) ($M_R^* = -21.8$) after correcting to an integrated magnitude. All the host galaxies have $L > 2L^*$.

5.2 Relation to 'normal' massive elliptical galaxies

5.2.1 Scalelengths, the Kormendy relation and axial ratios

The distribution of derived host-galaxy scalelengths is shown in Fig. 4. With the exception of the RLQ 2141+175, for which accurate scalelength determination is problematic due to the complexity of the observed interaction, the half-light scalelengths of all the host galaxies are consistent to within a factor of 3. The homogeneity of these host galaxies is striking when they are plotted on the $\mu_e - r_e$ projection of the fundamental plane (see Fig. 5), where we find that they describe a Kormendy relation essentially identical to that displayed by 'normal' massive ellipticals (Schneider, Gunn & Hoessel 1983; Capaccioli, Caon & D'Onofrio 1992); a least-squares fit yields the relationship $\mu_{1/2} = 3.34_{\pm 0.50} \log_{10} r_{1/2} + 17.95_{\pm 0.53}$. Thus the basic morphological parameters of these host galaxies appear to be indistinguishable from those of normal, inactive massive ellipticals.

If this conclusion is correct, then the host galaxies should also display a distribution in axial ratios which is indistinguishable from that displayed by the normal elliptical galaxy population,

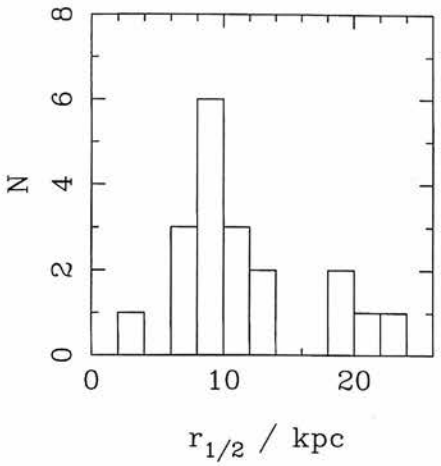

Figure 4. The distribution of scalelengths displayed by the best-fitting host galaxies. All scalelengths are presented as half-light radii ($r_{1/2}$) to facilitate ease of comparison between the sizes of disc and elliptical hosts.

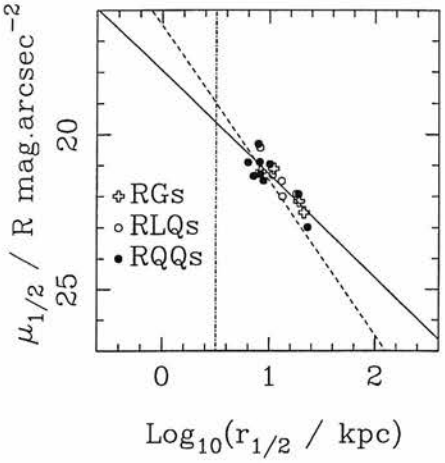

Figure 5. The Kormendy surface brightness/scalelength relation ($\mu_{1/2}$ versus $r_{1/2}$) displayed by the host galaxies of the RGs (crosses), RLQs (open circles) and RQQs (filled circles). Also shown on the plot are the best-fitting relation described in the text (solid line; slope $\simeq 3$), a line indicating the locus of constant galaxy luminosity (dashed line; slope = 5), and the dividing line between normal ellipticals and brightest cluster members as determined by Capaccioli et al. (1992) (dot-dashed line).

which peaks at $b/a > 0.8$ (Sandage, Freeman & Stokes 1970; Ryden 1992). The axial ratios yielded by the model-fitting are given in Table 2, and the resulting host-galaxy axial-ratio distribution is plotted in Fig. 6. It is perfectly consistent with the distribution displayed by normal ellipticals and, with only one object displaying an axial ratio $b/a < 0.6$, is completely at odds with the recent results of Hooper et al. (1997), who reported that *most* of the hosts of bright quasars at $z \simeq 0.4$ have low axial ratios $b/a < 0.6$. However, Hooper et al. expressed the concern that their result might reflect high-surface-brightness features such as bars or tidal tails, rather than the axial ratio of the underlying stellar population, and our very different result, based on proper modelling of the underlying host, indicates that this is almost certainly the correct explanation for their apparently contradictory conclusion.

5.2.2 *Colours*

One of the reasons we elected to use the F675W filter rather than

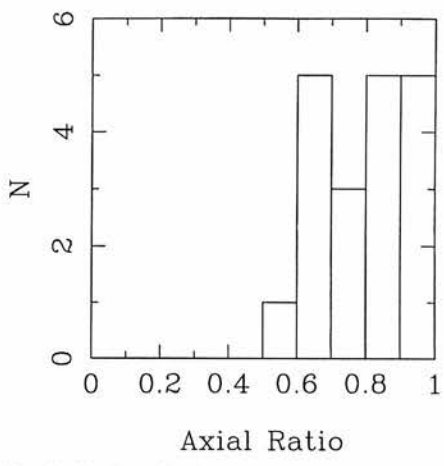

Figure 6. The distribution of axial ratios displayed by the model host galaxies. The distribution is consistent with that displayed by the normal elliptical galaxy population, which peaks at $b/a > 0.8$ (Sandage, Freeman & Stokes 1970; Ryden 1992).

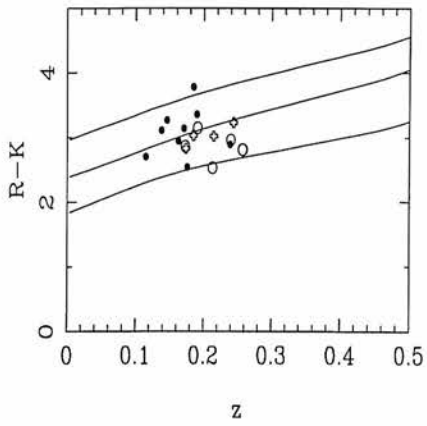

Figure 7. The apparent $R-K$ colours of the hosts (RGs = crosses, RLQs = open circles, RQQs = filled circles) plotted against redshift, compared with the colours predicted from simple k-correction of stellar populations with ages of 8, 12 and 16 Gyr (Guiderdoni & Rocca-Volmerange 1987). The uncertainty in the $R-K$ colours of the radio galaxies is only $\simeq 0.15$ mag, and it is striking that these four objects track almost perfectly the k-correction derived from the SED of an old (12 Gyr) elliptical galaxy. The uncertainties associated with removal of the nuclear contribution mean that the $R-K$ colours of the quasar hosts are somewhat more uncertain ($\simeq$ 0.3–0.5 mag), but with the present data it is clear that the hosts of all three classes of powerful AGN have colours which are consistent with each other, and with that of mature stellar populations.

the F606W filter used by Bahcall et al. was the evidence, gleaned from our deep off-nuclear spectroscopy of quasar hosts (Kukula et al. 1997; Hughes et al. 1999), that most quasar hosts appear to be rather red galaxies with a clear 4000-Å break in their spectrum. We are now, for the first time, in a position to check whether this is indeed the case by combining our new R-band *HST* results with the K-band results of Taylor et al. (1996) to measure the $R-K$ colours of the RGs and quasar hosts. The results are listed in Table 4, and plotted in Fig. 7, where the observed colours are compared with those predicted from simple k-correction of stellar populations with ages of 8, 12 and 16 Gyr (Guiderdoni & Rocca-Volmerange 1987). The uncertainty in the $R-K$ colours of the radio galaxies is only $\simeq 0.15$ mag, and it is striking that these four objects track almost perfectly the k-correction derived from the

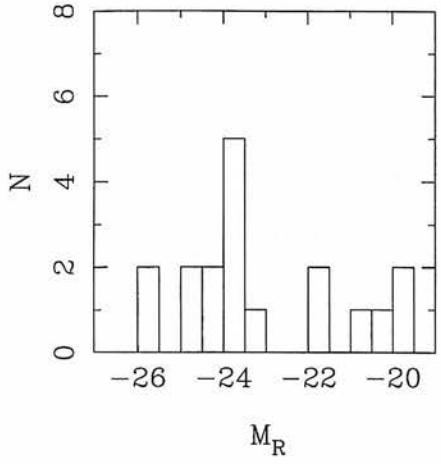

Figure 8. The distribution of R-band absolute magnitudes (M_R) displayed by the best-fitting unresolved nuclear components.

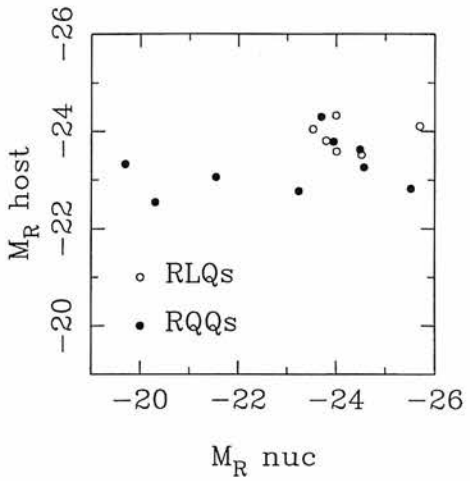

Figure 9. Absolute host galaxy magnitude plotted against absolute nuclear magnitude at R (RLQs = open circles, RQQs = filled circles). The correlation is not statistically significant ($p = 0.376$), but is consistent with the existence of a minimum host-galaxy luminosity for the production of a luminous quasar.

SED of an old (12 Gyr) elliptical galaxy. The uncertainties associated with removal of the nuclear contribution mean that the $R-K$ colours of the quasar hosts are somewhat more uncertain ($\simeq$ 0.3–0.5 mag), but with the present data it is clear that the hosts of all three classes of powerful AGN have colours which are consistent with each other, and with that of old, passively evolving stellar populations. Model-independent support for this conclusion can be gleaned by comparing Fig. 8 with the $R-K$ versus z plot for objects detected in a K-band survey reaching $K \simeq 17.3$ (Glazebrook et al. 1995); the host galaxy $R-K$ colours shown in Fig. 8 track well the red envelope displayed by K-band selected galaxies at comparable redshifts.

This is the first clear evidence that the dominant stellar populations in not only RGs, but also quasar hosts have ages comparable to the oldest known elliptical galaxies, and thus must have formed at high redshift ($z > 4$; Dunlop 1999). It also means that any substantial star formation activity associated with the triggering of AGN activity must either be dust-enshrouded, or confined either to the nuclear regions of the galaxy (in which case it will have been attributed to the quasar nucleus in our modelling procedure) or to obvious tidal tails, which we have excised prior to modelling the host galaxy.

5.2.3 *Interactions*

Previous *HST* studies have emphasized the variety of environments found around quasars, ranging from highly distorted or obviously interacting systems to apparently isolated, undisturbed galaxies (e.g. Disney et al. 1995; Bahcall et al. 1997). In their sample of 20 quasars with $z < 0.3$, Bahcall et al. found only three host galaxies currently undergoing major interactions (although as many as 13/20 quasar hosts had close companions with at least the possibility of gravitational interaction).

At first sight our own images appear to tell a similar story, with a relatively low occurrence of obvious, large-scale disturbance. However, as can be seen from panel D in Figs 1(a)–(s), removal of the axisymmetric model for the underlying host galaxy makes it relatively easy to identify morphological peculiarities such as excess flux, tidal tails, close companions and secondary nuclei, all of which have been linked to galaxy interactions, often at considerably lower surface brightness levels than the more obvious morphological distortions masked out prior to host-galaxy modelling. A full statistical analysis of the prevalence and strength of such features is deferred until completion of the sample, but here we simply note that, despite our basic conclusion that the host galaxies are relatively passive massive ellipticals, three out of the four RGs, five out of the six RLQs and six out of the nine RQQs observed to date show one or other of the morphological peculiarities mentioned above.

This tally serves to emphasize that most of these AGN may have been triggered into action by the interaction of their (perhaps previously completely passive) host galaxy with a companion object. However, we add the cautionary note that the true significance of such apparently impressive interaction statistics (14 out of 19 AGN) can only really be judged against the results of a comparably detailed investigation of the morphologies of 'inactive' massive ellipticals. This issue will be covered in more detail by Dunlop et al. (in preparation).

5.3 The AGN–host connection

The absolute magnitudes (M_R) of the fitted nuclear components are given in Table 4, and the resulting distribution is presented in Fig. 8. The nuclear absolute magnitudes are then plotted against the host absolute magnitudes in Fig. 9. Only a weak correlation ($p = 0.376$, using the Spearman rank correlation test) is seen, consistent with our previous finding at K. However, the fact that the hosts of the two faintest quasars in our sample contain a significant disc component suggests that a more significant correlation might be revealed if only bulge luminosity is considered for comparison with nuclear power. This possibility is explored below in the context of recent studies of nearby galaxies which suggest that black hole mass does indeed depend primarily on bulge mass rather than total galaxy mass.

5.3.1 *The black hole–spheroid connection*

Our unambiguous finding that all the quasars in our sample with $M_R < -23.5$ lie in massive elliptical galaxies, irrespective of radio power, clearly refutes the long-standing hypothesis that, like the majority of Seyferts, radio-quiet quasars lie in predominantly disc

Table 5. The results of calculating spheroid mass, and hence black hole mass/luminosity from host-galaxy spheroid luminosity. Column 2 gives the derived spheroid mass (in units of $10^{11}\,M_\odot$), calculated from the values of M_R given in Table 4 using the mass:light ratio relation given by Magorrian et al. (1998). Column 3 then gives the estimated mass of the central black hole (in units of $10^9\,M_\odot$) derived from the data in column 2 using the high-mass form of the $m_{sph} : m_{bh}$ relation deduced by Magorrian et al. (1998), while columns 4 and 5 give alternative estimates of m_{bh} based on P^{total}_{5-GHz} and P^{core}_{5-GHz}. Finally column 6 gives the predicted Eddington M_R corresponding to m^a_{bh} given in column 3.

Source	$m_{sph}/10^{11}\,M_\odot$	$m^a_{bh}/10^9\,M_\odot$	$m^b_{bh}/10^9\,M_\odot$	$m^c_{bh}/10^9\,M_\odot$	M_R(Eddington)
RG					
0345+337	6.3	5.0	20		−24.8
0917+459	22	33	25	25	−28.3
0958+291	7.8	6.9	17	34	−25.4
2141+279	20	27	16	19	−27.9
RLQ					
0137+012	18	25	17	58	−27.8
0736+017	11	12	22		−26.4
1004+130	20	28	13	15	−28.0
2141+175	10	11	12		−26.2
2247+140	14	17	18		−27.1
2349−014	25	40	12	45	−28.6
RQQ					
0054+144	12	13	0.9	3.7	−26.5
0157+001	24	38	2.2	11	−28.5
0244+194	4.6	3.2	<0.6	<2.3	−24.0
0257+024	3.2	1.8	1.2	4.2	−22.9
0923+201	7.8	6.9	<0.8	<3.0	−25.4
0953+415	4.9	3.4	<0.8	<3.1	−24.1
1012+008	14	16	1.0	4.2	−26.2
1635+119	6.3	5.0	2.5	12	−24.8
2344+184	2.9	1.6	<0.5	<1.8	−22.6

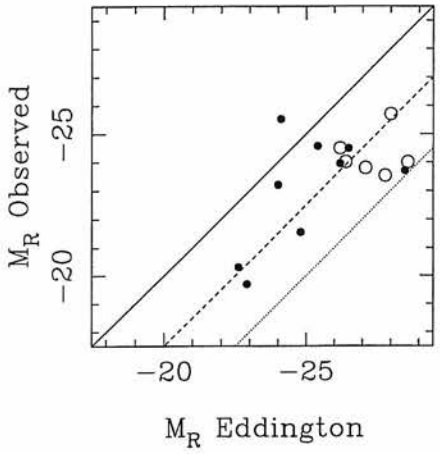

Figure 10. The observed absolute magnitude M_R of the nuclear component in each quasar plotted against the absolute magnitude, which is predicted by assuming that each quasar contains a black hole of mass $m_{bh} = 0.006 m_{spheroid}$, and that the black hole is emitting at the Eddington luminosity(RLQs = open circles, RQQs = filled circles). The black hole mass has been calculated from the host galaxy bulge luminosity, assuming the mass to light ratio and $m_{spheroid} - m_{BH}$ correlation given in Magorrian et al. (1998). The solid line shows where the quasars should lie if they were all radiating at their respective Eddington luminosities, while the dashed line indicates 10 per cent of predicted Eddingtion luminosity, and the dotted line indicates 1 per cent of predicted Eddington luminosity. As in previous figures, the RLQs are indicated by open circles, while the RQQs are indicated by filled circles. The nuclear components of the radio galaxies are not plotted, because all the evidence suggests they are substantially obscured by dust.

galaxies. However, if it is accepted that all quasars (radio-loud and radio-quiet) result from accretion of material on to a supermassive black hole, then our result can be seen as a natural consequence of the black hole/spheroid mass correlation recently derived for nearby galaxies by Magorrian et al. (1998), as we now briefly explain.

Magorrian et al. find that the available kinematic data on nearby galaxies are consistent with the relation $m_{bh} = 0.006 m_{sph}$ where m_{sph} is the mass of the hot stellar component (i.e., the spheroidal bulge), strengthening the previous conclusion of Kormendy & Richstone (1995). They also show that m_{sph} can be estimated from the luminosity of the spheroidal component using a mass:light ratio which is proportional to $M^{0.18}$ (their equation 10), broadly consistent with the fundamental-plane correlation predicted using the virial theorem (e.g. Bender, Burstein & Faber 1992).

Since we now possess the first reliable determinations of the spheroid luminosity for the hosts of a significant sample of AGN, we have explored the result of applying these two relations to estimate (albeit rather crudely) the spheroidal mass M_{sph} of each host, and hence the *expected* mass of the black hole at the centre of each galaxy. The results of this calculation are listed in Table 5, columns 2 and 3. We have then proceeded to calculate the Eddington luminosity, Eddington temperature, and hence Eddington absolute magnitude M_R for the putative black hole at the centre of each host galaxy, and the results of this calculation are given in column 6 of Table 5, and compared with the observed nuclear absolute magnitude of each quasar (i.e., after host galaxy removal) in Fig. 10.

In our view, this is a surprisingly successful calculation. As can be seen from Fig. 10, the maximum luminosity produced by any quasar is comparable with the predicted Eddington limit, while the

majority appear to be radiating at a few per cent of the Eddington luminosity. Moreover, despite the large number of sources of potential scatter, the correlation between observed M_R and predicted Eddington M_R is stronger ($p = 0.164$) than that between raw host-galaxy luminosity and nuclear lumonsity [and becomes significant ($p = 0.07$) if 0953+415 is excluded from the analysis], and both the radio-quiet and radio-loud quasars display a similar relation. This suggests that, in both classes of quasar, the *optical* luminosity arises from a similar process of accretion on to a massive black hole, and that RLQs and RQQs of comparable absolute magntiude $M_R < -23.5$ are powered by black holes of comparable mass $M > 3 \times 10^9\,M_\odot$.

The results of this calculation can be regarded as providing independent evidence that the relation of Magorrian et al. still applies for large galaxy and black hole masses. To reiterate, this relation would predict that such massive black holes can only be housed in galaxies with a spheroid mass of $> 5 \times 10^{11}\,M_\odot$ which is equivalent to an absolute magnitude of $M_R < -23$, which is exactly what we find. Galaxies with such massive spheroidal components must inevitably be classed as giant ellipticals, in which case it could be regarded as a (now successful) prediction of the black hole/spheroid mass relation that all luminous quasars must reside in massive elliptical galaxies more luminous than $\simeq 2L^*$.

5.3.2 *The black hole–radio power connection*

Finally, we combine our estimates of black hole mass derived from host-galaxy spheroid mass (Table 5) with the radio data available to us for each object to investigate how our results compare with the radio luminosity–black hole mass correlations recently derived for low-redshift galaxies by Franceschini, Vercellone & Fabian (1998).

Franceschini et al. found a remarkably tight relationship between black hole mass and both total and nuclear radio centimetric luminosity, with a very steep dependence of the radio power on the mass of the black hole $m_{\rm bh}$ ($P^{\rm tot}_{5\,\rm GHz} \propto m_{\rm bh}^{2.7}$). In Fig. 11(a) we have replotted their data which demonstrate the relation between total 5-GHz radio luminosity and black hole mass in nearby galaxies, along with their best-fitting straight-line relation, highlighting the location of the Milky Way and M87. We have then added the relevant datapoints (or upper limits) for the AGN studied in this paper. Whereas Franceschini et al. were able to determine $m_{\rm bh}$ directly from high-resolution spectroscopy, the value of $m_{\rm bh}$ plotted for each of our AGN has of course had to be inferred from the mass of the spheroidal component of its host galaxy. However, the location of our AGN on this diagram, particularly the radio-loud AGN, strongly suggests that our host-galaxy-based black hole mass estimates are reasonable, despite the large uncertainties involved in extrapolating from spheroid luminosity.

To put this another way, one can derive two completely independent estimates of the mass of the black hole at the heart of each of our AGN using either (i) the luminosity of the host spheroid and the relations given by Magorrian et al. as described above, or (ii) the $P_{5\,\rm GHz} : m_{\rm bh>}$ regression line of Franceschini et al. shown in Fig. 11(a), and for the radio-loud AGN in our sample these values agree to within a factor of typically 2 (rms – see columns 3 and 4 of Table 5).

Since the RGs and RLQs appear so consistent with the $P_{5\,\rm GHz} : m_{\rm bh}$ relation, it is inevitable that the RQQs should lie below it, but a striking feature of Fig. 11(a) is that (albeit that a number of upper limits are involved), there does still appear to be a correlation between radio luminosity and host-galaxy-derived $m_{\rm bh}$ within the RQQ subsample. This suggests that the radio luminosities of the RQQs might also be linked to those of lower

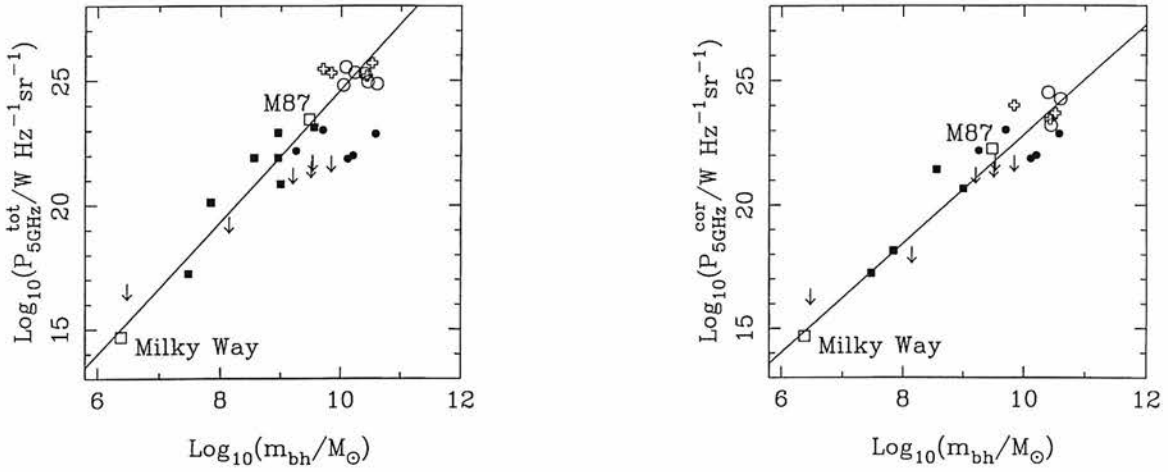

Figure 11. (a) Total radio luminosity $P^{\rm total>}_{5\,\rm GHz}$ versus black hole mass showing the data on low-redshift 'normal' galaxies from Franceschini, et al. (1998), and the AGN discussed in this paper (RGs = crosses, RLQs = open circles, RQQs = filled circles). The solid line is simply the best-fitting relation to the nearby galaxy data given by Franceschini et al. – $\log(P^{\rm total}_{5\,\rm GHz}) = 2.73\log(m_{\rm bh}) - 2.87$. For the nearby galaxies $m_{\rm bh}$ has been estimated directly from stellar dynamics, while for the AGN $m_{\rm bh}$ has been estimated from host-galaxy spheroid luminosity using the relations derived by Magorrian et al. (1998). (b) Core radio luminosity $P^{\rm core}_{5\,\rm GHz}$ versus black hole mass showing the data on low-redshift 'normal' galaxies from Franceschini et al. (1998), and the AGN discussed in this paper (RGs = crosses, RLQs = open circles, RQQs = filled circles) for which a core radio flux was available in the literature, with little evidence for a signficant beamed component. The solid line is the relation $P \propto m_{\rm bh}^{2.2}$ expected for simple advection-dominated accretion models (Fabian & Rees (1995), or indeed for any model in which the emission is mostly dependent of the emitting area available around a black hole) normalized to the Milky Way. Unlike Franceschini et al., we have attributed all the radio emission from M31 (after removal of very extended radio emission linked to star formation) to the core, because the AGN contribution in M31 would in fact be remain unresolved at the distance of most of the objects in even the local sample; this appears to the reason that we find the core radio data to be linked to $m_{\rm bh}$ through a flatter relation $P^{\rm core}_{5\,\rm GHz} \propto m_{\rm bh}^{2.2}$ than did Franceschini et al.

mass objects via a simple relation. Since the study of Kukula et al. (1998) has shown that the radio emission from these RQQs, where detectable, arises entirely from a compact core-like component, we have therefore investigated whether the radio properties of RQQs can be linked to those of nearby galaxies if only compact radio emission is included.

This is explored in Fig. 11(b). Franceschini et al. also found a strong correlation between core 5-GHz radio luminosity and black hole mass, and so we have again reproduced their data for nearby galaxies, this time plotting $P^{\rm core}_{\rm 5\,GHz}$ versus $m_{\rm bh}$, along with the relation $P \propto m_{\rm bh}^{2.2}$ expected for simple advection-dominated accretion models (Fabian & Rees 1995), or indeed for any model in which the emission is mostly dependent on the emitting area available around a black hole. We have replotted all the RQQ data points shown in Fig.11(a), but this time have only plotted datapoints for the cores of the lobe-dominated radio-loud AGN (to minimize the impact of beaming; Giovannini et al. 1988; Lister & Gower 1994). We note that in this case the RQQs apparently form a natural extension of the local galaxy sample, as do the least luminous cores of the radio-loud AGN, and that the plotted relation provides an excellent description of the data. A number of points are worthy of comment. First, unlike Franceschini et al. we have attributed all the radio emission from M31 (after removal of very extended radio emission linked to star formation) to the core because the AGN contribution in M31 would in fact remain unresolved at the distance of most of the objects in even the local sample; this appears to be the reason that we find the core radio data to be linked to $m_{\rm bh}$ through a flatter relation $P^{\rm core}_{\rm 5\,GHz} \propto m_{\rm bh}^{2.2}$ than did Franceschini et al.. Second, it is noteworthy that M87 moves from the 'radio-loud' relation in Fig. 11(a), to the 'radio-quiet' relation in Fig. 11(b) once its extended radio emision is removed, as do several of the radio-loud AGN. Third, as is clear from the figure, several of the RQQs currently only possess upper limits on radio luminosity; if $P^{\rm core}_{\rm 5\,GHz}$ and $m_{\rm sph}$ really are both good indicators of the black hole mass in these objects, then we would predict that the radio emission from these RQQs should be detected by radio observations reaching only an order of magnitude below the current limits.

Because it is undoubtedly possible that $P^{\rm core}_{\rm 5\,GHz}$ is a better indicator of black hole mass than is $m_{\rm sph}$, we have used the relation shown in Figure 11(b) to obtain an independent prediction of $m_{\rm bh}$ for each quasar, and the results are presented in column 5 of Table 5. In Fig. 12 we plot $m_{\rm bh}$ derived from $P^{\rm core}_{\rm 5\,GHz}$ against $m_{\rm bh}$ derived from host galaxy luminosity. These *completely independent estimates* of $m_{\rm bh}$ are clearly extremely well correlated ($p = 0.003$), and for individual sources the discrepancy is no greater than a factor of 4, and is frequently smaller. However, use of the $P^{\rm core}_{\rm 5\,GHz} - m_{\rm bh}$ relation shown in Fig. 11(b), does tend to yield smaller black hole masses for the RQQs than the use of $m_{\rm sph}$.

5.4 The origin of radio loudness

Despite the good agreement between the black hole masses of the radio-loud AGN as estimated from $P^{\rm total}_{\rm 5\,GHz}$ and host galaxy luminosity, it seems unlikely that the relation shown in Fig. 11(a) can be a fair indicator of the black hole masses in the RQQs, because then the more luminous RQQs such as 0054+144 would appear to have an optical luminosity an order of magnitude greater than the Eddington luminosity.

This leaves either $P^{\rm core}_{\rm 5\,GHz}$ or host-galaxy luminosity as potential

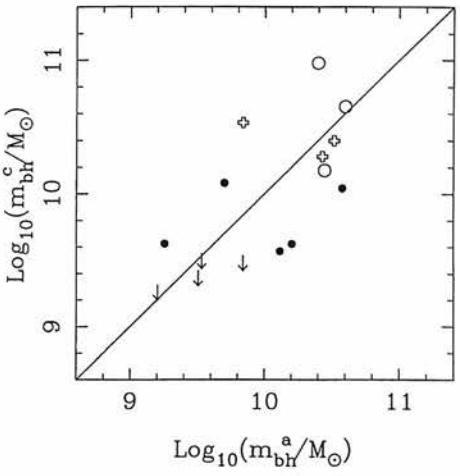

Figure 12. Black hole mass ($m^{\rm c}_{\rm bh}$ – as given in column 5 of Table 5) as estimated from core radio flux $P^{\rm core}_{\rm 5\,GHz}$ plotted against black hole mass ($m^{\rm a}_{\rm bh}$ – as given in column 3 of Table 5) estimated from host galaxy luminosity. These two completely independent estimators of black hole mass are highly correlated ($p = 0.003$), and for individual objects agree to no worse than a factor of 4.

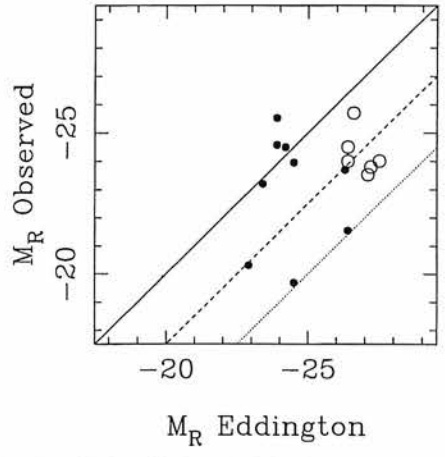

Figure 13. As Fig. 11, but this time with Eddington M_R derived using the values of $m_{\rm bh}$ estimated from $P^{\rm core}_{\rm 5\,GHz}$.

alternative estimators of black hole mass, and while Fig. 12 demonstrates that both quantities lead to reasonably consistent values for $m_{\rm bh}$, the implication for the physical origin of radio loudness depends rather crucially on which of these is the more reliable predictor of $m_{\rm bh}$. The reason for this is that, for the radio-loud objects, comparison of columns 3, 4 and 5 in Table 5 shows that essentially all routes of black hole mass estimation lead to values of $m_{\rm bh} > 10^{10}\,{\rm M}_{\odot}$. However, for the RQQs, use of $P^{\rm core}_{\rm 5\,GHz}$ to estimate $m_{\rm bh}$ produces values typically a factor of 2 smaller than inferred from host-galaxy luminosity, and implies that *no* RQQ in the sample has a black hole more massive than $m_{\rm bh} = 10^{10}\,{\rm M}_{\odot}$. There is already a suggestion in Fig. 10 that, despite the comparable observed absolute magnitudes of the RQQs and RLQs, the predicted Eddington luminosities of the RQQs are somewhat smaller. If the values of $m_{\rm bh}$ derived from $P^{\rm core}_{\rm 5\,GHz}$ are used to predict Eddington M_R, the difference becomes even more stark (as shown in Fig. 13), and shows that in selecting optically matched samples of RQQs and RLQs we may in fact have selected lower mass ($\simeq 10^9\,{\rm M}_{\odot}$) black holes radiating close to the

Eddington limit for comparison with higher mass ($\simeq 10^{10}\,M_\odot$) black holes radiating (in the optical) at around 10 per cent of their Eddington luminosity.

In summary, our results to date can be interpreted in two distinct ways, depending on whether $P^{\rm core}_{5\,\rm GHz}$ or host-galaxy luminosity is the more reliable predictor of black hole mass. If the former, then the difference between radio-loud and radio-quiet AGN may simply be that FRII radio sources require black holes of mass $m_{\rm bh} > 10^{10}\,M_\odot$. If the latter, then at least some of the RQQs in our sample would also appear to be powered by black holes with $m_{\rm bh} > 10^{10}\,M_\odot$, and some other explantion (e.g., black hole angular momentum) would be required to explain why black holes of comparable mass can produce radio sources which differ by two orders of magnitude in radio power, despite the fact that both are radiating in the optical with comparable efficiency.

Completion of our sample, coupled with proposed deeper radio observations of the undetected RQQs should assist in clarifying this issue.

6 CONCLUSIONS

In this paper we have presented and analysed the deep WFPC2 R675W images of the 19 objects (RGs, RLQs and RQQs) observed with the *HST* during the first year of our comparative *HST* imaging study of the host galaxies of luminous AGN. The results indicate that this carefully controlled study will, as hoped, be able to identify unambiguously the morphological type of the host galaxy of every AGN in our final 33-source sample. From the images analysed in this paper we find that the underlying hosts of *all three* classes of luminous AGN are massive elliptical galaxies, with scalelengths $\simeq 10$ kpc. Since the RQQ subsample is already close to completion, we can therefore for the first time state with some confidence that essentially all RQQs brighter than $M_R = -24$ reside in massive ellipticals, a result which removes the possibility that 'radio loudness' is directly linked to host-galaxy morphology.

The existence of comparably detailed modelling of deep K-band images of all the sources in our sample (Dunlop et al. 1993; Taylor et al. 1996) has allowed us to use our new R-band results to derive the first reliable optical–infrared colours for the hosts of a substantial sample of AGN. The preliminary results indicate that the hosts of all three classes of AGN have underlying stellar populations with ages comparable to that observed in normal, old ellipticals at similar redshift, despite the evidence for superimposed acivity arising from interactions/mergers. We also find that the distribution of host-galaxy axial ratios is consistent with that displayed by the normal elliptical galaxy population.

The RG and RLQ subsamples have been designed to be matched in terms of radio luminosity, radio spectral index, and redshift. Comparison of the host-galaxy properties of the (still small) RG and RLQ subsamples observed to date indicates that their hosts are indistinguishable in terms of morphological type, luminosity, axial ratio, and $R-K$ colour, consistent with unification via orientation.

The RQQ and RLQ samples were designed to be matched in terms of optical luminosity and redshift, and the image analysis presented here indicates that, with the exception of two low-luminosity interlopers in the RQQ sample (0257+024 and 2344+184, which should really be reclassified as Seyferts), the distributions of nuclear absolute magnitude for the RQQ and RLQ subsamples do indeed appear to be well matched. Interestingly, therefore, with the exception of 0257+024 and 2344+184, we find the host galaxies of the RQQs also to be massive elliptical galaxies, albeit approximately 0.5 mag fainter on average than their radio-loud counterparts. With the present subsamples this difference is not significant, but when the black hole mass in these quasars is inferred from the luminosity of their host spheroid, it implies that the typical black hole mass for the RQQs in our sample is $\simeq 7\times10^9\,M_\odot$, while for the RLQs it is $\simeq 15\times10^9\,M_\odot$, and that several of the luminous RQQs we have selected are radiating close to their Eddington limit (whereas very few of the RLQs appear to be radiating at more than $\simeq$10 per cent of predicted Eddington luminosity).

Finally, we find that the black hole mass estimates obtained from the luminosity of the host spheroid are in good agreement with independent estimates based on extrapolation of the relation between black hole mass and core radio luminosity established for nearby galaxies, and it seems hard to escape the conclusion that all the radio-loud AGN in our sample have black hole masses in excess of $10^{10}\,M_\odot$. However, if the latter relation is adopted as the most reliable estimator, we would conclude that our RQQ sample is even more biased towards objects emitting close to their Eddington limit, and contains no object powered by a black hole as massive as $10^{10}\,M_\odot$. If this is correct, then the physical origin of radio loudness ($P_{5\,\rm GHz} > 10^{24}\,{\rm W\,Hz^{-1}\,sr^{-1}}$) may simply be the presence of a black hole more massive than $10^{10}\,M_\odot$, and this relatively clean result may have been previously concealed from us by the selection effects involved in striving to produce a bright RQQ sample for comparison with a (radio-selected) RLQ sample, coupled with substantial scatter in the $m_{\rm bh}$: host-luminosity relation. Alternatively, if our values of $m_{\rm bh}$ derived from host-galaxy spheroid luminosity are more reliable, then at least some of the RQQs in our sample would have black hole masses $m_{\rm bh} > 10^{10}\,M_\odot$, comparable to RLQs, and some explanation other than simply black hole mass would still be required to account for the fact that the RLQs are two orders of magnitude more luminous at radio wavelengths. Completion of our *HST* study, coupled with deeper radio observations of the as-yet-undetected RQQs, should help to distinguish between these two alternative scenarios.

ACKNOWLEDGMENTS

Based on observations with the NASA/ESA *Hubble Space Telescope*, obtained at the Space Telescope Science Institute, which is operated by the Association of Universities for Research in Astronomy, Inc. under NASA contract No. NAS5-26555. This research has made use of the NASA/IPAC Extragalactic Database (NED) which is operated by the Jet Propulsion Laboratory, California Institute of Technology, under contract with the National Aeronautics and Space Administration. MJK acknowledges the award of a PPARC PDRA, and also acknowledges support for this work provided by NASA through grant numbers 00548 and 00573 from the Space Telescope Science Institute, which is operated by AURA, Inc., under NASA contract NAS5-26555. RJM acknowledges a PPARC studentship. DHH acknowledges the award of a PPARC PDRA.

REFERENCES

Akujor C. E., Spencer R. E., Zhang F. J., Davis R. J., Browne I. W. A., Fanti C., 1991, MNRAS, 250, 215

Antonucci R. R. J., 1985, ApJS, 59, 499

Bahcall J. N., Kirhakos S., Schneider D. P., 1994, ApJ, 435, L11
Bahcall J. N., Kirhakos S., Schneider D. P., 1995a, ApJ, 447, L1
Bahcall J. N., Kirhakos S., Schneider D. P., 1995b, ApJ, 450, 486
Bahcall J. N., Kirhakos S., Schneider D. P., 1996, ApJ, 457, 557
Bahcall J. N., Kirhakos S., Saxe D. H., Schneider D. P., 1997, ApJ, 479, 642
Barthel P. D., 1989, ApJ, 336, 606
Capaccioli M., Caon N., D'Onofrio M., 1992, MNRAS, 259, 323
Carballo R., Sánchez S. F., González-Serrano J. I., Benn C. R., Vigotti M., 1998, AJ, 115, 1234
De Koff S. et al., 1996, ApJS, 107, 621
Disney M. J. et al., 1995, Nat, 376, 150
Dunlop J. S., 1997, in Bremer M. et al., eds, Observational Cosmology with the New Radio Surveys. Kluwer, Dordrecht, p. 157
Dunlop J. S., 1999, in Rottgering H. J. A., Best P., Lehnert M. D., eds, The Most Distant Radio Galaxies, KNAW Colloquium Amsterdam. Kluwer, Dordrecht, p. 71
Dunlop J. S., Taylor G. L., Hughes D. H., Robson E. I., 1993, MNRAS, 264, 455
Ellingson E., Yee H. K. C., Green R. F., 1991, ApJ, 371, 41
Fabian A. C., Rees M. J., 1995, MNRAS, 277, L55
Feigelson E. D., Isobe T., Kembhavi A., 1984, AJ, 89, 1464
Franceschini A., Vercellone S., Fabian A. C., 1998, MNRAS, 297, 817
Giovannini G., Feretti L., Gregorini L., Parma P., 1988, A&A, 199, 73
Glazebrook K., Peacock J. A., Miller L., Collins C. A., 1995, MNRAS, 275, 169
Gower A. C., Hutchings J. B., 1984a, PASP, 96, 19
Gower A. C., Hutchings J. B., 1984b, AJ, 89, 1658
Guiderdoni B., Rocca-Volmerange B., 1987, A&A, 186, 1
Haehnelt M. G., Rees M. J., 1993, MNRAS, 263, 168
Heckman T. M., Bothun G. D., Balick B., Smith E. P., 1984, AJ, 89, 958
Heckman T. M. et al., 1986, ApJ, 311, 526
Hooper E. J., Impey C. D., Foltz C. B., 1997, ApJ, 480, L95
Hughes D. H., Kukula M. J., Dunlop J. S., Boroson T. B., 1999, MNRAS, submitted
Hutchings J. B., 1995, Nature News & Views, 376, 118
Hutchings J. B., Morris S. C., 1995, AJ, 109, 1541
Hutchings J. B., Neff S. G., 1992, AJ, 104, 1
Hutchings J. B., Neff S. G., 1997, AJ, 113, 550
Hutchings J. B., Johnson I., Pyke R., 1988, ApJS, 66, 361
Hutchings J. B., Janson T., Neff S. G., 1989, ApJ, 342, 660
Hutchings J. B., Holtzman J., Sparks W. B., Morris S. C., Hanisch R. J., Mo J., 1994, ApJ, 429, L1
Kormendy J., Richstone D., 1995, ARA&A, 33, 581
Kotilainen J. K., Ward M. J., 1994, MNRAS, 266, 953
Kukula M. J., Dunlop J. S., Hughes D. H., Rawlings S., 1998, MNRAS, 297, 366
Kukula M. J. et al., 1997, in Clements D. L., Pérez-Fournon I., eds, Quasar Hosts, Proc. ESO/IAC conference. Springer-Verlag, Berlin, p. 177
Leahy J. P., Pooley G. G., Riley J. M., 1986, MNRAS, 222, 753
Lin H., Kirshner P. P., Schectman S. A., Landy S. D., Oemler A., Tucker D. L., Schechter P. L., 1996, ApJ, 464, 60
Lister M. L., Gower A. C., 1994, AJ, 108, 821
MacKenty J. W., 1990, ApJS, 72, 231
McCarthy P. J., van Breugel W., Kapahi V. K., 1991, ApJ, 371, 478
McLeod K. K., Rieke G. H., 1994a, ApJ, 420, 58
McLeod K. K., Rieke G. H., 1994b, ApJ, 431, 137
McLeod K. K., Rieke G. H., 1995a, ApJ, 441, 96
McLeod K. K., Rieke G. H., 1995b, ApJ, 454, L77
McLure R. J. et al., 1999, MNRAS, submitted
Magorrian J. et al., 1998, AJ, 115, 2285
Miley G. K., Hartsuijker A. P., 1978, A&AS, 34, 129
Miller P., Rawlings S., Saunders R., 1993, MNRAS, 263, 425
Peacock J. A., 1987, in Kundt W., ed., Astrophysics Jets and Their Engines. Reidel, Dordrecht, p. 185
Romney J. et al., 1984, A&A, 135, 289
Ryden S., 1992, ApJ, 396, 445
Sandage A. R., Freeman K. C., Stokes N. R., 1970, ApJ, 160, 831
Schneider D. P., Gunn J. E., Hoessel J. G., 1983, ApJ, 268, 476
Silk J., Rees M., 1999 8, A&A, 331, L1
Small T. A., Blandford R. D., 1992, MNRAS, 259, 725
Smith E. P., Heckman T. M., 1990, ApJ, 348, 38
Smith E. P., Heckman T. M., Bothun G. D., Romanishin W., Balick B., 1986, ApJ, 306, 64
Stockton A., Farnham T., 1991, ApJ, 371, 525
Taylor G. T., Dunlop J. S., Hughes D. H., Robson E. I., 1996, MNRAS, 283, 930
Trauger J. T. et al., 1994, ApJ, 435, L3
Turnshek D. A., Bohlin R. C., Williamson R., Lupie O., Koornneef J., Morgan D., 1990, AJ, 99, 1243
Urry C. M., Padovani P., 1995, PASP, 107, 803
van Breugel W., Miley G., Heckman T., 1984, AJ, 89, 5
Véron-Cetty M. P., Woltjer L., 1990, A&A, 236, 69
Véron-Cetty M. P., Woltjer L., Roy A. L., 1991, A&A, 246, L73
Young S. et al., 1998, MNRAS, 294, 478

APPENDIX A: THE IMAGES

The images, two-dimensional model fits, and model-subtracted residual images. A grey-scale/contour image of the final reduced F675W *R*-band image of each AGN is shown in the top-left panel (panel A) of each of Figs A1–A19, which shows a region 12.5×12.5 arcsec^2 centred on the target source. The surface brightness of the lowest contour level is indicated in the top-right corner of the panel with the grey-scale designed to highlight structure close to this limit. Higher surface brightness contours are spaced at intervals of 0.5 mag arcsec^{-2}, and have been superimposed to emphasize brighter structure in the centre of the galaxy/quasar. Panel B in each figure shows the best-fitting two-dimensional model, complete with unresolved nuclear component (after convolution with the empirical PSF) contoured in an identical manner to panel A. Panel C shows the best-fitting host galaxy as it would appear if the nuclear component were absent, while panel D is the residual image which results from subtraction of the full two-dimensional model (in panel B) from the raw *R*-band image (in panel A), in order to highlight the presence of morphological peculiarities such as tidal tails, interacting companion galaxies, or secondary nuclei. All panels are displayed using the same grey-scale.

This paper has been typeset from a TEX/LATEX file prepared by the author.

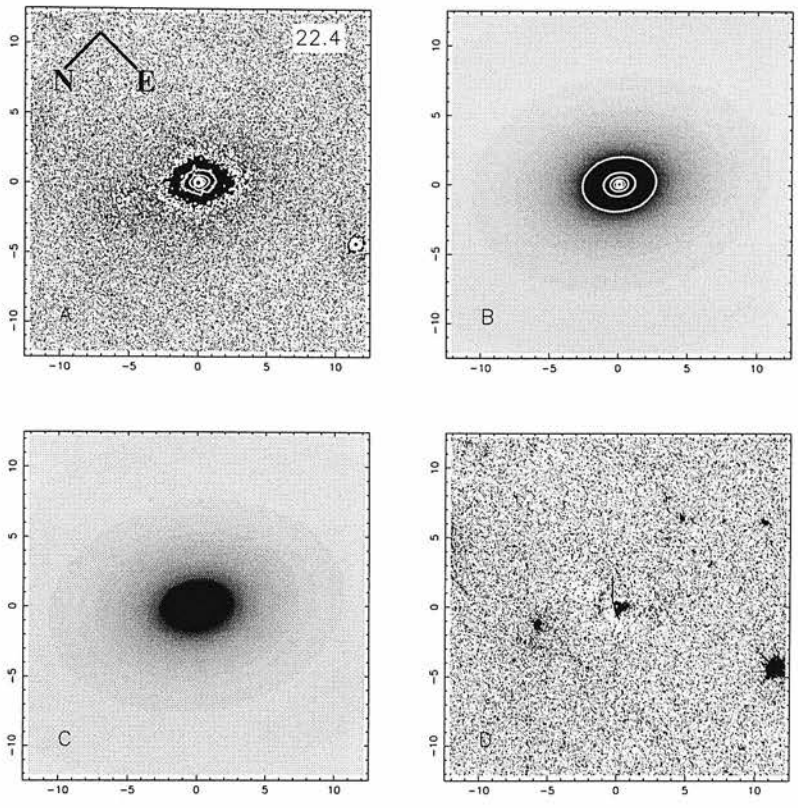

Figure A1. The radio galaxy 0345+337.

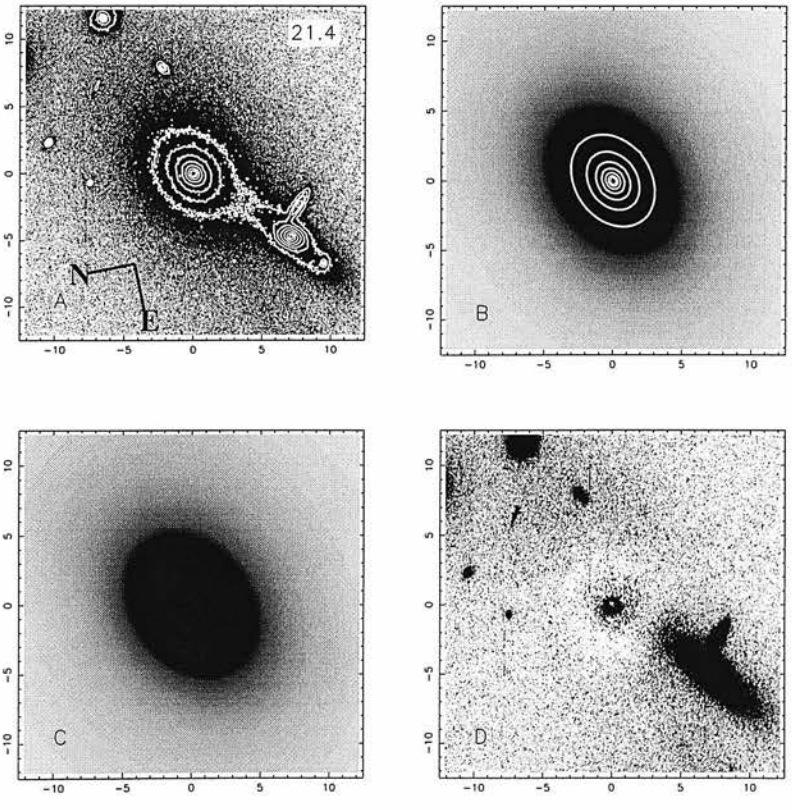

Figure A2. The radio galaxy 0917+459.

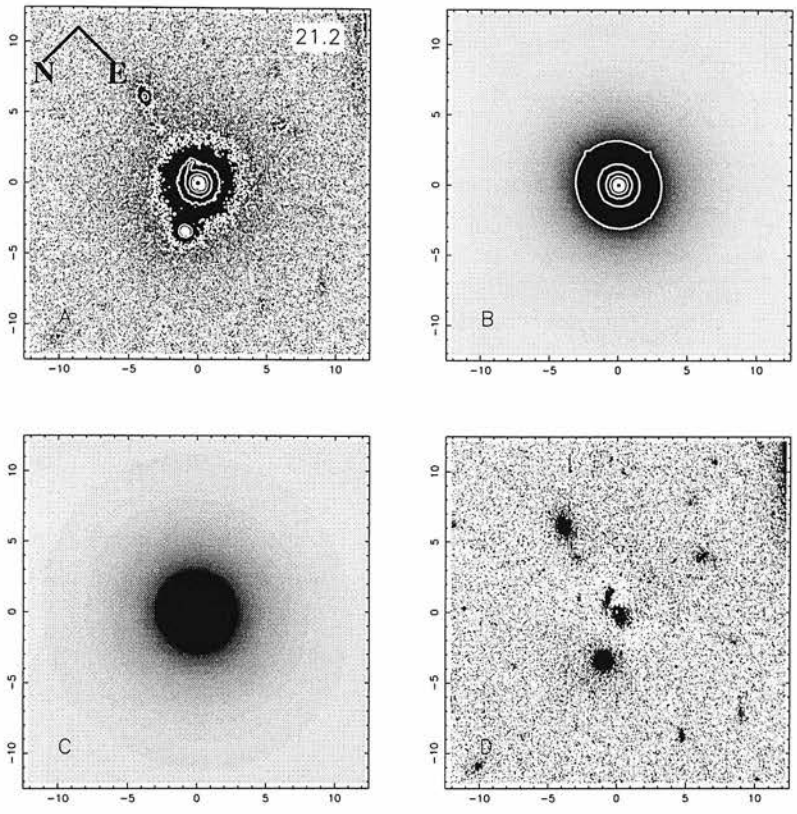

Figure A3. The radio galaxy 0958+291.

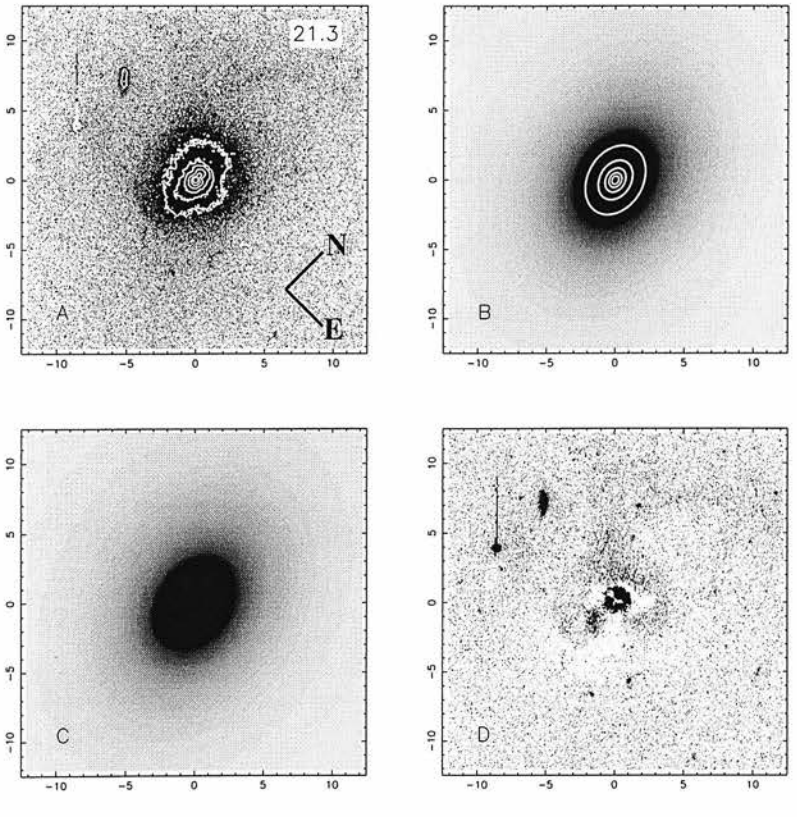

Figure A4. The radio galaxy 2141+279.

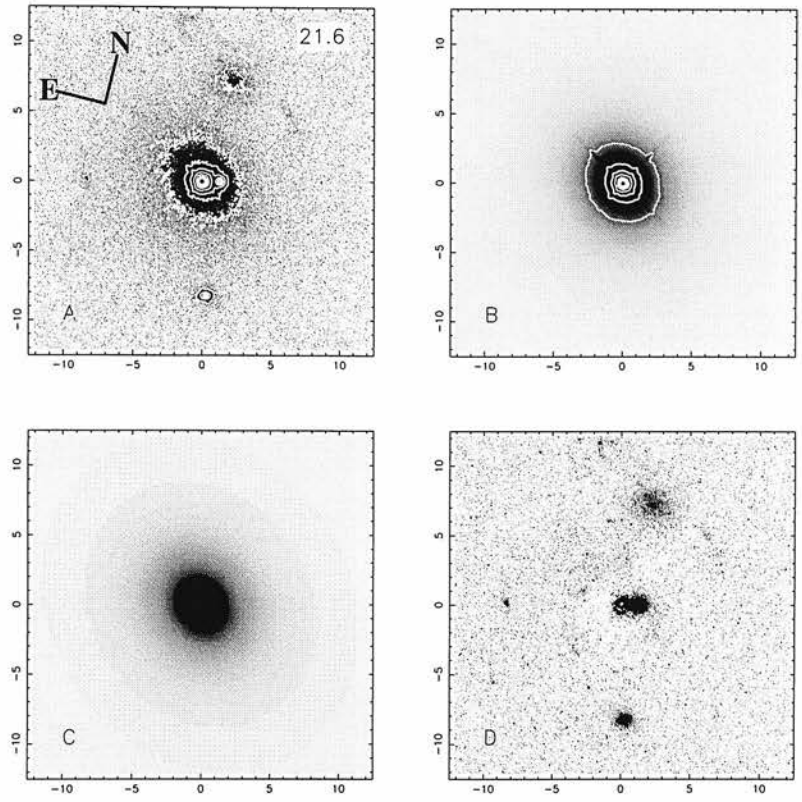

Figure A5. The radio-loud quasar 0137+012.

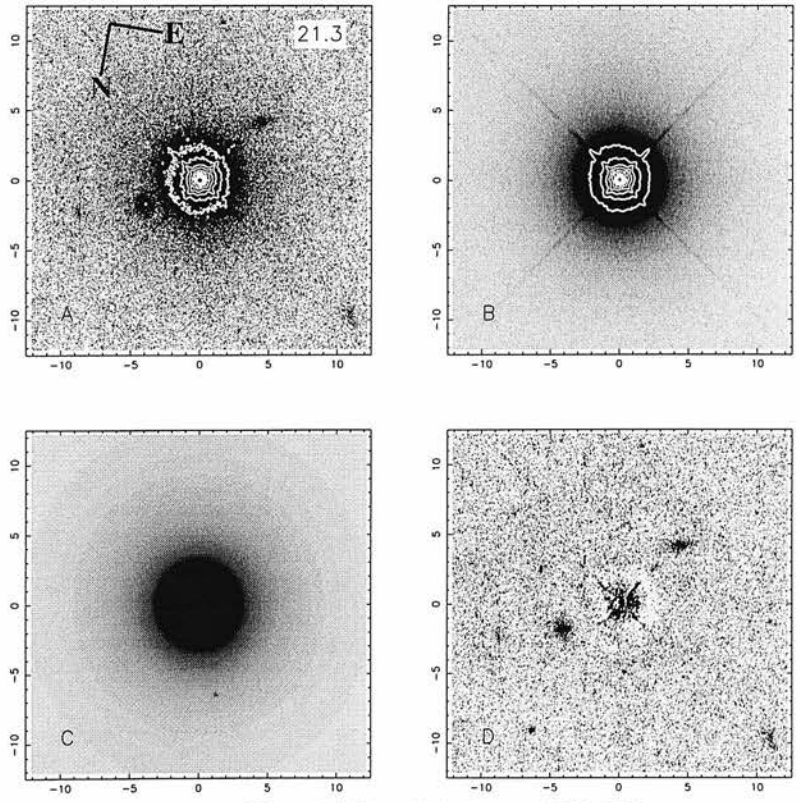

Figure A6. The radio-loud quasar 0736+017.

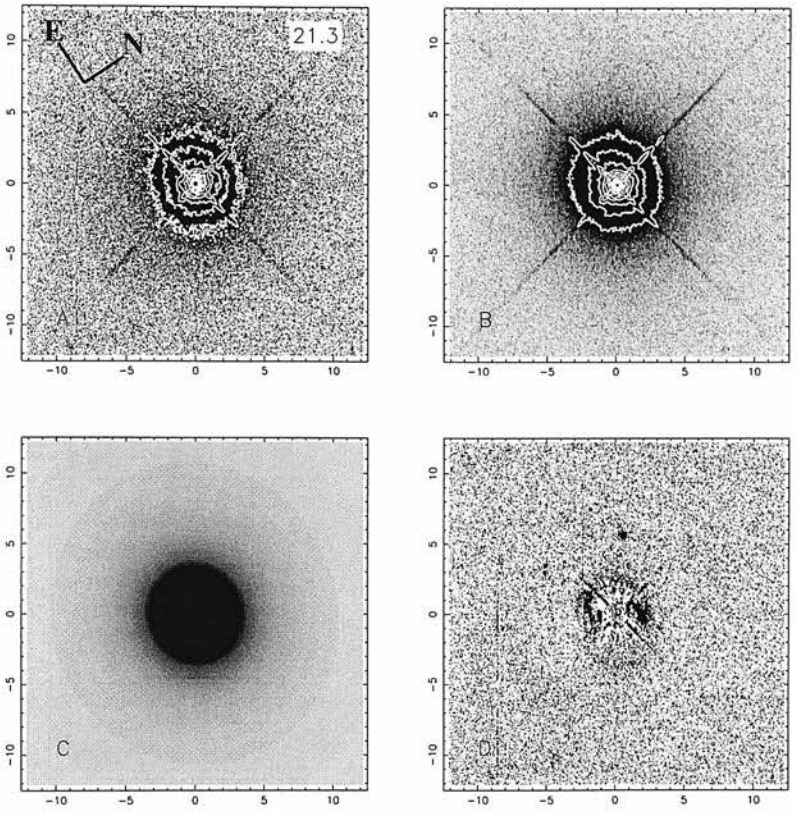

Figure A7. The radio-loud quasar 1004+130.

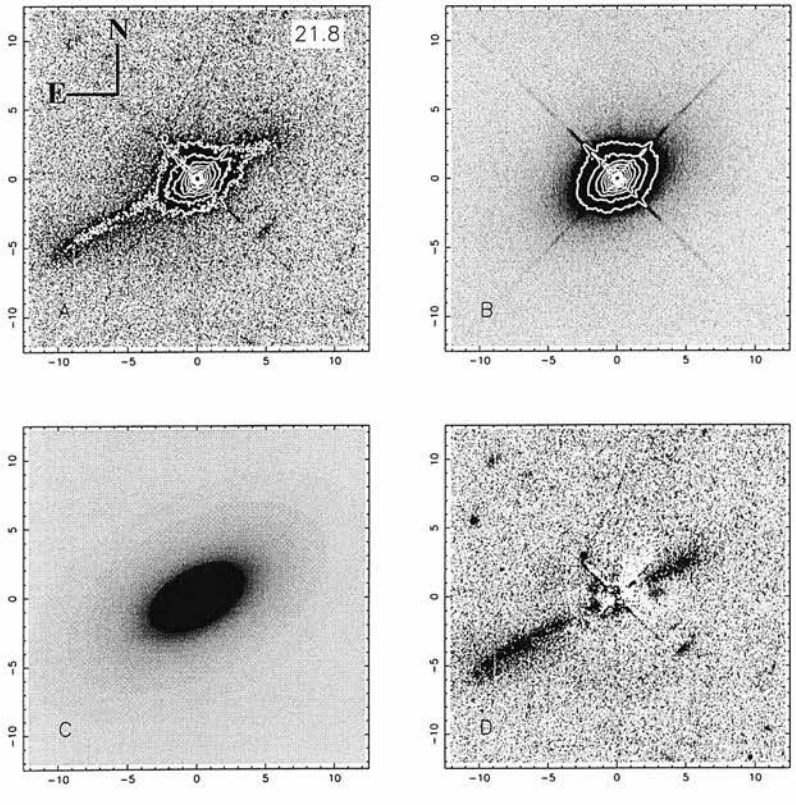

Figure A8. The radio-loud quasar 2141+175.

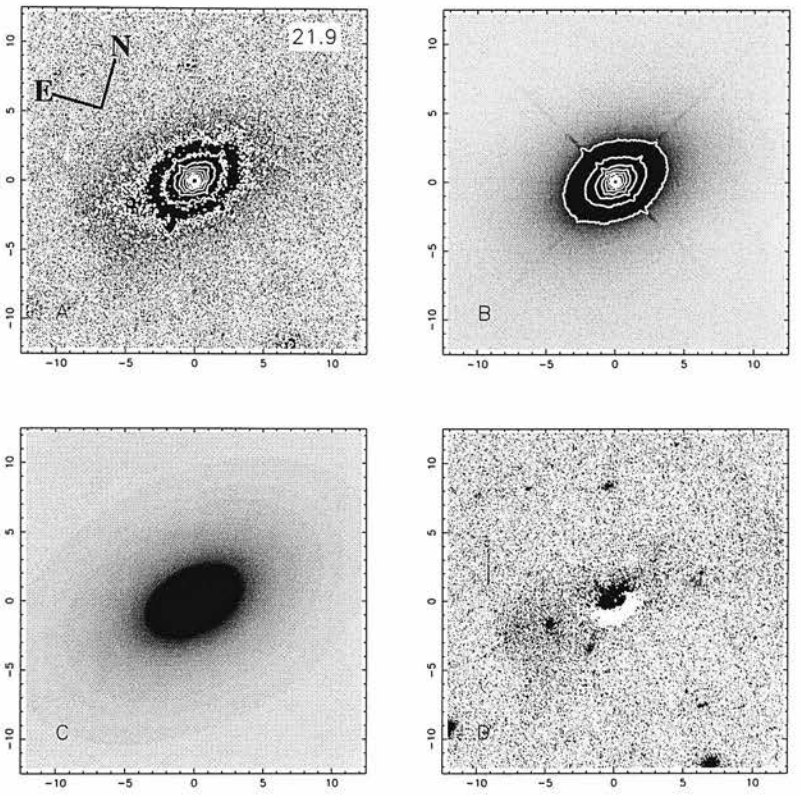

Figure A9. The radio-loud quasar 2247+140.

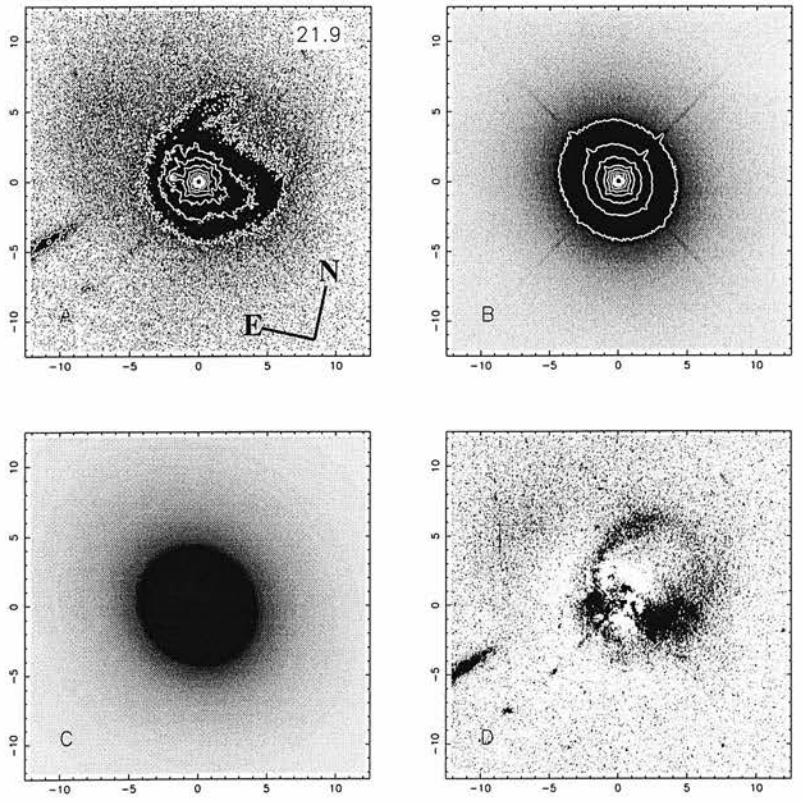

Figure A10. The radio-loud quasar 2349+014.

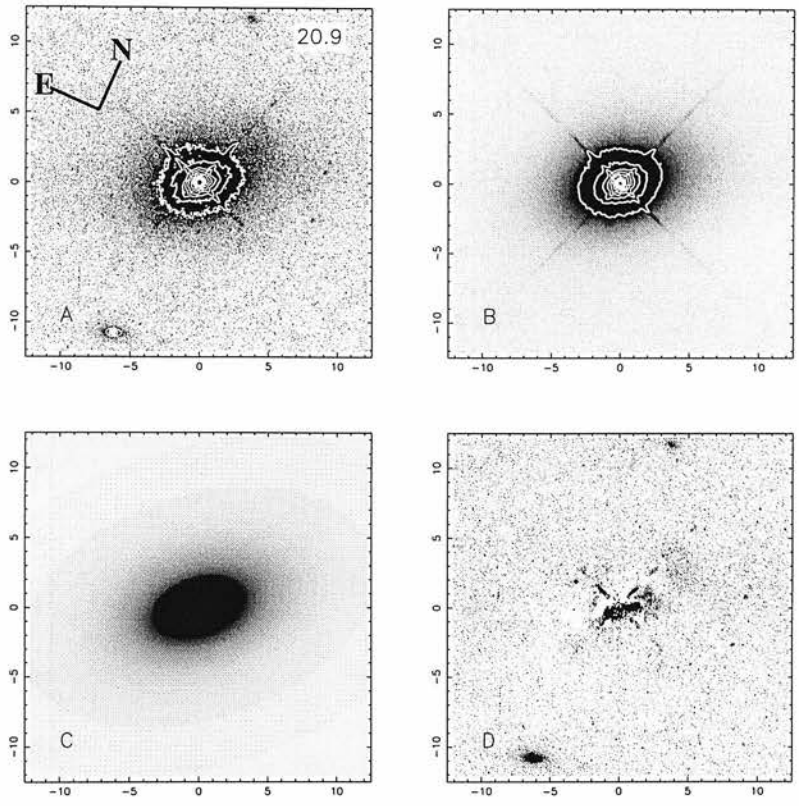

Figure A11. The radio-quiet quasar 0054+144.

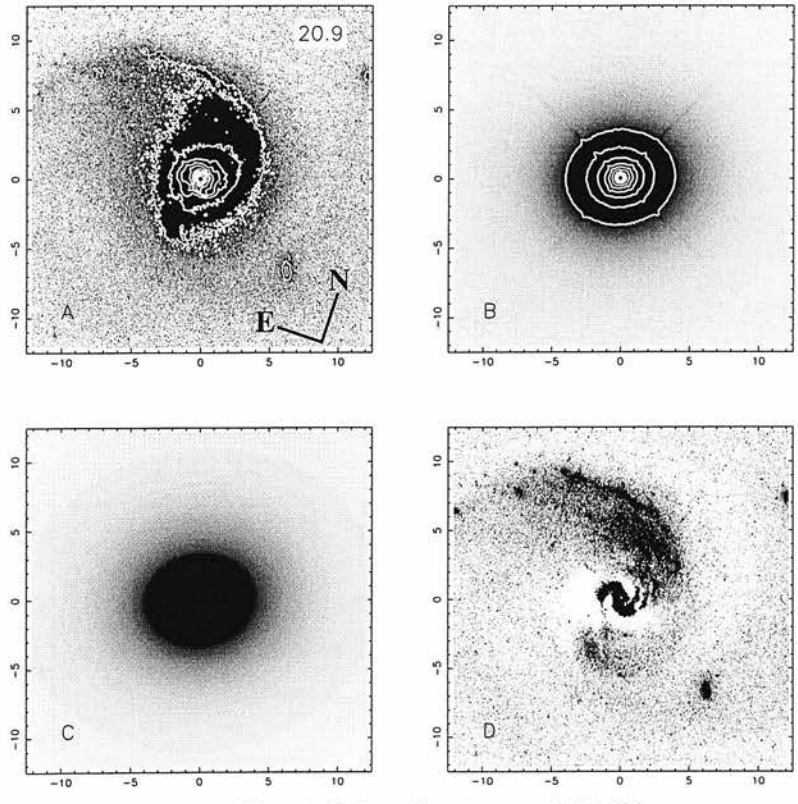

Figure A12. The radio-quiet quasar 0157+001.

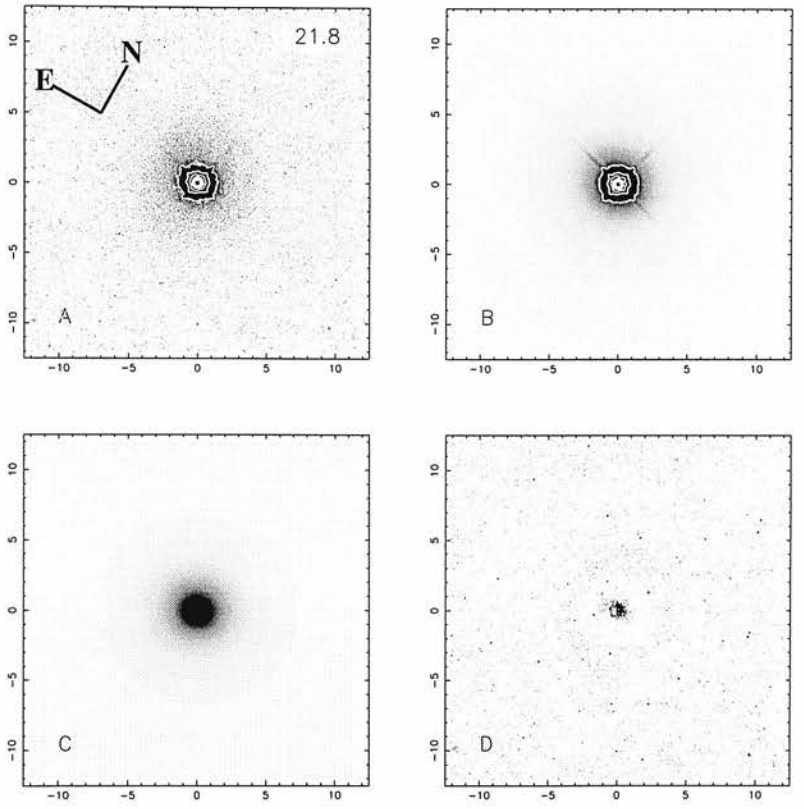

Figure A13. The radio-quiet quasar 0244+194.

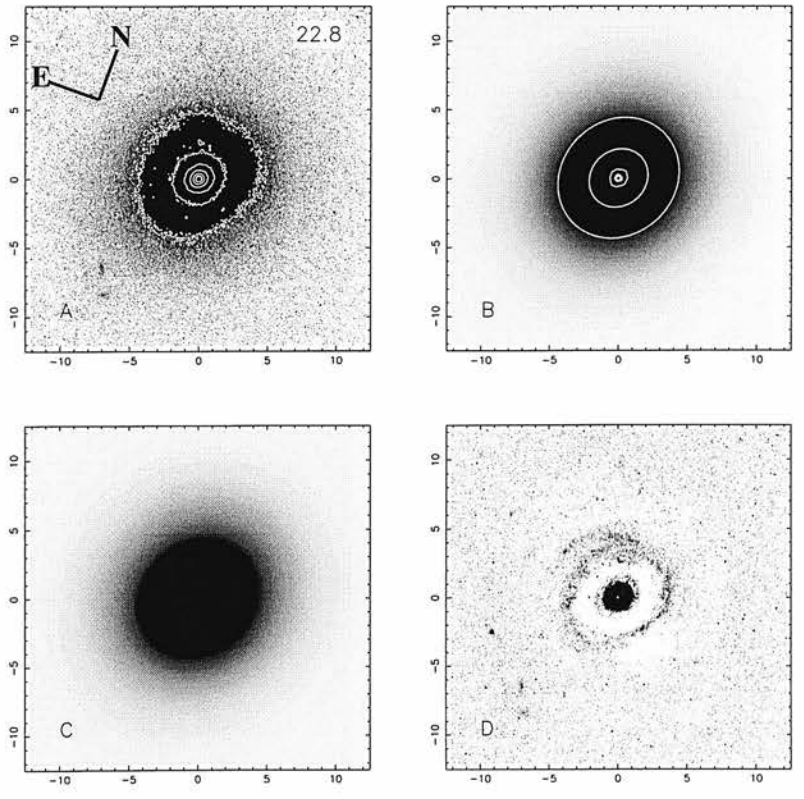

Figure A14. The radio-quiet quasar 0257+024.

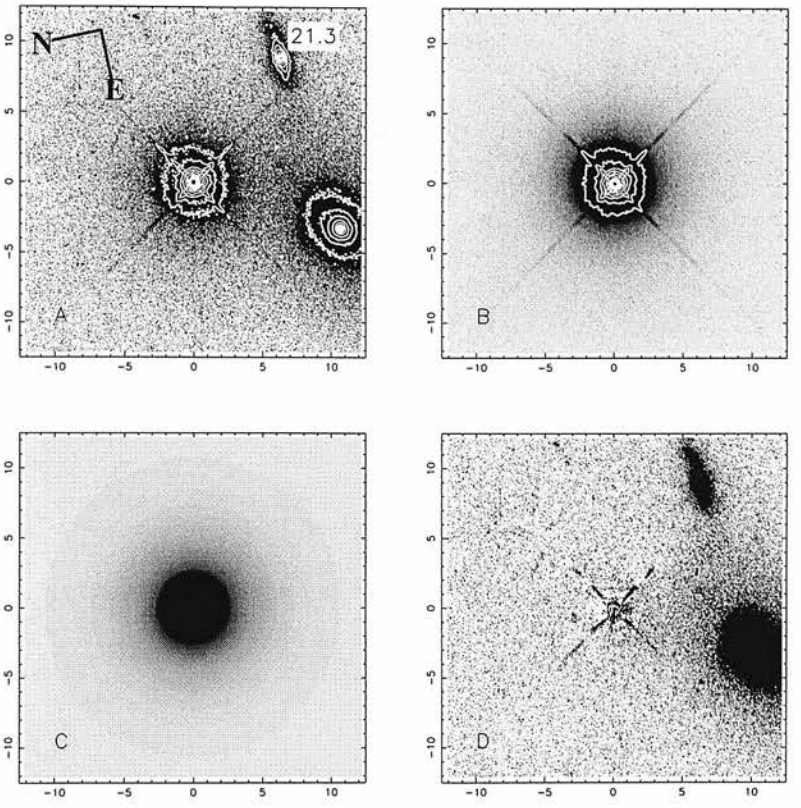

Figure A15. The radio-quiet quasar 0923+201.

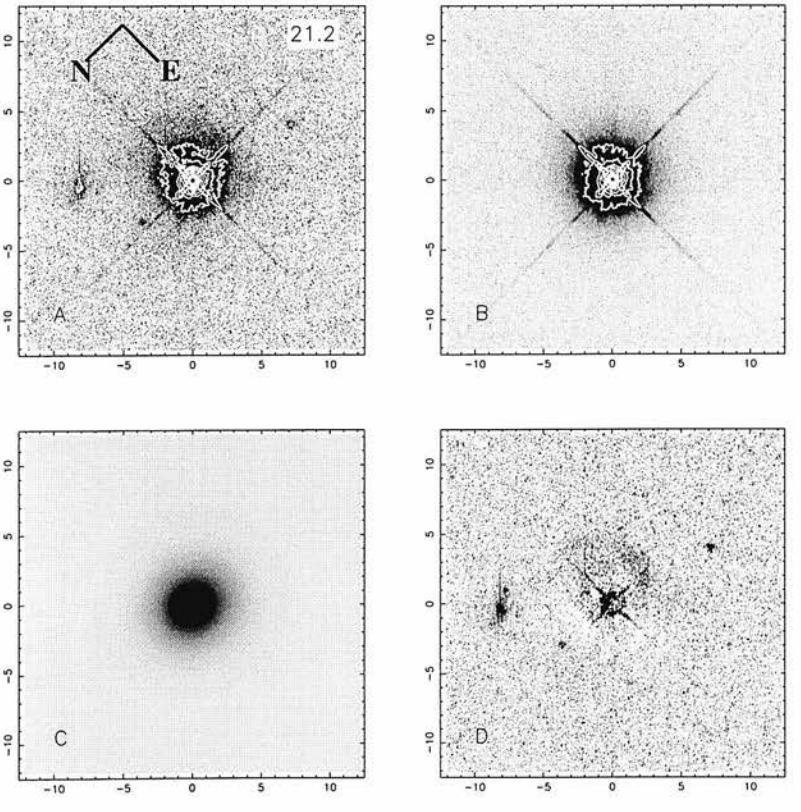

Figure A16. The radio-quiet quasar 0953+415.

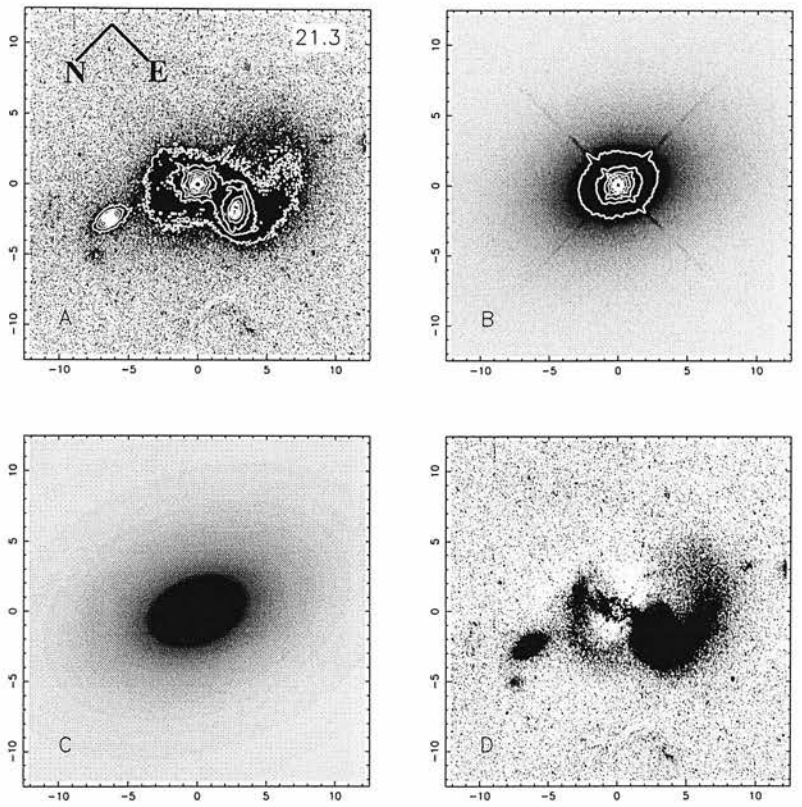

Figure A17. The radio-quiet quasar 1012+008.

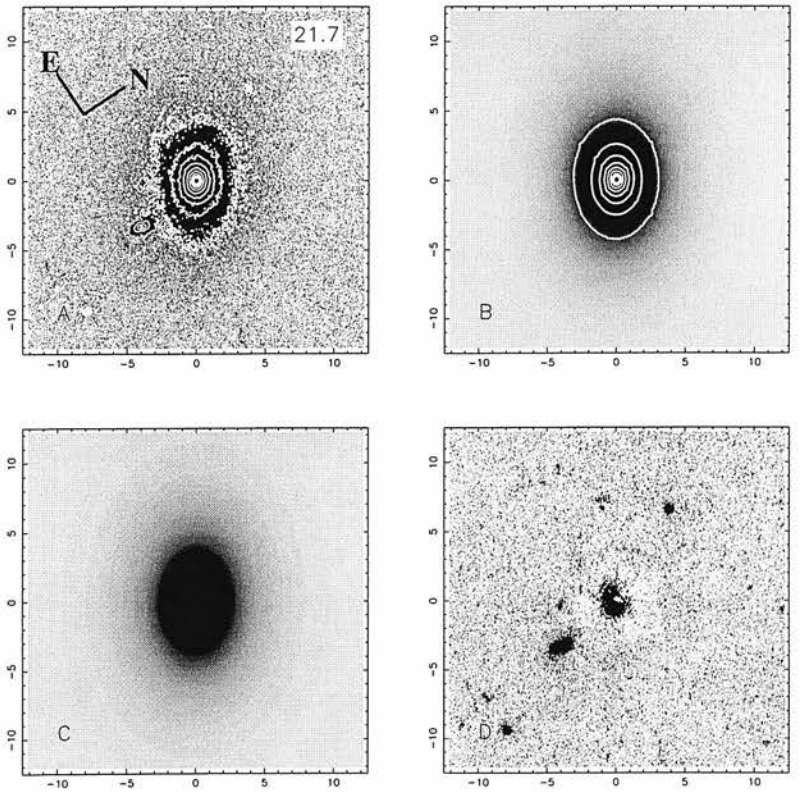

Figure A18. The radio-quiet quasar 1635+119.

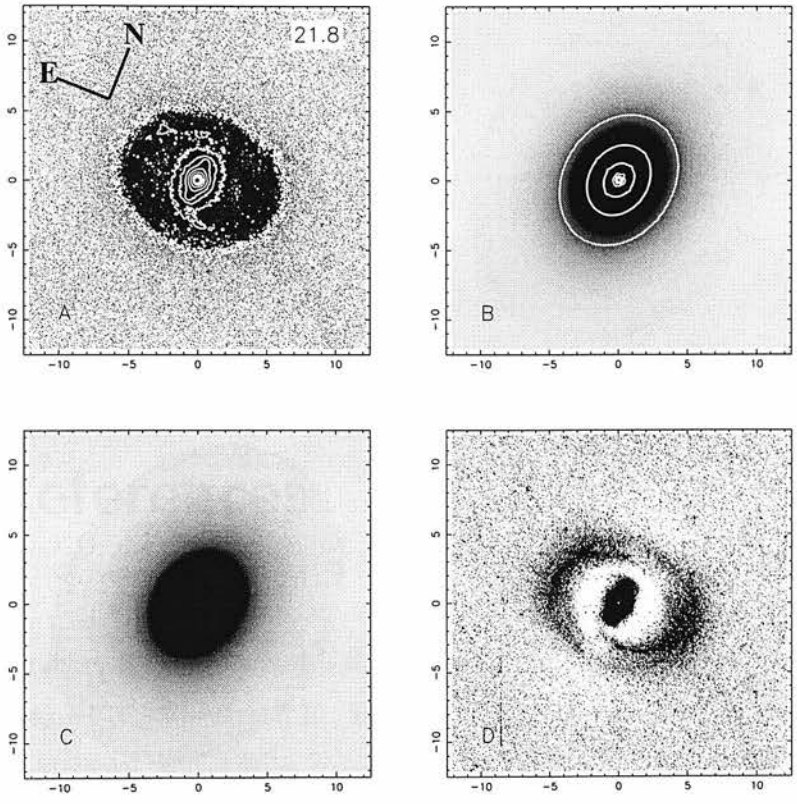

Figure A19. The radio-quiet quasar 2344+184.

Appendix D

References

Abraham R.G., Crawford C.S., McHardy I.M., 1992, ApJ, 401, 474

Akujor C.E., Spencer R.E., Zhang F.J., Davis R.J., Browne I.W.A., Fanti C., 1991, MNRAS, 250, 215

Antonucci R.J.J., 1985, ApJ, 59, 499

Antonucci R., Miller J.S., 1985, ApJ, 297, 621

Antonucci R., 1993, ARAA, 31, 473

Aragón-Salamanca A., Baugh C.M., Kauffmann G., 1998, MNRAS, 297, 427

Bahcall J.N., Kirhakos S., Schneider D.P., 1994, ApJ, 435, L11

Bahcall J.N., Kirhakos S., Schneider D.P., 1995a, ApJ, 447, L1

Bahcall J.N., Kirhakos S., Schneider D.P., 1995b, ApJ, 450, 486

Bahcall J.N., Kirhakos S., Schneider D.P., 1996, ApJ, 457, 557

Bahcall J.N., Kirhakos S., Saxe D.H., Schneider D.P., 1997, ApJ, 479, 642

Barthel P.D., 1989, ApJ, 336, 606

Best P.N., Longair M.S., Röttgering H.J.A., 1997, MNRAS, 292, 758

Best P.N., Longair M.S., Röttgering H.J.A., 1998, MNRAS, 295, 549

Biretta J.A., et al., 1996, WFPC2 Instrument Handbook Version 4.0

Blandford R.D., Konigl A., 1979, ApJ, 232, 34

Boroson T.A., Oke J.B., 1982, Nature, 296, 397

Boyce P.J., et al., 1998, MNRAS, 298, 121

Brinkmann W., Yaun W., Siebert J., 1997, A&A, 319, 413

Bruzual G., Charlot S., 1993, ApJ, 405, 538

Capaccioli M., Caon N., D'Onofrio M., 1992, MNRAS, 259, 323

Canalizo G., Stockton A., 1997, ApJ, 480, L5

Charlot, S., Worthey G., Bressan. A., 1996, ApJ, 457, 43

Clarke D.A., et al., 1992, ApJ, 385, 173

Clements D.L., et al., 1996, MNRAS, 279, 477

Collins C.A., Mann R.G., 1998, MNRAS, 297, 128

Crawford C.S., Fabian A.C., 1995, MNRAS, 273, 827

Davies R.I., Sugai H., Ward M.J., 1998, MNRAS, 300, 388

De Koff S., et al., 1996, ApJS, 107, 621

De Vaucouleurs G., Capaccioli M., 1978, ApJS, 40, 699

De Vries W.H., et al., 1998, ApJ, 503, 156

Dickinson M., 1997, in Tanvir N.R., Aragón-Salamanca A., Wall J.V., eds, HST and the high redshift Universe. Singapore: World Scientific

Disney M.J. et al., 1995, Nature, 376, 150

D'Onofrio M., Capaccioli M, Caon N., 1994, MNRAS, 271, 523

Dunlop J.S., et al., 1989, MNRAS, 238, 1171

Dunlop J.S., Peacock J.A., 1993, MNRAS, 262, 936

Dunlop J.S., 1998, In: *'The Most Distant Radio Galaxies'*, KNAW Colloquium Amsterdam, eds. Röttgering, H.J.A., Best, P., Lehnert, M.D., Kluwer, in press (astro-ph/9801114)

Dunlop J.S., Taylor G.L., Hughes D.H., Robson E.I., 1993, MNRAS, 264, 455

Eales S., Rawlings S., Law-Green D., Cotter G., Lacy M., 1997, MNRAS, 291, 593

Elvis M., et al., 1984, ApJ, 280, 574

Fanaroff B.L., Riley J.M., 1974, MNRAS, 167, 31

Feigelson E.D., Isobe T., Kembhavi A., 1984, AJ, 89, 1464

Ford H.C. et al., 1994, ApJ, 435, L27

Franceschini A., Vercellone S., Fabian A.C., 1998, MNRAS, 297, 817

Freeman K.C, 1970, ApJ, 160, 811

Fukugita M., Shimasaku K., Ichikawa T., 1995, PASP, 107, 945

Gaidos, E.J., 1997, AJ, 114, 474

Giovannini G., Feretti L., Gregorini L., Parma P., 1988, A&A, 199, 73

Graham A., et al., 1996, ApJ, 465, 534

Guiderdoni B., Rocca-Volmerange B., 1987, A&A, 186, 1

Glazebrook K., Peacock J.A., Miller L., Collins C.A., 1995, MNRAS, 275, 169

Goldschimdt P., et al., 1999, ApJ, 551, 612

Goncalves A.C., Véron P., Véron-Cetty P., 1998, A&AS, 127, 107

Goodrich R.W., et al., 1996, ApJ, 456, L9

Gower A.C., Hutchings J.B., 1984a, PASP, 96, 19

Gower A.C., Hutchings J.B., 1984b, AJ, 89, 1658

Granato G.L., et al., 1999, astro-ph/9903349

Hamabe M., Kormendy J., 1987, in: deZeeduw, T. eds, Proc. IAU Symp. 127 Structure & Dynamics of Elliptical Galaxies, p.379

Harms R.J., et al., 1994, ApJ, 435, L35

Heckman T.M., et al., 1984, ApJ, 89, 958

Heckman T.M., et al., 1986, ApJ, 311, 526

Hill G.J., Lilly S.J., 1991, ApJ, 367, 1

Hoessel J.G., Schneider D.P., 1985, ApJ, 90, 1648

Holtzman J.A., et al., 1995, PASP, 107, 1065

Hooper E.J., Impey C.D., Foltz C.B., 1997, ApJ, 480, L95

Hughes D.H., Kukula M.J., Dunlop J.S., Boroson T.B., 1999, MNRAS, in press

Hutchings J.B., Neff S.G., 1992, AJ, 104, 1

Hutchings J.B., Neff S.G., 1997, AJ, 113, 550

Hutchings J.B., et al., 1994, ApJ, 429, L1

Iwasawa K., et al., 1996, MNRAS, 282, 1038

Jimenez R., MacDonald J., 1996, MNRAS, 283, 721

Kauffmann G., Charlot S., 1999, astro-ph/9810031

Koehler et al., 1997, A&A, 325, 502

Kormendy J., 1977, ApJ, 217, 406

Kormendy J., Richstone D., 1995, ARA&A, 33, 581

Kotilainen J.K., Falomo R., Scarpa R., 1998, A&A, 336, 479

Krist J., 1998, TinyTim User Manual

Krist J., Burrows C., 1994, WFPC2 Instrument Science Report 94-01

Kristian J., 1973, ApJ, 179, L61

Kukula M.J., Dunlop J.S., Hughes D.H., Rawlings S., 1998, MNRAS, 297, 366

Kukula M.J., 2000, MNRAS, in preparation

Laing R.A., Riley J.M., Longair M.S., 1983, MNRAS, 204, 151

Lauer T.R., et al., 1995, AJ, 110, 2622

Leahy J.P., Pooley G.G., Riley J.M., 1986, MNRAS, 222, 753

Leyshon G., Eales S.A., 1998, MNRAS, 295, 10L

Lilly S.J., Longair M.S., 1984, MNRAS, 211, 833

Lilly S.J., Prestage R.M., 1987, MNRAS, 225, 531

Lin H., et al., 1996, ApJ, 464, 60

Lister, M.L., Gower, A.C., 1994, AJ, 108, 821

McCarthy P.J., Spinrad H., van Breugel W., 1995, ApJs, 99, 27

McCarthy P.J., van Breugel W., Kapahi V.K., 1991, ApJ, 371, 478

McLeod K.K., Rieke G.H., 1994, ApJ, 431, 137

McLeod K.K., Rieke G.H., 1995, ApJ, 454, L77

McLure R.J., et al., 1999, MNRAS, 308, 377

Macchetto et al., 1994, ApJ, 435, L15

Magorrian J., et al., 1998, AJ, 115, 2285

Marscher A., 1988, ApJ, 334, 552

Matthews T.A., Sandage A.R., 1963, ApJ, 138, 30

Meurs E.J.A., Unger S.W., 1991, A&A, 252, 63

Miley G.K., Hartsuijker A.P., 1978, A&AS, 34, 129

Miller L., Peacock J.A., Mead A.R.G., 1990, MNRAS, 244, 207

Miller P., Rawlings S., Saunders R., 1993, MNRAS, 263, 425

Miyoshi M., et al., 1995, Nature, 373, 127

Murphy T.W., et al., 1996, AJ, 111, 1025

Neugebauer G., et al., 1987, ApJS, 63, 615

Orr M.J.L., Browne I.W.A., 1982, MNRAS, 200, 1067

Osterbrock D.E., 1978, Proc. Natl. Acad. Sci. USA, 75, 540

Osterbrook D.E., 1981, ApJ, 249, 462

Peacock J.A., 1987, in Astrophysical Jets and Their Engines, ed. W. Kundt (Dordrecht Reidel) p.185

Pervical W., 1999, MNRAS, in preparation

Peterson B.M., 1997, "An Introduction to Active Galactic Nuclei", Cambridge University Press

Prestage R.M., Peacock J.A., 1988, MNRAS, 230, 131

Press W.H., 1989, "Numerical Recipes", Cambridge University Press

Rybicki, G.B., Lightman A.P., 1979, "Radiative Processes in Astrophysics", John Wiley and Sons: New York

Robson I., 1996, "Active Galactic Nuclei", John Wiley and Sons: New York

Rocca-Volmerange B., Guiderdoni B., 1988, A&AS, 75, 93

Romney J. et al., 1984, A&A, 135, 289

Ryden, S., 1992, ApJ, 396, 445

Sandage A.R., Freeman K.C., Stokes N.R., 1970, ApJ, 160, 831

Sanders D.B., et al., 1988, ApJ, 328, L35

Scheuer P.A.G., Readhead A.C.S., 1979, Nature, 277, 182

Schneider D.P., Gunn J.E., Hoessel J.G., 1983, ApJ, 268, 476

Schmidt M., 1963, Nature, 197, 1040

Schmidt M., 1965, ApJ, 141, 1295

Schombert J.M., 1987, ApJS, 64, 643

Sersic J.L., 1968, Atlas de Galaxies australes. Observatorio Astronomico Cordoba

Seyfert C., 1943, ApJ, 97, 28

Smith E.P., et al., 1986, ApJ, 306, 64

Smith E.P., Heckman T.M., 1989, ApJ, 341, 658

Spinrad H., et al., 1997, ApJ, 484, 581

Stiavelli M., et al., 1999, A&A, 343, L25

Stocke J.T, et al., 1983, ApJ, 273, 458

Stockton A., Farnham T., 1991, ApJ, 371, 525

Surace J.A., 1998, ApJ, 492, 116

Tanaka Y. et al, 1995, Nature, 375, 659

Taylor G.T., 1995, "The Environments of Active Galactic Nuclei", PhD. Thesis

Taylor G.T., Dunlop J.S., Hughes D.H., Robson E.I., 1996, MNRAS, 283, 930

Terlevich R., et al., 1992, MNRAS, 255, 713

Thaun T.X., Puschell J.J., 1989, ApJ, 346, 34

Turnshek, D.A., et al., 1990, AJ, 99, 1243

Urry C.M., Padovani P., 1995, PASP, 107, 803

Urry C.M., et al., 1999, ApJ, in press

van Breugel W., Miley G., Heckman T., 1984, AJ, 89, 5

Véron-Cetty M.P., Woltjer L., 1990, A&A, 236, 69

Véron-Cetty M.P., Veron P., 1991, ESO Scientific Report, Garching, European Southern Observatory (ESO), 5th ed.

Warren S.J., Hewett P.C., Osmer P.S., 1994, ApJ 421, 412

Wills B.J., Brandt W.N., 1999, ApJ, 520, L91

Wilson A.S., Colbert E.J.M., 1995, ApJ, 438, 62

Wilson A.S., Tsvetanov Z.I., 1994, AJ, 107, 1227

Wright S.C., McHardy I.M., Abraham R.G., 1998, MNRAS, 295, 799

Young P.J., 1978, ApJ, 221, 721

Young S. et al., 1998, MNRAS, 294, 478

Yuan W., Brinkmann W., Siebert J., Voges W., 1998, A& A, 330, 108

Zel'dovich, Ya.B., Novikov I.D., 1964, Sov. Phys. Dokl., 158, 811